

AD-A258 842



①

AFIT/ENY/GAE/92D-09

DTIC  
ELECTE  
JAN 07 1993  
S E D

APPLICATION OF THE PROGRAM PROFILE FOR  
THE DESIGN OF LOW-SPEED, LOW-  
OBSERVABLE CONFIGURATION AIRFOILS

THESIS

Gregory A. Sharp, Captain, USAF

AFIT/GAE/ENY/92D-09

93-00120  


Approved for public release: distribution unlimited

93 1 04 008

AFIT/GAE/ENY/92D-09

APPLICATION OF THE PROGRAM PROFILE FOR THE DESIGN OF LOW-  
SPEED, LOW-OBSERVABLE CONFIGURATION AIRFOILS

THESIS

Presented to the Faculty of the School of Engineering  
of the Air Force Institute of Technology

Air University

In Partial Fulfillment of the  
Requirements for the Degree of  
Master of Science in Aeronautical Engineering

Gregory A. Sharp, B.S.  
Captain, USAF

December 1992

Accession For	
NTIS CRA&I	<input checked="checked" type="checkbox"/>
DTIC TAB	<input type="checkbox"/>
Unannounced	<input type="checkbox"/>
Justification	
By	
Distribution/	
Availability Codes	
Dist	Avail and/or Special
A-1	

Approved for public release: distribution unlimited

### Acknowledgements

This research could not have been done without the contributions of many individuals. Most importantly, I give thanks to the Lord and Savoir, Jesus Christ, for giving me the ability, strength, and perseverance to complete this thesis.

I would like to express my sincere thanks to my advisor, Dr. Paul King, for his guidance during all phases of this project. Also, I would like to thank the members of my thesis committee, Dr. Philip Beran and Lt. Col. Gerald A. Hasen, for their advise. Thanks to my sponsor, Dr. Don Kinsey. He always had the time to listen and gave me sound ideas along the way. Thanks to Mr. Doug Hall and Mr. Dan Somers. They were indispensable in helping me get through problems and answering questions about PROFILE.

To my wife, Michelle, thank you just does not seem enough to say for all the sacrifices you have made for me. All I can say is I love you. To my beloved son, Paul, your smile and laugh melted away the hardest days. Finally to my moms and dads, Mr. & Mrs. Clyde Sharp and Mr. & Mrs. Fred Slack, thank you for all the support and help you have given us during the past year. Your efforts were greatly appreciated and helped me more than you will ever know.

Gregory Allen Sharp

## Table of Contents

Acknowledgements . . . . .	ii
List of Figures . . . . .	v
List of Tables . . . . .	xi
Table of Symbols . . . . .	xii
Abstract . . . . .	xvi
I. Introduction . . . . .	1
Background . . . . .	1
Scope . . . . .	2
Objectives . . . . .	3
II. Theory . . . . .	5
Potential-Flow Design Method . . . . .	5
Potential-Flow Analysis Method . . . . .	13
Boundary-Layer Method . . . . .	14
General Equations . . . . .	15
Laminar Boundary-Layers . . . . .	17
Turbulent Boundary-Layers . . . . .	18
Boundary-Layer Transition . . . . .	19
III. Analysis and Limitations . . . . .	21
Amount and Location of the Pressure Recovery . . . . .	22
Boundary-Layer Displacement Iteration . . . . .	25
Viscous Corrections to Section Lift Coefficient (Separation) . . . . .	28
Specification of the Velocity Distribution . . . . .	30
IV. Results and Comparisons . . . . .	36
Case Summary . . . . .	36

Case 1. $A = 1$ . . . . .	36
Case 2. $A = 1/2$ . . . . .	37
Case 3. $A = 1/3$ . . . . .	38
Case 4. $A = 1/4$ . . . . .	38
Case 5. $A = 1/5$ . . . . .	39
Case Comparisons . . . . .	40
Design Implications . . . . .	41
Comparison of T-Series Airfoils with NACA 4-Digit Airfoils . . . . .	42
V. Conclusions and Recommendations . . . . .	48
Conclusions . . . . .	48
Recommendations for Further Study . . . . .	49
References . . . . .	51
Appendix A: Summary of the $(v_i, \alpha_i^*)$ Pairs . . . . .	182
Appendix B: Code Input . . . . .	189
Appendix C: Summary of Input Files . . . . .	192
Vita. . . . .	198

## List of Figures

Figure	Page
1. Mathematical Planes for Conformal Mapping . . . . .	53
2. Arc Limit Description . . . . .	54
3. Pressure Recovery and Closure Contributions . . . . .	55
4. Airfoil E398 and Pressure Distributions - t/c = 14.27% - Incompressible . . . . .	56
5. Sensitivity of Pressure Distribution to Changes in Location of Specified Main Pressure Recovery - Airfoil G48 - $\alpha = 2^\circ$ . . . . .	57
6. Terminology Summary . . . . .	58
7. Sensitivity of Thickness-to-Chord Ratio and Maximum Lift Coefficient to the Location of the Secondary Pressure Recovery - Airfoil G48 . . . . .	59
8. Velocity Distributions - Airfoils SH9 - Incompressible - $\alpha = 2^\circ$ . . . . .	60
9. Velocity Distributions - Airfoil SH9 - Incompressible - $\alpha = 2^\circ$ . . . . .	61
10. Pressure Distributions - NACA 4415 - $M = .4$ - $\alpha = 4^\circ$ . . . . .	62
11. NACA 0006 $C_1$ vs $\alpha$ Curve . . . . .	63
12. Correction to $C_1$ Due to Separation . . . . .	64
13. Airfoil G31 - t/c = 4.95% . . . . .	65
14. Airfoil G31 Leading-Edge - t/c = 4.95% . . . . .	66
15. Airfoil G31 - $C_1$ vs $\alpha$ curve . . . . .	67
16. Effect of $\alpha_{i^*,le}$ on the Thickness-to-Chord Ratio . . . . .	68
17. Effect of $\alpha_{i^*,le}$ on the Leading-Edge Radius . . . . .	69
18. Pressure Distributions - NACA 0006 vs NACA 0012 - Incompressible . . . . .	70
19. TA2-TA5 Curves - Proposed $\alpha^*$ - $\lambda$ Relationships . . . . .	71
20. Airfoil TA2 - t/c = 12.5% . . . . .	72

21.	Airfoil TA2 Leading-Edge - $t/c = 12.5\%$ . . . . .	73
22.	Pressure Distributions - TA2 - Incompressible . .	74
23.	Airfoil TA3 - $t/c = 9.05\%$ . . . . .	75
24.	Airfoil TA3 Leading-Edge - $t/c = 9.05\%$ . . . . .	76
25.	Pressure Distributions - TA3 - Incompressible . .	77
26.	Airfoil TA4 - $t/c = 5.56\%$ . . . . .	78
27.	Airfoil TA4 Leading-Edge - $t/c = 5.56\%$ . . . . .	79
28.	Pressure Distributions - TA4 - Incompressible . .	80
29.	Airfoil TA5 - $t/c = 2.37\%$ . . . . .	81
30.	Airfoil TA5 Leading-Edge - $t/c = 2.37\%$ . . . . .	82
31.	Pressure Distributions - TA5 - Incompressible . .	83
32.	Power Law Relationships ( $A=1$ ) . . . . .	84
33.	Power Law Relationships ( $A=1/2$ ) . . . . .	85
34.	Power Law Relationships ( $A=1/3$ ) . . . . .	86
35.	Power Law Relationships ( $A=1/4$ ) . . . . .	87
36.	Power Law Relationships ( $A=1/5$ ) . . . . .	88
37.	Airfoil T25 - $t/c = 2.96\%$ . . . . .	89
38.	Airfoil T25 Leading-Edge - $t/c = 2.96\%$ . . . . .	90
39.	Pressure Distributions - T25 - Incompressible . .	91
40.	Airfoil T25 vs $C_l, C_m$ vs $\alpha$ Curves . . . . .	92
41.	Airfoil T30 - $t/c = 3.59\%$ . . . . .	93
42.	Airfoil T30 Leading-Edge - $t/c = 3.59\%$ . . . . .	94
43.	Pressure Distributions - T30 - Incompressible . .	95
44.	Airfoil T30 - $C_l, C_m$ vs $\alpha$ Curves . . . . .	96
45.	Airfoil T3 - $t/c = 4.09\%$ . . . . .	97
46.	Airfoil T3 Leading-Edge - $t/c = 4.09\%$ . . . . .	98
47.	Pressure Distributions - T3 - Incompressible . . .	99

48.	Airfoil T3 - $C_l, C_m$ vs $\alpha$ Curves . . . . .	100
49.	Airfoil T4 - $t/c = 5.17\%$ . . . . .	101
50.	Airfoil T4 Leading-Edge - $t/c = 5.17\%$ . . . . .	102
51.	Pressure Distributions - T4 - Incompressible . . .	103
52.	Airfoil T4 - $C_l, C_m$ vs $\alpha$ Curves . . . . .	104
53.	Airfoil T402 - $t/c = 3.44\%$ . . . . .	105
54.	Airfoil T402 Leading-Edge - $t/c = 3.44\%$ . . . . .	106
55.	Pressure Distributions - T402 - Incompressible .	107
56.	Airfoil T402 - $C_l, C_m$ vs $\alpha$ Curves . . . . .	108
57.	Airfoil T22 - $t/c = 4.75\%$ . . . . .	109
58.	Airfoil T22 Leading-Edge - $t/c = 4.75\%$ . . . . .	110
59.	Pressure Distributions - T22 - Incompressible . .	111
60.	Airfoil T22 - $C_l, C_m$ vs $\alpha$ Curves . . . . .	112
61.	Airfoil T503 - $t/c = 3.79\%$ . . . . .	113
62.	Airfoil T503 Leading-Edge - $t/c = 3.79\%$ . . . . .	114
63.	Pressure Distributions - T503 - Incompressible .	115
64.	Airfoil T503 - $C_l, C_m$ vs $\alpha$ Curves . . . . .	116
65.	Airfoil T603 - $t/c = 5.08\%$ . . . . .	117
66.	Airfoil T603 Leading-Edge - $t/c = 5.08\%$ . . . . .	118
67.	Pressure Distributions - T603 - Incompressible .	119
68.	Airfoil T603 - $C_l, C_m$ vs $\alpha$ Curves . . . . .	120
69.	Airfoil T504 - $t/c = 3.25\%$ . . . . .	121
70.	Airfoil T504 Leading-Edge - $t/c = 3.25\%$ . . . . .	122
71.	Pressure Distributions - T504 - Incompressible .	123
72.	Airfoil T504 - $C_l, C_m$ vs $\alpha$ Curves . . . . .	124
73.	Airfoil T604 - $t/c = 4.3\%$ . . . . .	125
74.	Airfoil T604 Leading-Edge - $t/c = 4.3\%$ . . . . .	126



75.	Pressure Distributions - T604 - Incompressible .	127
76.	Airfoil T604 - $C_l, C_m$ vs $\alpha$ Curves . . . . .	128
77.	Airfoil T234 - $t/c = 4.97\%$ . . . . .	129
78.	Airfoil T234 Leading-Edge - $t/c = 4.97\%$ . . . . .	130
79.	Pressure Distributions - T234 - Incompressible .	131
80.	Airfoil T234 - $C_l, C_m$ vs $\alpha$ Curves . . . . .	132
81.	Airfoil T505 - $t/c = 2.89\%$ . . . . .	133
82.	Airfoil T505 Leading-Edge - $t/c = 2.89\%$ . . . . .	134
83.	Pressure Distributions - T505 - Incompressible .	135
84.	Airfoil T505 - $C_l, C_m$ vs $\alpha$ Curves . . . . .	136
85.	Airfoil T605 - $t/c = 3.82\%$ . . . . .	137
86.	Airfoil T605 Leading-Edge - $t/c = 3.82\%$ . . . . .	138
87.	Pressure Distributions - T605 - Incompressible .	139
88.	Airfoil T605 - $C_l, C_m$ vs $\alpha$ Curves . . . . .	140
89.	Airfoil T6605 - $t/c = 4.58\%$ . . . . .	141
90.	Airfoil T6605 Leading-Edge - $t/c = 4.58\%$ . . . . .	142
91.	Pressure Distributions - T6605 - Incompressible .	143
92.	Airfoil T6605 - $C_l, C_m$ vs $\alpha$ Curves . . . . .	144
93.	Thickness-to-Chord Ratio vs $d$ . . . . .	145
94.	Leading-Edge Radius vs Thickness-to-Chord Ratio .	146
95.	Comparison of NACA 4-digit vs Airfoil T3 - $t/c = 4.09\%$ . . . . .	147
96.	Airfoil T3 vs NACA 4-Digit Airfoil Pressure Distributions - $\alpha = 4^\circ$ - Incompressible . . . . .	148
97.	$C_l(\alpha)$ Curve - NACA 4-digit airfoil vs Airfoil T3 . . . . .	149
98.	$C_l-C_d$ plot - Airfoil T3 vs NACA 4-digit airfoil - $t/c = 4.09\%$ . . . . .	150

99.	Lift-drag ratio - Airfoil T3 vs NACA 4-digit airfoil . . . . .	151
100.	Boundary-Layer Development - Upper Surface - Airfoil T3 - $Re = 3.0 \times 10^6$ . . . . .	152
101.	Boundary-Layer Development - Upper Surface - NACA 4-digit Airfoil - $t/c = 4.09\%$ - $Re = 3.0 \times 10^6$ . . . . .	153
102.	Comparison of NACA 4-digit vs Airfoil T22 - $t/c = 4.75\%$ . . . . .	154
103.	Airfoil T22 vs NACA 4-Digit Airfoil Pressure Distributions - $\alpha = 6^\circ$ - Incompressible . . . . .	155
104.	$C_l(\alpha)$ Curve - NACA 4-digit airfoil vs Airfoil T22 . . . . .	156
105.	$C_l-C_d$ plot - Airfoil T22 vs NACA 4-digit airfoil - $t/c = 4.75\%$ . . . . .	157
106.	Lift-drag ratio - Airfoil T22 vs NACA 4-digit airfoil . . . . .	158
107.	Boundary-Layer Development - Upper Surface - Airfoil T22 - $Re = 3.0 \times 10^6$ . . . . .	159
108.	Boundary-Layer Development - Upper Surface - NACA 4-digit Airfoil - $t/c = 4.75\%$ - $Re = 3.0 \times 10^6$ . . . . .	160
109.	Comparison of NACA 4-digit vs Airfoil T603 - $t/c = 5.08\%$ . . . . .	161
110.	Airfoil T603 vs NACA 4-Digit Airfoil Pressure Distributions - $\alpha = 6^\circ$ - Incompressible . . . . .	162
111.	$C_l(\alpha)$ Curve - NACA 4-digit airfoil vs Airfoil T603 . . . . .	163
112.	$C_l-C_d$ plot - Airfoil T603 vs NACA 4-digit airfoil - $t/c = 5.08\%$ . . . . .	164
113.	Lift-drag ratio - Airfoil T603 vs NACA 4-digit airfoil . . . . .	165
114.	Boundary-Layer Development - Upper Surface - Airfoil T603 - $Re = 3.0 \times 10^6$ . . . . .	166
115.	Boundary-Layer Development - Upper Surface - NACA 4-digit Airfoil - $t/c = 5.08\%$ - $Re = 3.0 \times 10^6$ . . . . .	167
116.	Comparison of NACA 4-digit vs Airfoil T234 - $t/c = 4.97\%$ . . . . .	168

117.	Airfoil T234 vs NACA 4-Digit Airfoil Pressure Distributions - $\alpha = 6^\circ$ - Incompressible . . . . .	169
118.	$C_l(\alpha)$ Curve - NACA 4-digit airfoil vs Airfoil T234 . . . . .	170
119.	$C_l-C_d$ plot - Airfoil T234 vs NACA 4-digit airfoil - $t/c = 4.97\%$ . . . . .	171
120.	Lift-drag ratio - Airfoil T234 vs NACA 4-digit airfoil . . . . .	172
121.	Boundary-Layer Development - Upper Surface - Airfoil T234 - $Re = 3.0 \times 10^6$ . . . . .	173
122.	Boundary-Layer Development - Upper Surface - NACA 4-digit Airfoil - $t/c = 4.97\%$ - $Re = 3.0 \times 10^6$ .	174
123.	Comparison of NACA 4-digit vs Airfoil T605 - $t/c = 3.82\%$ . . . . .	175
124.	Airfoil T605 vs NACA 4-Digit Airfoil Pressure Distributions - $\alpha = 4^\circ$ - Incompressible . . . . .	176
125.	$C_l(\alpha)$ Curve - NACA 4-digit airfoil vs Airfoil T605 . . . . .	177
126.	$C_l-C_d$ plot - Airfoil T605 vs NACA 4-digit airfoil - $t/c = 3.82\%$ . . . . .	178
127.	Lift-drag ratio - Airfoil T605 vs NACA 4-digit airfoil . . . . .	179
128.	Boundary-Layer Development - Upper Surface - Airfoil T605 - $Re = 3.0 \times 10^6$ . . . . .	180
129.	Boundary-Layer Development - Upper Surface - NACA 4-digit Airfoil - $t/c = 3.82\%$ - $Re = 3.0 \times 10^6$ .	181

# List of Tables

Table	Page
1. Summary for TA-Series Airfoils . . . . .	34
2. T-Series Airfoil Summary ( $A = 1$ ) . . . . .	37
3. T-Series Airfoil Summary ( $A = 1/2$ ) . . . . .	38
4. T-Series Airfoil Summary ( $A = 1/3$ ) . . . . .	38
5. T-Series Airfoil Summary ( $A = 1/4$ ) . . . . .	39
6. T-Series Airfoil Summary ( $A = 1/5$ ) . . . . .	40
7. Leading-Edge Radius (T-Series & NACA 4-Digit Airfoils) . . . . .	44
8. Maximum Lift Coefficient (T-Series & NACA 4-Digit Airfoils) . . . . .	45
A.1 Summary of $(v_i, \alpha_i^*)$ Pairs for TA-Series Airfoils . . . . .	183
A.2 Summary of $(v_i, \alpha_i^*)$ Pairs for T-Series Airfoils ( $A = 1$ ) . . . . .	184
A.3 Summary of $(v_i, \alpha_i^*)$ Pairs for T-Series Airfoils ( $A = 1/2$ ) . . . . .	185
A.4 Summary of $(v_i, \alpha_i^*)$ Pairs for T-Series Airfoils ( $A = 1/3$ ) . . . . .	186
A.5 Summary of $(v_i, \alpha_i^*)$ Pairs for T-Series Airfoils ( $A = 1/4$ ) . . . . .	187
A.6 Summary of $(v_i, \alpha_i^*)$ Pairs for T-Series Airfoils ( $A = 1/5$ ) . . . . .	188

### Table of Symbols

Symbols	Definition
A	coefficient of power law relationship
$a_m, b_m$	power-series coefficients
$C_p$	pressure coefficient
c	airfoil chord
$C_l$	section lift coefficient
$C_m$	section pitching-moment coefficient about quarter-chord point
d	exponent of power law relationship
$D^*$	dissipation function for laminar boundary layer
F	complex potential function
$H_{12}$	boundary-layer shape factor
$H_{32}$	boundary-layer shape factor
I	total number of airfoil segments
K	constant in upper-surface pressure-recovery function
$\bar{K}$	constant in lower-surface pressure-recovery function
$K_H$	exponent of upper-surface closure contribution
$\bar{K}_H$	exponent of lower-surface closure contribution
$K_R$	desired value of $K_S$
$K_S$	sum of exponents of upper- and lower-surface closure contributions, $K_H + \bar{K}_H$
$K_{tol}$	tolerance on achievement of $K_R$
L	reference length

N	NQ-1
NQ	total number of airfoil points
Q	conjugate harmonic function of $P(\phi)$
$Re_{\zeta_2}$	Reynolds number based on local conditions and boundary-layer momentum thickness
$r_t$	leading-edge radius (nondimensionalized)
$s_{sep}$	arc length along which boundary-layer is separated
$t/c$	thickness-to-chord ratio
U	potential-flow velocity
$U_\infty, V_\infty$	free-stream velocity
u	x-component of boundary-layer velocity
V	absolute value of complex velocity; local velocity on airfoil
$v^*$	local velocity on airfoil for velocity specification in design method
$v_0$	normal velocity at surface in boundary-layer method
$\bar{w}$	complex velocity, $ve^{-i\theta}$
x	airfoil abscissa, m; axis in streamwise direction, tangential to surface in boundary-layer method
$x_w$	chord location of beginning of main pressure-recovery region
y	airfoil ordinate, m; axis normal to surface in boundary-layer method
$\alpha$	angle of attack relative to zero-lift line
$\alpha^*$	angle of attack relative to zero-lift line for velocity specification in design method
$\alpha_i^*$	$\alpha^*$ for ith segment of $\zeta$ circle or airfoil
$\alpha_{i,le}^*$	$\alpha^*$ for last segment of upper surface
$\Gamma$	circulation

$\Delta C_1$	section lift-coefficient correction due to separation
$\Delta \alpha$	angle-of-attack correction due to separation
$\Delta \phi$	angle between points on $\zeta$ unit circle,
$\delta$	slope of airfoil surface near trailing edge
$\delta_1$	boundary-layer displacement thickness
$\delta_2$	boundary-layer momentum thickness
$\delta_3$	boundary-layer energy thickness
$\epsilon^*$	skin friction function
$\zeta$	complex variable
$\gamma$	argument of complex velocity
$\eta$	ordinate in complex plane
$\xi$	abscissa in complex plane
$\lambda$	beginning of upper-surface main pressure-recovery region
$\lambda^*$	beginning of upper-surface closure contribution
$\bar{\lambda}$	beginning of upper-surface main pressure-recovery region
$\bar{\lambda}^*$	beginning of upper-surface closure contribution
$\mu$	exponent of upper-surface main pressure recovery
$\bar{\mu}$	exponent of lower-surface main pressure recovery
$\rho$	air density
$\tau_o$	skin friction
$\phi$	argument of $\zeta$
$\phi_I$	arc limit of lower-surface trailing edge
$\phi_i$	arc limit on $\zeta$ unit circle

$\phi_{i,le}$	arc limit of leading-edge
$\phi_s$	arc limit of beginning of upper-surface closure-contribution region
$\bar{\phi}_s$	arc limit of beginning of lower-surface closure-contribution region
$\phi_w$	arc limit of beginning of upper-surface main pressure-recovery region
$\bar{\phi}_w$	arc limit of beginning of lower-surface main pressure-recovery region
$\psi$	integration variable
$\omega$	total amount of upper-surface main pressure recovery
$\bar{\omega}$	total amount of lower-surface main pressure recovery
$\omega'$	initial slope of upper-surface main pressure recovery
$\bar{\omega}'$	initial slope of lower-surface main pressure recovery

Subscripts:

$i, j$	index; 1,2,3,....,
le	leading-edge
ls	lower surface
max	maximum
min	minimum
sep	separation
R	reference value
te	trailing edge
us	upper surface



### Abstract

This study investigated the use of the program PROFILE for the design of low-speed, low-observable configuration airfoils. For our purposes, low-observable configuration is defined as being characterized by a small leading-edge radius of less than 1.18 percent chord and a thickness-to-chord ratio of 2.5 to 5.5 percent. A methodology was developed whereby the input parameters to prescribe the velocity distribution over the airfoil could be determined by a power law relationship. This relationship enables the designer to develop symmetric airfoils with the desired thickness-to-chord and leading-edge radius within the stated constraints. The resulting symmetric airfoils compared very well with NACA 4-digit airfoils of like thickness-to-chord ratio. The resulting airfoils have an increased stall angle compared to the NACA 4-digit airfoils.

# APPLICATION OF THE PROGRAM PROFILE FOR THE DESIGN OF LOW-SPEED, LOW-OBSERVABLE CONFIGURATION AIRFOILS

## I. Introduction

### Background

In the 1950's, the United State's reconnaissance and intelligence communities made the first serious attempts to make less detectable military aircraft. Through these efforts, a standard for detectability was established to compare and measure the performance of any system. This standard is called the radar cross-section, (RCS), which is determined by first measuring or calculating the amount of radar energy reflected from the target to an observer. Then, the RCS is determined by the size of a reflective sphere that would return the same amount of radar energy. From this point in time, the race for low-observability has continued and has expanded from the reconnaissance world to all military aircraft.

Most recently, the Stealth fighter's success in Operation Desert Storm proved the military advantage and lethality of low-observable technology for today's Air Force. It also emphasized the importance this technology will play in subsequent tactical aircraft.

However, a problem exists for today's airfoil designers dealing with this technology. Currently, a shortage of data

exists in the open literature for configurations representative of general, low-observable airfoils. The problem may come about since most data is a result of either reduced radar cross section airfoils or radar absorbing materials testing, and is therefore classified. Beyond the classification problem, the data is usually limited to persons with special access clearances. Therefore, these reports could not be located in a normal classified literature search.

To address the problem, the Flight Dynamics Directorate of Wright Laboratory (WL/FIMM), Wright-Patterson Air Force Base, through consultation with the Naval Air Weapons Center, Warminster, Pennsylvania, obtained the analysis program, PROFILE. This program was developed by Richard Eppler (1) of the University of Stuttgart. This program applies an inverse design method that has been developed over a period of about twenty years. An airfoil velocity or pressure distribution is prescribed from which an airfoil geometry is obtained. The program consists of a conformal mapping method for the design of airfoils with imposed velocity-distribution characteristics, a panel method for the analysis of the potential flow about a given airfoil, and a boundary-layer method.

### Scope

For the purpose of this thesis, we will define the general low-observable airfoil configuration as being

characterized by both a small, leading-edge radius ( $r_t$ ) and a small thickness-to-chord ratio ( $t/c$ ). More specifically, for this investigation, the desired airfoil  $t/c$  range is  $2.5\% \leq t/c \leq 5.5\%$ . The defining factor in limiting the leading-edge radius will be the threat frequency. Better qualities of low-observability are obtained if the scattering return of the radar energy is reduced. A reduction is achieved if the radius of the illuminated surface is less than the wavelength of the threat radar (2). For this investigation, a threat frequency of 10 gigahertz was specified by WL/FIMM. This results in a wavelength of three centimeters or approximately 1.18 inches.

The investigation is based on the assumption that the airfoil has a minimum chord,  $c$ , of 100 inches. This specifies an upper limit of 0.0118 for  $r_t$ . Note,  $r_t$  has been nondimensionalized by the chord. For a current perspective, the Advanced Tactical Fighter has a  $r_t \approx 0.0025$ .

### Objectives

This investigation has three goals. The first goal is to determine the applicability and define any limitations of PROFILE to airfoils with small leading-edge radii and small thickness-to-chord ratio. The second goal is to develop a method for designing airfoils of this class by defining a range of input parameters. The final goal is to compare the resulting data for these low-observable airfoils with

existing NACA 4-digit airfoil data of equivalent thickness-to-chord ratio. This comparison will show if the low-observable airfoils have any improved aerodynamic characteristics over the equivalent thickness NACA 4-digit airfoils.

## II. Theory

### Potential-Flow Design Method

This section will overview the basic theory used in PROFILE. Eppler (1,3,4,6) provides a more detailed analysis from which this section is based. The design method is based on the conformal mapping of the complex  $\zeta$ -plane into a complex  $z$ -plane (Figure 1). In the  $\zeta$ -plane, there is an infinite flow around a unit circle given by

$$\zeta = \xi + i\eta. \quad (1)$$

With the rear stagnation point located at  $\zeta = 1$ , the complex potential is defined by

$$F(\zeta) = e^{-i\alpha\zeta} + e^{i\alpha\zeta^{-1}} - \frac{\Gamma}{2\pi i} \ln \zeta \quad (2)$$

and the circulation given by

$$\Gamma = 4\pi C \sin(\alpha) \quad (3)$$

where  $C = 1$ . This choice of  $C$  provides a unit flow velocity at infinity. The flow is mapped into the  $z$ -plane by a complex function given by

$$z(\zeta) = \beta_1 \zeta + \sum_{v=0}^{\infty} \beta_{-v} \zeta^{-v} \quad (\beta_1 \neq 0) \quad (4)$$

with  $|\zeta| \geq 1$  for a convergent power series. This equation satisfies the following conditions

$$z(\infty) = \infty \quad \left( \frac{dz}{d\zeta} \right)_{\infty} = 1. \quad (5)$$

These conditions mandate that the unit circle in the  $\zeta$ -plane will map into the  $z$ -plane as an infinite flow ( $C = 1$ ) at an angle of attack,  $\alpha$ , around an arbitrary airfoil profile. From complex theory, we know the complex conjugate velocity vector  $\bar{w}$  in the  $z$ -plane is given by

$$\bar{w} = ve^{-i\theta} = \frac{dF}{dz} = \frac{\frac{dF}{d\zeta}}{\frac{dz}{d\zeta}} \quad (6)$$

where  $v$  is the modulus and  $\theta$  is its argument. From Equation (2), we can obtain the function  $dF/d\zeta$ . Thus, the problem remaining is to determine  $z(\zeta)$  so that along the airfoil profile there will be a prescribed velocity distribution.

However, the problem is defined in the  $\zeta$ -plane on the unit circle ( $\zeta = e^{i\phi}$ ) and not in the  $z$ -plane. The variables  $x$  and  $\phi$  are related by

$$x \approx \frac{c}{2}(1 + \cos \phi), \quad (7)$$

where  $c$  is the airfoil chord. Since, the velocity  $v(\phi)$  is specified, the problem can be solved by taking the logarithm of Equation (6), giving

$$\ln \frac{dz}{dF} = \ln \frac{dz}{d\zeta} - \ln \frac{dF}{d\zeta} = -\ln v + i\theta. \quad (8)$$

This equation shows that  $-\ln v$  can be obtained directly as the real part of  $\ln(dz/dF)$ . If  $\ln(dz/dF)$  is known, then  $dz/d\zeta$  is determined by Equations (8) and (2), and the

mapping function  $z(\zeta)$  can be obtained. Therefore, a trial solution for  $\ln(dz/dF)$  is introduced in accordance with Equation (8) and, with several manipulations, an equation is introduced as

$$\ln \frac{dz}{d\zeta} = \ln(1-\zeta^{-1}) + \sum_{m=0}^{\infty} (a_m + ib_m)\zeta^{-m}. \quad (9)$$

The function  $dz/d\zeta$  resulting from Equation (9) must be compared to the requirements from Equation (4) and must also be analytical in satisfying the condition  $|\zeta| > 1$ . It is important to note that Equation (9) can be ordered in decreasing powers of  $\zeta$ . A comparison of this form of Equation (9) with the derivative of Equation (4) points out that

$$a_0 = 0 \quad b_0 = 0 \quad a_1 = 1 \quad b_1 = 0. \quad (10)$$

Examining the summation in Equation (9) along the boundary ( $\zeta = e^{i\phi}$ ), the real and imaginary parts can be expressed, respectively, as follows,

$$P(\phi) = \sum_{m=0}^{\infty} (a_m \cos m\phi + b_m \sin m\phi) \quad (11)$$

$$Q(\phi) = \sum_{m=0}^{\infty} (b_m \cos m\phi - a_m \sin m\phi). \quad (12)$$

Equation (9) can thus be rewritten as



$$\left[ \ln \frac{dz}{d\zeta} - \ln(1 - \zeta^{-1}) \right]_{\zeta=e^{i\phi}} = P(\phi) + iQ(\phi). \quad (13)$$

Using Equations (2), (6), and (9) the real part of equation (13) is determined to be

$$P(\phi) = -\ln \left[ \frac{v(\phi)}{2 \left| \cos \left( \frac{\phi}{2} - \alpha \right) \right|} \right]. \quad (14)$$

The imaginary part is the conjugate harmonic function of  $P(\phi)$ , which is defined by

$$Q(\phi) = \frac{1}{2\pi} \int_0^{2\pi} P(\psi) \cot \frac{\psi - \phi}{2} d\psi. \quad (15)$$

In this method, the function  $Q(\phi)$  is numerically evaluated. Now, if Equation (14) is substituted into Equation (13), after some manipulation, it is determined that

$$\left( \frac{dz}{d\phi} \right) = -4 \sin \frac{\phi}{2} \left| \cos \left( \frac{\phi}{2} - \alpha \right) \right| \frac{1}{v(\phi)} e^{i \left( Q + \frac{\phi}{2} \right)}. \quad (16)$$

Equation (16) can be numerically integrated and then split into its real and imaginary parts directly. By examination of Equations (13-16), it can be seen that the airfoil coordinates can be found if  $Q(\phi)$  is known.

In this method, the velocity distribution is not completely arbitrary. The problem is still constrained by the conditions in Equation (5) and those subsequently found in Equation (10). With this information, the following

conditions are found from the Fourier expansion of Equation (11).

$$\int_0^{2\pi} P(\phi) d\phi = 0 \quad (17)$$

$$\int_0^{2\pi} P(\phi) \cos \phi d\phi = 1 \quad (18)$$

$$\int_0^{2\pi} P(\phi) \sin \phi d\phi = 0. \quad (19)$$

Therefore, the evaluation of the airfoil coordinates is specified by Equations (11-16) under the conditions of Equations (17-19).

In this method, an airfoil is produced by selecting angles of attack,  $\alpha = \alpha^*$ , over segments of the unit circle for which the velocity distribution  $v(\phi, \alpha^*)$  is to be constant. Thus  $P(\phi)$  is shown to be

$$P(\phi) = -\ln \left[ \frac{v^*(\phi, \alpha^*)}{2 \left| \cos \left( \frac{\phi}{2} - \alpha^* \right) \right|} \right]. \quad (20)$$

Equation (9) indicates the coefficients  $a_m$  and  $b_m$  are the keys to determining the mapping function  $z(\zeta)$ , which gives the airfoil shape. Thus, Equation (9) indicates the importance of  $P(\phi)$  in the determination of the airfoil shape. It is important to note in examining Equation (9), that any change in the angle of attack,  $\alpha$ , does not change the mapping function,  $z(\zeta)$ . Since  $P(\phi)$  is independent of  $\alpha$ ,

the velocity distribution for any arbitrary  $\alpha$  is found from the following relationship:

$$\frac{v(\phi, \alpha)}{|\cos(\frac{\phi}{2} - \alpha)|} = \frac{v^*(\phi, \alpha^*)}{|\cos(\frac{\phi}{2} - \alpha^*)|}. \quad (21)$$

The invariance with respect to  $\alpha$  makes it possible to designate  $v^*$  by choosing values of  $\alpha^*$  over several segments of the airfoil. It is necessary that  $v(\phi, \alpha)$  be continuous over the airfoil. However, this does not constrain  $\alpha^*$  to be continuous, it only requires that  $v^*(\phi, \alpha)$  counteract any discontinuity in  $\alpha^*$ . Thus, the following matching condition must hold between the values of  $\alpha^*$  for adjoining arc segments:

$$\lim_{\epsilon \rightarrow 0} \left| \frac{v^*(\phi_i + \epsilon, \alpha_{i+1}^*)}{\cos(\frac{\phi_i}{2} - \alpha_{i+1}^*)} \right| = \lim_{\epsilon \rightarrow 0} \left| \frac{v^*(\phi_i - \epsilon, \alpha_i^*)}{\cos(\frac{\phi_i}{2} - \alpha_i^*)} \right|. \quad (22)$$

Examination of Equation (20) reveals that  $P(\phi)$  is undefined at the stagnation point. This problem is eliminated by introducing an arc limit,  $\phi_{i,le}$ , near the leading-edge. In this method,  $\phi_{i,le}$  is not specified in the input, but is left as a free parameter to be determined through satisfaction of the conditions in Equation (10).

The unit circle is divided into  $I$  arcs, where each arc  $i$  extends from  $\phi_{i-1}$  to  $\phi_i$ , with the following definitions,  $\phi_0 = 0$  and  $\phi_I = 2\pi$ . The specified velocity distribution is

represented by

$$v(\phi, \alpha^*) = v_i w(\phi) \quad (\phi_{i-1} \leq \phi \leq \phi_i), \quad (23)$$

where  $v_i$  is a constant determined from solving the transcendental equation for  $\phi_{i,1e}$  and  $w(\phi)$  is an empirical function introducing the main pressure recovery and a closure contribution on each surface of the airfoil. A discussion on Eppler's (1,3) meaning of main pressure recovery as it applies to this class of airfoils will be addressed in Chapter III. Eppler gives the function  $w(\phi)$  as

$$w(\phi) = \left[ 1 + K \left\{ \frac{\cos \phi - \cos \phi_w}{1 + \cos \phi_w} \right\} \right]^{-\mu} \left[ 1 - 0.36 \left\{ \frac{\cos \phi - \cos \phi_s}{1 - \cos \phi_s} \right\}^2 \right]^{K_H} \quad (24)$$

for  $(0 \leq \phi \leq \phi_{i,1e})$ , and

$$w(\phi) = \left[ 1 + \bar{K} \left\{ \frac{\cos \phi - \cos \bar{\phi}_w}{1 + \cos \bar{\phi}_w} \right\} \right]^{-\bar{\mu}} \left[ 1 - 0.36 \left\{ \frac{\cos \phi - \cos \bar{\phi}_s}{1 - \cos \bar{\phi}_s} \right\}^2 \right]^{\bar{K}_H} \quad (25)$$

for  $(\phi_{i,1e} < \phi \leq 2\pi)$ . The terms enclosed by the braces,  $\{ \}$ , are to be dealt with as a specially defined function,  $f(\phi)$ :

$$\{f(\phi)\} = \begin{cases} 0 & f(\phi) \leq 0 \\ f(\phi) & f(\phi) > 0. \end{cases} \quad (26)$$

The first factor in both Equations (24) and (25) represents the main pressure recovery contribution. Figure 3 shows the total amount of pressure recovery,  $\omega$ , which is

defined as the ratio of the velocity at the airfoil's trailing-edge to the velocity at the specified recovery location. The length of the recovery is specified by  $\phi_w$  and  $\bar{\phi}_w$  for the upper and lower surfaces, respectively. We see from Equation (24) that for the upper surface the total amount of pressure recovery is represented by

$$\omega = \frac{v(0, \alpha^*)}{v(\phi_w, \alpha^*)} = \left[ 1 + K \left( \frac{1 - \cos \phi_w}{1 + \cos \phi_w} \right) \right]^{-\mu}. \quad (27)$$

The relative slope at the beginning of the pressure recovery ( $\phi = \phi_w$ ) is

$$\omega' = \frac{\mu K}{\frac{1}{2}(1 + \cos \phi_w)}. \quad (28)$$

As we can see from Equations (27) and (28), the total amount of pressure recovery and the shape of the recovery are found by specifying any two of  $\omega$ ,  $\omega'$ ,  $K$ , or  $\mu$ .

The second term in Equations (24) and (25) represent the closure contribution for the trailing-edge. Eppler (4) suggests this area is usually confined to a small area around the trailing-edge ( $\phi_s \approx 24^\circ - 36^\circ$ ). For the purposes of this investigation,  $\phi_s$  will be held constant at  $24^\circ$  for all the subsequent runs for both the upper and the lower surface. The values of  $K_H$  and  $\bar{K}_H$  are not specified in the input. They are determined by an iteration procedure that ensures that the profile obtained will have a closed trailing-edge. In the program, Eppler provides nine trailing-edge iteration mode options (1,7). This

investigation addresses symmetrical airfoils which warrants choosing iteration mode three for our computations. With iteration mode three, all upper-surface  $\alpha_i^*$  are replaced by  $\alpha_i^* + \Delta\alpha$  and all the lower surface  $\alpha_i^*$  are replaced by  $\alpha_i^* - \Delta\alpha$ .

In summary the complete specification of  $v(\phi)$  needs the following information:

- (1) Arc limits,  $\phi_i$  (not including  $\phi_{i,le}$ )
- (2) Angle of attack values,  $\alpha_i^*$  for all arcs
- (3) Pressure recovery specifications
- (4) Length of the closure contributions

Thus, we are left with  $I$  constants  $v_i$ ,  $\phi_{i,le}$ , and as mentioned above,  $K_H$  and  $\bar{K}_H$  as free parameters. Also, there are the  $I$  matching conditions from Equation (26) and Equations (17-19) to be satisfied. These conditions are satisfied in closed form, leading to a transcendental equation for  $\phi_{i,le}$ . This equation is solved (Regula falsi), allowing for the determination of  $v_i$ ,  $K_H$  and  $\bar{K}_H$ .

#### Potential-Flow Analysis Method

In PROFILE, Eppler utilizes a panel method with vorticities distributed parabolically along each panel (1). With the airfoil coordinates determined from the potential-flow design method, the geometry of each panel is determined by a spline fit of the coordinates. The panels are defined with the airfoil coordinates as their endpoints. At each airfoil coordinate, the condition that the inner tangential

velocity be zero is satisfied. This mathematical condition corresponds to the physical condition of the flow being tangent to the surface. The analysis is made at  $\alpha = 0^\circ$  and  $\alpha = 90^\circ$  and any other angle of attack is derived by the superposition of these two solutions. The trailing-edge singularities resulting from the circulation  $\Gamma$  around the airfoil are addressed according to whether the shape of the trailing-edge is sharp or blunt (1).

The importance of using the parabolic vorticity distribution for this application is shown by Hess (5), since this class of airfoil will result in very thin trailing-edges. Hess (5) indicates the method will provide remarkably accurate solutions for airfoils with these characteristics.

#### Boundary-Layer Method

Eppler (1,4,6) employs an integral method for the analysis of the boundary-layer. A basic overview of the method will be presented here for clarity.

Nondimensional Variables. In this method, the unit system selected is in terms of a characteristic length,  $L$ , a characteristic velocity,  $V_R$ , and a characteristic density,  $\rho_R$ , of the problem. In this system, for example, time is measured in  $L/V_R$  and mass in  $\rho_R L^3$ . As a result of this system, in an incompressible problem the only density in the problem is the reference density, or  $\rho \equiv 1$ . All equations

are transformed to the nondimensional variables by setting  $\rho_R \equiv 1$ ,  $V_R \equiv 1$ , and  $L \equiv 1$ . For the problem of flow around an airfoil, the length unit,  $L$ , is the chord,  $c$ , the velocity unit,  $V_R$ , is the free stream velocity,  $U_\infty$ , and the density unit is  $\rho_R = \rho_\infty$ .

General Equations. The conventional coordinate system is used, where  $x$  is streamwise along the surface and  $y$  is normal to the surface. The governing equations for this method are the two-dimensional, incompressible boundary-layer equations,

$$u \left( \frac{\partial u}{\partial x} \right) + v \left( \frac{\partial u}{\partial y} \right) = - \frac{\partial p}{\partial x} + \frac{\partial \tau}{\partial y} \quad (29)$$

$$\frac{\partial u}{\partial x} + \frac{\partial v}{\partial y} = 0. \quad (30)$$

The potential flow velocity  $U(x)$  is defined by

$$U(x) = \lim_{y \rightarrow \infty} u(x, y). \quad (31)$$

The displacement thickness, the momentum thickness, and the energy thickness are defined respectively, as follows:

$$\delta_1(x) = \int_0^\infty \left( 1 - \frac{u(x, y)}{U(x)} \right) dy \quad (32)$$

$$\delta_2(x) = \int_0^\infty \frac{u(x, y)}{U(x)} \left( 1 - \frac{u(x, y)}{U(x)} \right) dy \quad (33)$$



$$\delta_3(x) = \int_0^{\infty} \frac{u(x,y)}{U(x)} \left[ 1 - \left( \frac{u(x,y)}{U(x)} \right)^2 \right] dy. \quad (34)$$

These thicknesses will be used to characterize the viscous effects of the boundary-layer. From these thicknesses, the shape factors  $H_{12}$  and  $H_{32}$  are defined as

$$H_{12} = \frac{\delta_1}{\delta_2} \quad (35)$$

$$H_{32} = \frac{\delta_3}{\delta_2}. \quad (36)$$

The boundary-layer equations can be manipulated and integrated in the  $y$  direction with the integral parameters above to obtain an integral momentum equation

$$\delta_2' + (\delta_1 + 2\delta_2) \frac{U'}{U} = C_f + \frac{v_o}{U} \quad (37)$$

and an integral energy equation

$$\delta_3' + 3 \delta_3 \frac{U'}{U} = C_D + \frac{v_o}{U}. \quad (38)$$

In the equations above,  $v_o$  is the normal velocity at the surface, where blowing is defined as positive and suction is negative, and the primes denote differentiation with respect to  $x$ . No blowing will be considered in this investigation, thus  $v_o = 0$ . The skin friction coefficient  $C_f$  is defined as

$$C_f = \frac{\tau_0}{\rho U^2} \quad (39)$$

and the dissipation coefficient,  $C_D$ , is

$$C_D = \frac{2}{\rho U^3} \int_0^{\infty} \tau \frac{\partial u}{\partial y} dy. \quad (40)$$

Laminar Boundary-Layers. At this point, the method follows Von Karman's idea to approximate solutions for laminar boundary-layers. It is assumed that  $u(x,y)$  is to be approximated by

$$u(x,y) = f\left(\lambda(x), \frac{y}{\delta(x)}\right) \quad (41)$$

where  $\delta(x)$  and  $\lambda(x)$  are unknowns. The value of  $\lambda$  determines the velocity profile shape with respect to  $y/\delta$ , and  $\delta$  is only able to stretch the profile in the  $y$ -direction. Eppler (6) discusses how Equation (38), used under the assumption of Equation (41), is the best approach since the shape factors  $H_{12}$  and  $H_{32}$  are only functions of  $\lambda$ . It is important to note that  $H_{12}$  is only a function of  $H_{32}$ . Now,  $C_f$  and  $C_D$  are found to be

$$C_f = \frac{\epsilon^*(H_{32})}{ReU\delta_2} \quad (42)$$

$$C_D = \frac{2D^*(H_{32})}{ReU\delta_2} \quad (43)$$

$$\text{where } Re_{\delta_2} = \frac{U_{\infty}L}{\nu} \frac{U\delta_2}{U_{\infty}L} = ReU\delta_2$$

based on the local flow velocity and the momentum thickness in accordance with the unit convention described earlier.

As is apparent, the precision of the approximate method is dependent on how well the exact solution of Equations

(29) and (30) are represented by Equation (41). Eppler (6) indicates that the Hartree profiles give the best approximation in regions of adverse pressure gradient ( $1.51509 < H_{32} < 1.57258$ ). A negative  $dp/dx$  is defined as a favorable pressure gradient and a positive  $dp/dx$  is defined as an adverse pressure gradient. The value of  $H_{32} = 1.51509$  specifies laminar separation. With all the assumptions made so far, the functions  $H_{12}$ ,  $\epsilon^*$ , and  $D^*$  in terms of  $H_{32}$  are derived as

$$\text{if } H_{32} < 1.57258$$

$$H_{12} = 4.02922 - (583.60182 - 724.5591H_{32} + 227.18220H_{32}^2)^* \quad (44)$$

$$\left( \sqrt{H_{32} - 1.51509} \right)$$

$$\epsilon^* = 2.512589 - 1.686096H_{32} + 0.39154H_{32}^2 - 0.031729H_{32}^3$$

$$\text{if } H_{32} > 1.57258$$

$$H_{12} = 79.870845 - 89.58214H_{32} + 25.715786H_{32}^2 \quad (45)$$

$$\epsilon^* = 1.372391 - 4.226253H_{32} + 2.221687H_{32}^2$$

$$D^* = 7.853976 - 10.260551H_{32} + 3.418898H_{32}^2. \quad (46)$$

With these functions, Equations (37) and (38) become coupled ordinary differential equations, which can be numerically integrated.

Turbulent Boundary-Layers. A turbulent boundary-layer can be addressed with Equations (37) and (38), also. However, The Reynolds stresses impart new problems which do

not allow the functions to be derived as efficiently as in the laminar case. Eppler (6) provides expressions derived from both empirical and semi-empirical investigations of turbulent boundary-layers from several researchers. The expressions are

$$H_{12} = \frac{11H_{32} + 15}{48H_{32} - 59} \quad (47)$$

$$C_f = 0.045716[(H_{12} - 1)ReU\delta_2]^{-0.232} e^{-1.26H_{12}} \quad (48)$$

$$C_D = 0.0100[(H_{12} - 1)ReU\delta_2]^{-\frac{1}{6}}. \quad (49)$$

With these expressions, Equations (37) and (38) again become coupled ordinary differential equations to be numerically integrated. For this case, it is not possible to define a fixed value of  $H_{32}$  as the separation point. But, it is known that for  $H_{32} > 1.58$  there will be no separation and for  $H_{32} < 1.46$  there definitely will be separation. Eppler (4) states that this method gives lower values of  $H_{32}$  for adverse pressure gradients than other methods, therefore turbulent separation is assumed to occur at  $H_{32} = 1.46$ .

Boundary-Layer Transition. The transition criterion for this program is based upon local, boundary-layer data (4). The expression used to indicate transition is

$$\ln Re_{\delta_2} \geq 18.4 H_{32} - 21.74 + 125m(H_{32} - 1.573)^2 - 0.36r \quad (50)$$

where  $r$  represents a roughness factor for  $0 \leq r \leq 6$  and  $m$  allows switching between the normal criterion ( $m=0$ ) and a modified criterion ( $m=1$ ). For the roughness factor,  $r = 0$  corresponds to smooth conditions and  $r = 6$  corresponds to a very rough surface or a very turbulent free stream. For this investigation, smooth conditions were assumed. The modified criterion was developed from flight test data to improve the performance of the normal criterion for cases where the shape factor was near laminar separation, at high Reynold's number  $Re$  in favorable pressure gradients. For airfoils in this class, the normal criterion and modified criterion results were not significant, so all data presented is with the normal criterion. When transition is indicated, the computations switch from Equations (44) through (46) to Equations (47) through (49). Physically, transition does not occur at one point, so the criterion in Equation (50) indicates where the laminar boundary-layer ends.

### III. Analysis and Limitations

For an inviscid, incompressible fluid, Bernoulli's equation can be written as

$$p + \frac{1}{2}\rho V^2 = \text{constant}. \quad (51)$$

It follows from this equation that in a given flow field, an increase in velocity results in a reduction of pressure and vice versa. In incompressible flow, Bernoulli's equation gives the relationship between the local values of  $p$  and  $V$  with those in the free stream as

$$p_{\infty} + \frac{1}{2}\rho V_{\infty}^2 = p + \frac{1}{2}\rho V^2 \quad (52)$$

which can be rearranged to

$$p - p_{\infty} = \frac{1}{2}\rho(V_{\infty}^2 - V^2). \quad (53)$$

At this point, it is useful to introduce a nondimensional difference between the local and free stream pressure,  $C_p$ . This pressure coefficient is defined by

$$C_p = \frac{p - p_{\infty}}{\frac{1}{2}\rho V_{\infty}^2}. \quad (54)$$

Thus, from Equations (53) and (54), we see that

$$C_p = 1 - \left(\frac{V}{V_{\infty}}\right)^2. \quad (55)$$

The local  $V$  is composed of three elements: the velocity

induced by the thickness of a symmetrical airfoil at zero angle of attack, the velocity corresponding to the camber, and the velocity corresponding to the change in angle of attack. For symmetrical airfoils, the velocity will only be dependent on the thickness and change in angle of attack. Since the term  $(V/V_\infty)^2$  in Equation (55) can never be negative, it follows that the value of  $C_p$  will be negative over the suction side of the airfoil. This will occur on the upper surface of the airfoil, since the flow is accelerating in this region. Thus, at some point the flow will reach a minimum pressure,  $C_{p_{min}}$ , and from this point the pressure recovery will start.

#### Amount and Location of the Pressure Recovery

Eppler (4) states that in designing airfoils there is no general rule for picking the parameters of the recovery function. Thus, it is essential to define the parameters best suited to develop a specific class of airfoils.

In the discussion of the input parameters, only the upper surface variables will be specified. All equations are identical for the lower surface, with the only difference being that the lower surface parameters are contrasted from the upper by an overbar.

In the input files,  $\phi_w$  is specified by the parameter  $\lambda$ .

The two parameters are related by the following expression:

$$\lambda = \frac{N}{360} \phi_w \quad (56)$$

where  $N$  is the total number of points representing the airfoil minus one (the point at the trailing-edge is included for both the upper and lower surfaces). Unless otherwise noted, the value of  $N = 60$  will be used.

In the previous chapter, the function  $w(\phi)$ , which was introduced in Equations (25) and (26), contains a factor that Eppler (1,4,6) refers to as the main pressure recovery contribution. Equations (27) and (28) defined the total amount of pressure recovery,  $\omega$ , and the relative slope of the recovery,  $\omega'$ . In both these equations, the value of  $\phi_w$ , the location of the beginning of the main pressure recovery, is significant.

First, Eppler's terminology for the pressure recovery will be explored. For comparison with a thin airfoil, the pressure recovery of a thick, cambered airfoil will be examined. Figure 4 shows pressure distributions for Airfoil E398 ( $t/c = .1427$ ), a thick, cambered airfoil developed by Eppler (4). For this airfoil, the main pressure recovery is specified to begin at approximately the mid-chord location. Figure 4 shows that through  $\alpha = 6^\circ$ , where  $\alpha$  is relative to the chord line for this cambered airfoil, Eppler's term of main pressure recovery describes very well the location specified by  $\phi_w$ . However, for  $\alpha > 6^\circ$ , a pressure recovery is also beginning near the leading-edge of the airfoil. By



$\alpha = 9^\circ$ , the pressure recovery at the leading-edge becomes significant and the distinction of main pressure recovery becomes blurred.

For the class of thin airfoils being examined, Eppler's choice of terms is especially confusing. If an airfoil's  $t/c$  is small, its leading-edge radius will also be small. Small leading-edge radii on low-speed airfoils may cause early separation, or leading-edge stall, as the angle of attack is increased. As the angle of attack increases, the magnitude of the upper surface suction peak increases and moves forward. Figure 5 shows, for Airfoil G48 ( $t/c = .0533$ ), that the dominant pressure recovery occurs near the leading-edge even for small angles of attack on thin airfoils. Figures 4 and 5 indicate that this occurs on both thick and thin airfoils, but the effect is more pronounced at smaller angles of attack for thin airfoils. Thus, we see it is not necessarily the main pressure recovery that is being defined by  $\phi_w$ , but what I will term a secondary pressure recovery. Figure 6 summarizes the terms used in the description of the pressure distributions used in this investigations.

Figure 5 also shows the influence of  $\phi_w$  on the pressure distribution. Moving the secondary pressure recovery (Eppler's main pressure recovery) from the trailing-edge to the leading-edge, by changing the value of  $\lambda$  in the input file, results in a damping effect on the dominant pressure recovery near the leading-edge. The important question to

answer, in obtaining a method for the design of these airfoils with small  $t/c$ , is defining the effect of the secondary pressure recovery placement. Figure 7 illustrates the effect of the placement of the secondary pressure location on  $t/c$  and  $C_{l_{max}}$ . It is apparent that the choice of  $\lambda = 0$  or  $29.99$  ( $\phi_w = 0$  or  $\approx 180$  degrees) gives the smallest  $t/c$ .

From Equations (27) and (28), if  $\phi_w$  is chosen to be zero, by definition  $\omega = 1$  and  $\omega' = 0$ . Therefore,  $K = 0$  and  $\mu = 1$  are chosen to satisfy both equations. Essentially, the effect of this choice is to disregard the secondary pressure recovery. These results make intuitive sense, since the thickness of the airfoil is related to the amount of pressure recovery. Figure 5 also shows a higher suction peak near the leading-edge for  $\lambda = 0$  or  $29.99$ , which would indicate an airfoil with a small  $t/c$  and leading-edge radius. Thus, the airfoils designed in this study will use a value of  $\phi_w = \lambda = 0$ .

#### Boundary-Layer Displacement Iteration

The program contains the option to add the displacement thickness to the airfoil shape obtained from the potential flow design (7). This will allow the analysis to be performed on an effective airfoil shape in a potential flow. This displacement iteration is performed for angles of attack specified in the potential analysis section.

The displacement thickness is computed in the boundary-

layer method. The displacement thickness is added to the contour for the specific angles of attack and Reynolds numbers specified. The resulting shape is then rerun through the panel method.

Unfortunately, problems were encountered with the utilization of this option in the program as described above. The problem arose because the program was set up to only output the new data through a plotting subroutine. Also, these subroutines were written for the plotting software used at the University of Stuttgart. At first, this appeared to be a very minor inconvenience. A modified procedure would be to have the program output the new velocity or pressure distributions before the data was sent to the plotting subroutines. However, upon close examination of this section of the code, it was found that the pressure or velocity distributions for the new shape were recalculated in a plotting subroutine. Even with this surprising discovery, it appeared the information could still be readily retrieved. Figure 8 shows the results. Unfortunately, the velocity distribution does not match Eppler's data (7). After many attempts and much time spent to find the error in the approach, it was concluded that some transformation must exist within the plotting subroutines that was not accounted for.

Therefore, an input file was created with the new airfoil coordinates, which were obtained in the main section of the boundary-layer calculations. Figure 8 shows that the

new airfoil profile matched with Eppler's profile (7). The program was reexecuted to perform the potential analysis on the airfoil created with the new coordinates. Figure 9 shows that the results compare very well to those of Eppler (7). Figure 9 shows, for this particular airfoil at the specified angle of attack and Reynolds number, there is not a significant difference between the two calculations.

Further confidence was gained in this modified procedure through the comparison of results found in Graham (8). Figure 10 shows a significant difference between the experimental data versus the potential flow solution with a compressibility correction for  $M = .4$ . But, Figure 10 also shows the results are very good when the boundary-layer displacement iteration is performed, as modified above.

The determination needed to be made to see if this calculation was essential to the analysis for the thin airfoils. The boundary-layer displacement effects on  $C_l$  are evaluated in a very simple way if the displacement iteration is not used. The lift curve slope,  $2\pi\eta$ , is reduced to  $2\pi$ , where the efficiency,  $\eta$ , is defined by Eppler (4) as,

$$\eta = 1 + 0.78t/c. \quad (57)$$

This reduction in lift-curve slope assumes that the potential flow thickness effects are canceled by the boundary-layer displacement effects. From inviscid, thin airfoil theory, where the potential flow streamline is at the airfoil surface, the lift-curve slope for an infinitely

thin airfoil is  $2\pi$ . For an airfoil with finite thickness, Equation (57) corrects for the resulting increase in the lift-curve slope as the thickness of the airfoil increases. For a viscous flow, the potential flow streamlines are displaced by the boundary-layer thickness. As the flow proceeds along the airfoil, the boundary-layer thickness increases. This results in a reduction in the lift-curve slope. Their combined effect proves to be negligible, resulting in a lift curve slope very close to the theoretical value of  $2\pi$  (9). Figure 11 shows that the  $C_l$  calculated with this simple method compares very well to experimental data for a NACA 0006 airfoil at  $Re = 3.0 \times 10^6$  (10). Thus, for the purpose of investigating the input parameters necessary to define a method of obtaining an airfoil of this class, it was not essential to run a boundary-layer displacement iteration.

#### Viscous Corrections to Section Lift Coefficient (Separation)

An inviscid section lift coefficient,  $C_l$  is easily obtained by

$$C_l = 2\pi\eta\sin(\alpha) \quad (58)$$

where  $\eta$  is the efficiency defined by Equation (57). Of course, boundary-layer separation will have a significant effect on the  $C_l$ . Eppler (4) corrects  $C_l$  using a method derived from Helmholtz potential flow-wake theory.

Considering the upper surface, the correction is made by

$$\Delta C_l = 2\pi \Delta\alpha \quad (59)$$

where

$$\Delta\alpha = -\frac{s_{sep}}{2c}(\delta_{us} + \alpha_c). \quad (60)$$

In Equation (60),  $s_{sep}$  is the length of separation calculated in the boundary-layer analysis,  $\delta_{us}$  is the airfoil slope near the trailing-edge, and  $\alpha_c$  is the angle of attack relative to the chord line. Equations (59) and (60) basically result in a reduction of the angle of attack,  $\alpha$ , by a factor  $\Delta\alpha$ . This is illustrated in Figure 12. This same procedure is used for the lower surface with the corresponding parameters. It should be noted that the method constrains the correction to be negative for the upper surface and positive for the lower surface.

As discussed earlier, an airfoil with a small t/c and small leading-edge radius is prone to early separation. As an example, Figures 13 and 14 show that Airfoil G31 is a symmetric airfoil with t/c = 0.0495 and practically no leading-edge radius. Figure 15 shows  $C_l(\alpha)$  for this airfoil at  $Re = 3.0 \times 10^6$ . This figure shows the airfoil stalling where  $\alpha$  is as low as  $0.5^\circ$ . Here we see a problem arising from the correction defined by Equations (59) and (60). After the stall, the program is predicting a negative lift for positive  $\alpha$  between approximately  $0.5$  and  $3$  degrees. This is not a realistic result for a symmetrical airfoil.

Examining Equation (60), it is seen that  $s_{sep}$  is the dominant parameter in the determination of  $\Delta\alpha$ , since the trailing-edge slope for thin airfoils are on the order of a couple of degrees or less. Hence, this viscous correction will predict negative values of  $C_l$  after the occurrence of stall for thin airfoils that have the characteristic of separation moving very abruptly toward the leading-edge at small angles of attack. Looking back to Figure 11, we see an example of an airfoil where stall does not occur at a very low angle of attack. The NACA 0006 has a much larger leading-edge radius than Airfoil G31 and is slightly thicker. However, the stall occurs abruptly for these airfoils. Again, the program does not predict  $C_l$  correctly after the stall, but, since the angle of attack is greater, a negative  $C_l$  is not predicted. However, it is important to note that the program's results compare very well in the calculation of the magnitude of  $C_{lmax}$ . The value of  $C_{lmax}$  will be used in the comparison with NACA 4-digit airfoils.

#### Specification of the Velocity Distribution

Presently, two of the four requirements for the complete specification of  $v(\phi)$  have been established, the length of the closure contributions and the secondary pressure recovery specifications. Now, the determination of the arc limits,  $\phi_i$ , and the  $\alpha_i^*$  values for the corresponding arcs must be made such that it results in an airfoil with  $2.5\% \leq t/c \leq 5.5\%$  and a small leading-edge radius.

As pointed out in Chapter II, the function  $P(\phi)$  plays a important part in the determination of the airfoil shape. Also, the invariant nature of  $P(\phi)$ , with respect to the angle of attack, gives us the relationship between the specified  $\alpha_i^*$  and the resulting velocity distribution. This can be seen by rearranging Equation (21), resulting in

$$v(\phi, \alpha) = v^*(\phi, \alpha^*) \frac{|\cos(\frac{\phi}{2} - \alpha)|}{|\cos(\frac{\phi}{2} - \alpha^*)|}. \quad (61)$$

Applying Equation (7), Eppler (3) points out that if  $V(x, \alpha)$  is considered with a certain  $\alpha$  for a segment on the upper surface with  $\alpha_i^*$  and  $V(x, \alpha^*)$  that

$$\frac{d}{dx}(V(x, \alpha)) > 0 \quad \text{if} \quad \alpha < \alpha_i^* \quad (62)$$

and

$$\frac{d}{dx}(V(x, \alpha)) < 0 \quad \text{if} \quad \alpha > \alpha_i^*. \quad (63)$$

Differentiating Equation (51) with respect to  $x$  yields

$$\frac{dp}{dx} = -\rho V \frac{dV}{dx} \quad (64)$$

which gives the familiar relationship between velocity and pressure gradient. Comparing Equations (62) and (63) with Equation (64) gives us a very important insight into the effect of the selection of  $\alpha_i^*$ , with respect to the  $\alpha$  of the incoming flow, on the velocity or pressure gradient produced. When  $\alpha < \alpha_i^*$ , a favorable pressure gradient will



occur over that upper surface segment and if  $\alpha > \alpha_i^*$ , an adverse pressure gradient occurs.

For example, in the previous section the Airfoil G31 was introduced in the discussion of early leading-edge separation. Airfoil G31 was defined by two arc segments on the upper surface as follows,

$$\begin{aligned}\alpha_{1e}^* &= 1^\circ \quad \text{for } 30 \geq v > 22.5 \\ \alpha_1^* &= 0^\circ \quad \text{for } 22.5 \geq v \geq 0\end{aligned}\tag{65}$$

where  $v_i = \frac{N}{360} \phi_i$

and with the negative values of  $\alpha_i^*$  for the corresponding segments on the lower surface. Obviously, these input parameters produced an airfoil with small t/c and a practically sharp leading-edge. However, since the magnitudes of the  $\alpha_i^*$  are small, an adverse pressure gradient develops at very small angles of attack, which induces a rapid separation. Figure 15 shows the stall for Airfoil G31 occurring at approximately  $\alpha = 0.5^\circ$ .

This is not a desirable characteristic for low-speed airfoils. What happens if we increase the value of  $\alpha_{1e}^*$  on this airfoil? Figures 16 and 17 indicate that as  $\alpha_{1e}^*$  is increased, both t/c and leading-edge radius will increase. On the upper surface, the favorable pressure gradient, or an accelerating velocity, over a wider  $\alpha$  regime on the front portion of the airfoil results in a thicker, more curved shape at the leading-edge. This causes a paradox. The

airfoil needs to have a small t/c and leading-edge radius (small values of  $\alpha^*$ ), yet stalling at very low angles of attack is undesirable.

Figure 18 compares the pressure distributions of a NACA 0006 and a NACA 0012 at  $\alpha = 3^\circ$  and  $\alpha = 8^\circ$  computed with the program. Considering the upper surface or the suction side of the airfoil, Figure 18 illustrates that for the thinner airfoil, the favorable pressure gradient region is very short and the initial pressure recovery has a steeper adverse pressure gradient than that of the thicker airfoil.

The previous analysis indicates that a function which produced a decreasing  $\alpha^*$  would appear to be a good compromise in the design process. Figure 19 shows the hand-drawn curves of decreasing  $\alpha^*$  created to test the above analysis. The values of  $\alpha^*$  from the TA2-TA5 curves (depicted in Figure 19 by symbols) were input into the program with the corresponding arc segments. The TA2-TA5 curves are not smooth because the curves shown are created with only the fourteen piecewise continuous values of  $\alpha^*$ , for each surface, chosen for input into the program. The  $(v_i, \alpha_i^*)$  pairs for the curves TA2-TA5 are shown in Appendix A, Table A.1.

The program allows for as many as 28 arc segments to be defined for one airfoil, including both upper and lower surfaces. A large percentage of the 14 arc segments per surface were placed near the leading-edge of the airfoil to capture the steep slopes of the functions near the leading-

edge. Figures 20-31 show the airfoil profile, leading-edge profile, and pressure distributions for the TA2-TA5 curves. Appendix B contains an introduction to the significant input lines used during this investigation. Appendix C contains the input files for each airfoil. The value of  $r_t$  was estimated from the figures of the airfoil's leading-edge. Table 1 summarizes the  $t/c$  and  $r_t$  for the TA-Series airfoils.

TABLE 1  
SUMMARY FOR TA-SERIES AIRFOILS

Airfoil	$t/c$ (%)	$r_t$	Comments
TA2	12.05	0.0170	No separation thru $10^\circ$
TA3	9.05	0.0158	No separation thru $10^\circ$
TA4	5.56	0.0100	separation between $8-10^\circ$
TA5	2.37	0.0042	separation between $4-6^\circ$

From this comparison, the TA4 and TA5 curves are shown to result in airfoils near the desired  $t/c$  band and prescribed  $r_t$  limit. These curves produce airfoils that fall within the prescribed  $r_t$  limit and are just outside the desired  $t/c$  band. However, TA4 has the preferred separation characteristic compared to TA5.

The TA4 and TA5 curves shed light on the characteristics of the  $\alpha^*$  distribution needed to reach the desired objective, since these curves resulted in airfoils within the prescribed  $t/c$  and  $r_t$  bands. The task will be to determine a reliable way to develop the input parameters

needed to produce an airfoil with a desired  $t/c$  and/or  $r_t$ .

To achieve this goal, the best approach seemed to be that of choosing a mathematical function for  $\alpha^*$  which produced the characteristics of TA4 and TA5 curves. The above analysis indicates that curves like TA4 and TA5 could be represented by a power law relationship of the form

$$\alpha^* = (x/c)^{-d} \quad (0 < d < 1). \quad (66)$$

This relationship will give a large value of  $\alpha^*$  near the leading-edge that will decrease rapidly. Thus, an investigation of the applicability of this function for developing this class of airfoils needed to be made. The program will not accept any value of  $\alpha^* \geq 90^\circ$ . Imposing this limit on Equation (66) constrains the value of the exponent,  $d$ , in the power law relationship, such that  $d \leq 0.592$ . However, it is obvious that values of  $d > 0.592$  can be used if a coefficient,  $A < 1$ , is included in the power law relationship such that,

$$\alpha^* = A(x/c)^{-d} \quad (0 < d < 1). \quad (67)$$

Figures 32-36 show the  $\alpha^*$  distribution obtained using Equation (67) for the following five values of  $A$ : 1, 1/2, 1/3, 1/4, and 1/5. Equation (67) was computed with a  $\Delta(x/c) = 0.0005$ . This spacing is needed to break out the arc segments required to define the leading-edge, as was done for the TA-series airfoils. The  $(v_i, \alpha_i^*)$  pairs derived from these power law curves are shown in Appendix A, Tables A.2 - A.6.

#### IV. Results and Comparisons

##### Case Summary

Figures 32-36 show the results from Equation (67) being evaluated at the different values of  $d$  for each of the five cases for A. Several  $d$  values were evaluated for each case. The values of  $d$  were determined in each case so to define a clear relationship between the thickness-to-chord ratio and the leading-edge radius throughout the specified thickness-to-chord regime. The establishment of this relationship will give the designer the ability to determine the input parameters needed to achieve a certain thickness-to-chord or leading-edge radius requirement. The values of  $\alpha^*$  are taken from the curves found in Figures 32-36, in the same manner as done for the TA-series. The values for the  $(v_i, \alpha_i^*)$  pairs are shown in Appendix A, Tables A.2-A.6. The airfoils created with these  $\alpha^*$  distributions will be referred to as the T-series airfoils. In the following cases only the airfoils falling into the specified thickness-to-chord and leading-edge radius bands will be presented.

Case 1. A = 1. For the values of  $d$  evaluated at this value of A, four airfoils meet the specified objectives for the thickness-to-chord ratio and the leading-edge radius. The airfoil profile, leading-edge, and section lift coefficient for Airfoils T25, T30, T3, and T4 are shown in Figures 37, 38, 40; 41, 42, 44; 45, 46, 48; and 49, 50, 52,

respectively. These figures show that as the value of  $d$  is increased both the thickness-to-chord ratio, the leading-edge radius, and the maximum lift coefficient increase. These airfoils are summarized in Table 2.

TABLE 2  
T-SERIES AIRFOIL SUMMARY ( $A = 1$ )

Airfoil	$d$	$t/c$ (%)	$r_t$	$C_{l_{max}}$ / Stall Angle ( $Re = 3 \times 10^6$ )
T25	0.25	2.96	0.0020	0.495 / $4.5^\circ$
T30	0.30	3.59	0.0030	0.66 / $6.0^\circ$
T3	0.333	4.09	0.0040	0.77 / $7.0^\circ$
T4	0.4	5.17	0.0075	0.935 / $8.5^\circ$

Case 2.  $A = 1/2$ . For the values of  $d$  evaluated at this value of  $A$ , two airfoils meet the specified objectives for the thickness-to-chord ratio and the leading-edge radius. The airfoil profile, leading-edge, and section lift coefficient for Airfoils T402 and T22 are shown in Figures 53, 54, 56; and 57, 58, 60, respectively. These figures show that as the value of  $d$  is increased both the thickness-to-chord ratio, the leading-edge radius, and the maximum lift coefficient increase. These airfoils are summarized in Table 3.

TABLE 3

T-SERIES AIRFOIL SUMMARY ( $A = 1/2$ )

Airfoil	d	t/c (%)	$r_t$	$C_{l_{max}}$ / Stall Angle ( $Re = 3 \times 10^6$ )
T402	0.4	3.44	0.0038	0.66 / $6.0^\circ$
T22	0.5	4.75	0.0060	0.88 / $8.0^\circ$

Case 3.  $A = 1/3$ . For the values of d evaluated at this value of A, two airfoils meet the specified objectives for the thickness-to-chord ratio and the leading-edge radius. The airfoil profile, leading-edge, and section lift coefficient for Airfoils T503 and T603 are shown in Figures 61, 62, 64; and 65, 66, 68, respectively. These figures show that as the value of d is increased both the thickness-to-chord ratio, the leading-edge radius, and the maximum lift coefficient increase. These airfoils are summarized in Table 4.

TABLE 4

T-SERIES AIRFOIL SUMMARY ( $A = 1/3$ )

Airfoil	d	t/c (%)	$r_t$	$C_{l_{max}}$ / Stall Angle ( $Re = 3 \times 10^6$ )
T503	0.5	3.79	0.0050	0.77 / $7.0^\circ$
T603	0.6	5.08	0.0085	0.95 / $8.7^\circ$

Case 4.  $A = 1/4$ . For the values of d evaluated at this value of A, three airfoils meet the specified objectives for the thickness-to-chord ratio and the leading-edge radius. The airfoil profile, leading-edge, and section lift

coefficient for Airfoils T504, T604 and T234 are shown in Figures 69, 70, 72; 73, 74, 76; and 77, 78, 80, respectively. These figures show that as the value of  $d$  is increased both the thickness-to-chord ratio, the leading-edge radius, and the maximum lift coefficient increase. These airfoils are summarized in Table 5.

TABLE 5  
T-SERIES AIRFOIL SUMMARY ( $A = 1/4$ )

Airfoil	$d$	$t/c$ (%)	$r_t$	$C_{l_{max}}$ / Stall Angle ( $Re = 3 \times 10^6$ )
T504	0.5	3.25	0.0040	0.605 / $5.5^\circ$
T604	0.6	4.3	0.0067	0.836 / $7.6^\circ$
T234	0.666	4.97	0.0080	0.943 / $8.6^\circ$

Case 5.  $A = 1/5$ . For the values of  $d$  evaluated at this value of  $A$ , three airfoils meet the specified objectives for the thickness-to-chord ratio and the leading-edge radius. The airfoil profile, leading-edge, and section lift coefficient for Airfoils T505, T605 and T6605 are shown in Figures 81, 82, 84; 85, 86, 88; and 89, 90, 92, respectively. These figures show that as the value of  $d$  is increased both the thickness-to-chord ratio, the leading-edge radius, and the maximum lift coefficient increase. These airfoils are summarized in Table 6.



TABLE 6  
T-SERIES AIRFOIL SUMMARY ( $A = 1/5$ )

Airfoil	d	t/c (%)	$r_t$	$C_{l_{max}}$ / Stall Angle ( $Re = 3 \times 10^6$ )
T505	0.5	2.89	0.0032	0.55 / $5.0^\circ$
T605	0.6	3.82	0.0055	0.77 / $7.0^\circ$
T6605	0.666	4.58	0.0075	0.903 / $8.3^\circ$

### Case Comparisons

Examining the pressure distribution and  $C_l(\alpha)$  curves shows the significant effect the leading-edge radius has on the characteristics of the airfoil. For example, focusing on the pressure distributions for  $\alpha = 0^\circ$  in Figures 33, 43, 47, and 51, we can see that as  $r_t$  increases (which increases as these figure numbers increase), the length of the area with a favorable pressure gradient near the leading-edge grows. Also, as the angle of attack is increased, the leading-edge radius is seen to have a great effect on the pressure distribution near the leading-edge. The leading-edge's influence on the pressure distribution affects the separation of the flow, because of the adverse pressure gradients. The results of this separation are reflected in Figures 40, 44, 48, 52, 56, 60, 64, 68, 72, 76, 80, 84, 88 and 92. The maximum lift coefficient, which indicates the onset of stall, increases as the leading-edge radius increases.

Also, Figures 40, 44, 48, 52, 56, 60, 64, 68, 72, 76, 80, 84, 88 and 92 show the maximum lift coefficient

increases as the Reynolds number increases. Reynolds number is basically a ratio of the inertial forces to the viscous forces. If Reynolds number is increased, the flow is energized, and the separation length along the airfoil is reduced. Also, this allows for a higher angle of attack before ultimate separation. For these thin airfoils, the stall characteristic is very abrupt. Therefore, the results we see are most significantly influenced by the latter of the two effects.

#### Design Implications

Using the power law relationship was very successful for developing symmetric, low-observable general configuration symmetric airfoils within the specified thickness-to-chord and leading-edge radius limits. Figure 93 shows the utilization of Equation (67), produces input  $\alpha^*$  distributions resulting in airfoils falling into the prescribed  $t/c$  band for  $0.25 \leq d < 0.75$  for various values of  $A$ . In the presentation of Cases 1-5, only the airfoils within the specified objectives for thickness-to-chord ratio and leading-edge radius were shown. However, Figure 94 shows the results for all the values of  $d$  evaluated in Cases 1-5. Figure 94 indicates that a significant portion of the airfoils created with Equation (67) fall simultaneously within both the defined  $t/c$  and  $r_t$  bands.

The most significant result from Figures 93 and 94 is that the designer now has a new tool for developing general

low-observable configuration, symmetrical airfoils. Once the designer assesses the threat that an airfoil will be facing, a determination can be made, based on the threat frequency as discussed earlier, on the constraints for  $t/c$  and  $r_t$ . From Figures 93 and 94, the designer can determine the values of  $A$  and  $d$  for Equation (67) needed to get the desired  $t/c$  and  $r_t$ . However, Figures 93 and 94 also show the designer is constrained, for a given  $r_t$ , to a  $t/c$  band of approximately one percent. For example, if the designer determines the desired airfoil will require a  $r_t = 0.0050$ , Figure 94 shows that an airfoil can be created with a thickness-to-cord ratio between approximately 3.5 - 4.5 percent from the curves shown.

#### Comparison of T-Series Airfoils with NACA 4-Digit Airfoils

The T-Series airfoils need to be evaluated against a similar airfoil geometry to contrast their performance characteristics. One of the major design parameters for the symmetric T-series airfoils has been thickness-to-chord ratio. The need for symmetric airfoils based on thickness-to-chord ratio lends itself directly to symmetric NACA 4-digit airfoils for comparison. The NACA 4-digit airfoils used in this investigation are not a reference to common NACA 4-digit airfoils (i.e. NACA 0006). The following symmetric NACA 4-digit airfoils are generated from the general equation for the thickness distribution for NACA 4-digit airfoils given by Abbott (10) as

$$\pm y_t = \frac{t/c}{.20} (.2969\sqrt{x} - .126x - .3516x^2 + .2843x^3 - .1015x^4). \quad (68)$$

The program contains the option to analyze NACA 4-digit airfoils with the potential-flow analysis method. The procedure requires the following information about the airfoil: the amount of camber, the location of the maximum camber, and the thickness-to-chord ratio. This information is readily available since these three pieces of information match that used in the numbering system of a NACA 4-digit airfoil. Eppler (7) addresses the more specific details of this option.

An airfoil from each of the five cases are chosen for comparison with the NACA 4-digit airfoil. Figures 95-101 show the comparisons of the airfoil shape, pressure distribution, lift coefficient, lift versus drag, lift-drag ratio versus angle of attack, and boundary-layer development between Airfoil T3 and the corresponding NACA 4-digit airfoil. The same comparisons are shown for Airfoil T22 in Figures 102-108, for Airfoil T603 in Figures 109-115, for Airfoil T234 in Figures 116-122, and for Airfoil T605 in Figures 123-129.

Figures 95, 102, 109, 116 and 123 show the T-series airfoils have a thicker front and more tapered tail than the NACA 4-digit airfoils. Also, the leading-edge radius is smaller for the NACA 4-digit airfoil. Abbott (10) gives the equation for the leading-edge radius of the NACA 4-digit airfoils to be

$$r_t = 1.1019(t/c)^2. \quad (69)$$

A comparison of the leading-edge radii is summarized in Table 7.

TABLE 7  
LEADING-EDGE RADII (T-SERIES & NACA 4-DIGIT AIRFOILS)

T-Series Airfoil	t/c (%)	$r_t$	NACA 4-Digit Airfoil $r_t$
T3	4.09	0.0040	0.0018
T22	4.75	0.0060	0.0025
T603	5.08	0.0085	0.0028
T234	4.97	0.0080	0.0027
T605	3.82	0.0055	0.0016

Table 7 shows that the leading-edge radius is larger for the T-series airfoils than the NACA 4-digit airfoil with the same t/c. Therefore, a NACA 4-digit airfoil with the same leading-edge radius as the T-series airfoil would have a much larger thickness-to-chord ratio. These thickness-to-chord ratios would not be acceptable to the specified constraints of this investigation. For example, in Table 7, Airfoil T3 has the smallest value of  $r_t$ . Using Equation (69), a NACA 4-digit airfoil with the same value of  $r_t$  would result in  $t/c = 6.03\%$ .

Figures 96, 103, 110, 117, and 124 show for a given angle of attack, the NACA 4-digit airfoils have a stronger adverse pressure gradient on the upper surface than the T-Series airfoils. As we have seen, this is an expected

result for an airfoil with a small thickness-to-chord ratio and small leading-edge radius.

The T-Series airfoils have larger leading-edge radii which allows for a smaller adverse pressure gradient in the recovery. Thus, the T-Series airfoils result in a trade-off of the smallest possible leading-edge radius for a given adverse pressure gradient. Figures 97, 104, 111, 118, and 125 show a benefit of this tradeoff in the section lift coefficient. The benefit of this tradeoff for the five airfoils are summarized in Table 8.

TABLE 8  
MAXIMUM LIFT COEFFICIENT (T-SERIES & NACA 4-DIGIT AIRFOILS)

T-Series Airfoil	t/c (%)	$C_{l_{max}}$	NACA 4-Digit Airfoil $C_{l_{max}}$
T3	4.09	0.77	0.57
T22	4.75	0.88	0.68
T603	5.08	0.95	0.71
T234	4.97	0.935	0.71
T605	3.82	0.77	0.55

Figures 97, 104, 111, 118, and 125 and Table 8 show the T-Series airfoils have an increased stall angle of approximately two degrees over a NACA 4-digit airfoil with the same t/c.

An increase in the stall angle indicates the location of the separation point has changed. Figures 100, 101, 107, 108, 114, 115, 121, 122, 126, and 127 show the boundary-

layer development plots for the upper surfaces. From Chapter I, the significant values of the shape function,  $H_{32}$  were shown to be:

$$H_{32} = 1.51509 \quad (\text{Laminar separation})$$

$$H_{32} = 1.46 \quad (\text{Turbulent separation}).$$

$$H_{32} > 1.58 \quad (\text{Turbulent reattachment}).$$

The transition line on these figures is based upon Equation (50) with  $m = 0$  and  $r = 0$ . It must be mentioned that, in these figures, the specific point where laminar separation or transition occur according to the analysis may not be shown intersecting the displayed lines for these events. This is a problem with the version of the code. In this code, the integral boundary-layer method evaluates the criteria between the points plotted in the figures. However, the results of the evaluation of these interior points are not shown in the figures.

All of the boundary-layer development analysis was done assuming a  $Re = 3.0 \times 10^6$ . Based on experiment, this Reynolds number is large enough so Reynolds number effects are small (11). In Figures 100, 101, 107, 108, 114, 115, 121, 122, 128, and 129, three angles of attack are plotted on each of the boundary-layer development plots. Each plot shows the case for  $\alpha = 0$ . The other two angles of attack were chosen so as to bracket the separation point. Figures 100, 101, 107, 108, 114, 115, 121, 122, 128, and 129 show that the boundary-layer development profile for  $\alpha = 0$ , for both the T-Series and the NACA 4-digit airfoils, indicate a

transition to a turbulent boundary-layer.

At the pre-separation angle of attack on each boundary-layer development plot for the T-Series airfoils, Figures 100, 107, 114, 121, and 128 all indicate laminar separation and reattachment with a turbulent boundary-layer. For the NACA 4-digit airfoils corresponding to Airfoils T3 and T605, Figures 101 and 129 show laminar separation followed by a reattachment with a turbulent boundary-layer. However, for the NACA 4-digit airfoils corresponding to Airfoils T22, T603, and T234, Figures 108, 115, and 122 show transition before laminar separation and then a reattachment of a turbulent boundary-layer.

Figures 98, 105, 112, 119, and 126 show the affect of the above phenomenon in  $C_l$  versus  $C_d$  plots. The transition to a turbulent boundary-layer before laminar separation reduces the drag (4). Figures 105, 112, and 119 show that when this occurs, on the NACA 4-digit airfoil, the bottom of the drag bucket is lower than for the T-Series airfoils. For the Airfoil T3 and T605 comparisons, Figures 98 and 126 show that there is no significant difference in the bottom of the curve.

Finally, Figures 99, 106, 113, 120, and 127 show the comparison of the lift-drag ratio curves. Clancy (12) indicates this relationship is important because it can be viewed as a measure of airfoil efficiency. Overall, there is not a significant difference in the efficiency of T-Series airfoils versus the NACA 4-digit airfoils.



## V. Conclusions and Recommendations

### Conclusions

This study has shown the applicability of PROFILE in the design of symmetric, low-speed, low-observable configuration airfoils. An objective of this investigation was to determine any limitations of the program for this application. As discussed, airfoils with small leading-edge radii and small thickness-to-chord ratios are prone to early separation and abrupt stall characteristics. For airfoils with very small leading-radii, the viscous correction for the section lift coefficient was not suitable after the stall since it resulted in unrealistic negative values. For the T-Series airfoils, the stall angles were larger, but the same effect was seen in the inability to predict post stall lift coefficients. The best results in obtaining this class of airfoils was achieved if the secondary pressure recovery was neglected by choosing  $\phi_w = 0$  for both the upper and lower surfaces.

The power law relationship between  $\alpha^*$  and  $x/c$  based on the physical relationships between the pressure distribution,  $\alpha^*$ , leading-edge shape, and the thickness of the airfoil proved very successful. In all five case studies performed for the different coefficients of the power law relationship, symmetrical airfoils were produced

within the imposed constraints on the leading-edge radius and the thickness-to-chord radius. The curves presented in Figures 91 and 92 give the designer a new ability to determine the input parameters needed to produce an airfoil with the desired thickness-to-chord ratio and leading-edge radius. However, for a given leading-edge radius, the designer is constrained to a band of available thickness-to-chord ratios with a width of approximately one percent.

The T-Series airfoils, produced with the power law relationship, showed improved performance compared to the NACA 4-digit airfoils. The T-Series airfoils had larger leading-edge radii than an equivalent thickness NACA 4-digit airfoils, which resulted in slightly higher drag. However, the stall angles were increased approximately two degrees. Therefore, the T-Series airfoils showed improved stall characteristics, for an airfoil meeting the low-observability criteria, compared to equivalent thickness NACA 4-digit airfoil.

#### Recommendations for Further Study

1. Investigate the possibility of extending the power law relationship for thin cambered airfoils.

2. Conduct a parametric study in which input parameters held constant in this investigation, are varied. The closure contribution parameters  $\phi_B$ ,  $K_R$ , and  $K_{tol}$  could be varied to determine their effects on the airfoil thickness and aerodynamic characteristics due to the change

in the shape of the trailing-edge.

3. Investigate the performance of airfoils created with a transonic analysis code.

## References

1. Eppler, Richard and Dan M. Somers. A Computer Program for the Design and Analysis of Low-Speed Airfoils. NASA TM-80210. Washington: National Aeronautics and Space Administration, 1980.
2. Alexander, Michael G., Capt. Personal interviews and notes. Wright Laboratory (WL/FIMM), Wright-Patterson AFB OH, March through November 1992.
3. Eppler, Richard. Direct Calculation of Airfoils from Pressure Distribution. NASA TT-F-15417. Washington: National Aeronautics and Space Administration, 1974.
4. Eppler, Richard. Airfoil Design and Data. Stuttgart: Springer-Verlag, 1989.
5. Hess, John L. "The Use of Higher-Order Surface Singularity Distributions to Obtain Improved Potential Flow Solutions for Two-Dimensional Lifting Airfoils," Computer Methods in Applied Mechanics and Engineering, 5:1: 11-35 (January 1975).
6. Eppler, Richard. Practical Calculation of Laminar and Turbulent Bled-Off Boundary Layers. NASA TM-75328 Washington: National Aeronautics and Space Administration, 1978.
7. Eppler, Richard. User's Guide. Stuttgart: University of Stuttgart, November 1988.
8. Graham, Donald J., Gerald E. Nitzberg and Robert N. Olsen. A Systematic Investigation of Pressure Distributions at High Speeds over Five Representative NACA Low-Drag and Conventional Airfoil Sections. NACA Report No. 832. Washington: National Advisory Committee for Aeronautics, 1945.
9. Somers, Dan M. Personal interviews. Airfoils Incorporated, State College PA, October through November 1992.
10. Abbott, Ira H. and Albert E. Von Doenhoff. Theory of Wing Sections. Dover Publications Inc.: New York, 1949.
11. Kinsey, Don. Personal interviews. Wright Laboratory (WL/FIMM), Wright-Patterson AFB OH, March through November 1992.

12. Clancy L. J. Aerodynamics. New York: John Wiley & Sons, 1975.

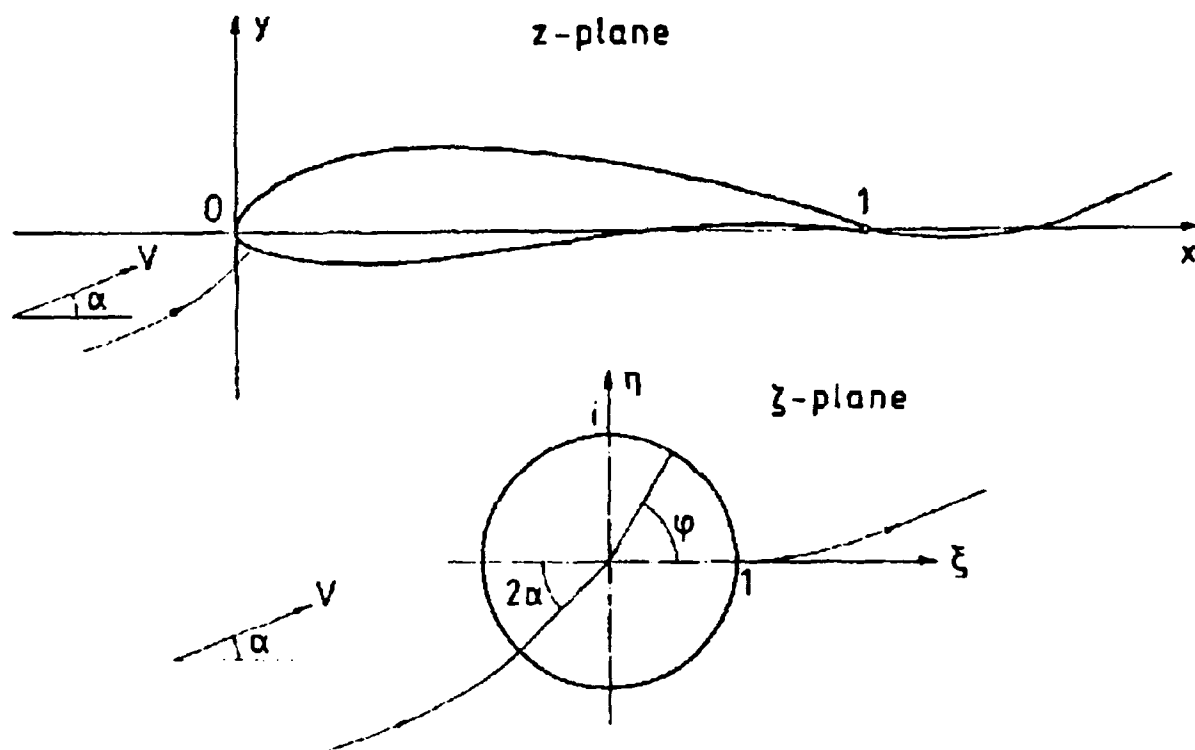


Figure 1. Mathematical Planes for Conformal Mapping (1:127)

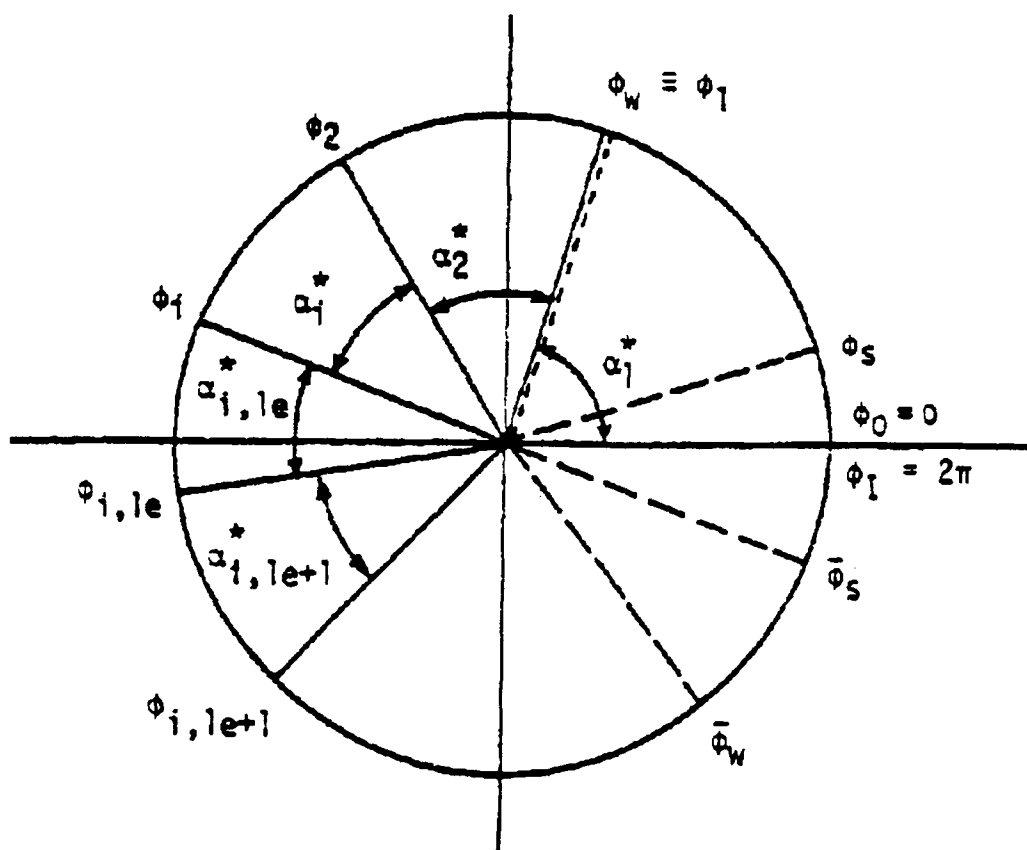


Figure 2. Arc Limit Description (1:129)

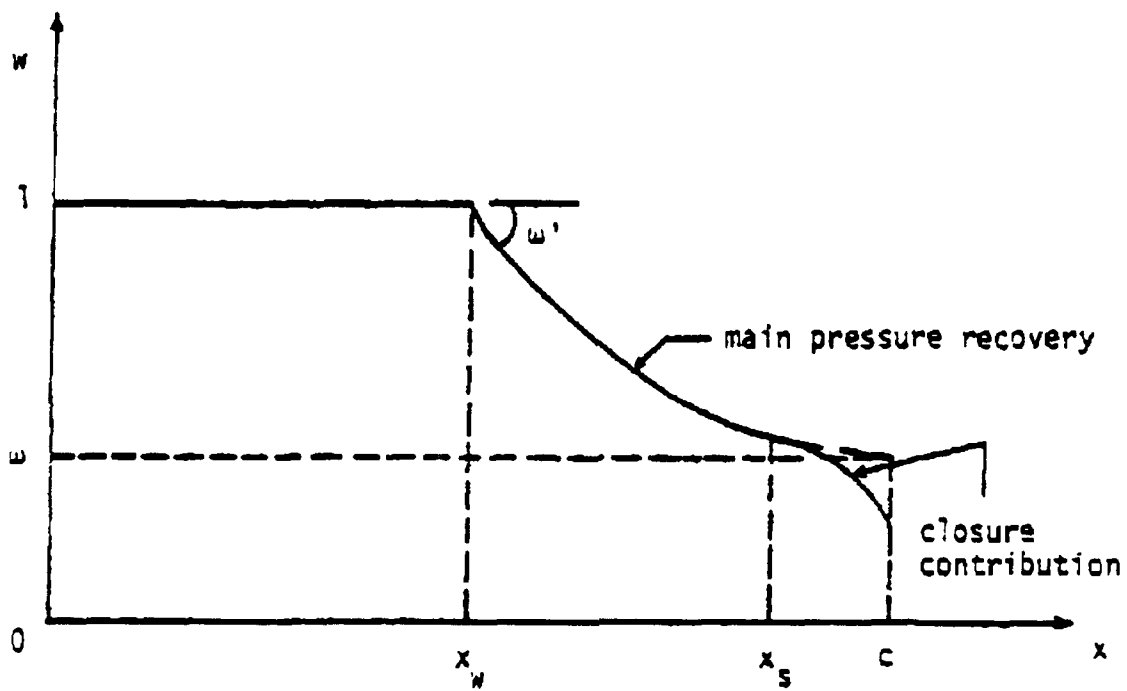


Figure 3. Pressure Recovery and Closure Contribution (1:128)



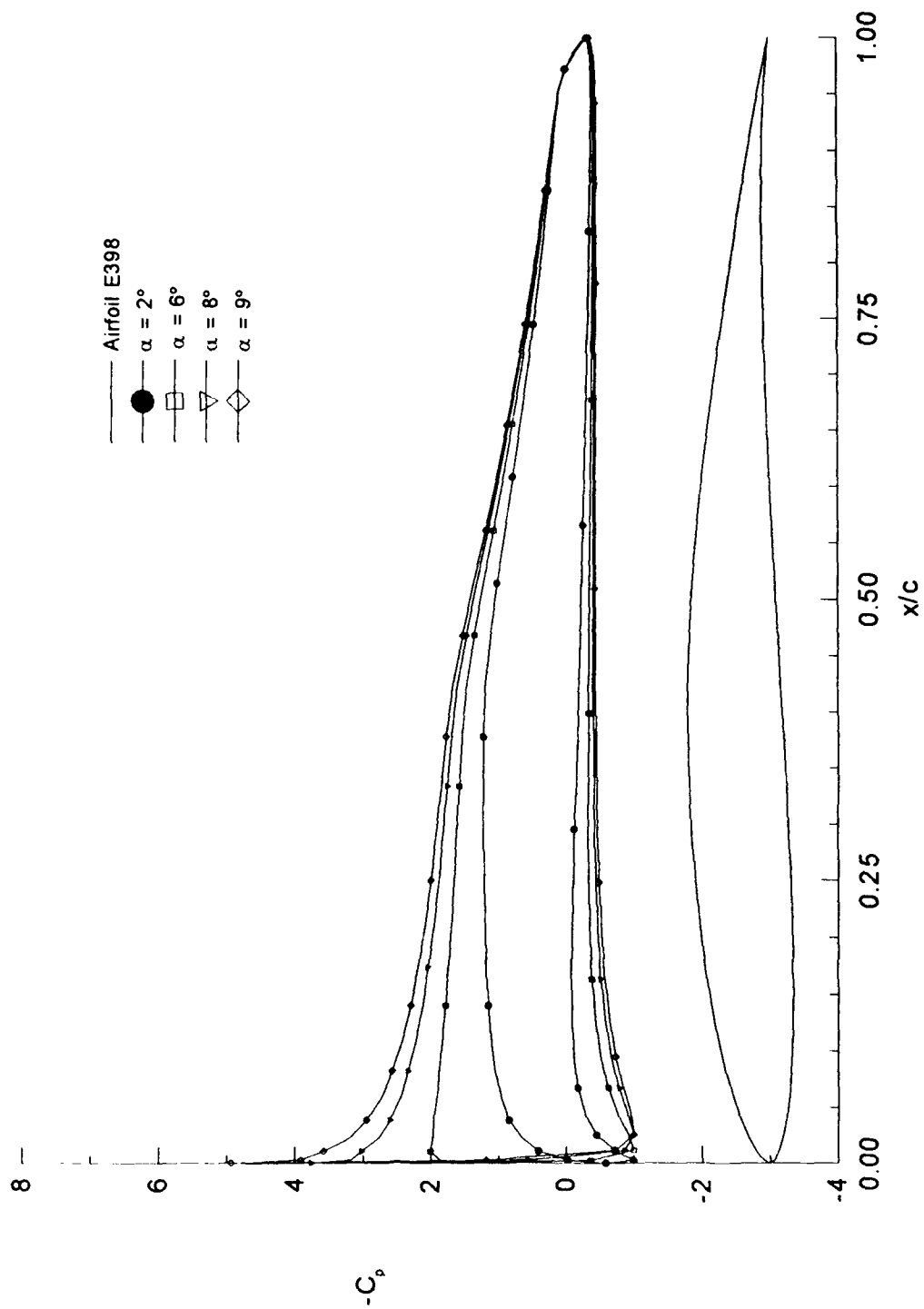


Figure 4. Airfoil E398 and Pressure Distributions -  $t/c = 14.27\%$  - Incompressible

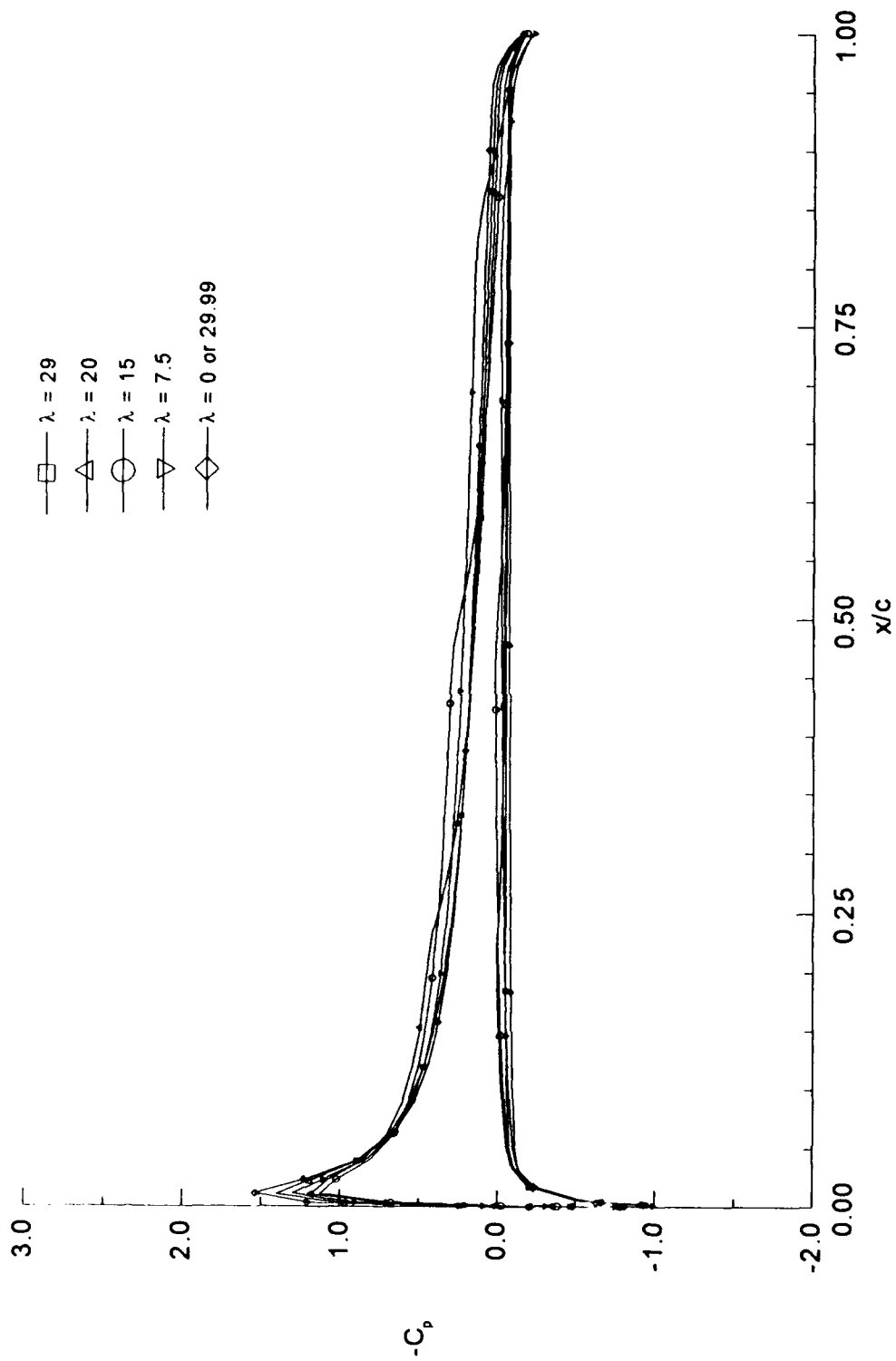


Figure 5. Sensitivity of Pressure Distribution to Changes in Location of Specified Main Pressure Recovery - Airfoil G48 -  $\alpha = 2^\circ$

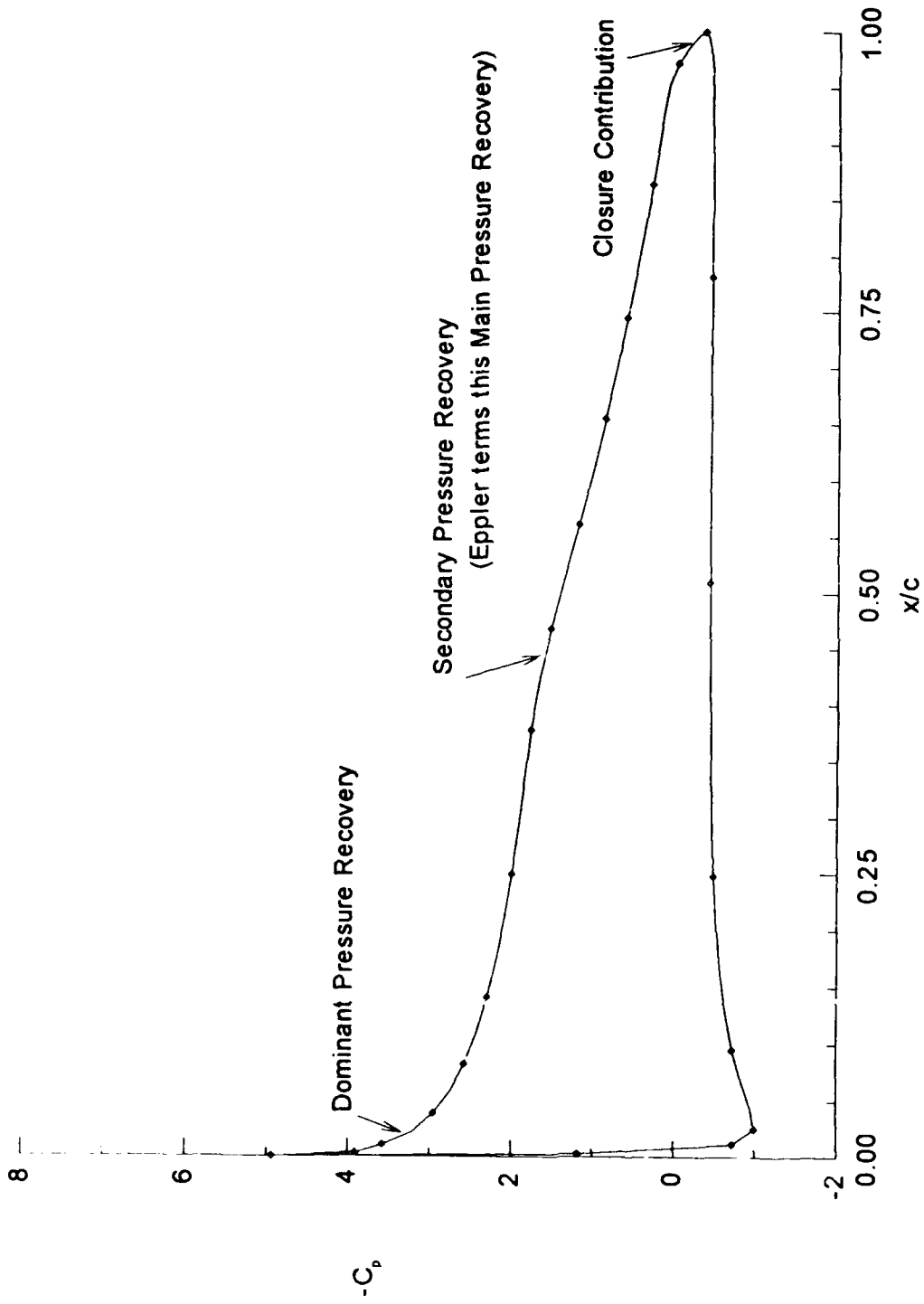


Figure 6. Terminology Summary

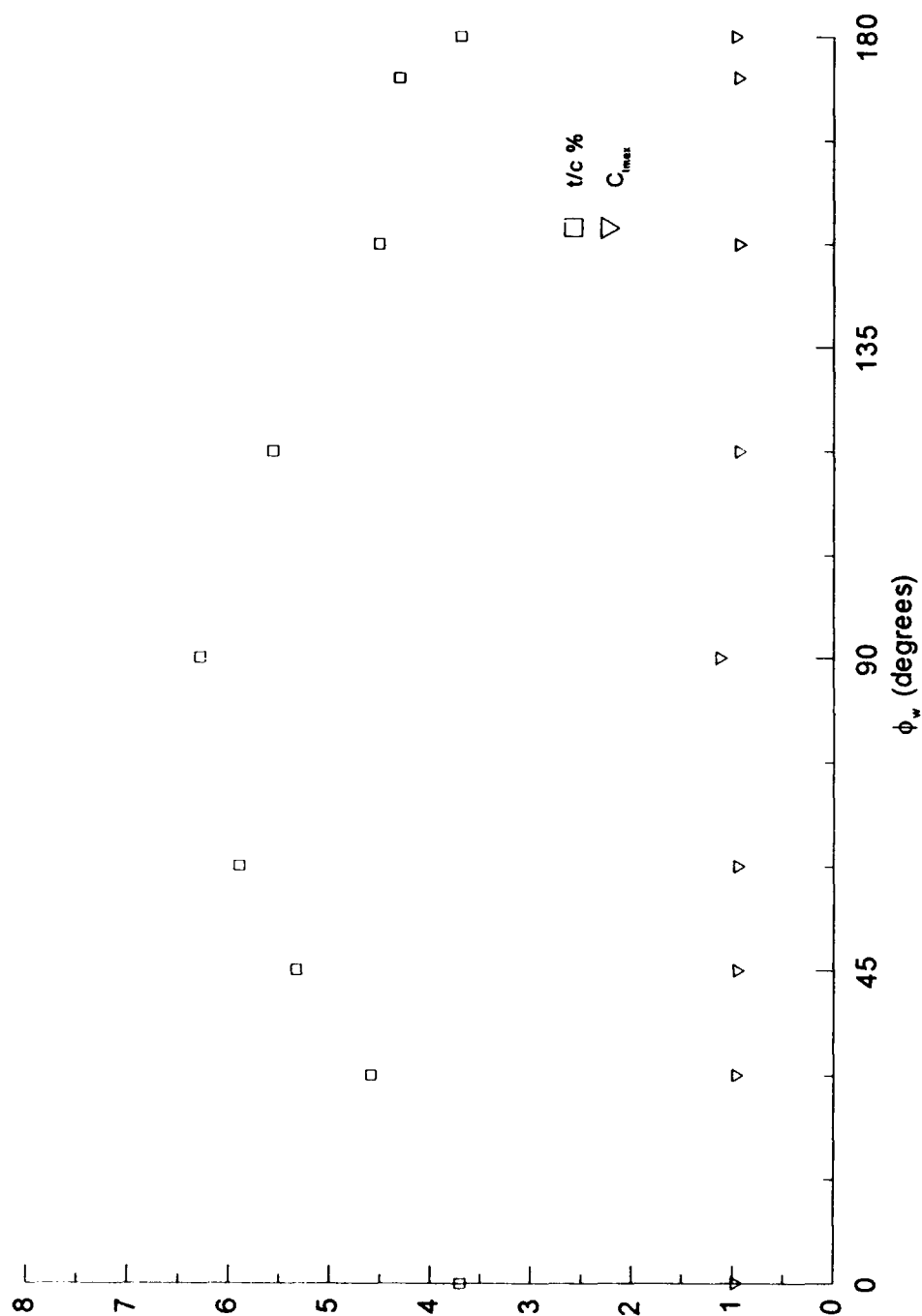


Figure 7. Sensitivity of Thickness-to-Chord Ratio and Maximum Lift Coefficient to the Location of the Secondary Pressure Recovery - Airfoil G48

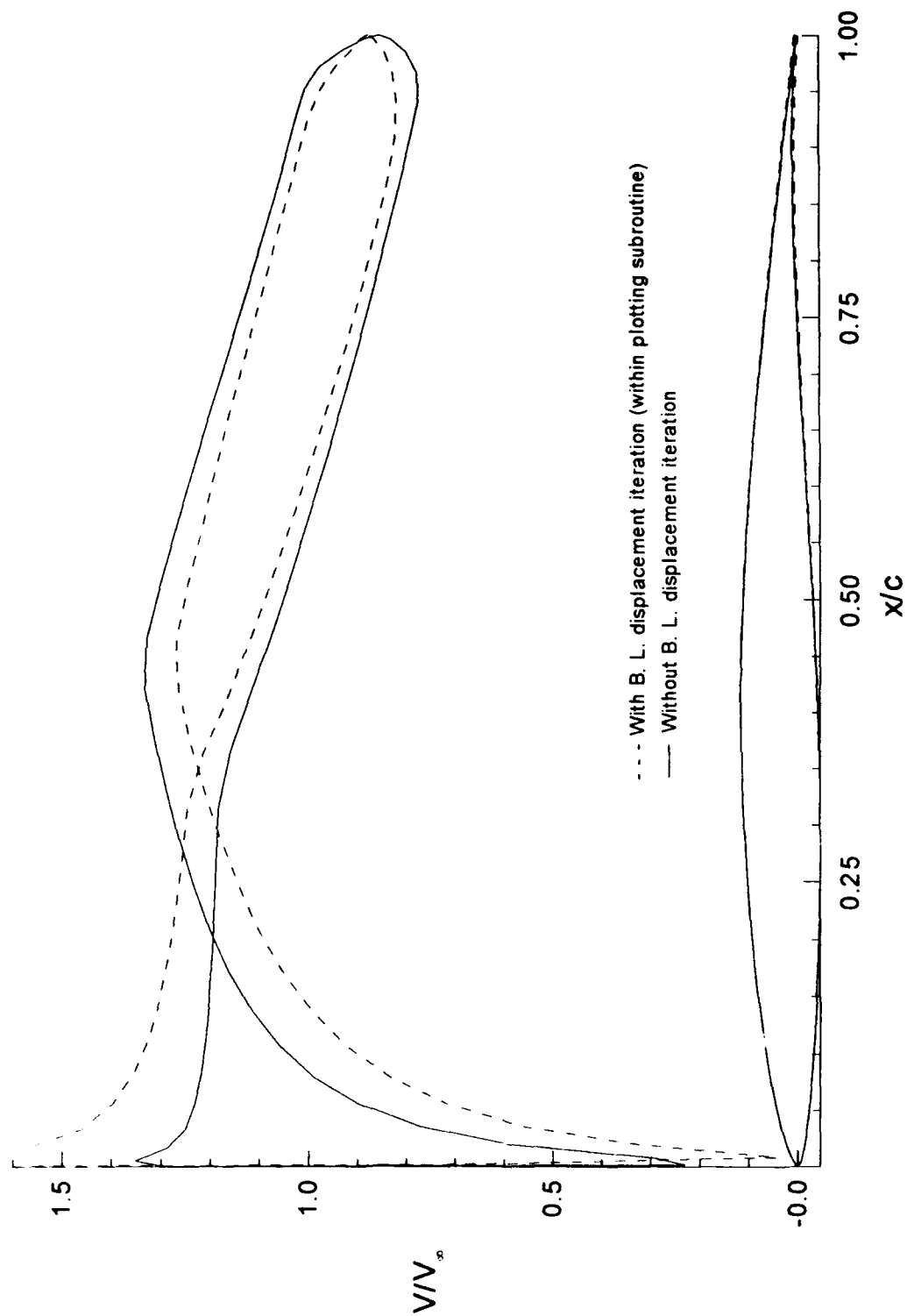


Figure 8. Velocity Distributions - Airfoil SH9 - Incompressible -  $\alpha = 2^\circ$

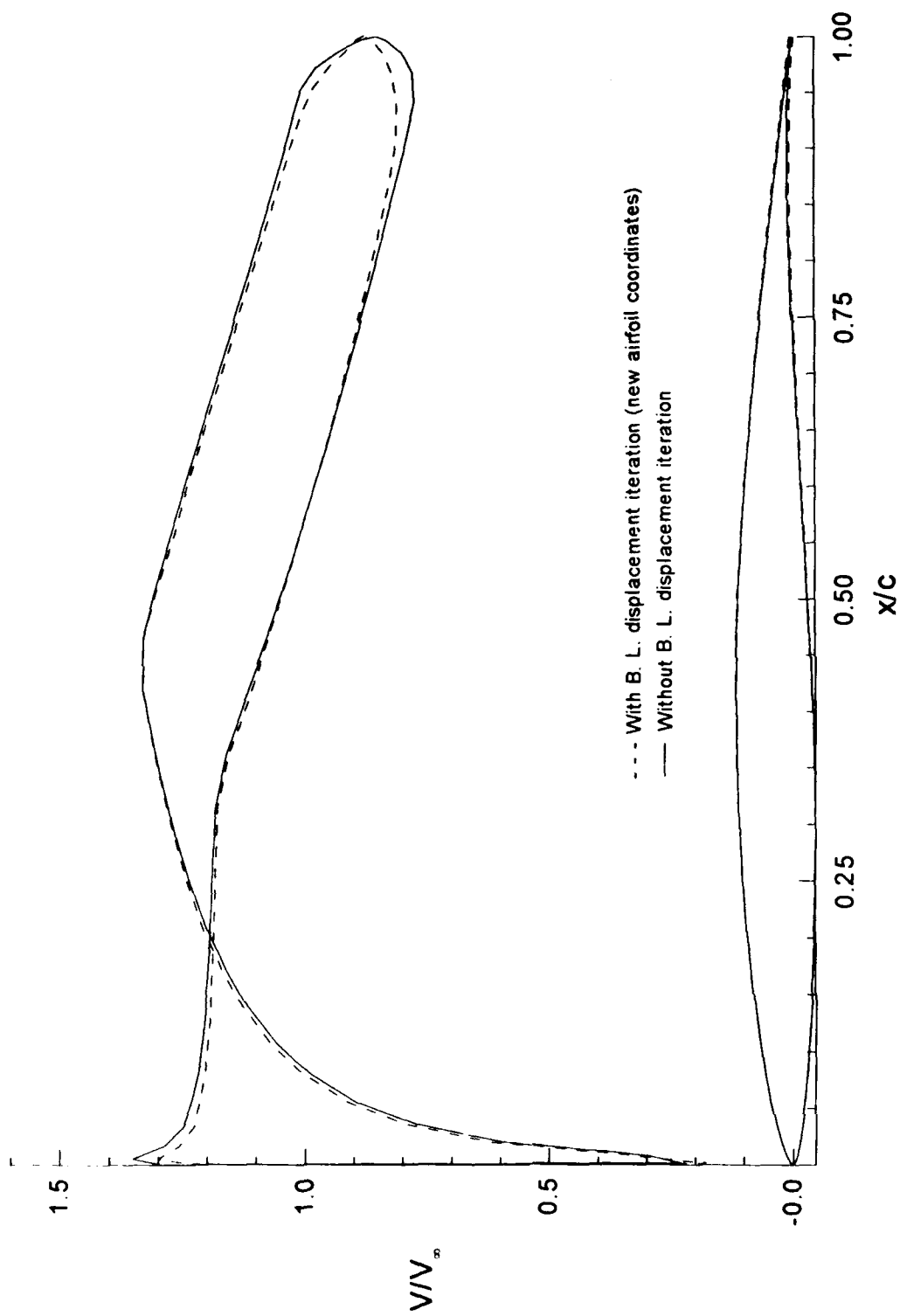


Figure 9. Velocity Distributions - Airfoil SH9 - Incompressible -  $\alpha = 2^\circ$

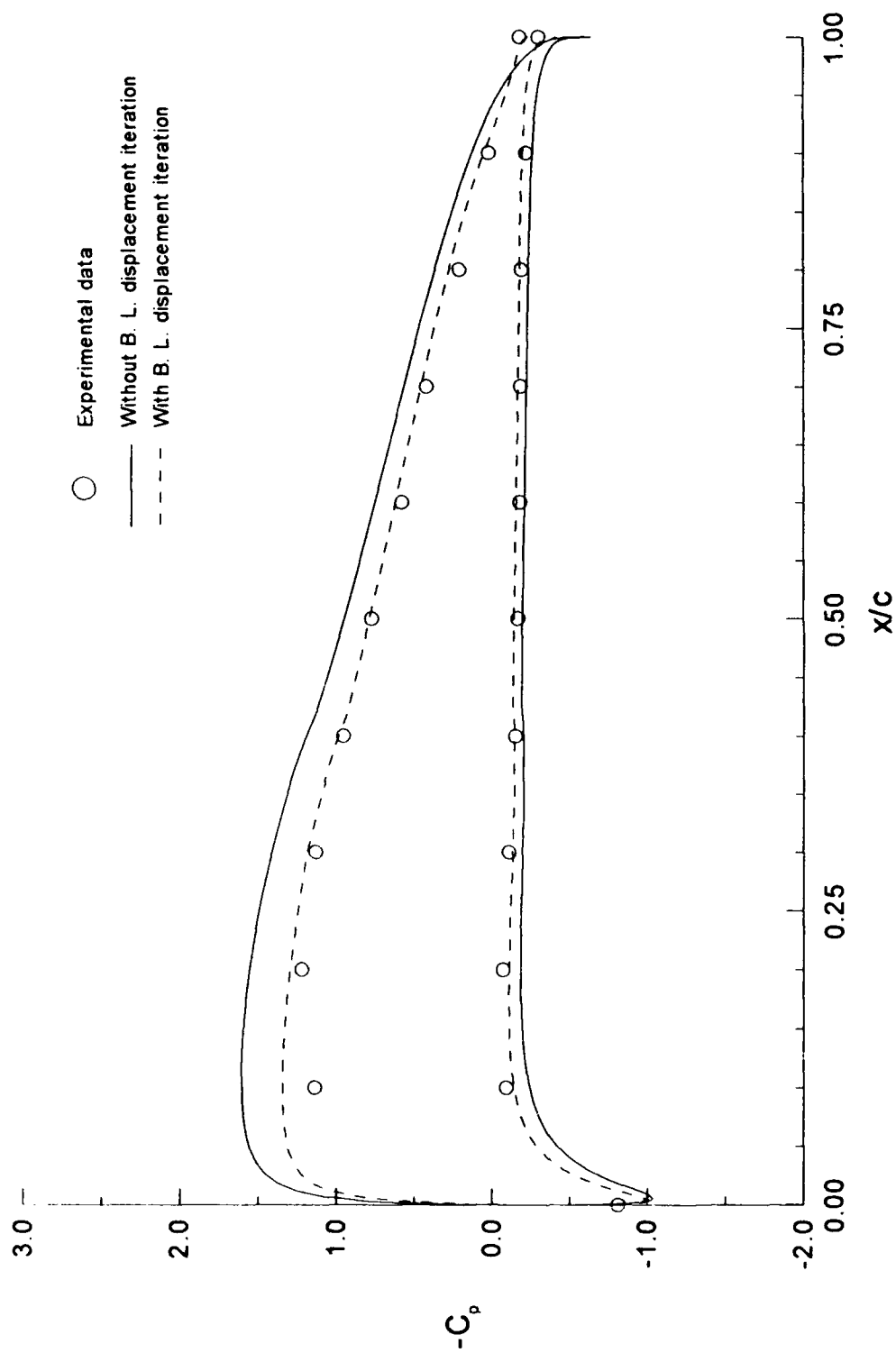


Figure 10. Pressure Distributions - NACA 4415 -  $M = .4$  -  $\alpha = 4^\circ$

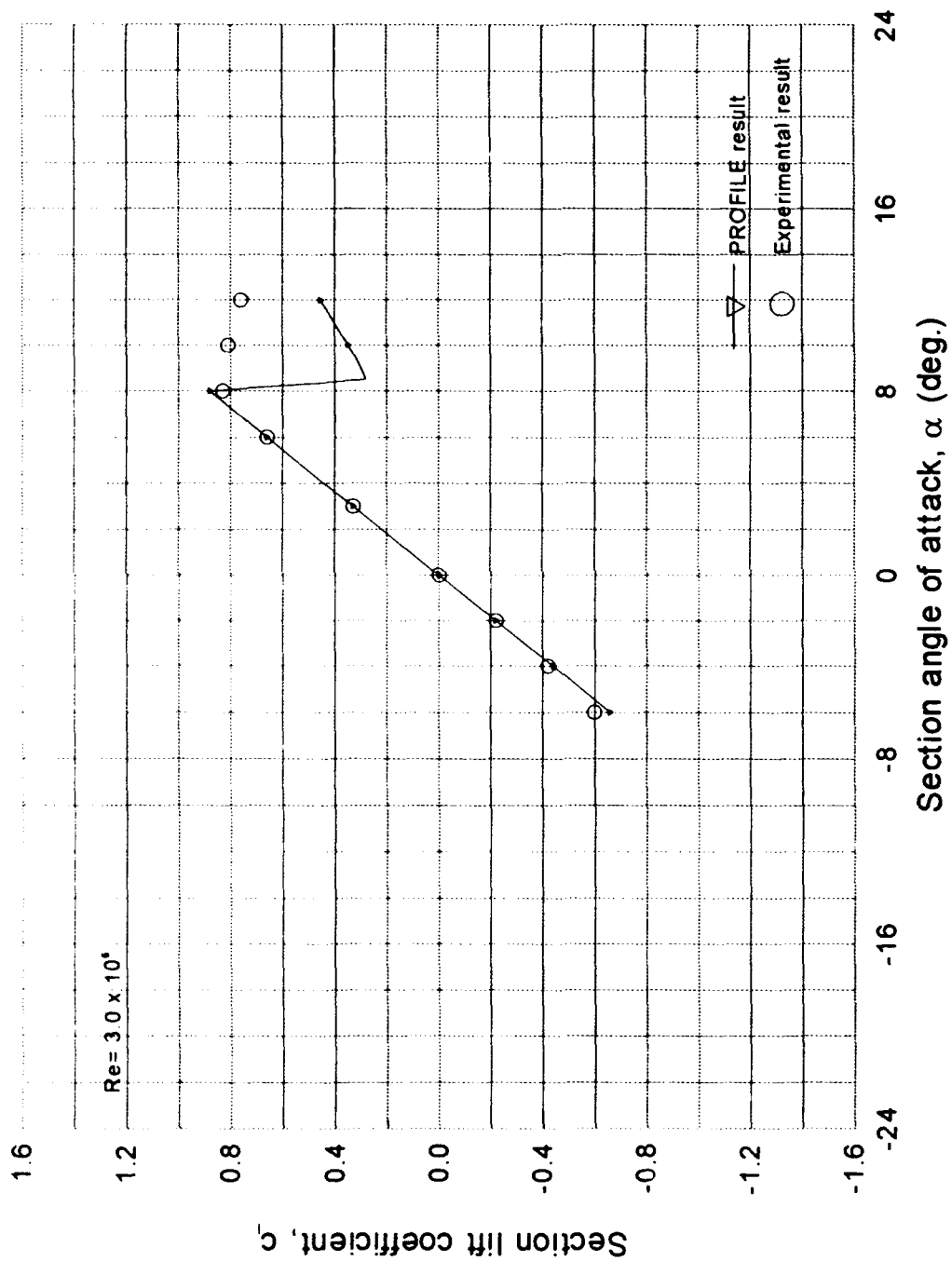


Figure 11. NACA 0006  $C_l$  vs  $\alpha$  Curves



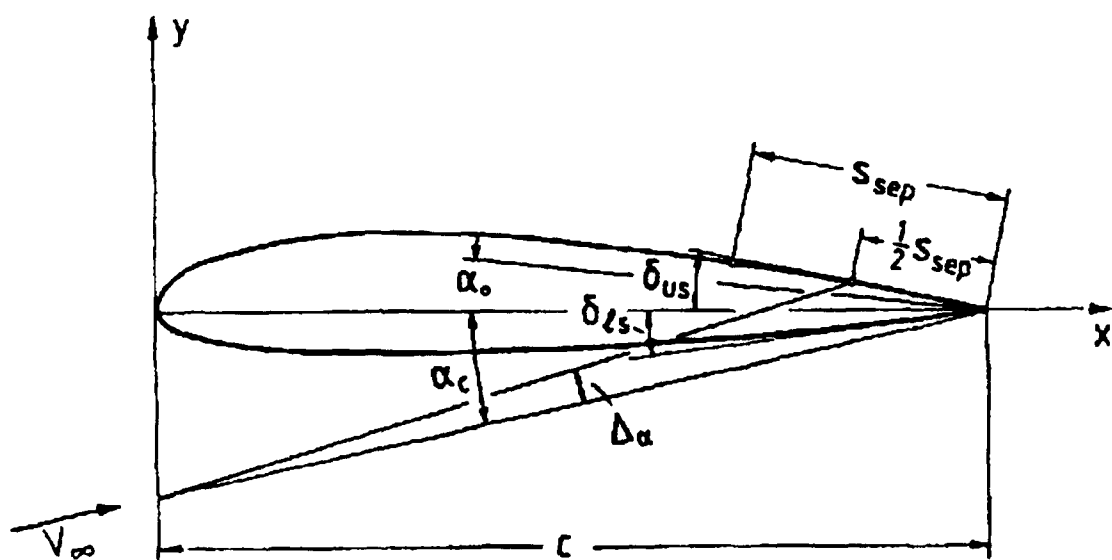


Figure 12. Correction to  $C_L$  Due to Separation (3:78)

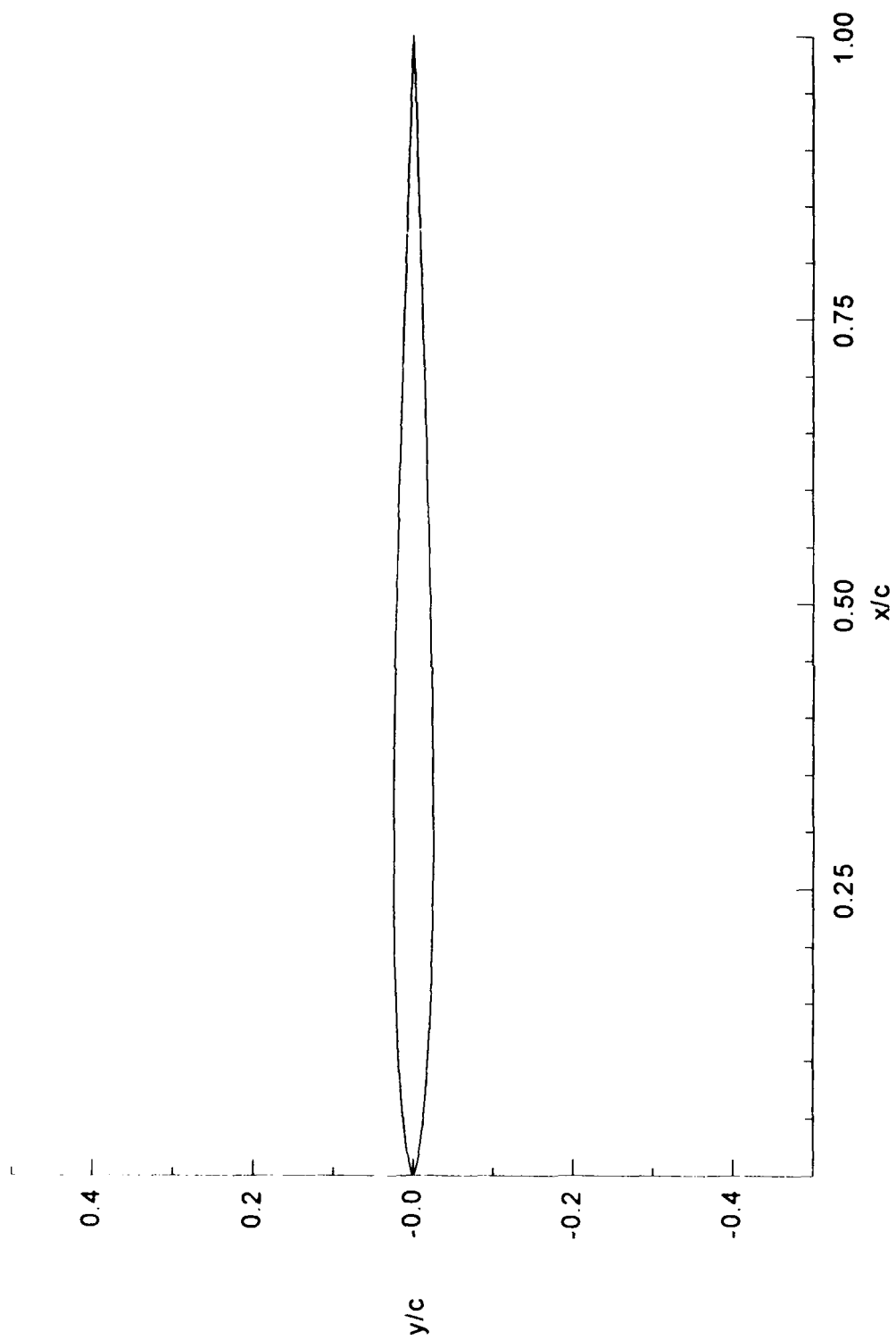


Figure 13. Airfoil G31 -  $t/c = 4.95\%$

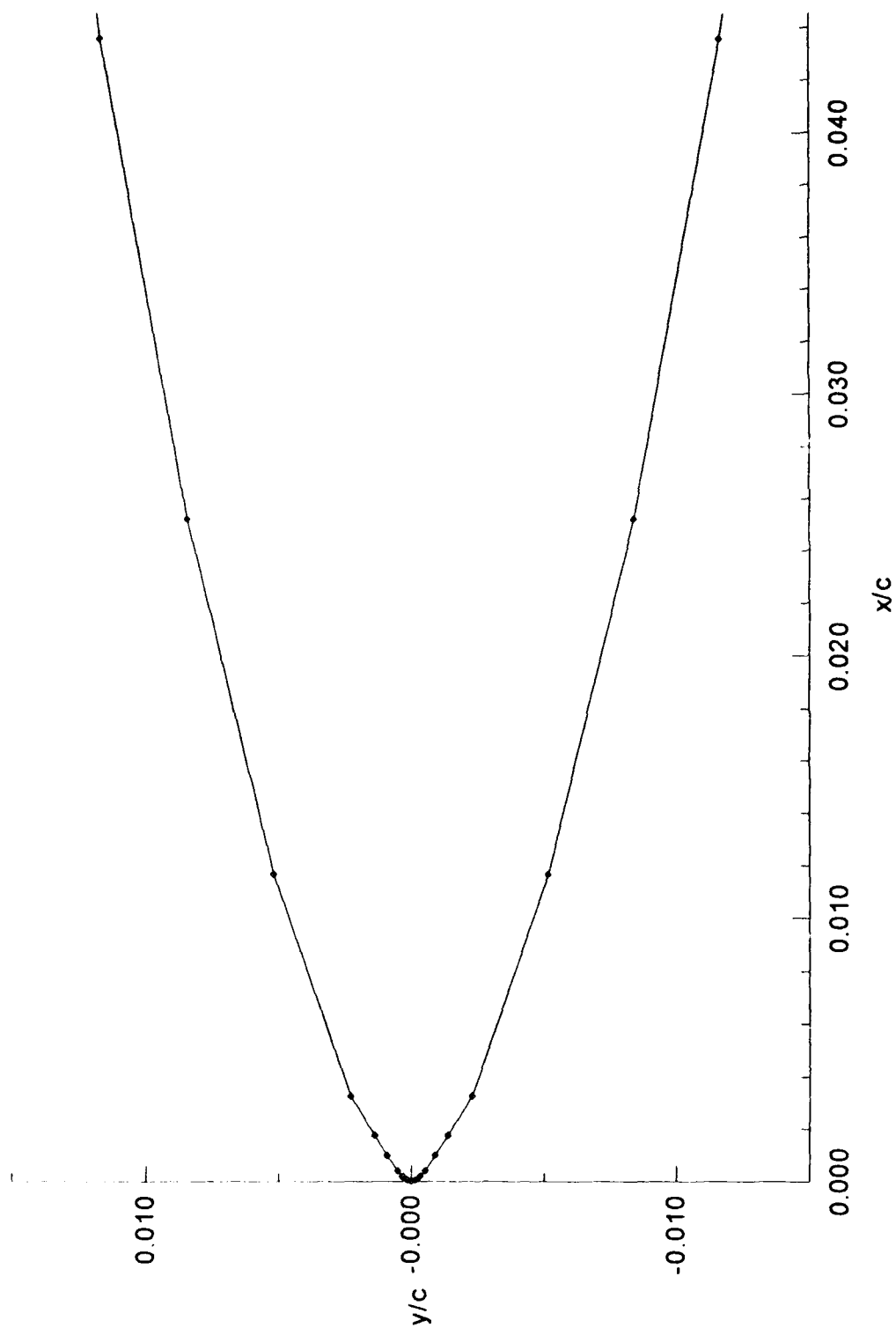


Figure 14. Airfoil G31 Leading-Edge -  $t/c = 4.95\%$

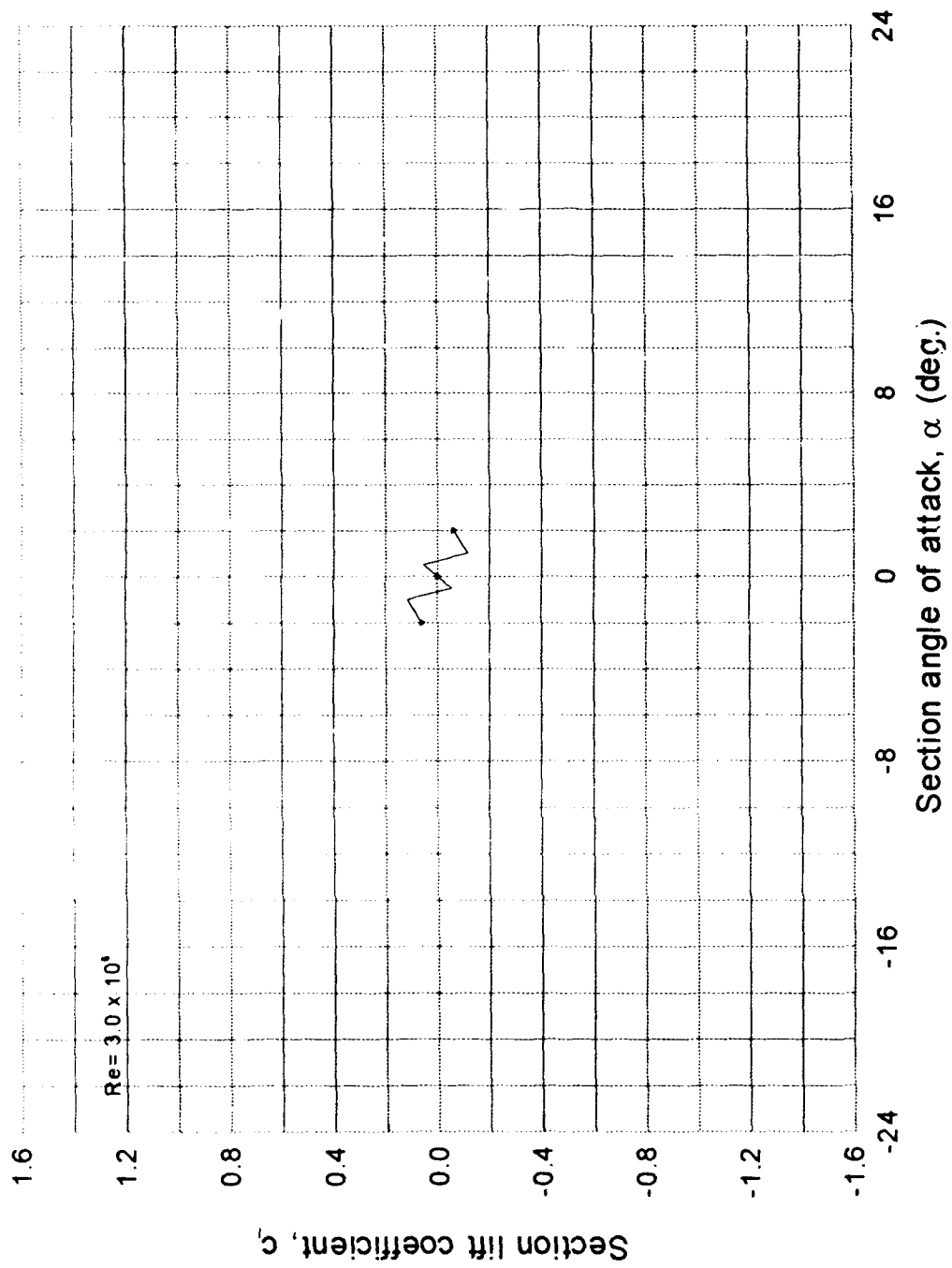


Figure 15. Airfoil G31 -  $C_l$  vs  $\alpha$  Curve

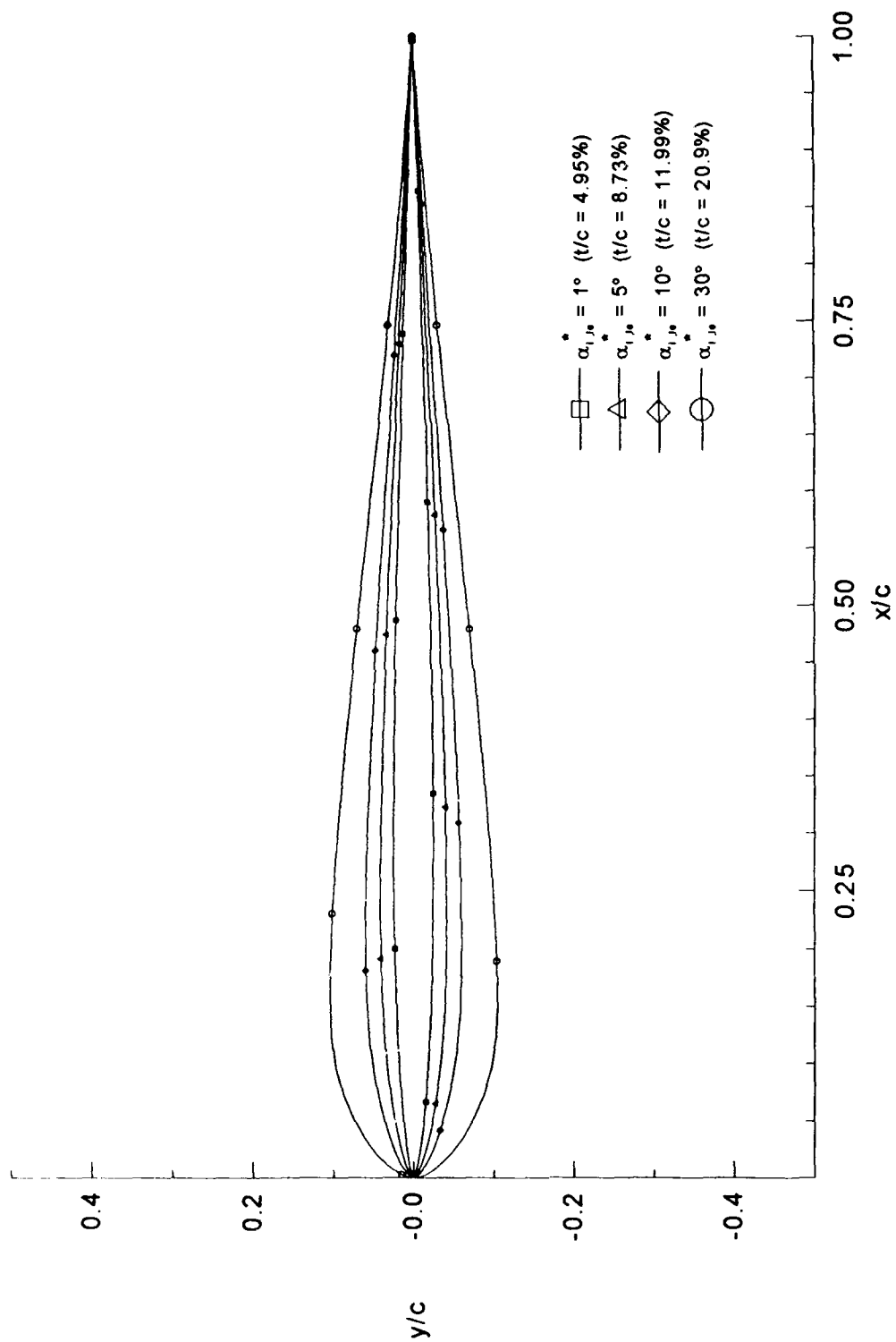


Figure 16. Effect of  $\alpha_{i,le}^*$  on Thickness-to-Chord Ratio

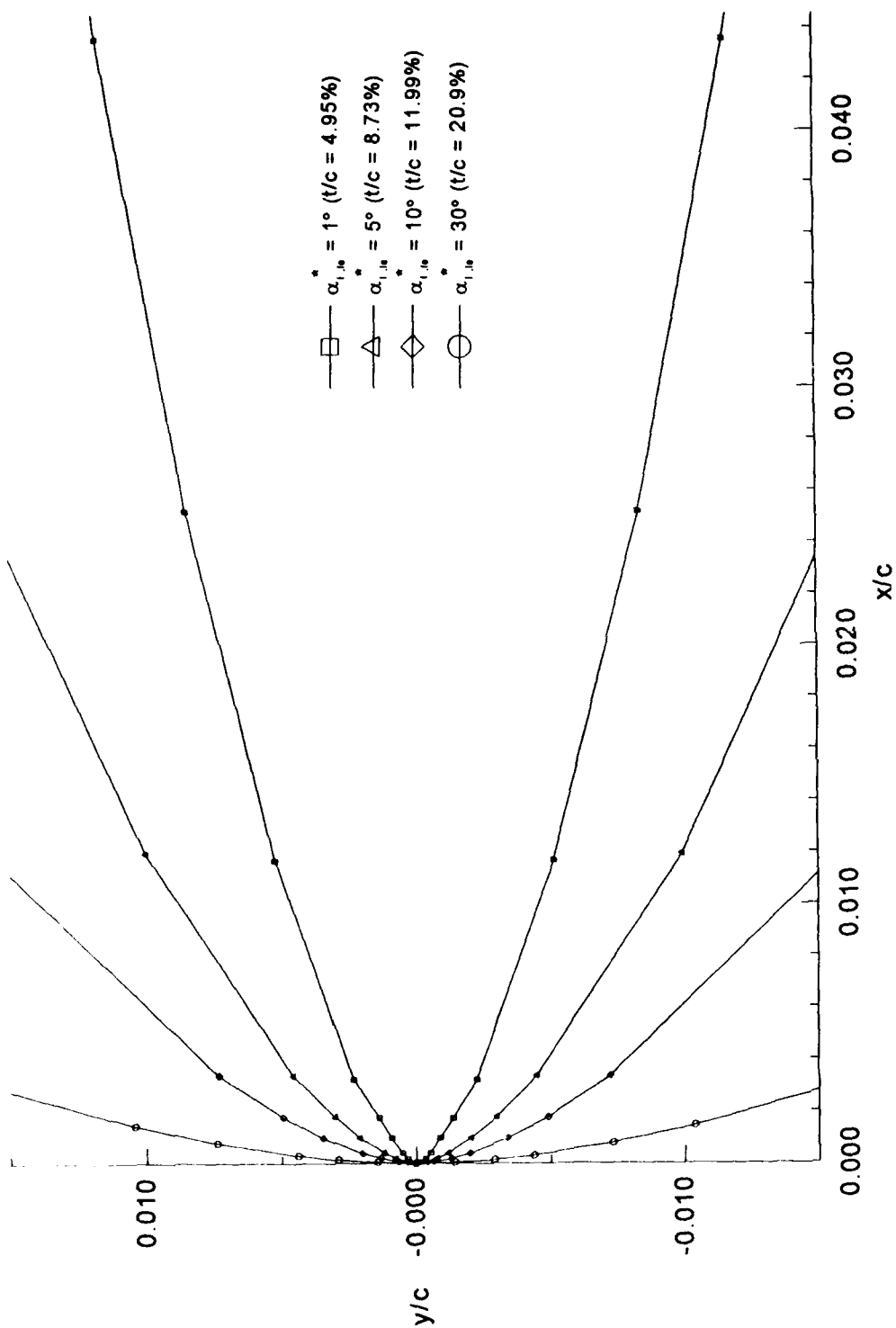


Figure 17. Effects of  $\alpha_{1,le}^*$  on Leading Edge-Radius

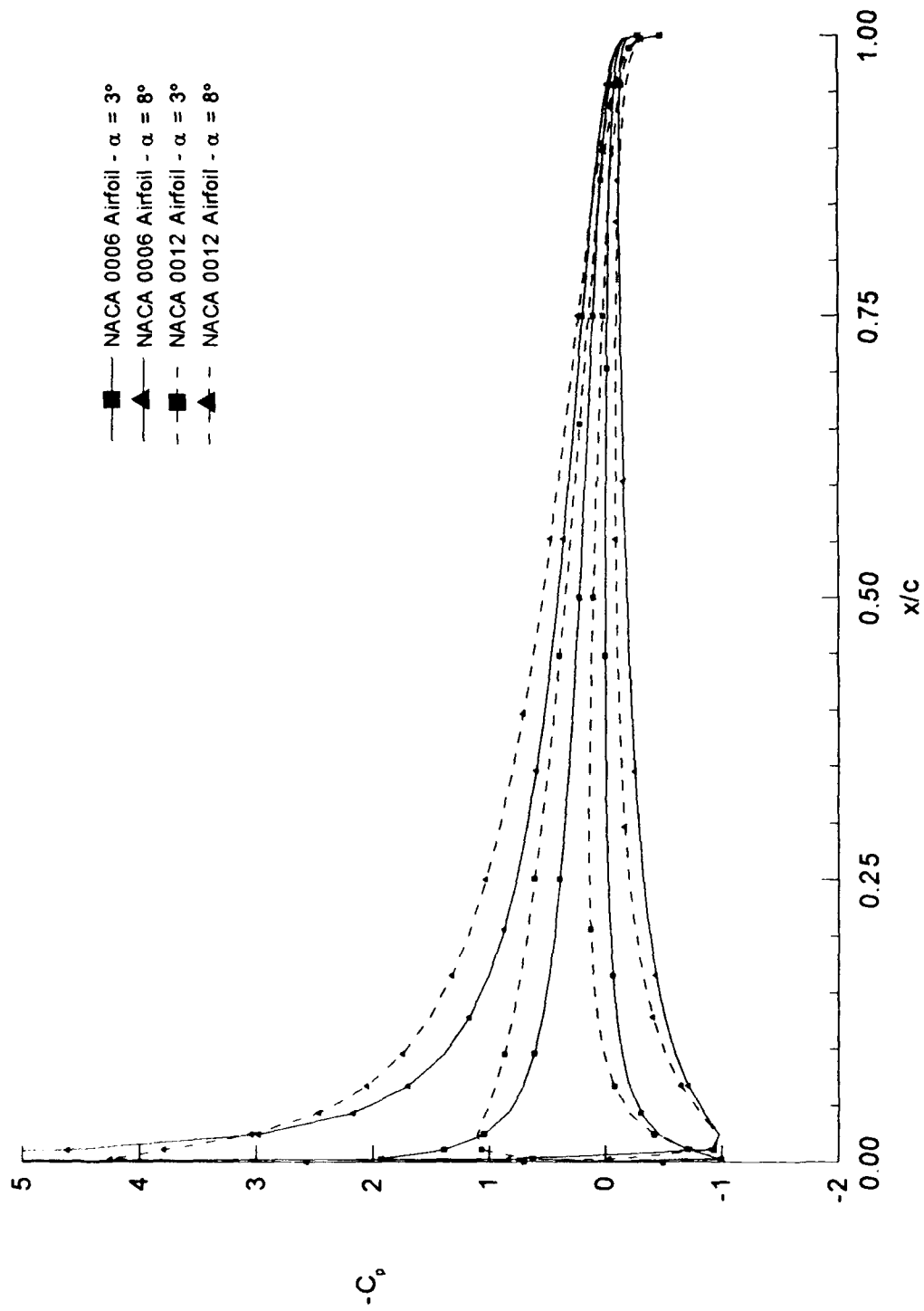


Figure 18. Pressure Distributions - NACA 0006 vs NACA 0012 - Incompressible

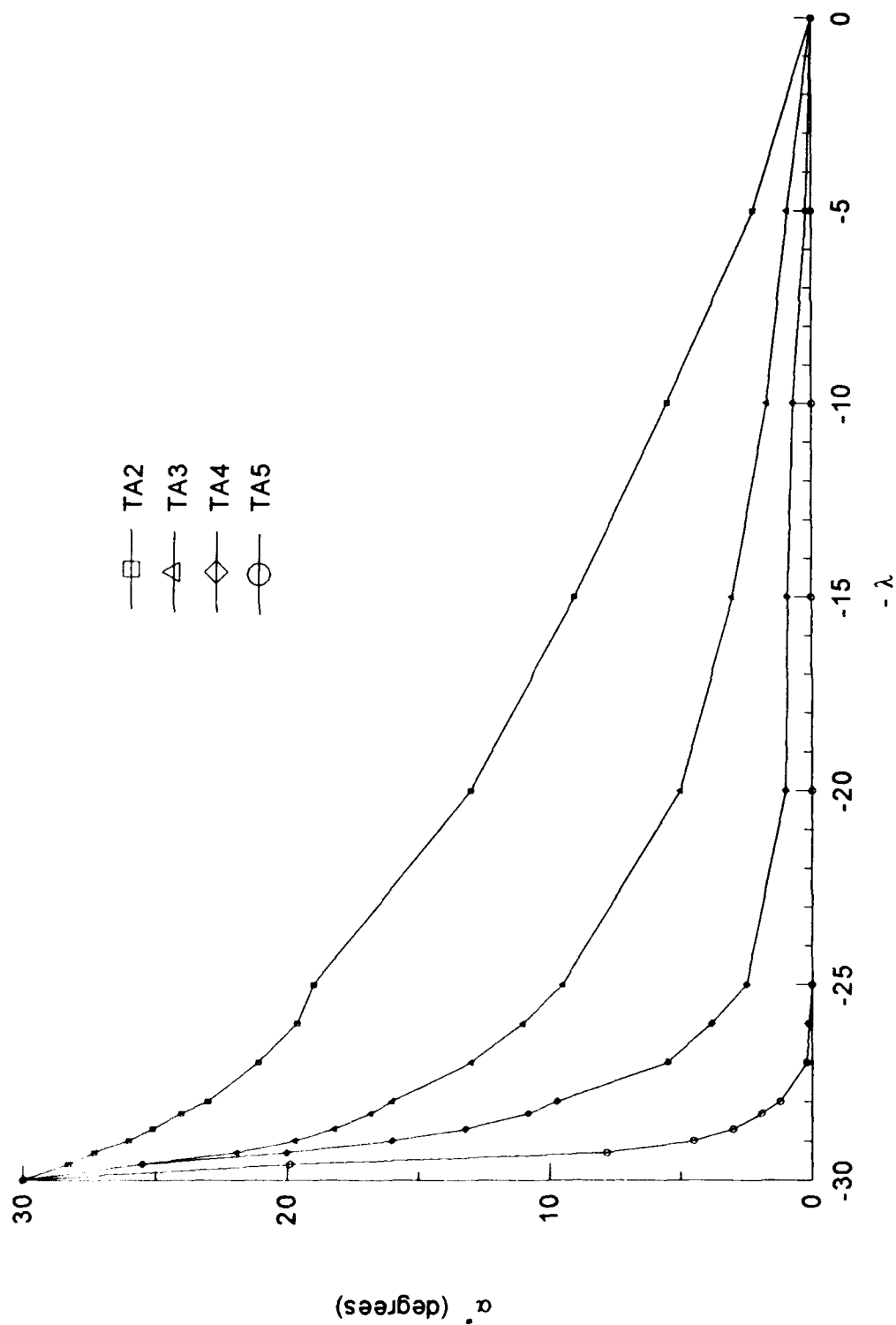


Figure 19. TA2-TA5 Curves - Proposed  $\alpha$  -  $\lambda$  Relationships



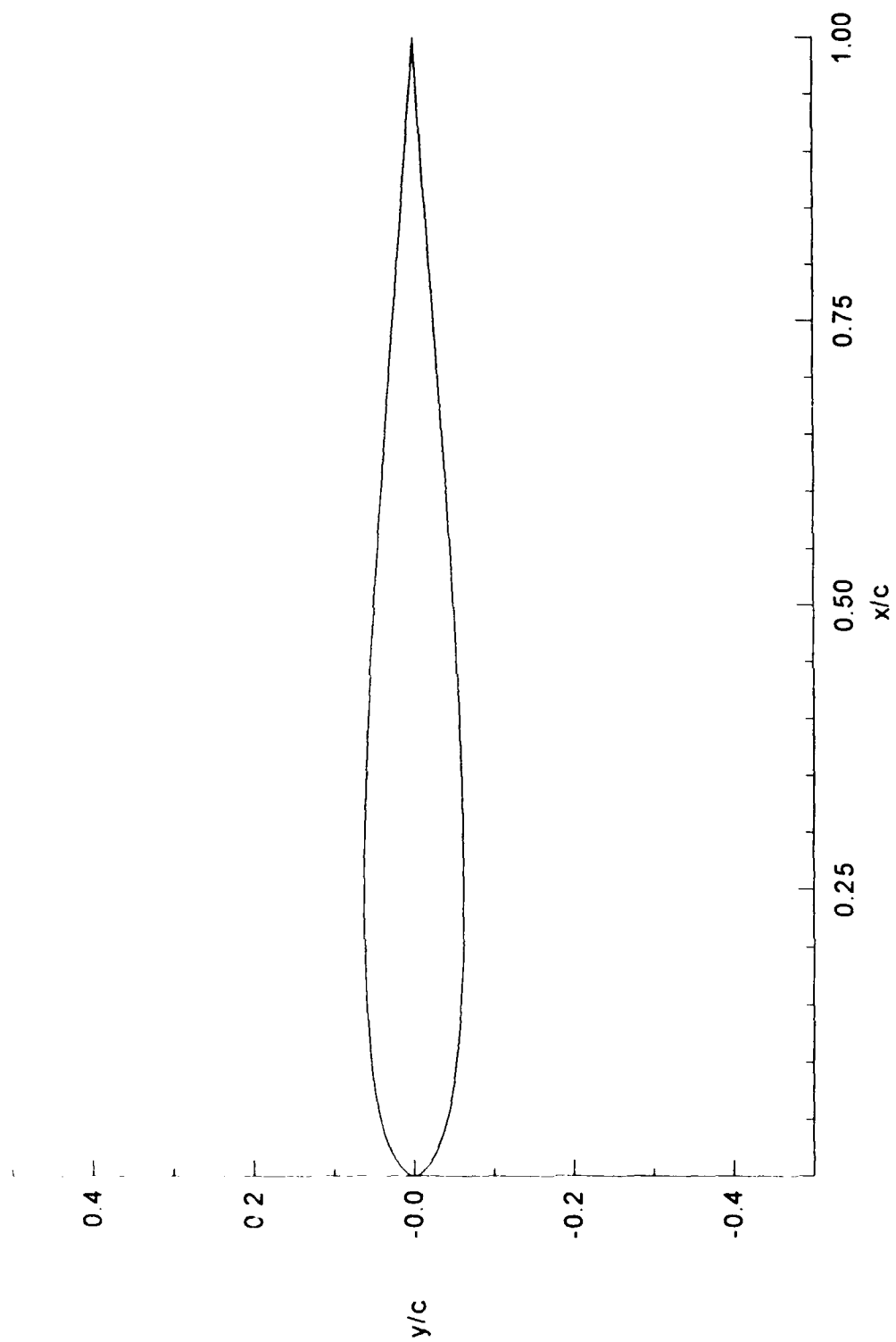


Figure 20. Airfoil TA2 -  $t/c = 12.5\%$

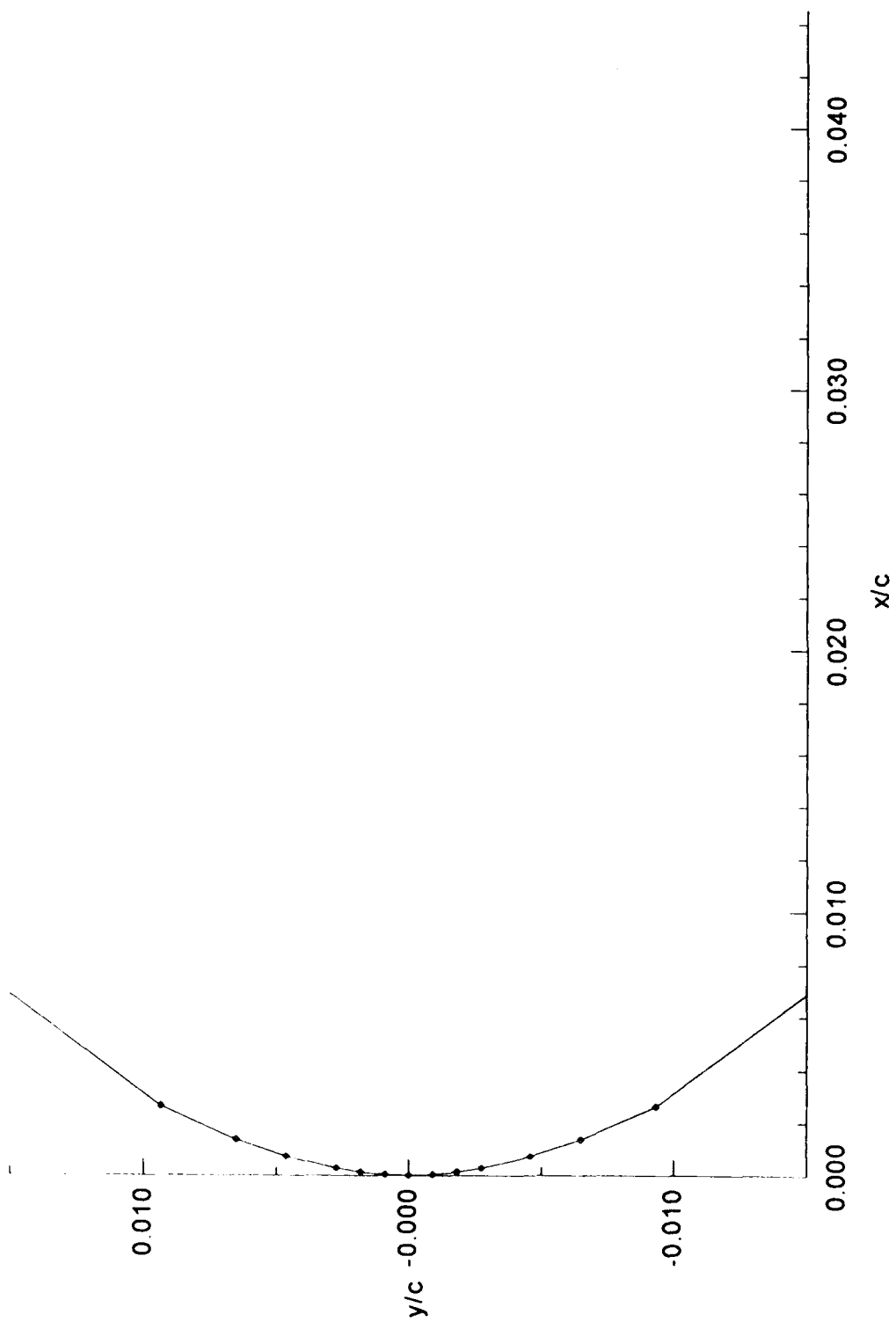


Figure 21. Airfoil TA2 Leading-Edge -  $t/c = 12.5\%$

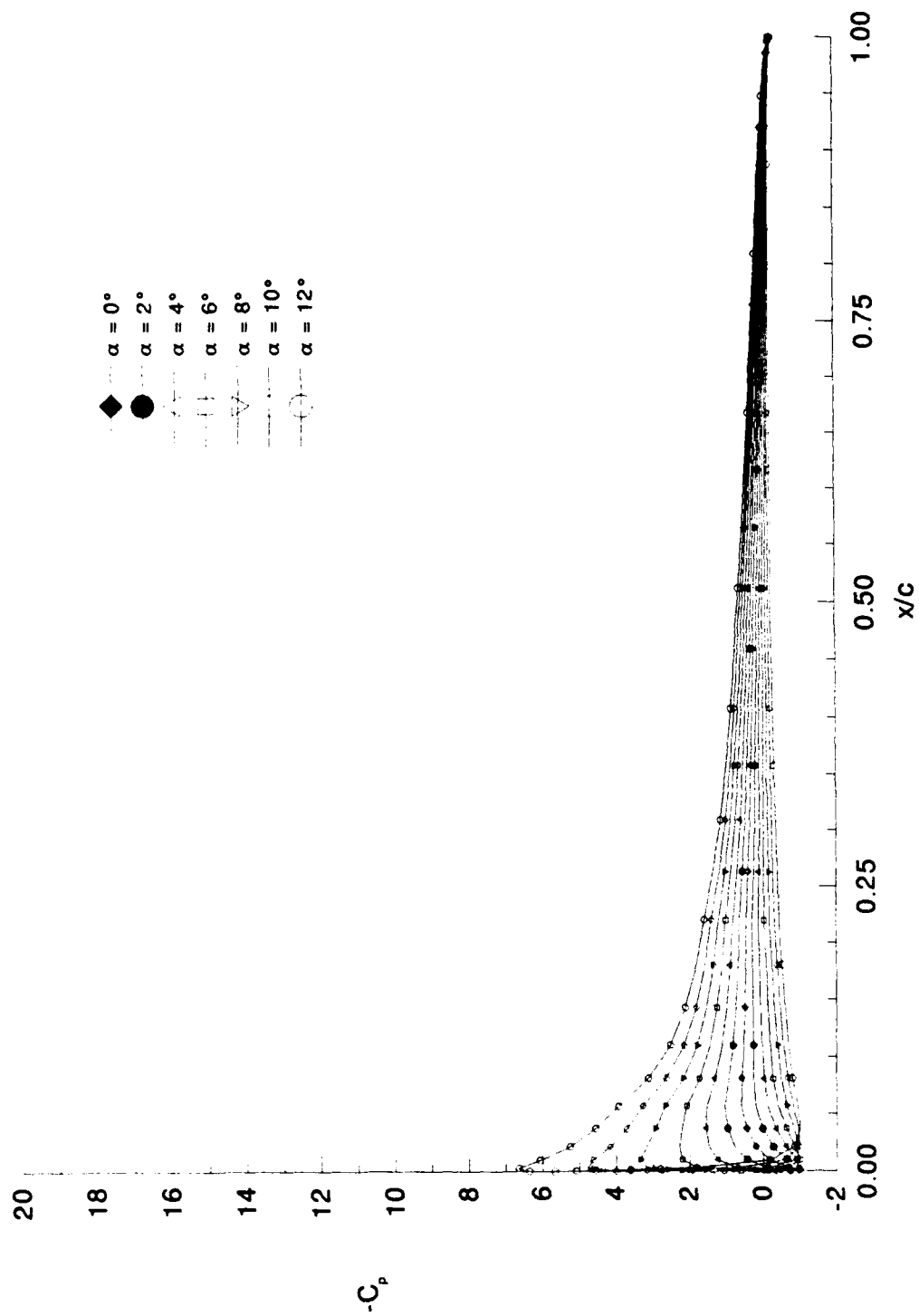


Figure 22. Pressure Distributions - TA2 - Incompressible

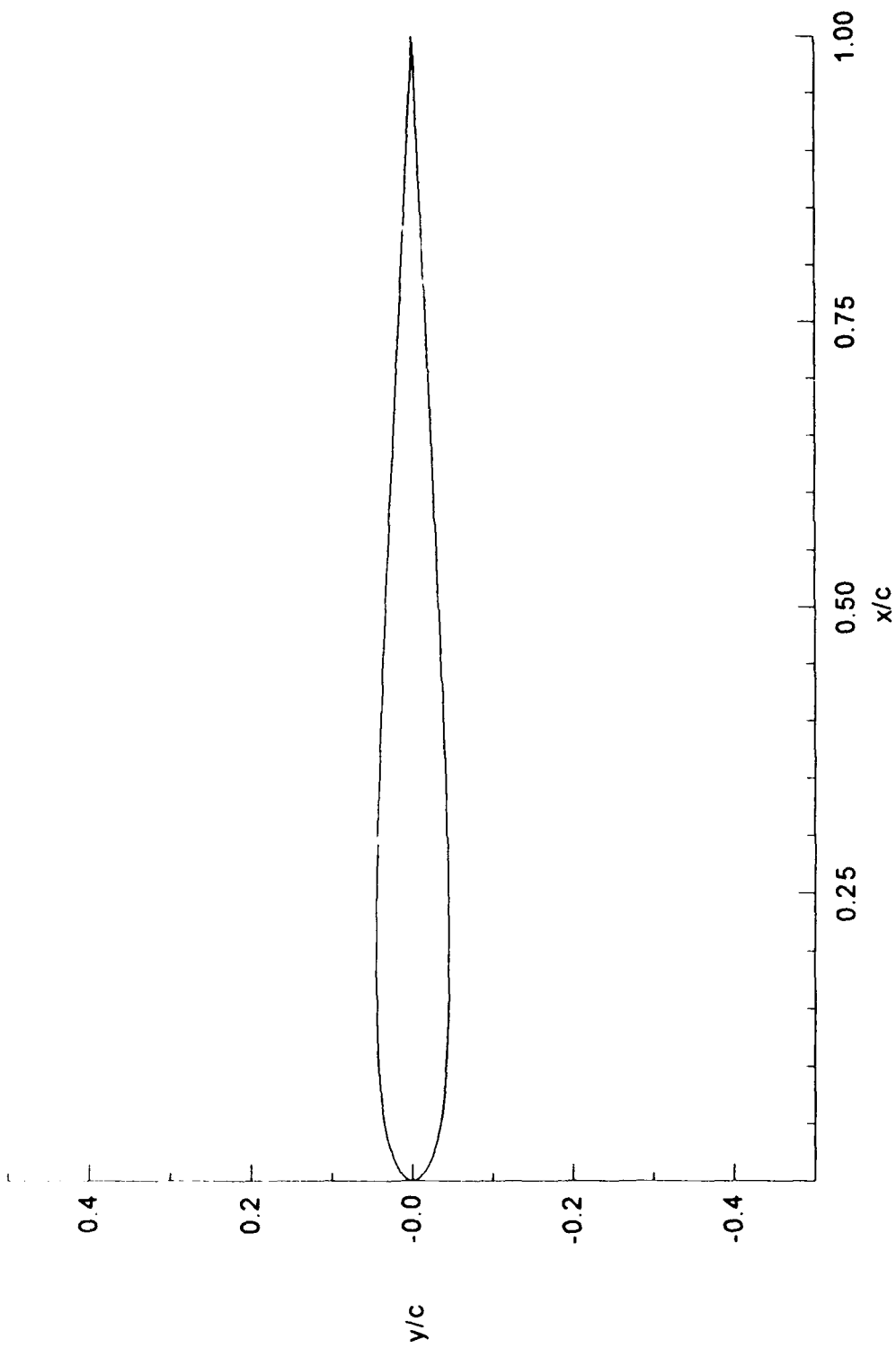


Figure 23. Airfoil TA3 -  $t/c = 9.05\%$

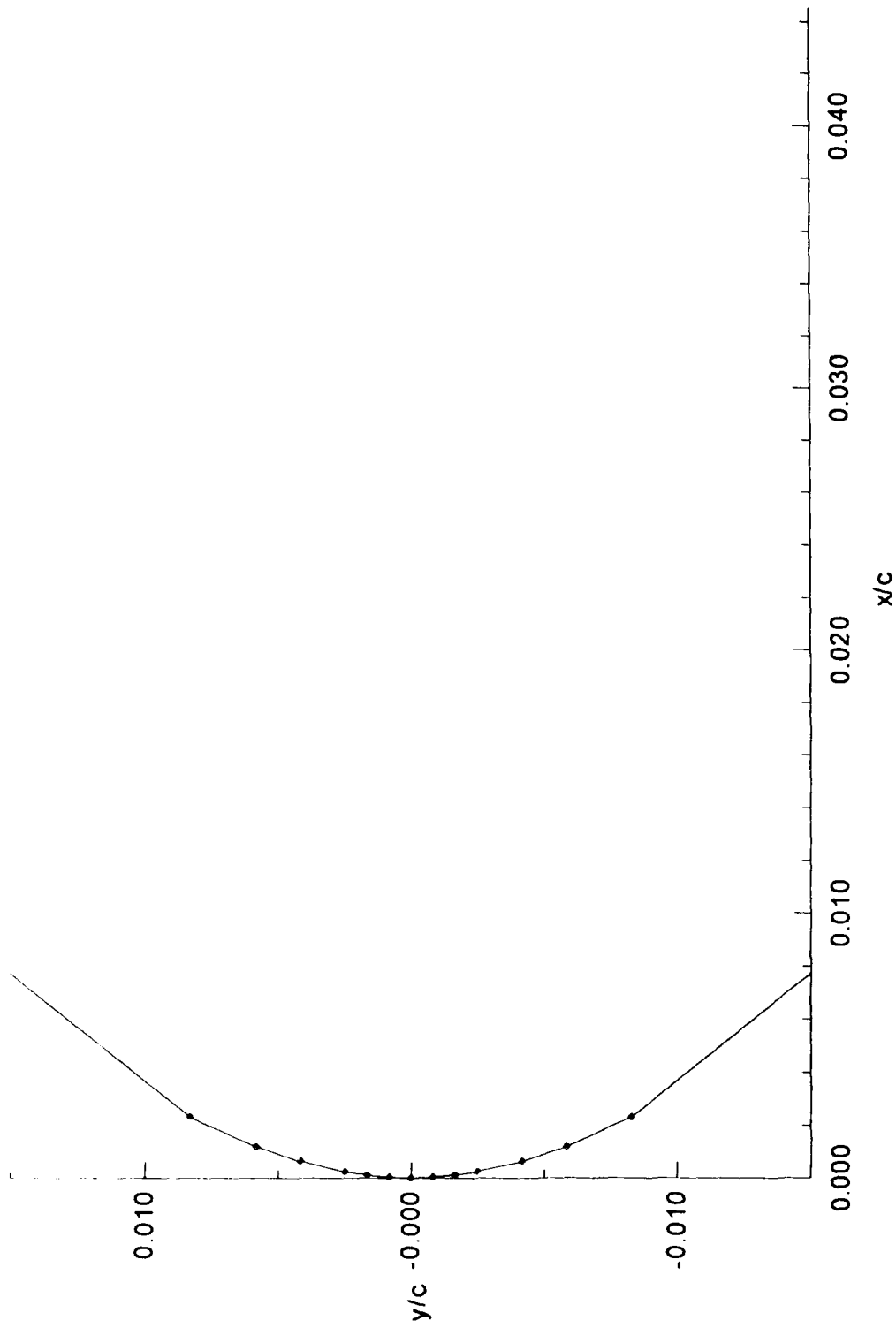


Figure 24. Airfoil TA3 Leading-Edge -  $t/c = 9.05\%$

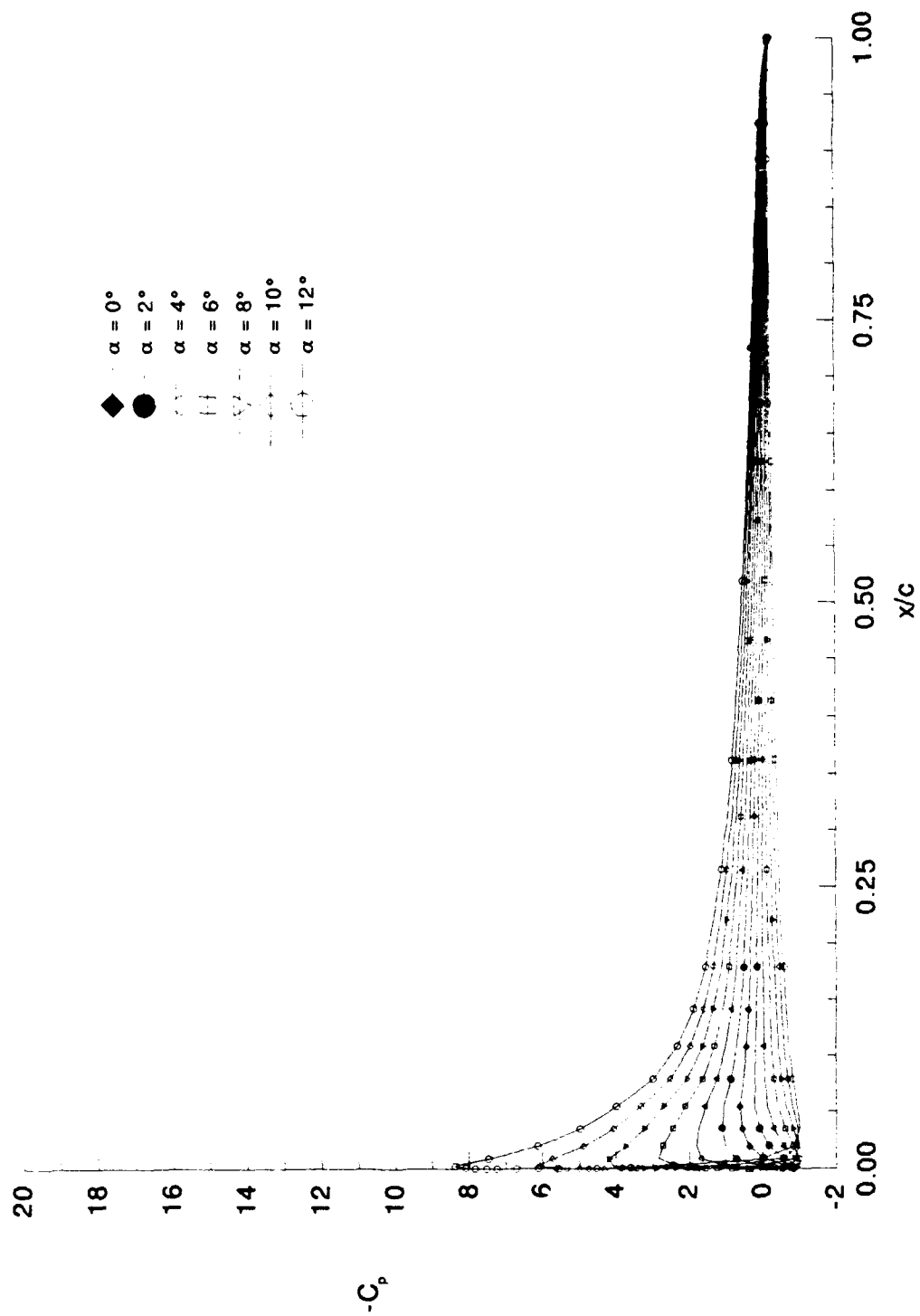


Figure 25. Pressure Distributions - TA3 - Incompressible

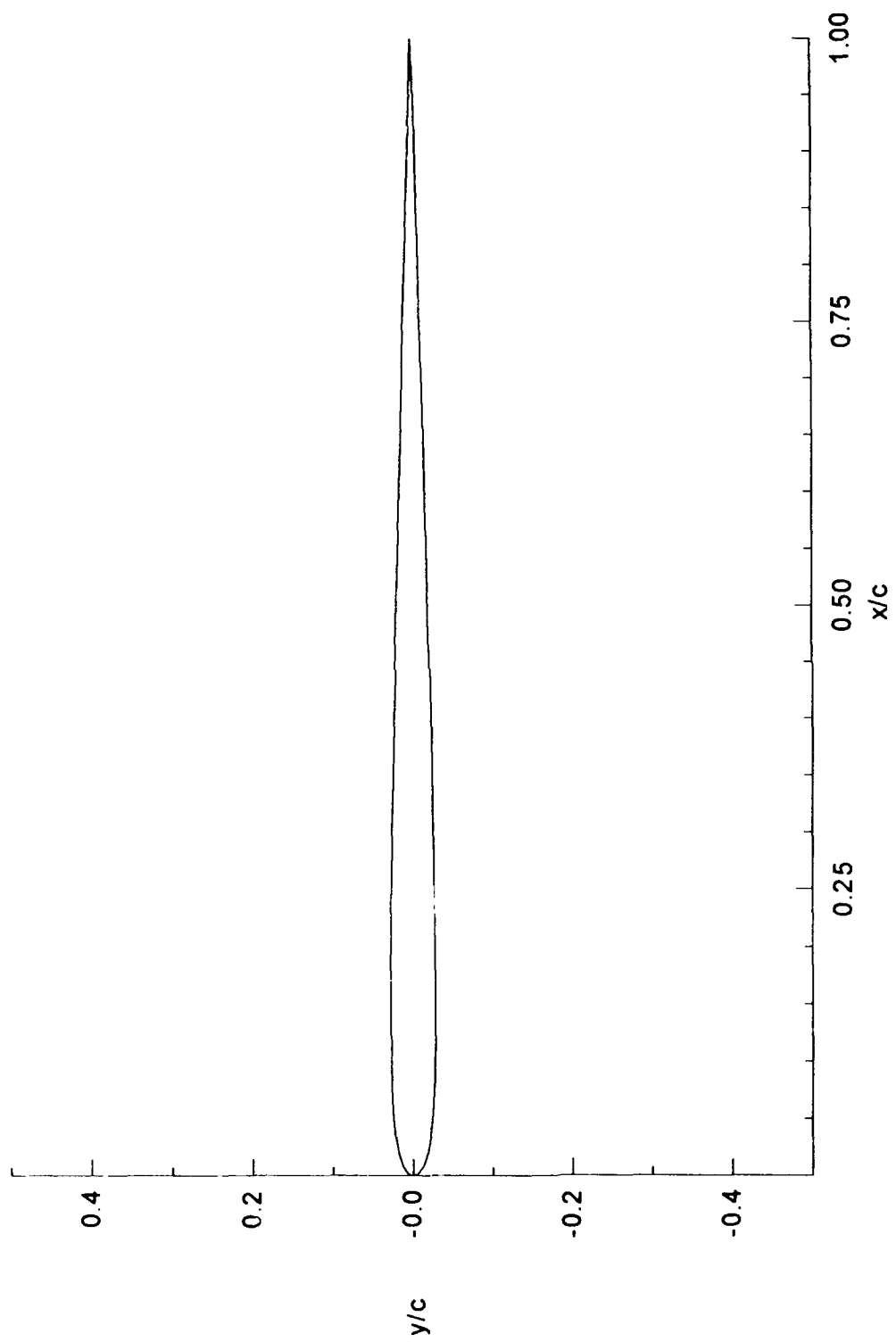


Figure 26. Airfoil TA4 -  $t/c = 5.56\%$

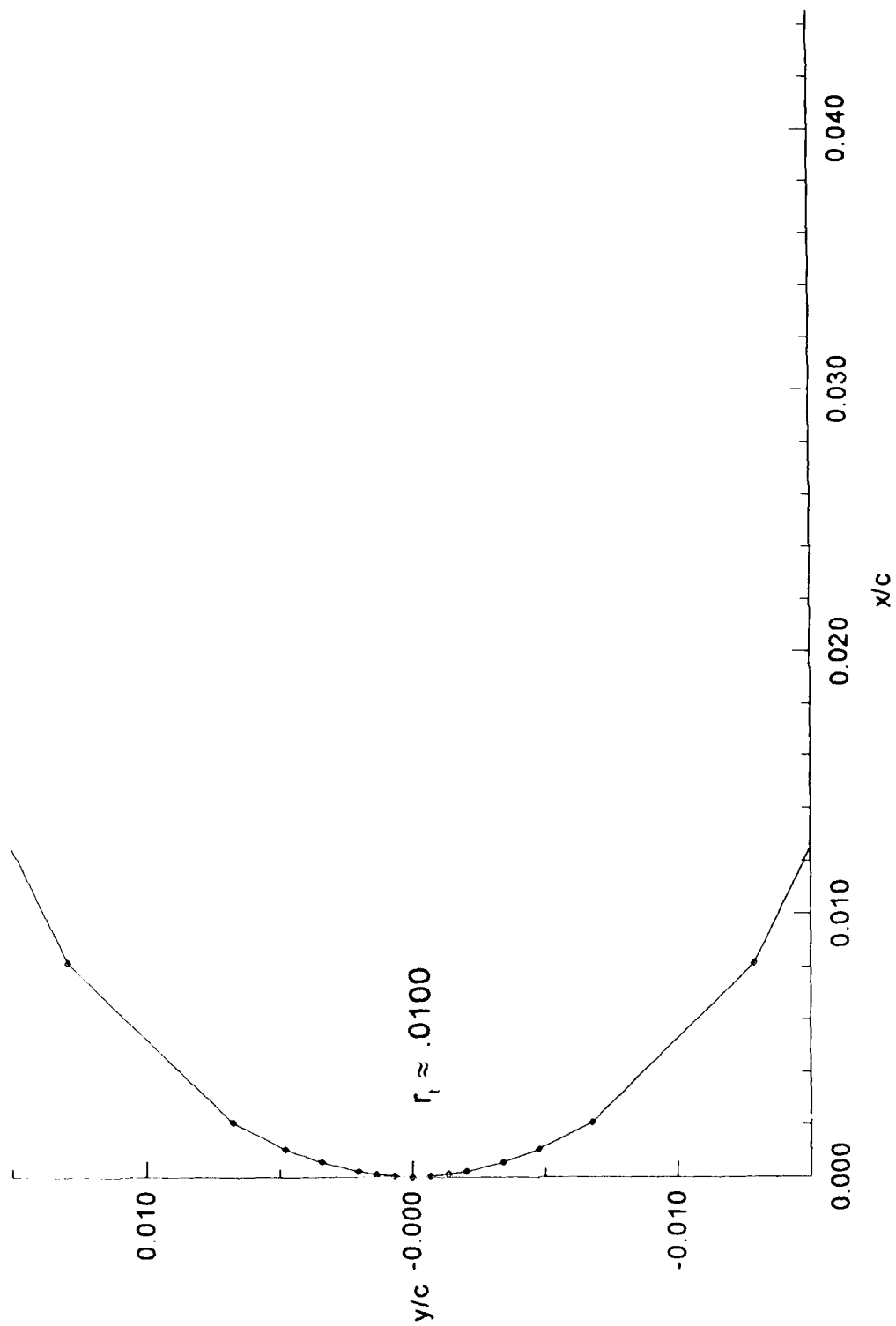


Figure 27. Airfoil TA4 Leading-Edge -  $t/c = 5.56\%$



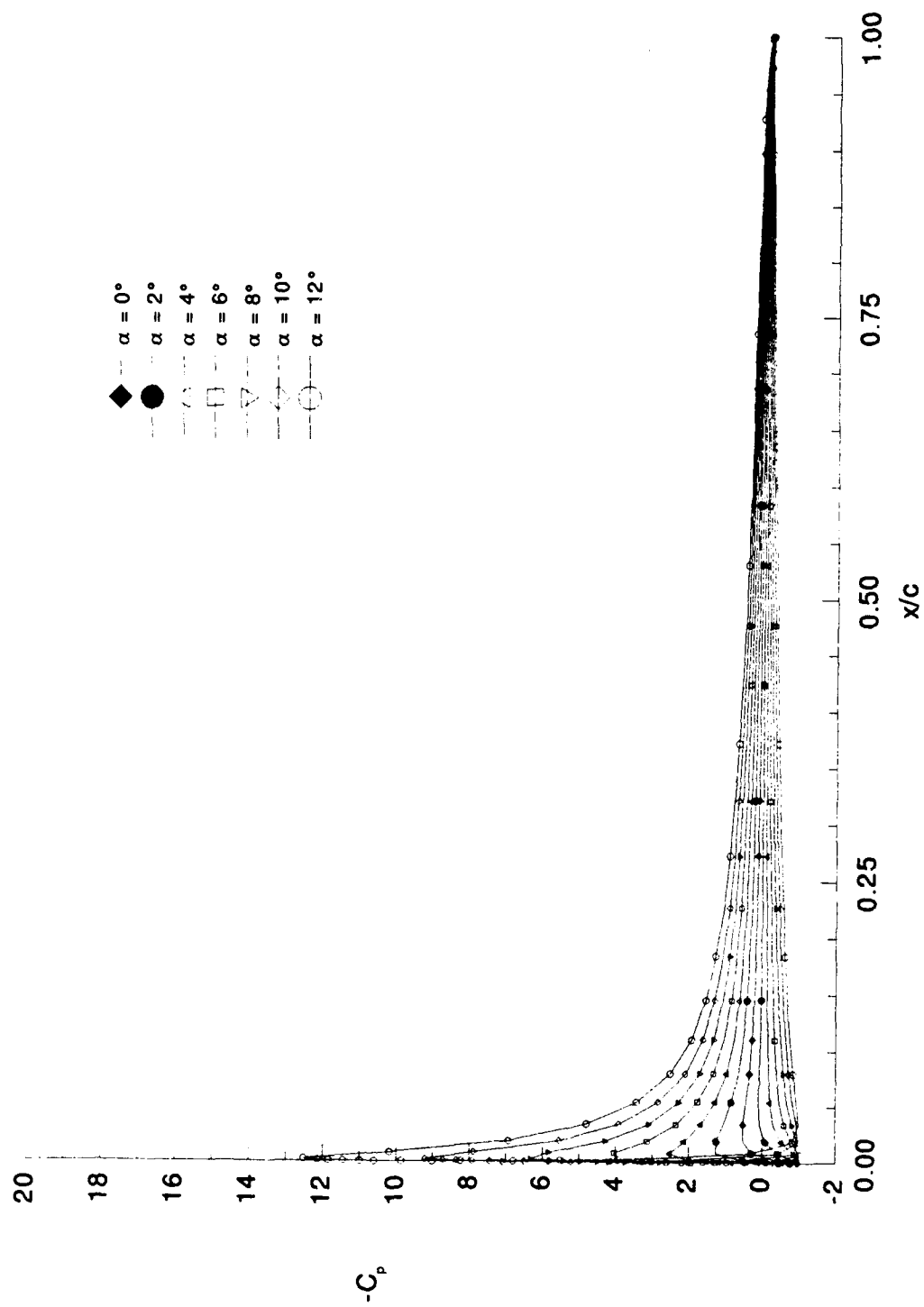


Figure 28. Pressure Distributions - TA4 - Incompressible

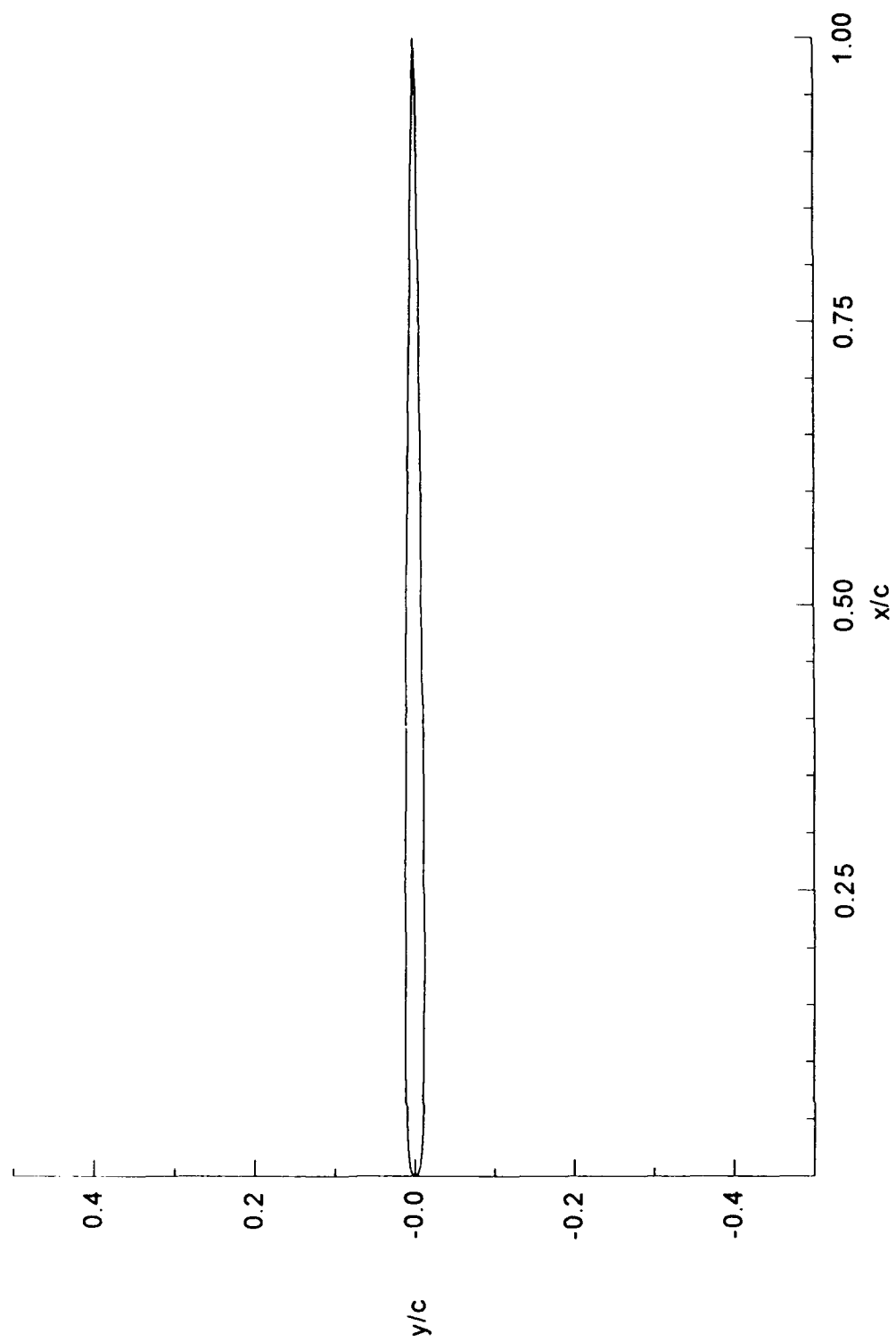


Figure 29. Airfoil TA5 -  $t/c = 2.37\%$

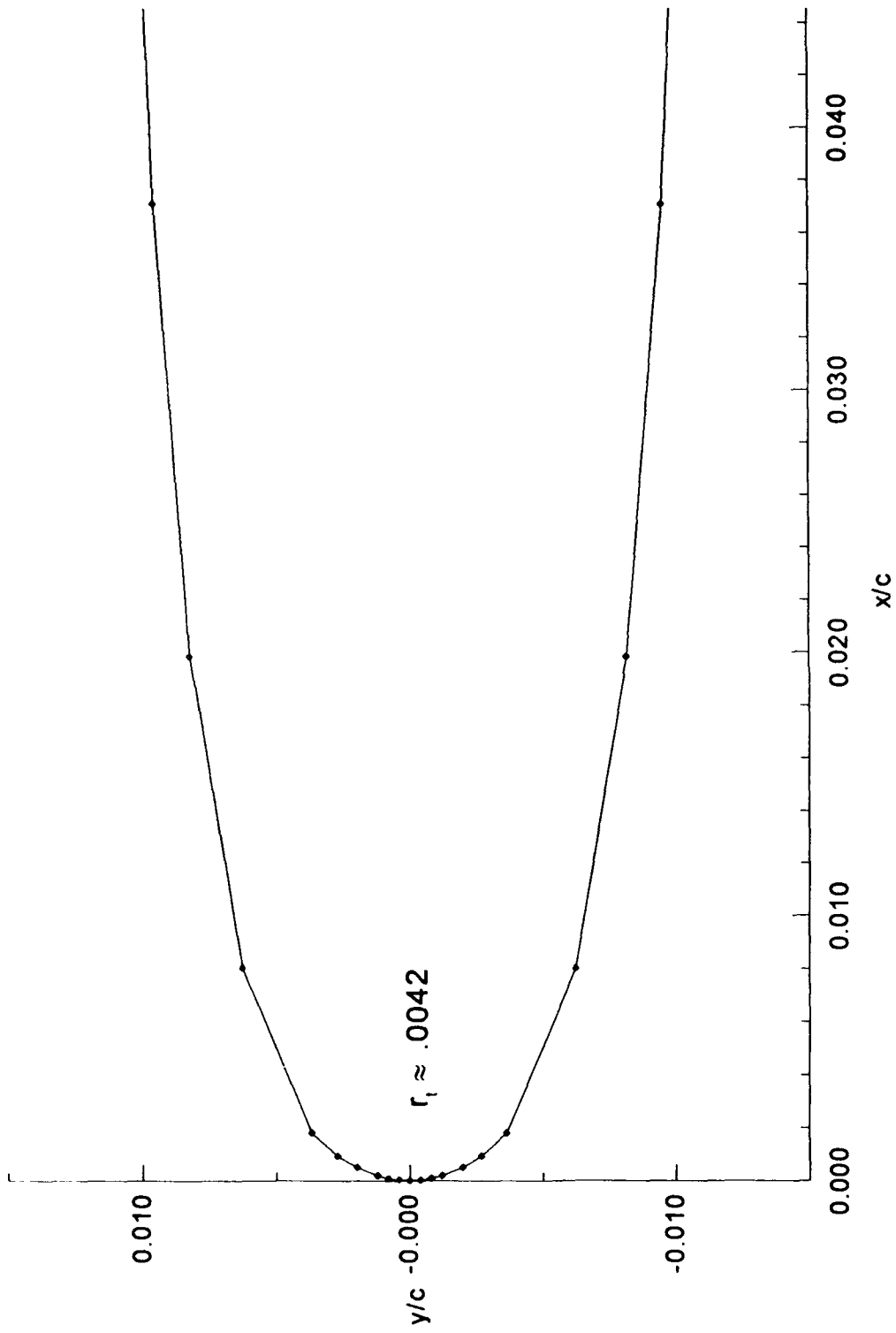


Figure 30. Airfoil TA5 Leading-Edge -  $t/c = 2.37\%$

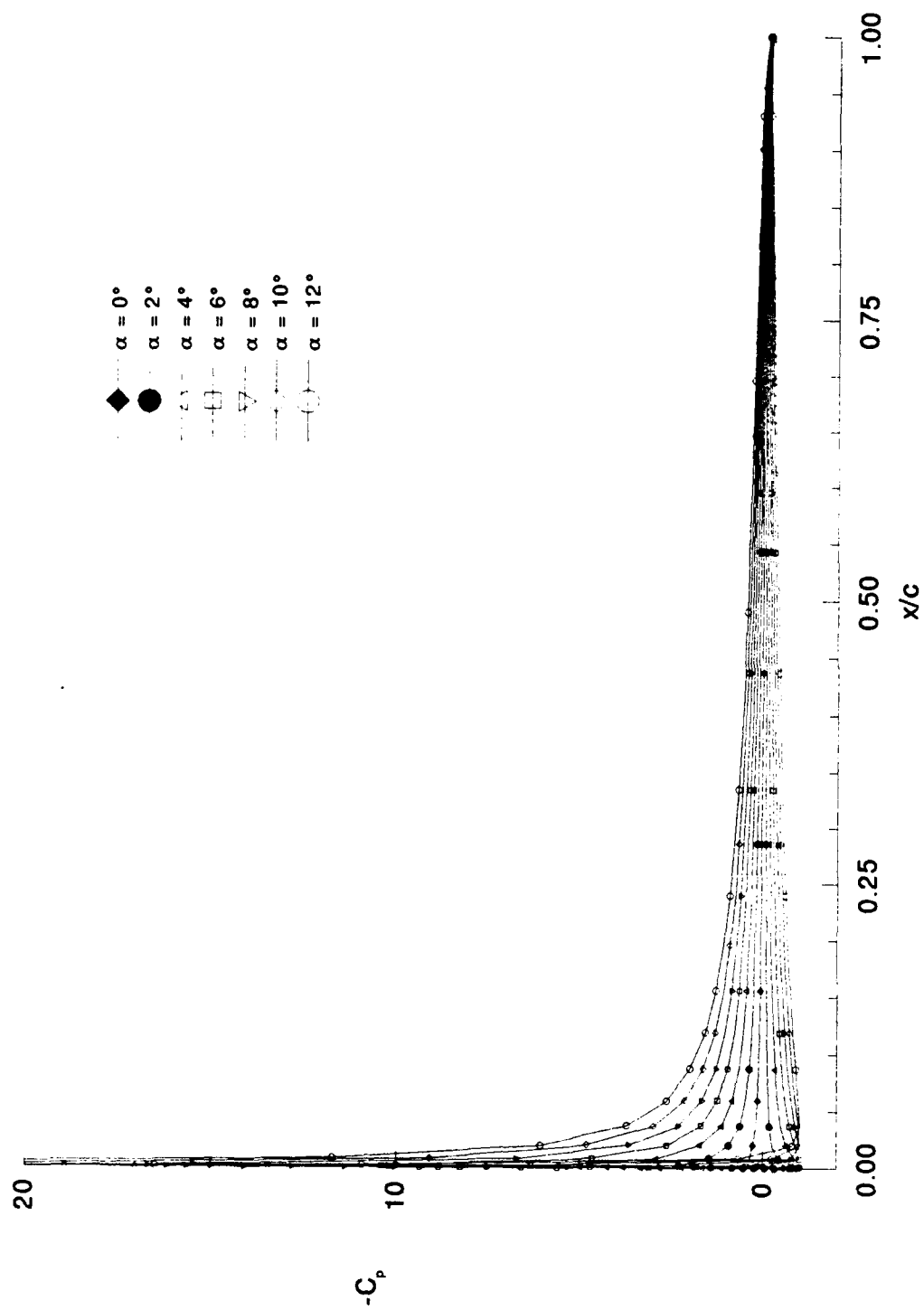


Figure 31. Pressure Distributions - TA5 - Incompressible

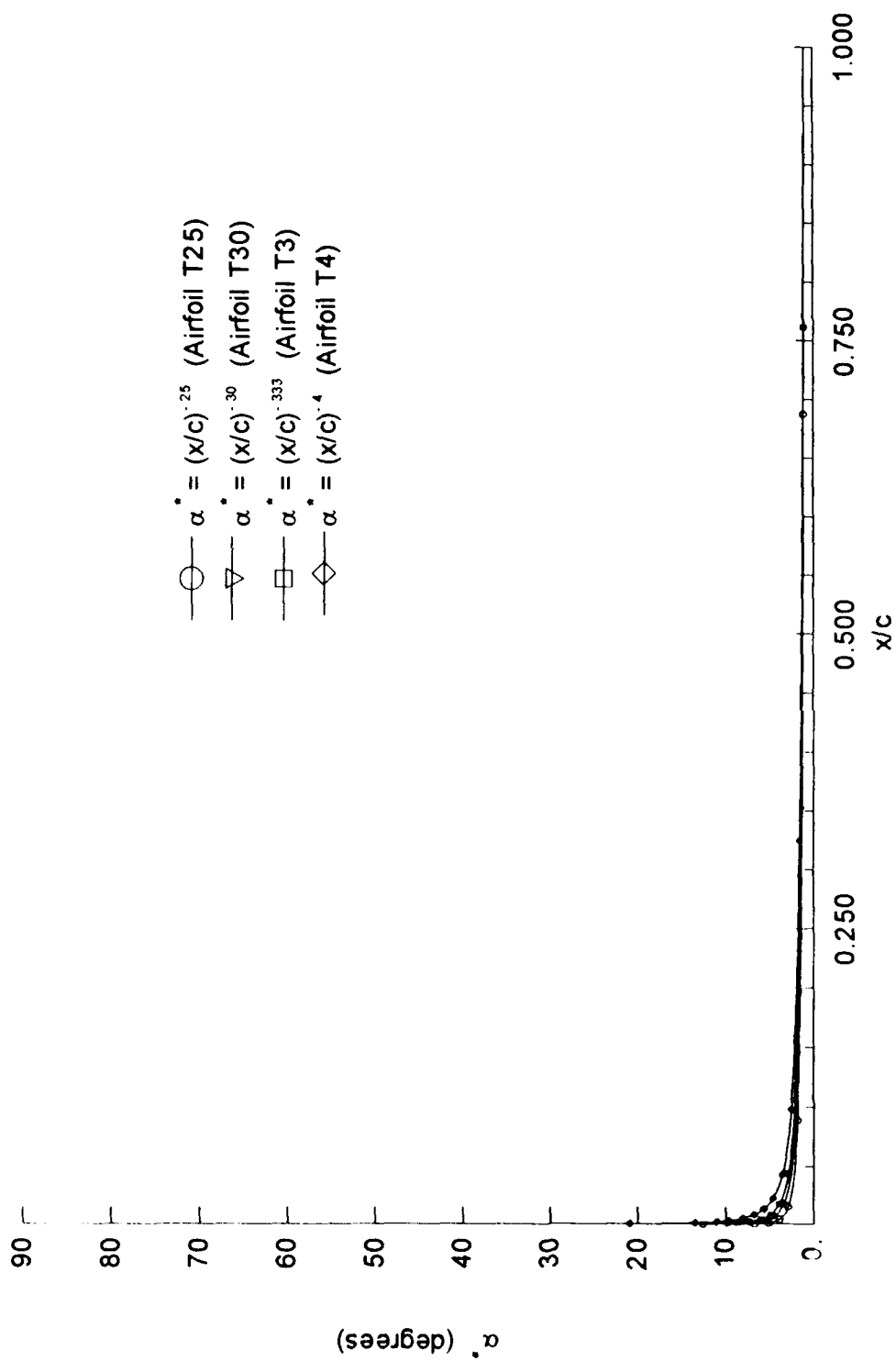


Figure 32. Power Law Relationships (A=1)

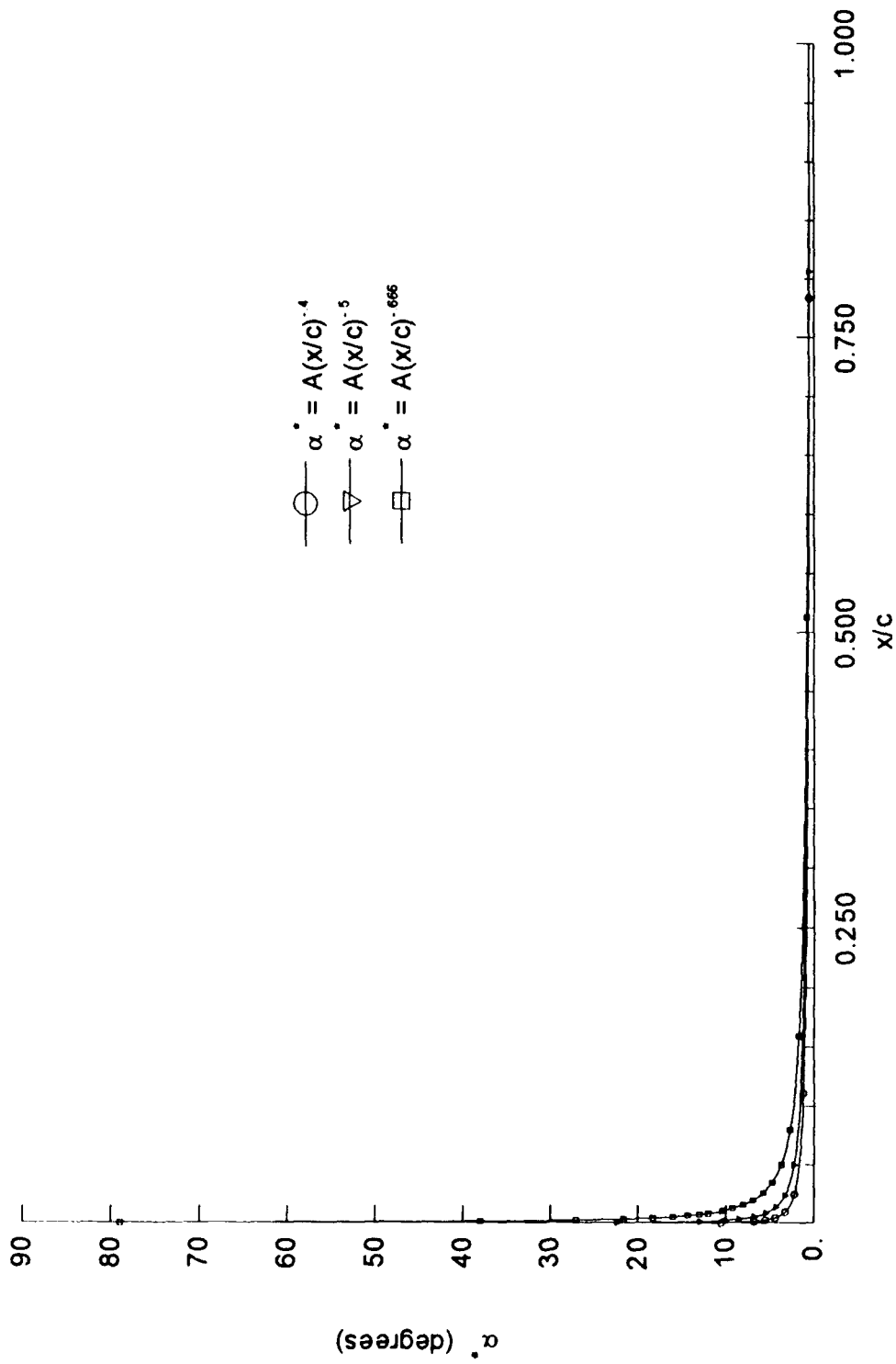


Figure 33. Power Law Relationships ( $A=1/2$ )

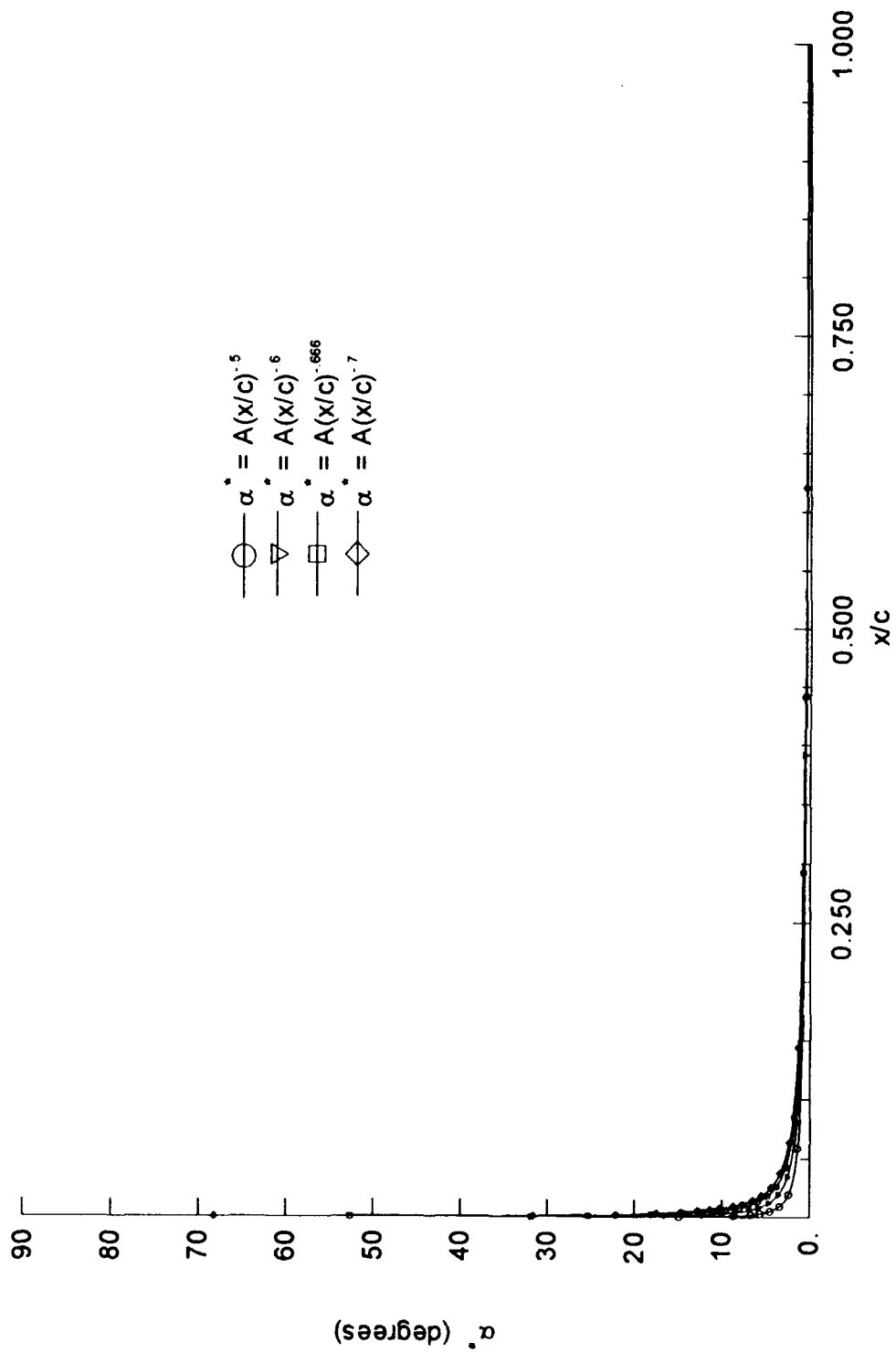


Figure 34. Power Law Relationships ( $A=1/3$ )

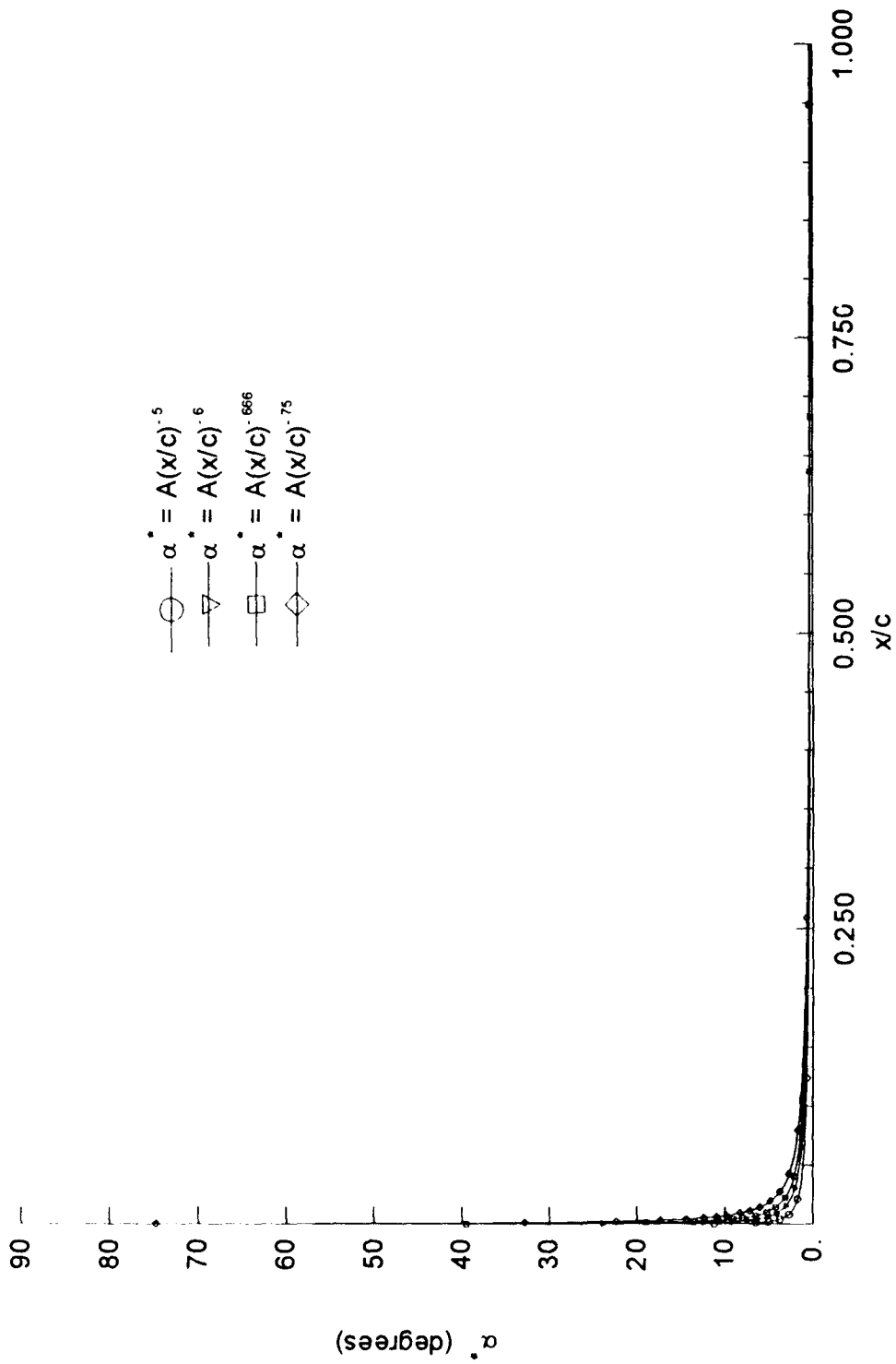


Figure 35. Power Law Relationships ( $A=1/4$ )



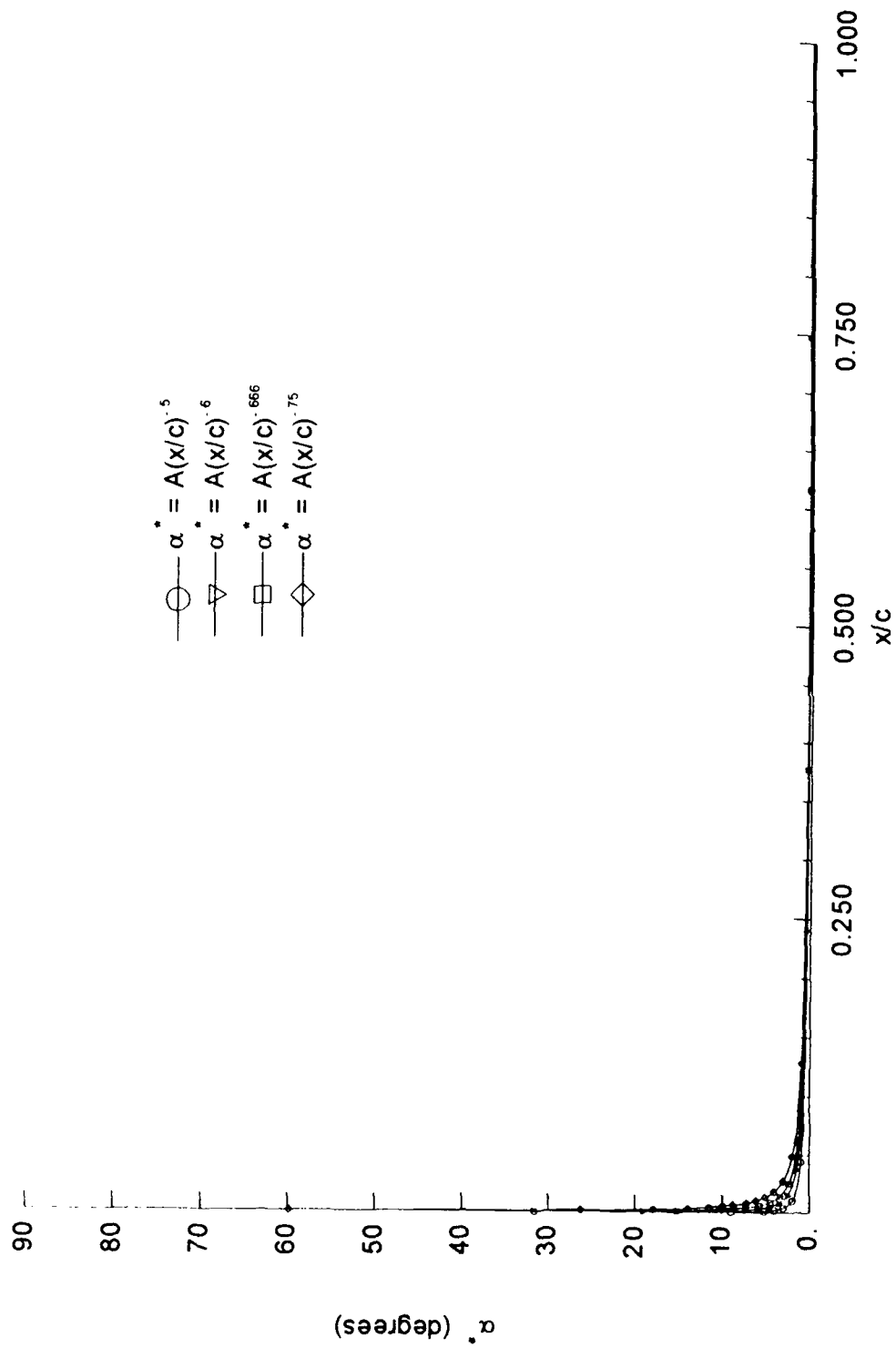


Figure 36. Power Law Relationships ( $A=1/5$ )

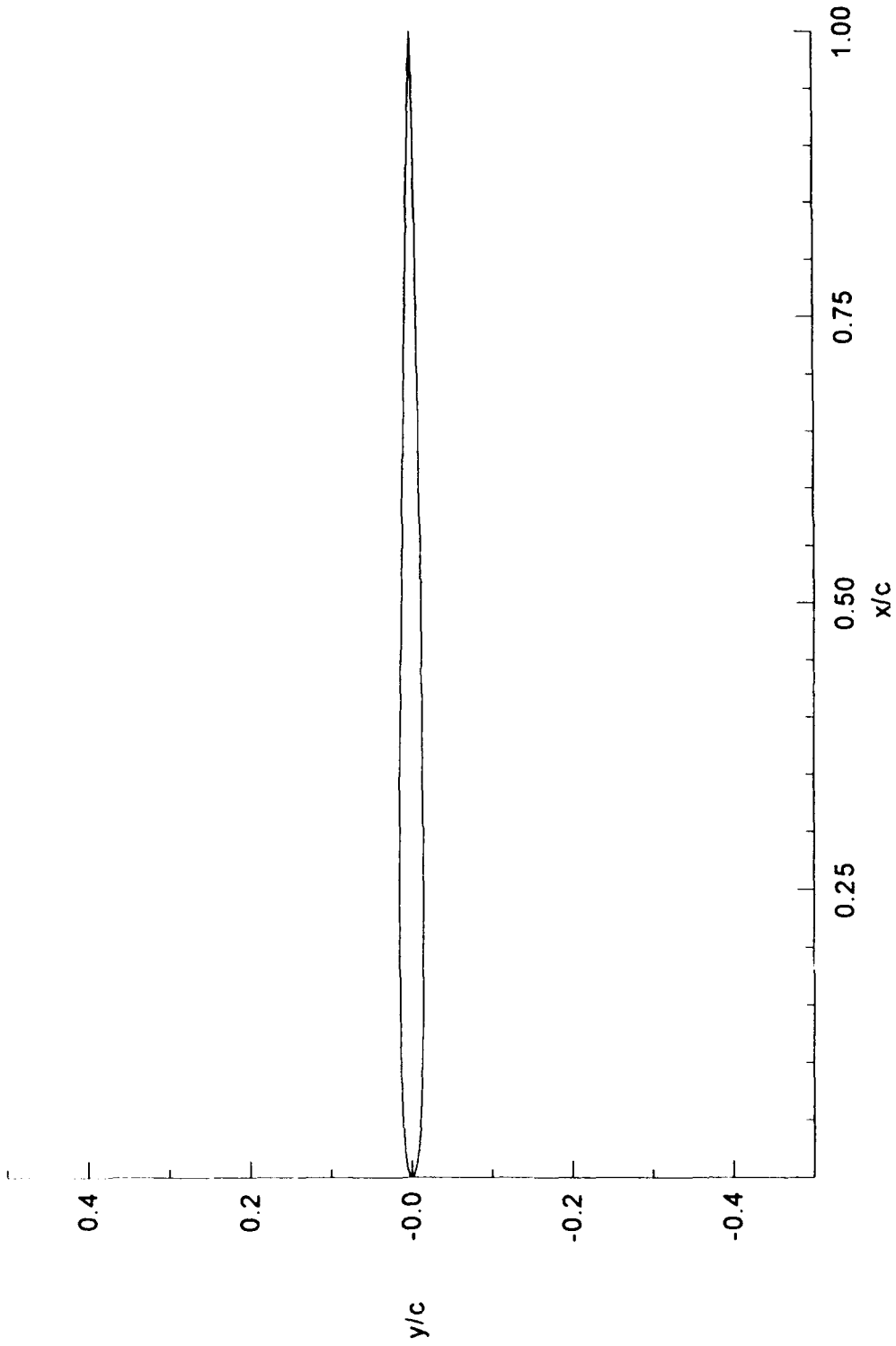


Figure 37. Airfoil T25 -  $t/c = 2.96\%$

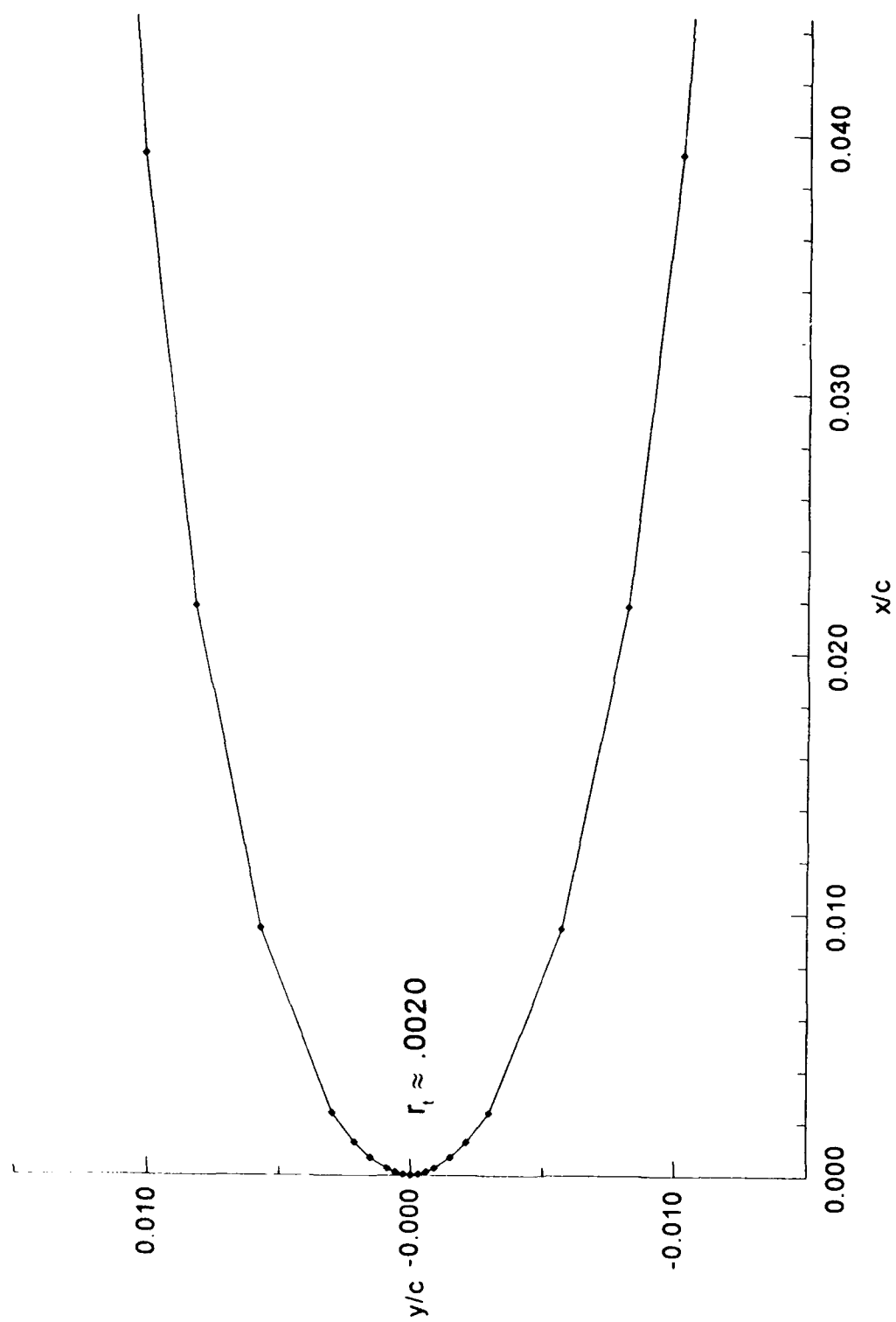


Figure 38. Airfoil T25 Leading-Edge -  $t/c = 2.96\%$

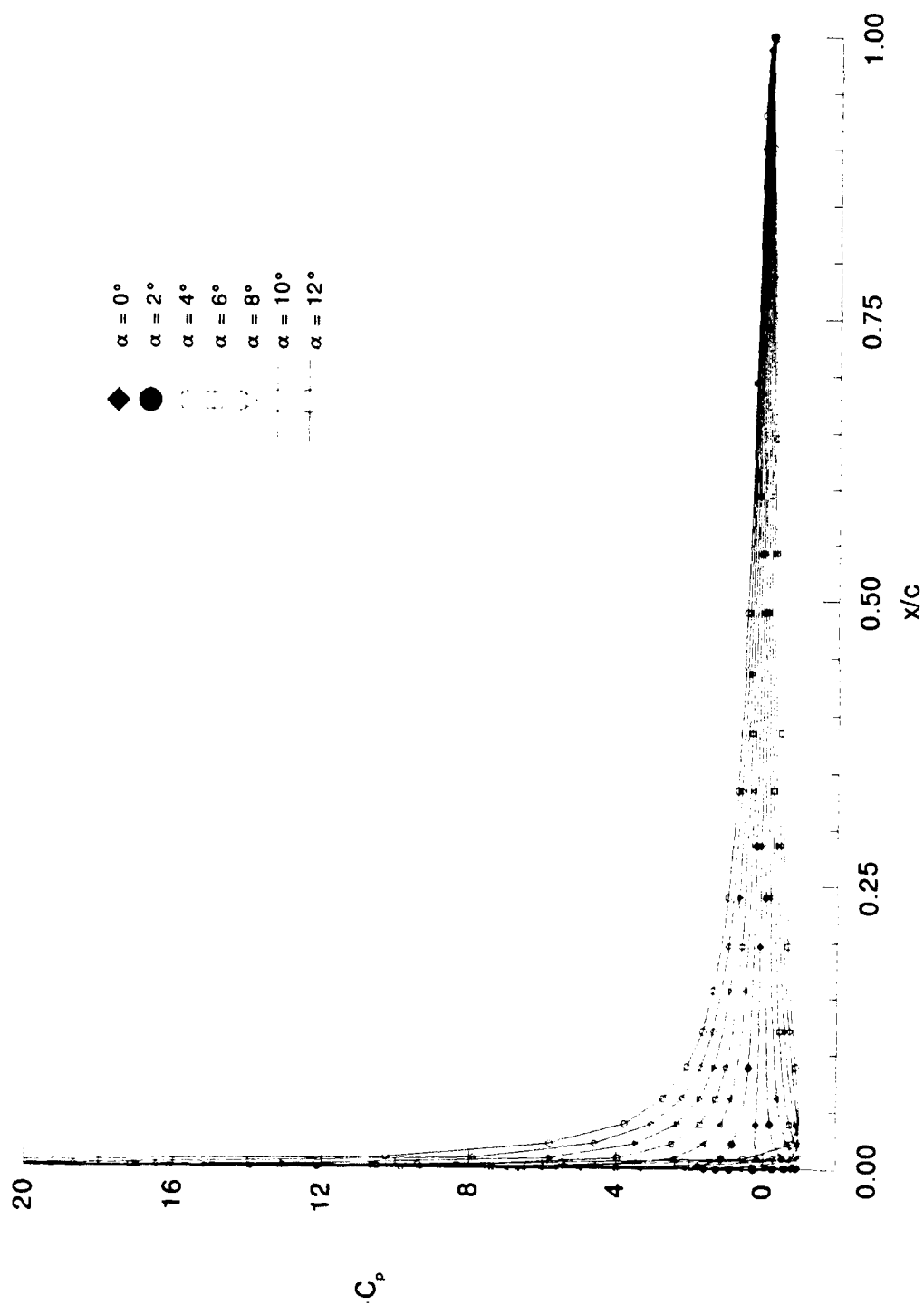


Figure 39. Pressure Distributions - T25 - Incompressible

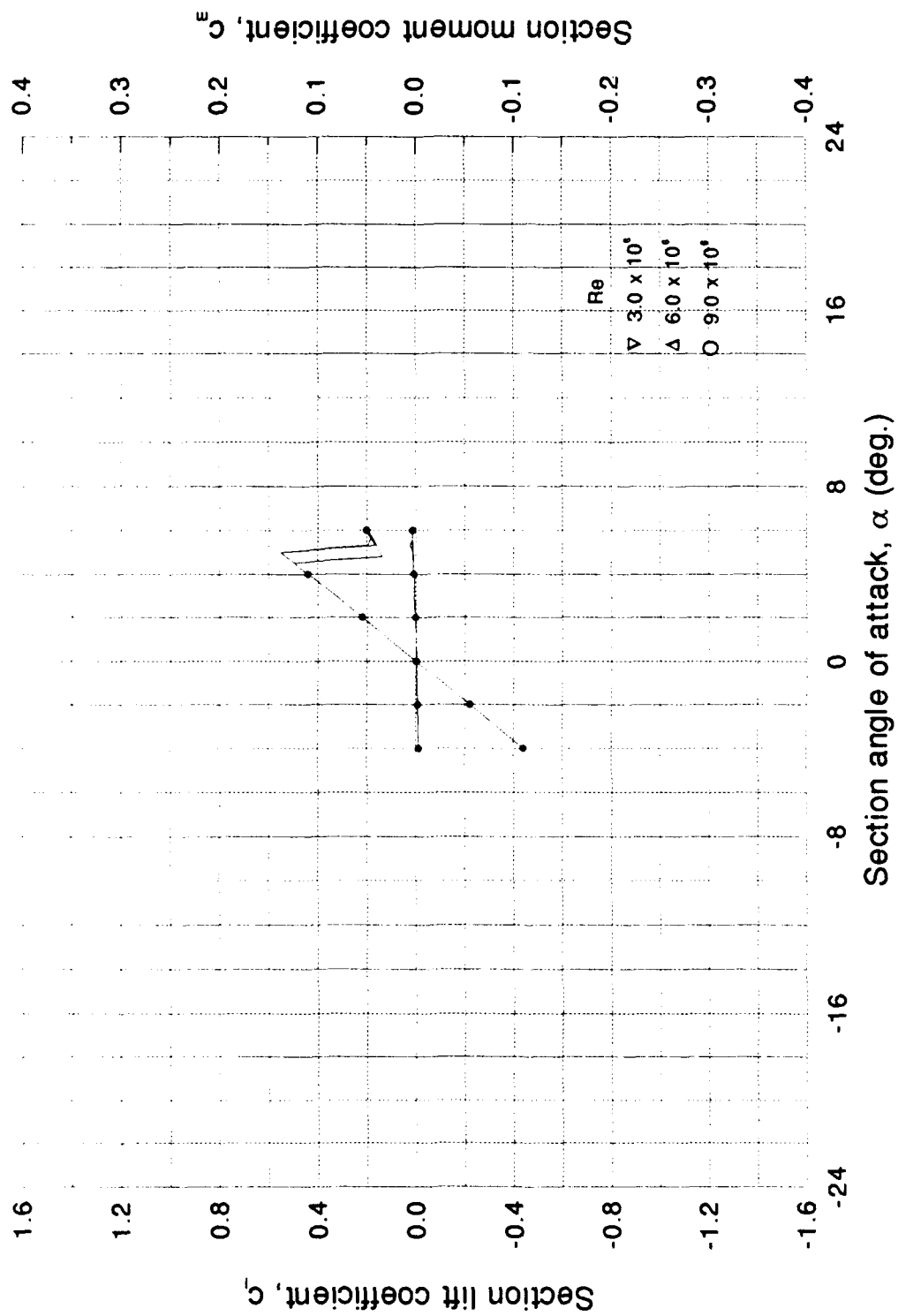


Figure 40. Airfoil T25 -  $C_l$ ,  $C_m$  vs  $\alpha$  Curves

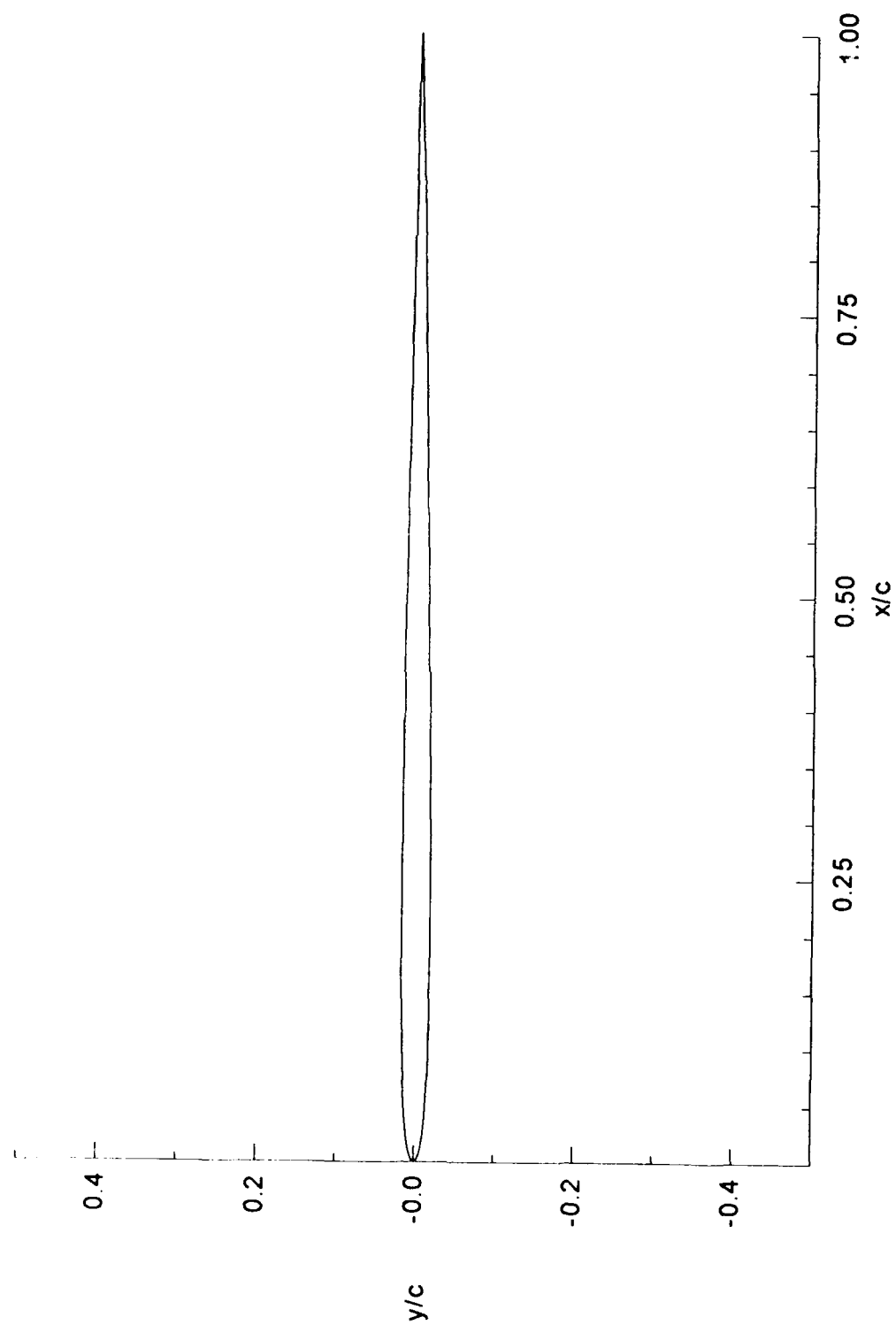


Figure 41. Airfoil T30 -  $t/c = 3.59\%$

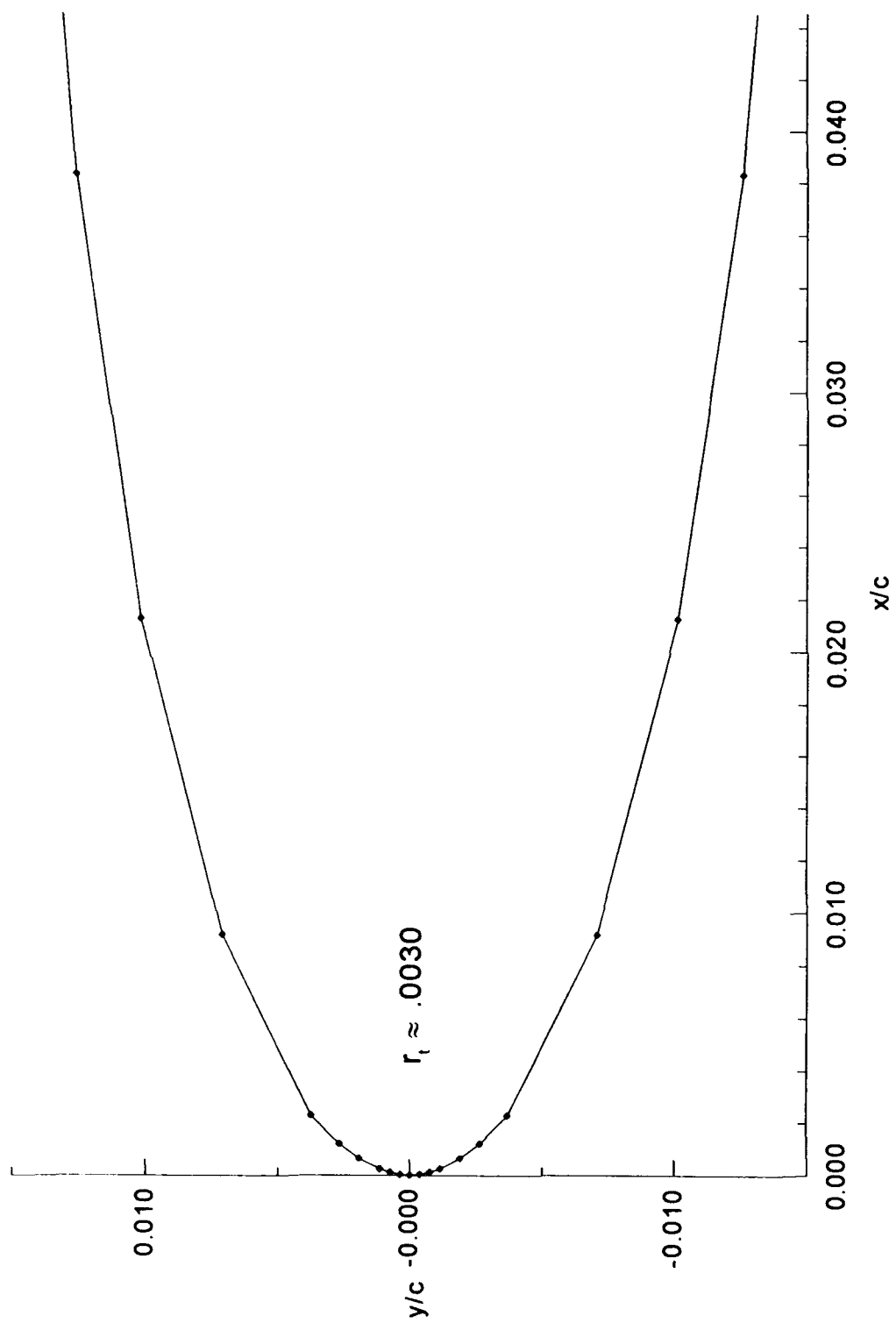


Figure 42. Airfoil T30 Leading-Edge -  $t/c = 3.59\%$

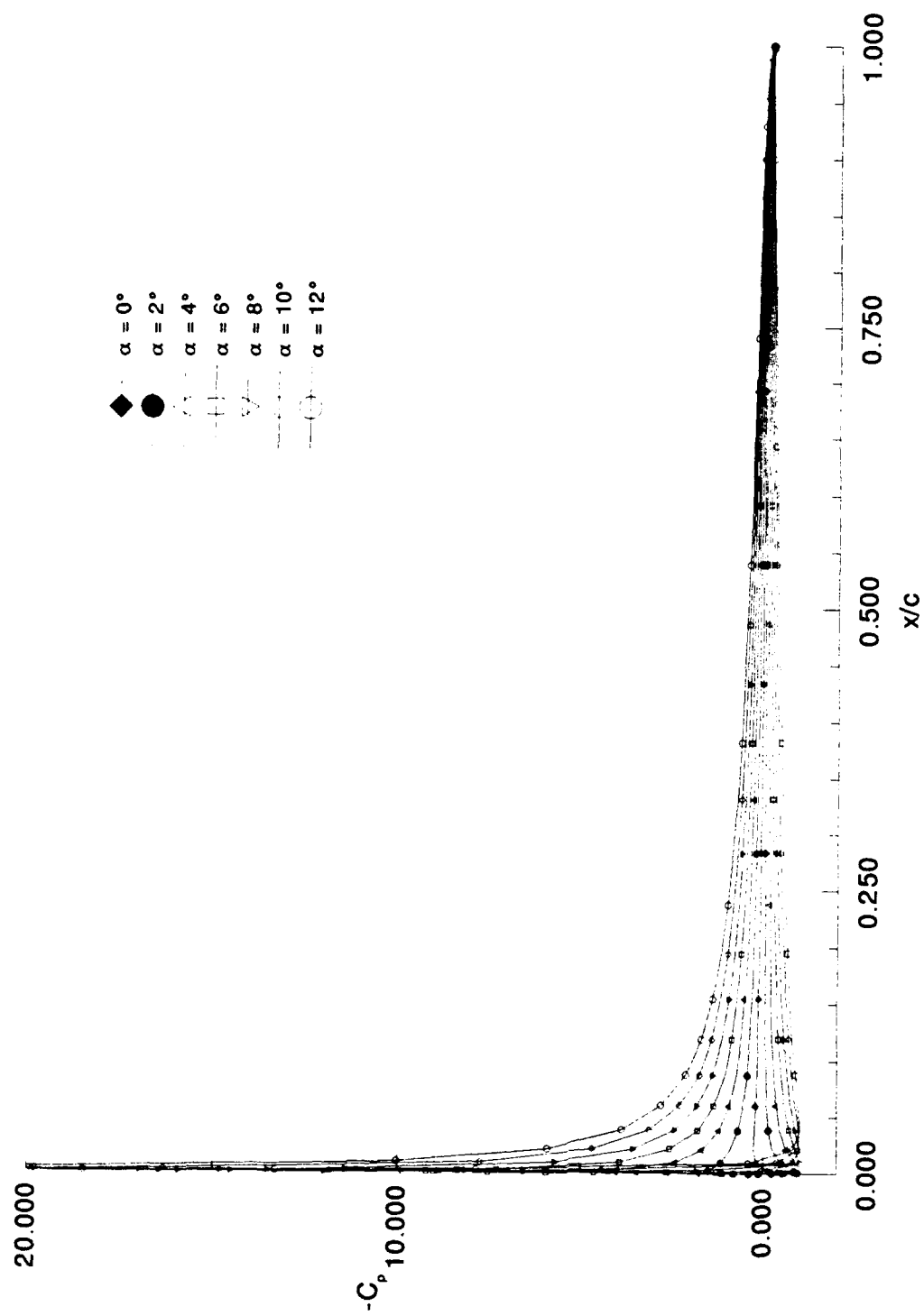


Figure 43. Pressure Distributions - T30 - Incompressible



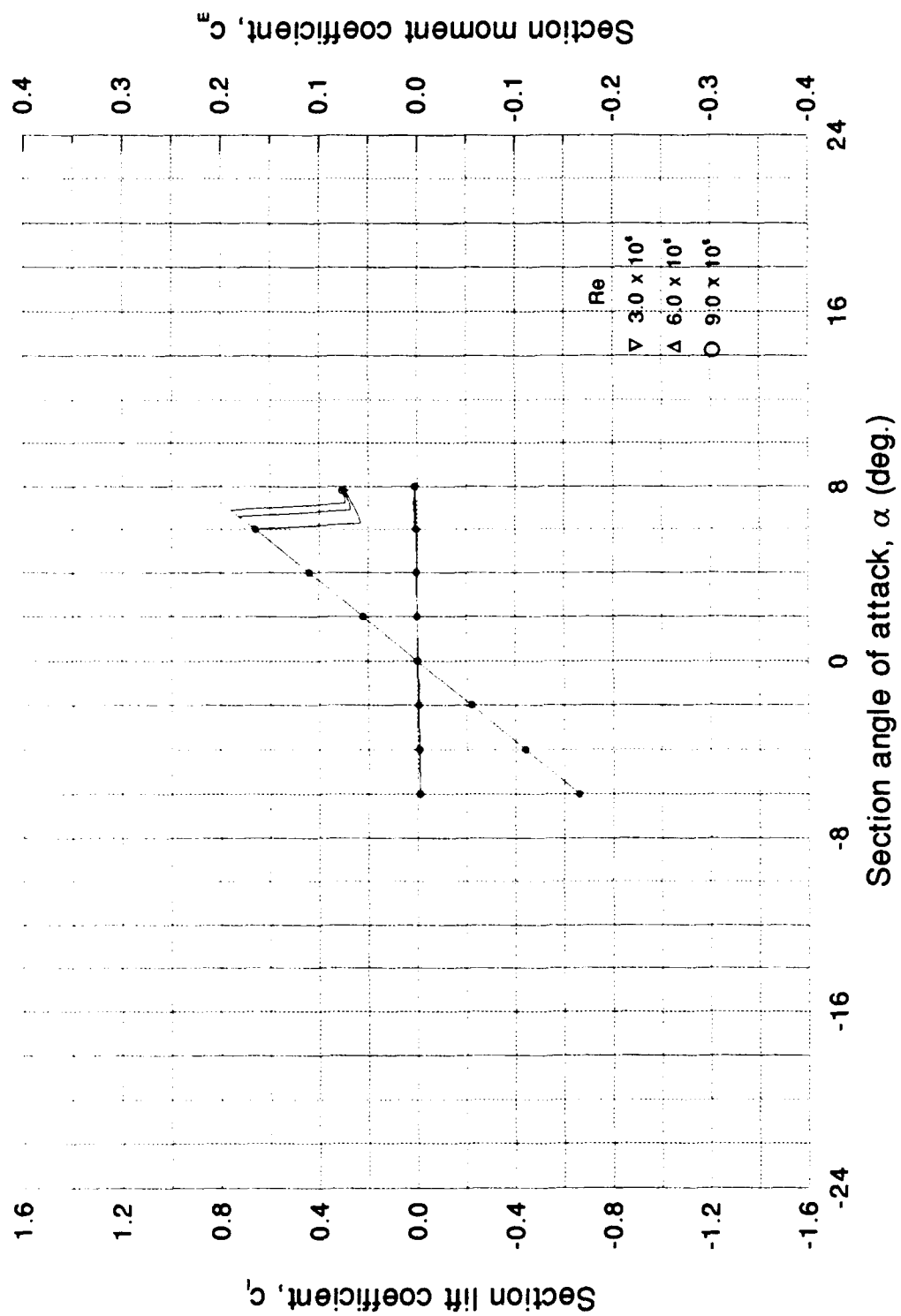


Figure 44. Airfoil T30 -  $C_l$ ,  $C_m$  vs  $\alpha$  Curves

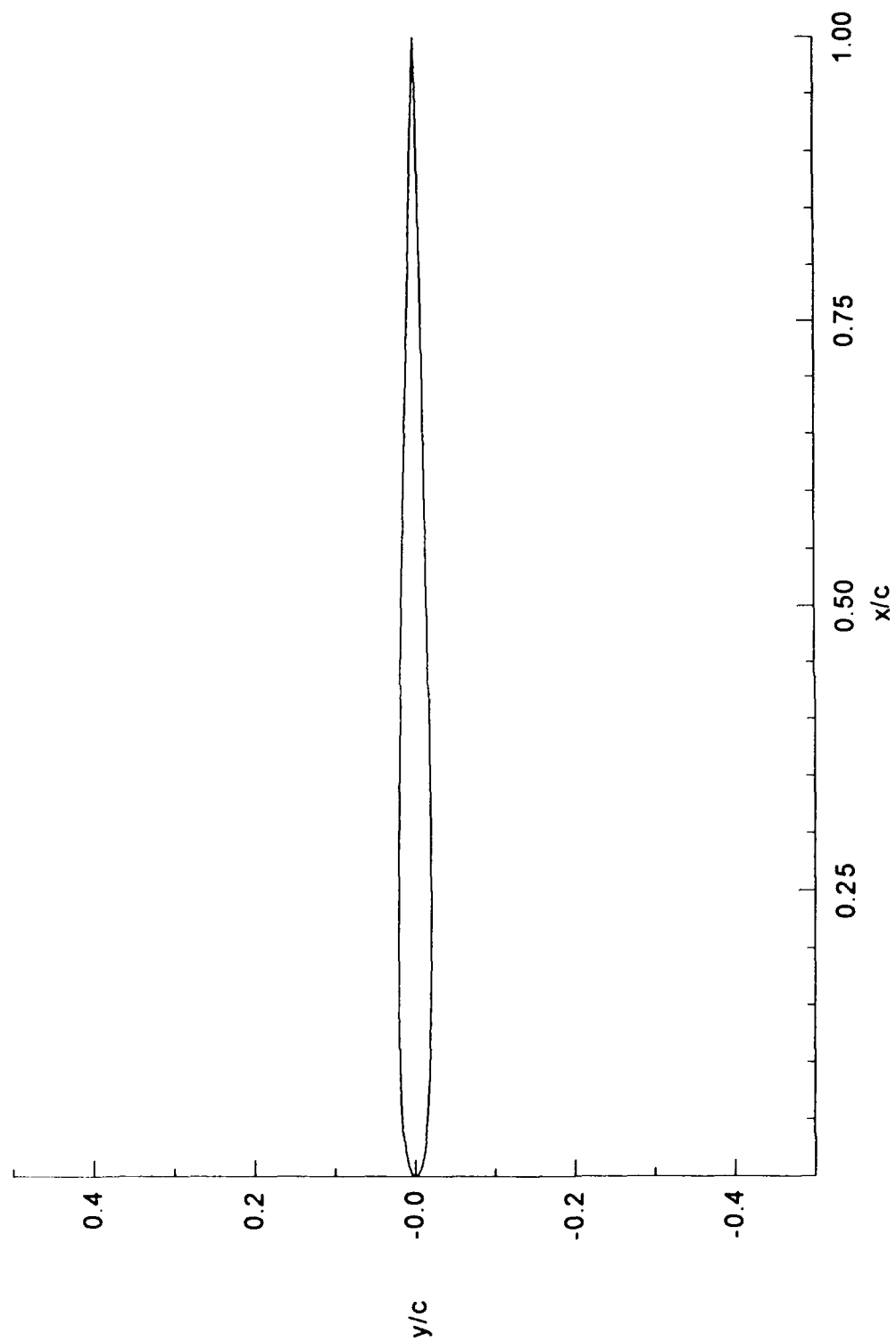


Figure 45. Airfoil T3 -  $t/c = 4.09\%$

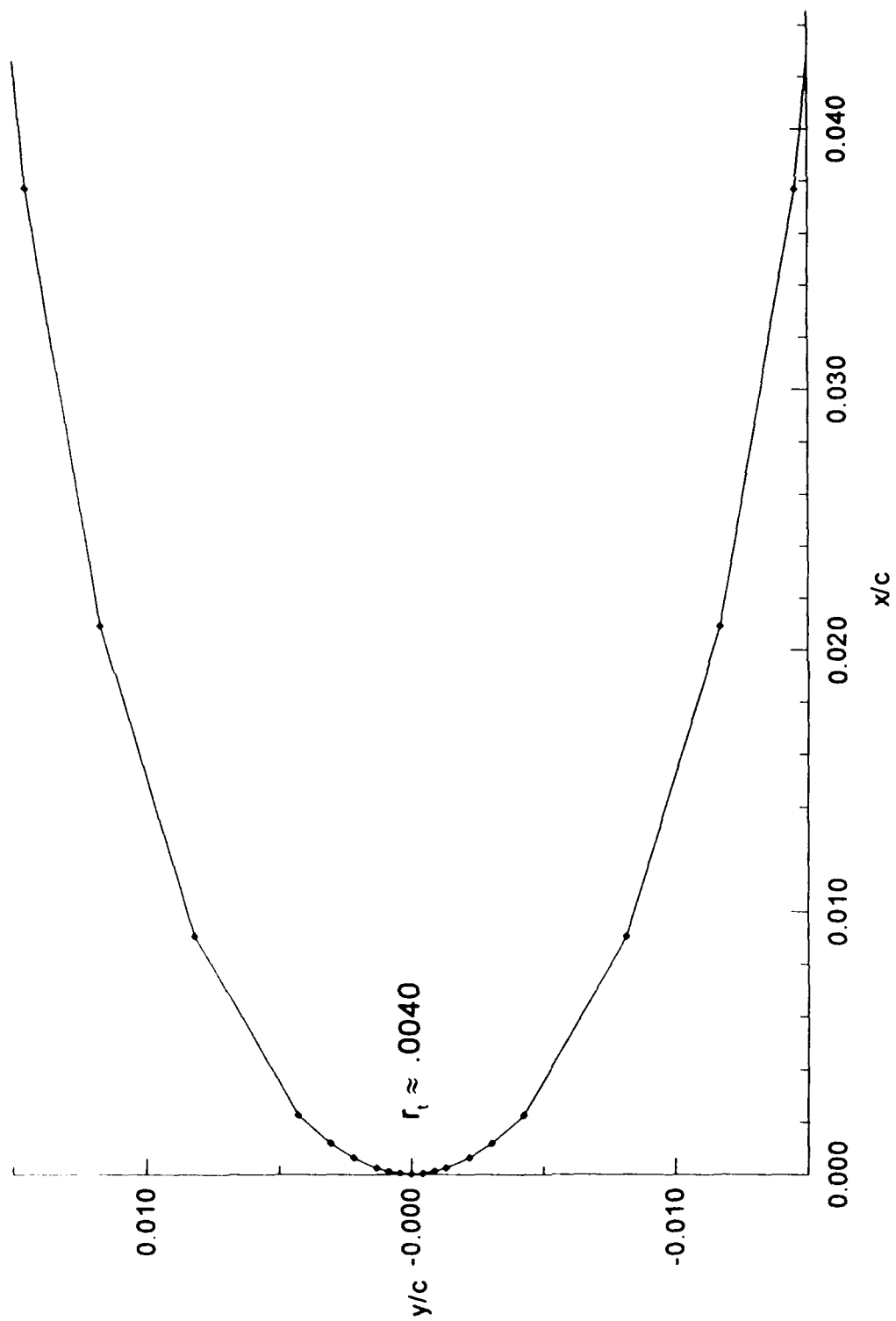


Figure 46. Airfoil T3 Leading-Edge -  $t/c = 4.09\%$

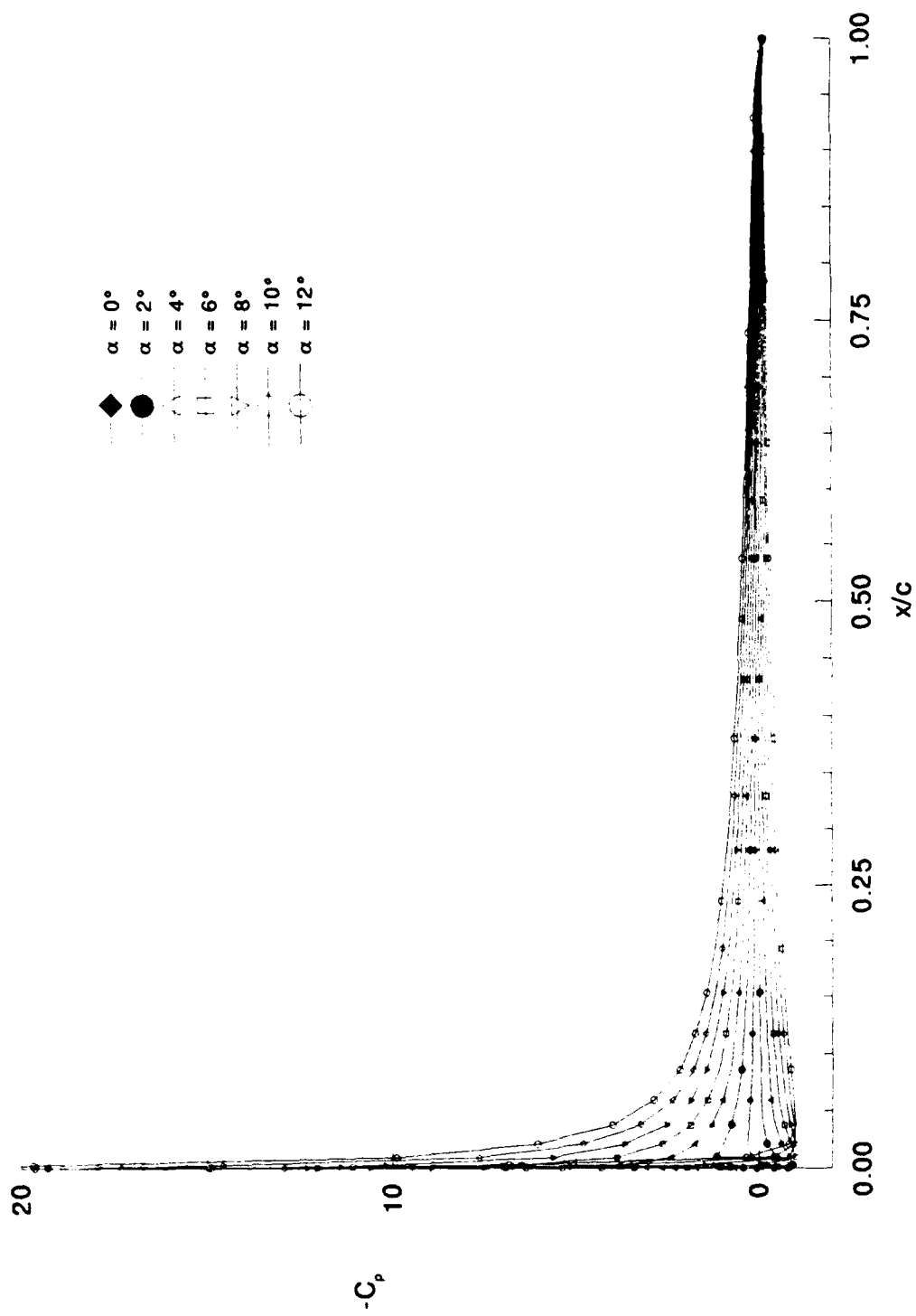


Figure 47. Pressure Distributions - T3 - Incompressible

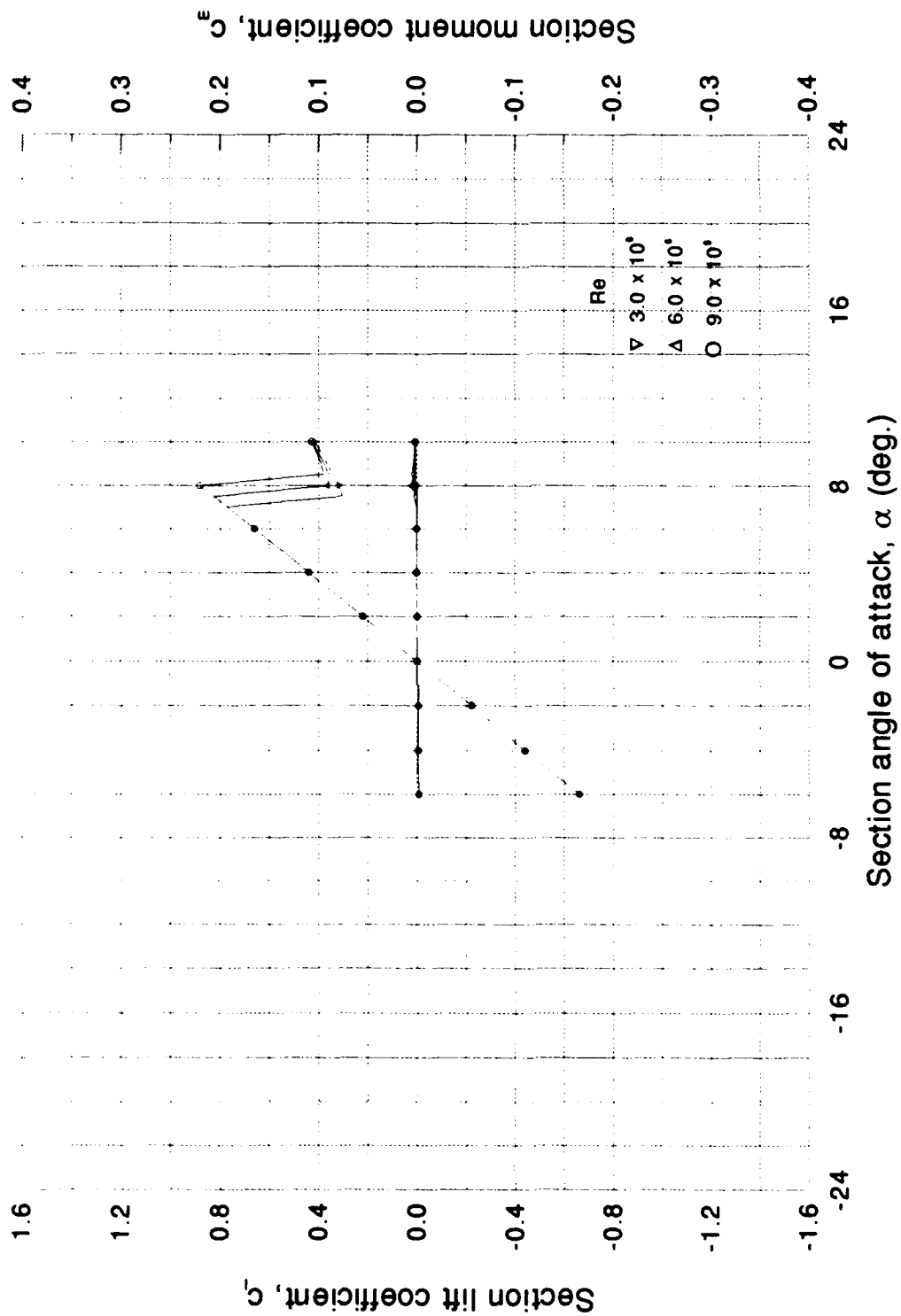


Figure 48. Airfoil T3 -  $C_l$ ,  $C_m$  vs  $\alpha$  Curves

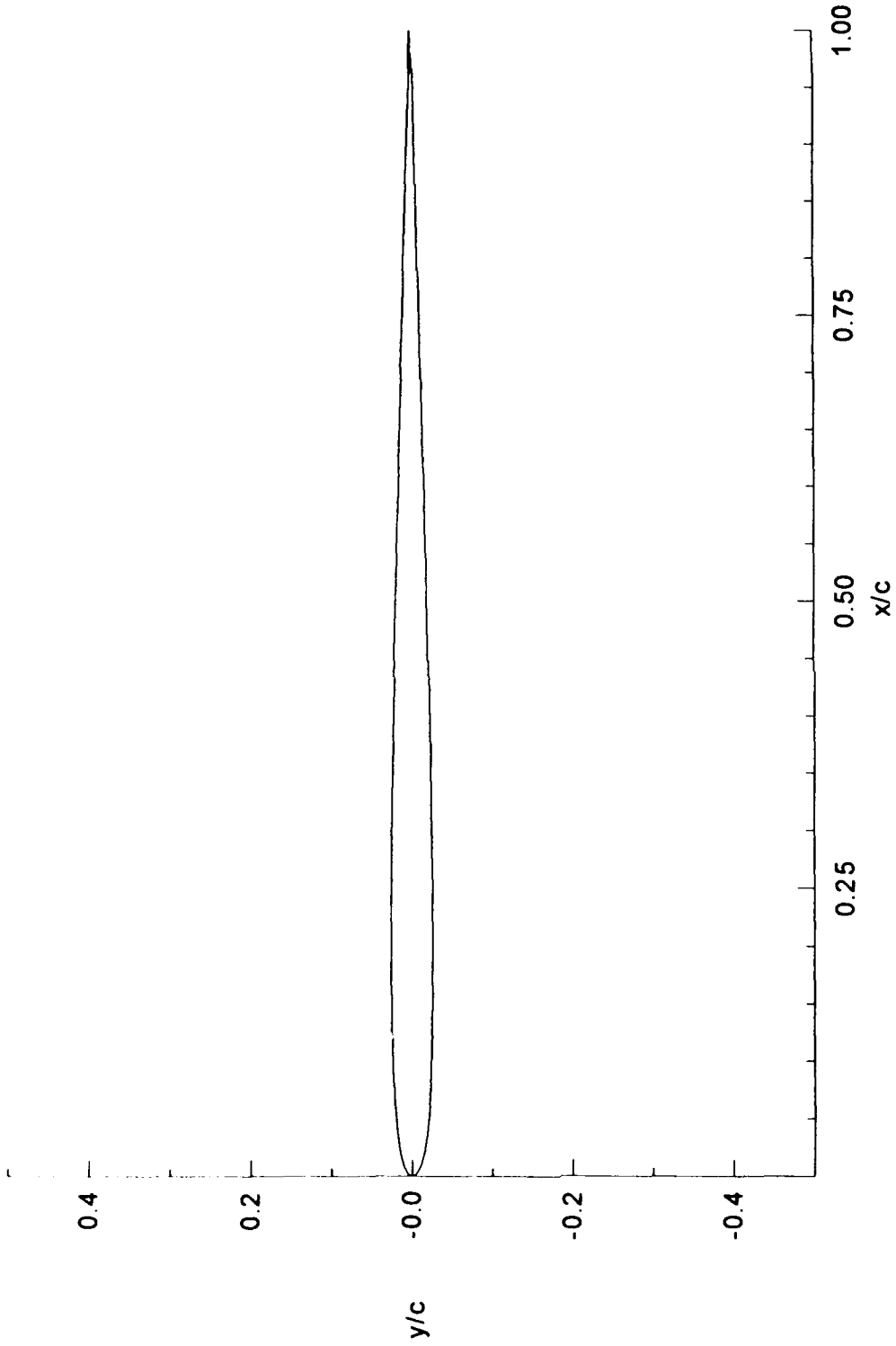


Figure 49. Airfoil T4 -  $t/c = 5.17\%$

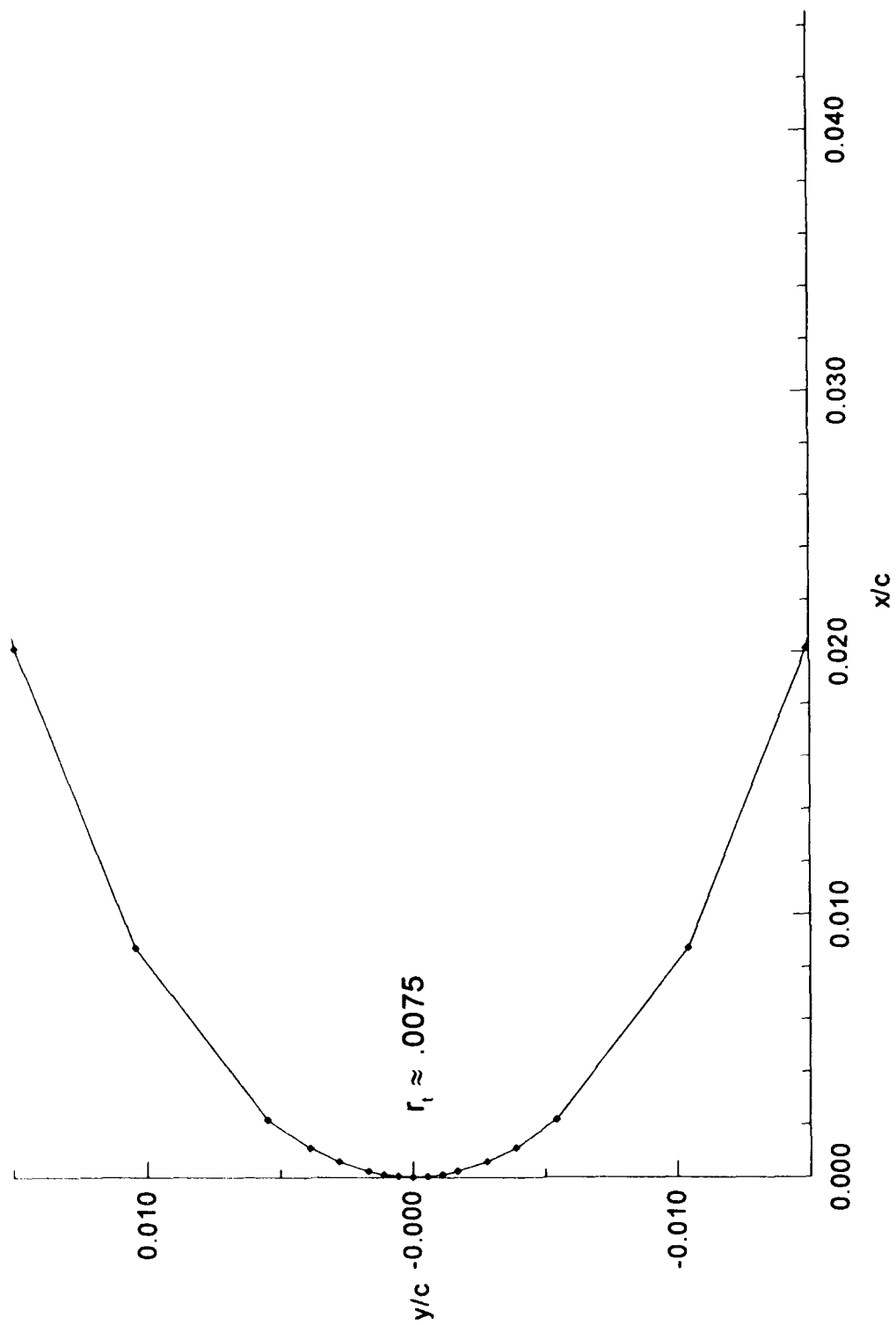


Figure 50. Airfoil T4 Leading-Edge -  $t/c = 5.17\%$

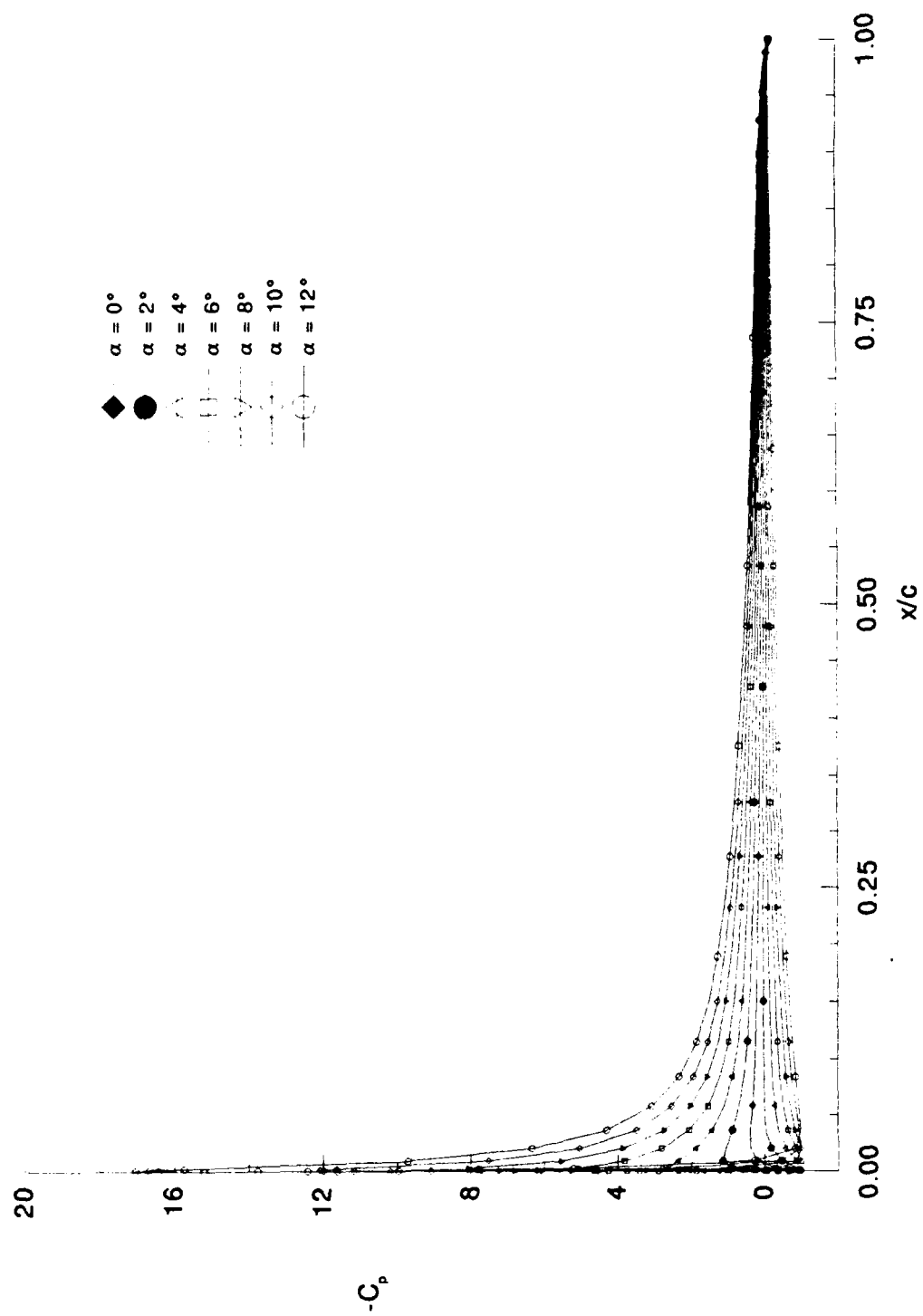


Figure 51. Pressure Distributions - T4 - Incompressible



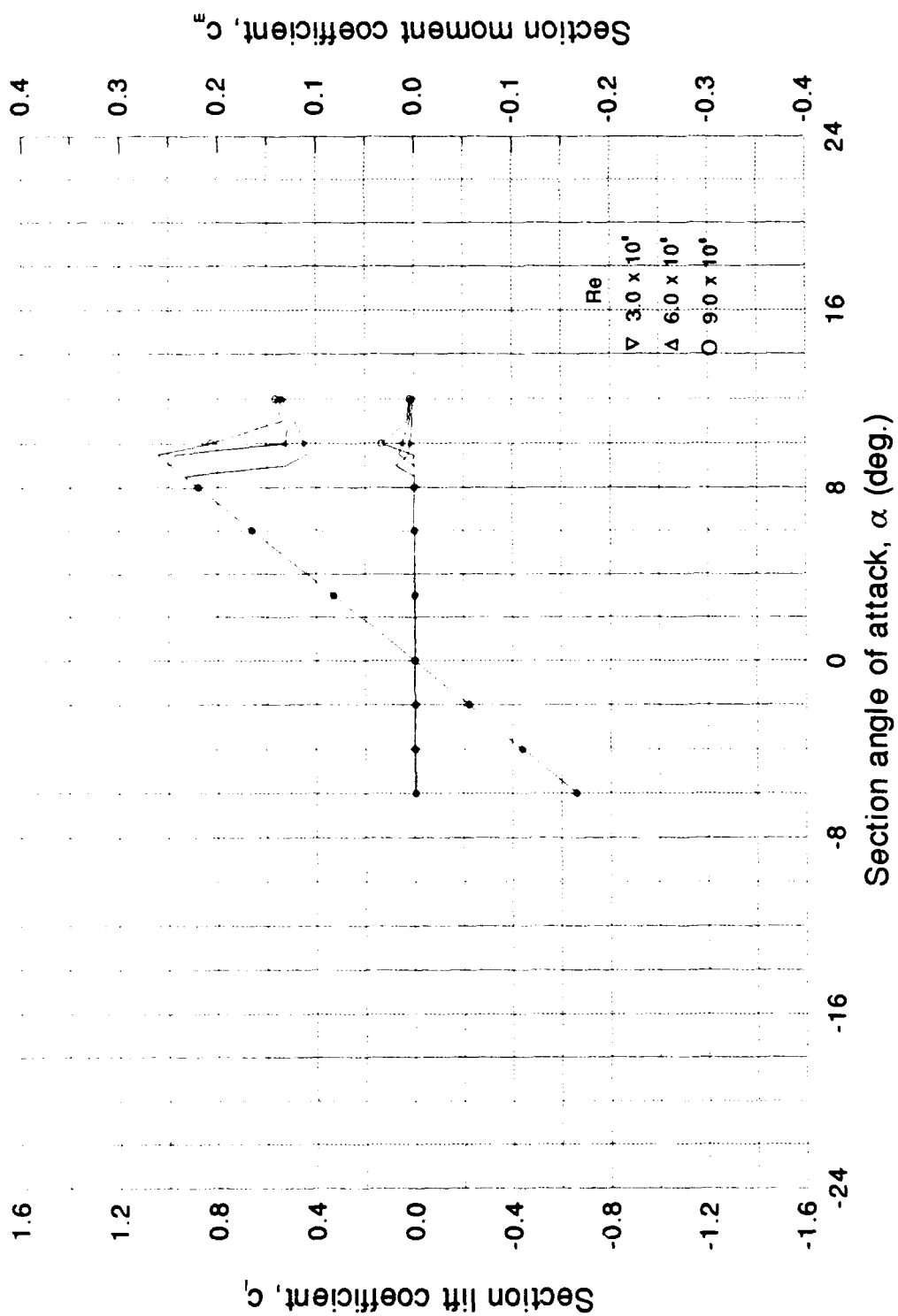


Figure 52. Airfoil T4 -  $C_l$ ,  $C_m$  vs  $\alpha$  Curves

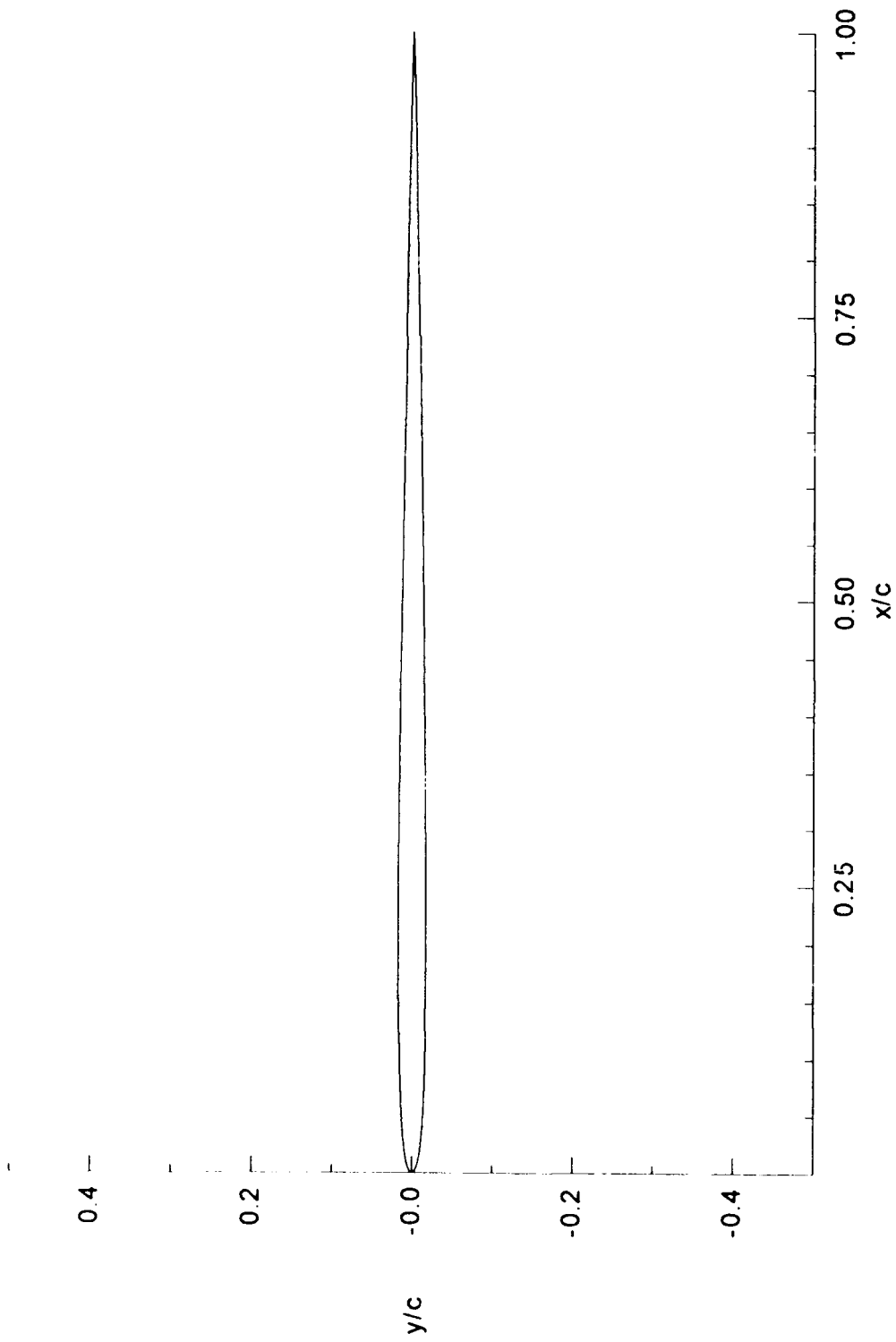


Figure 53. Airfoil T402 -  $t/c = 3.44\%$

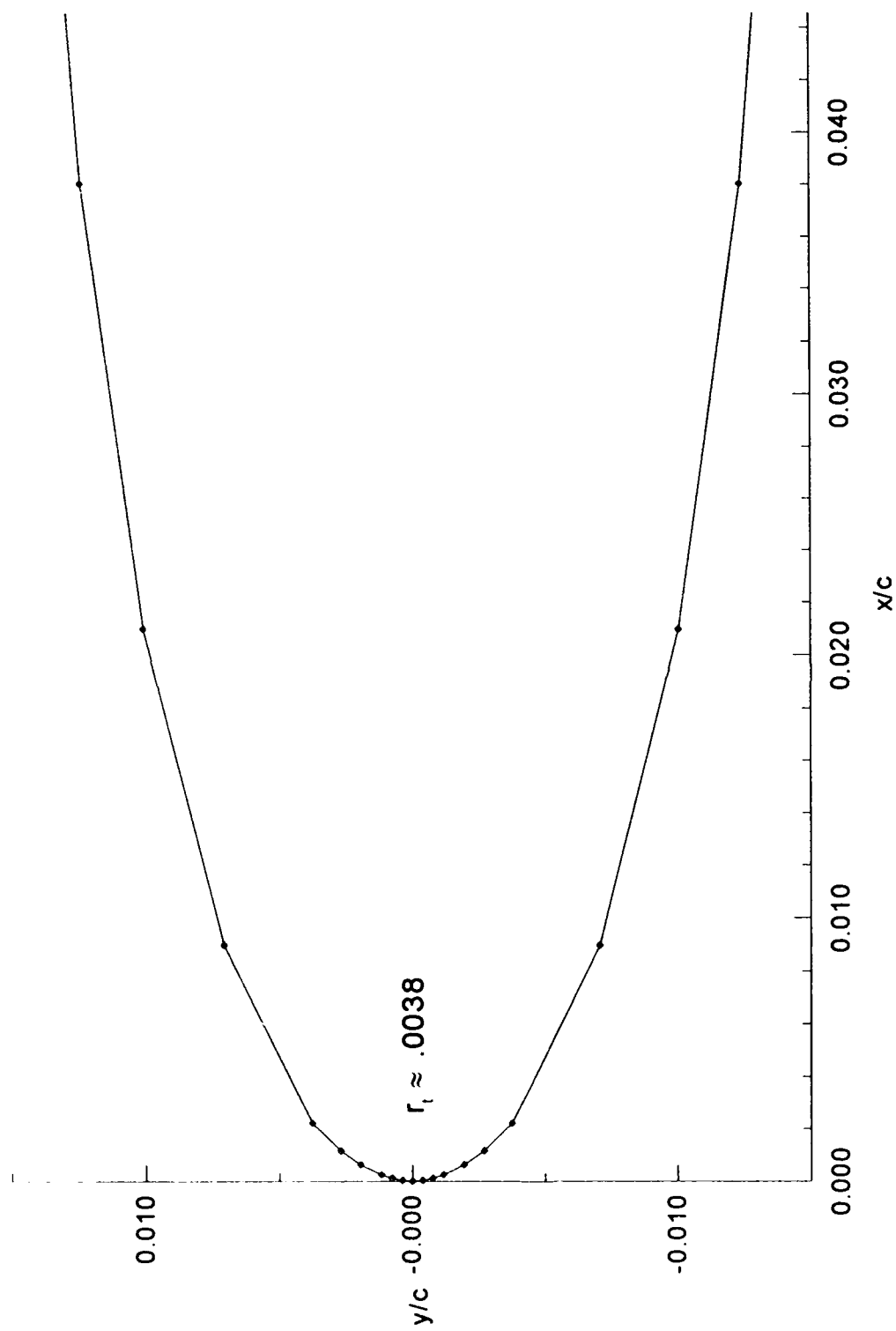


Figure 54. Airfoil T402 Leading-Edge -  $t/c = 3.44\%$

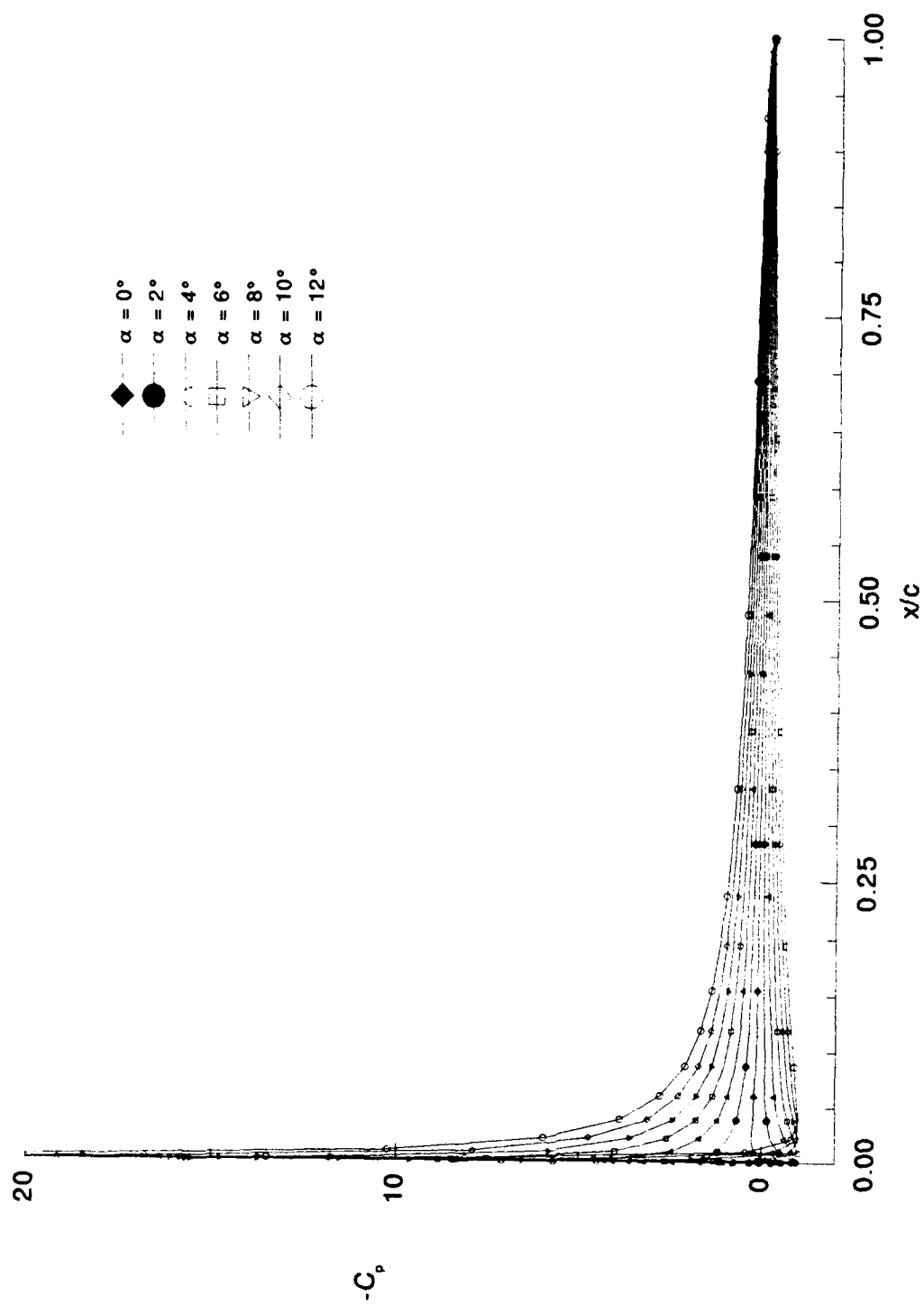


Figure 55. Pressure Distributions - T402 - Incompressible

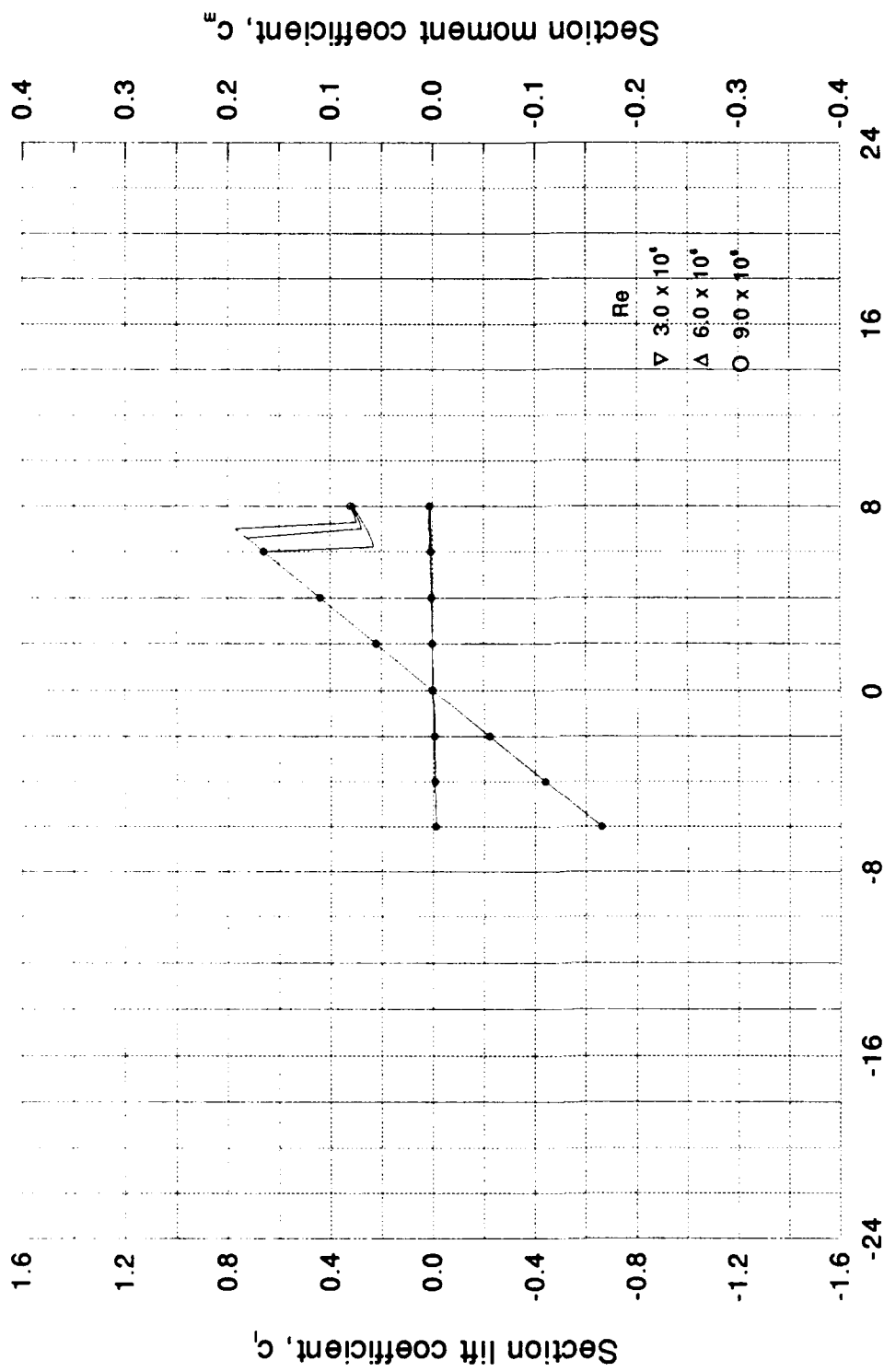


Figure 56. Airfoil T402 -  $C_l, C_m$  vs  $\alpha$  Curves

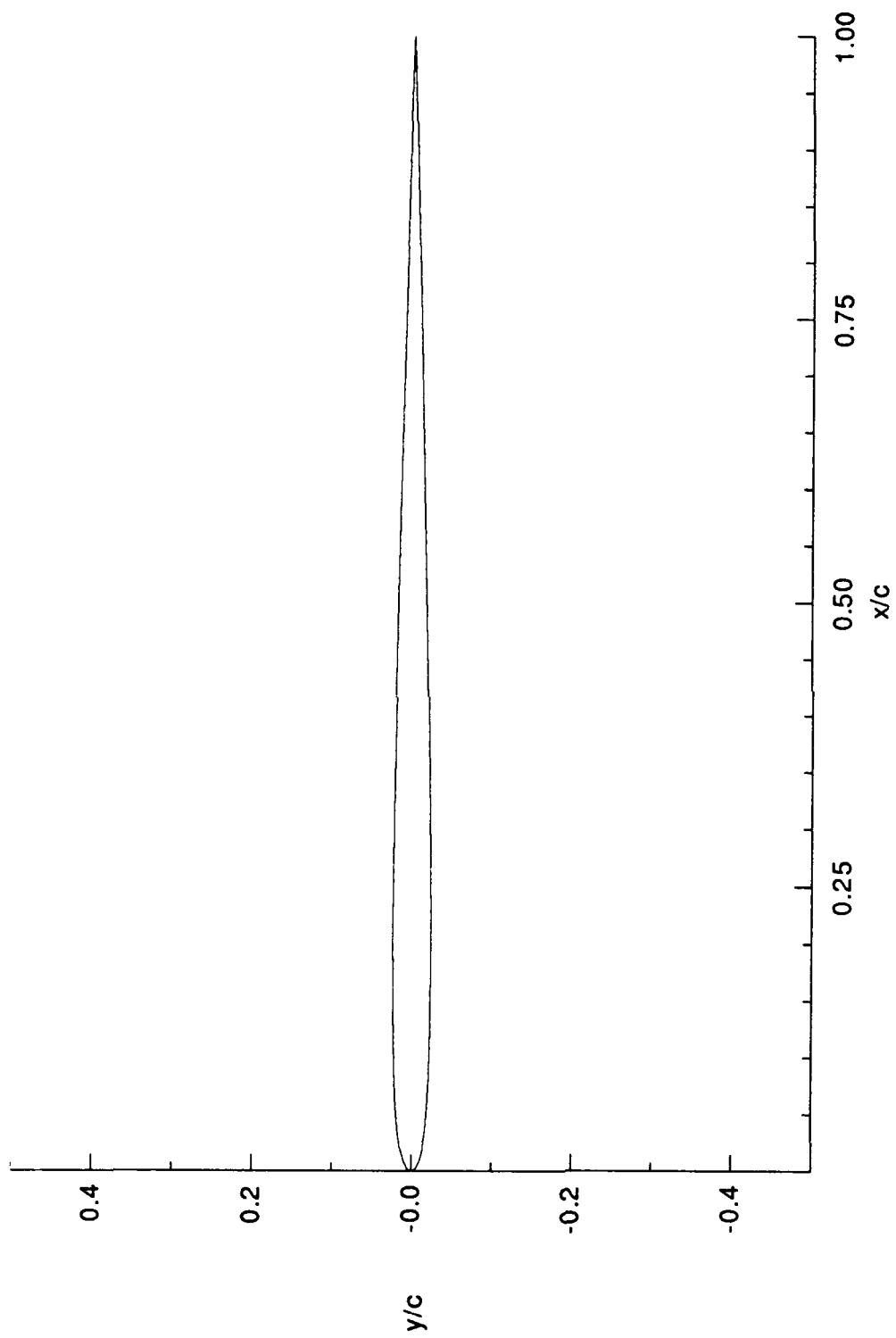


Figure 57. Airfoil T22 -  $t/c = 4.75\%$

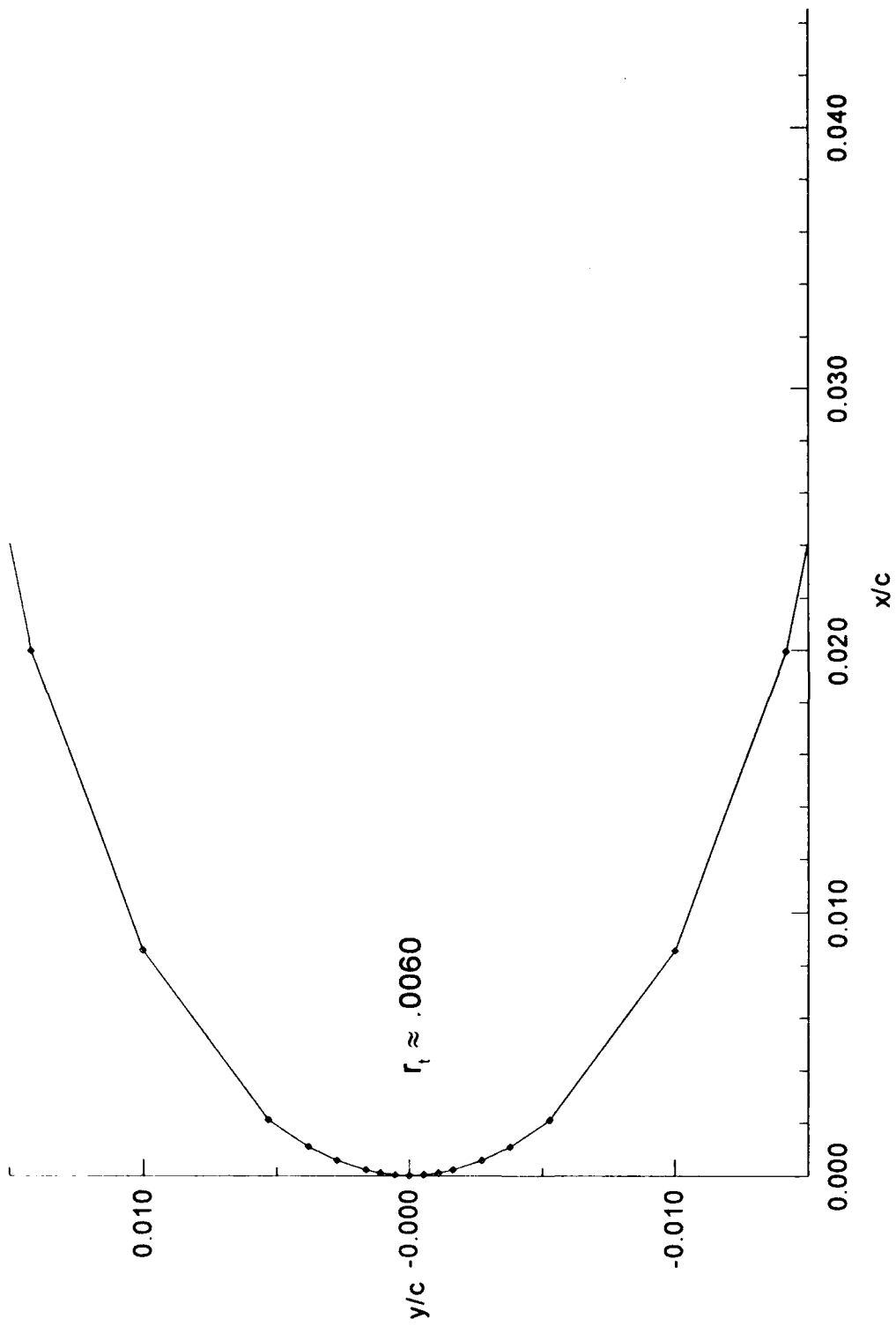


Figure 58. Airfoil T22 Leading-Edge -  $t/c = 4.75\%$

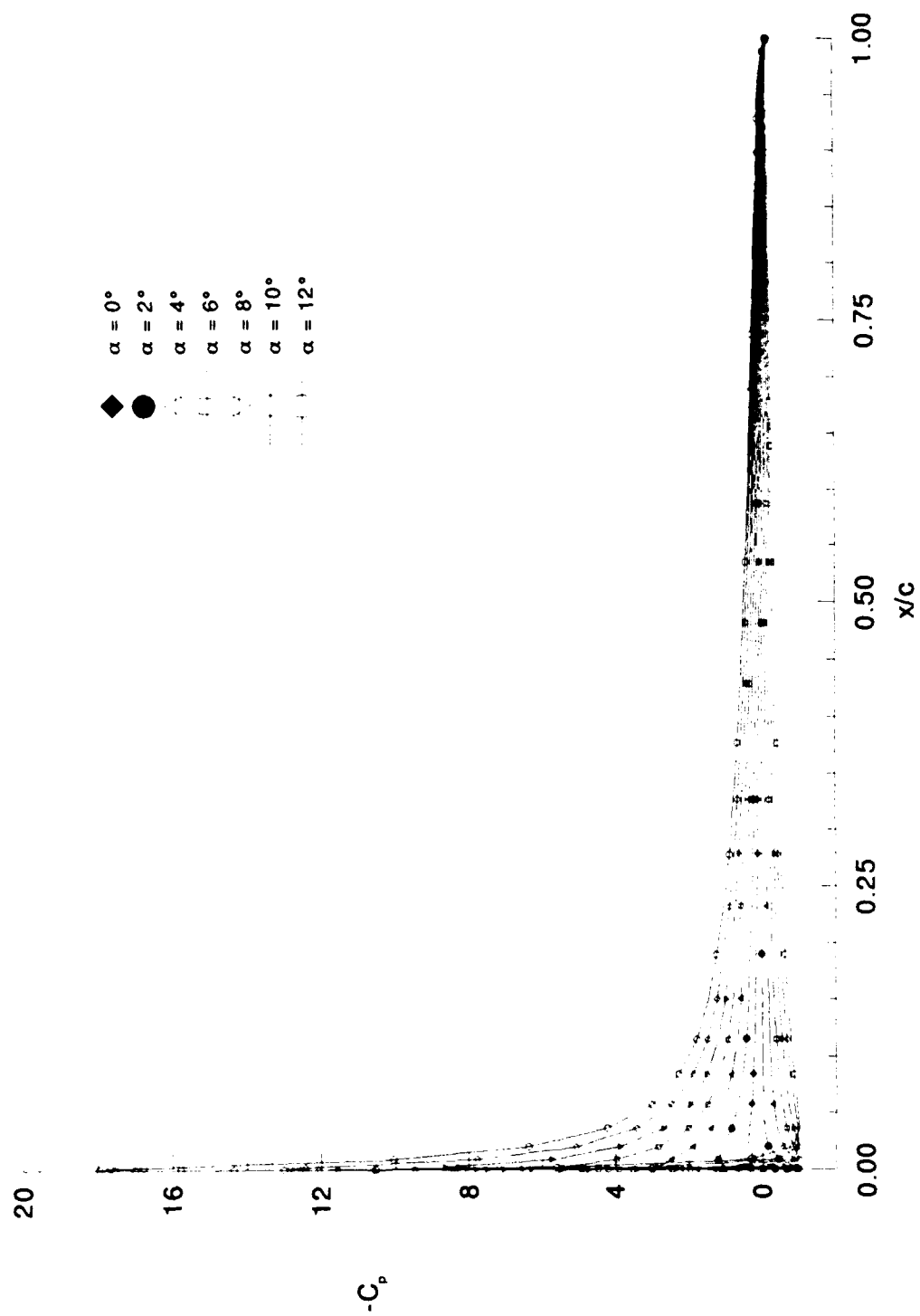


Figure 59. Pressure Distributions - T22 - Incompressible



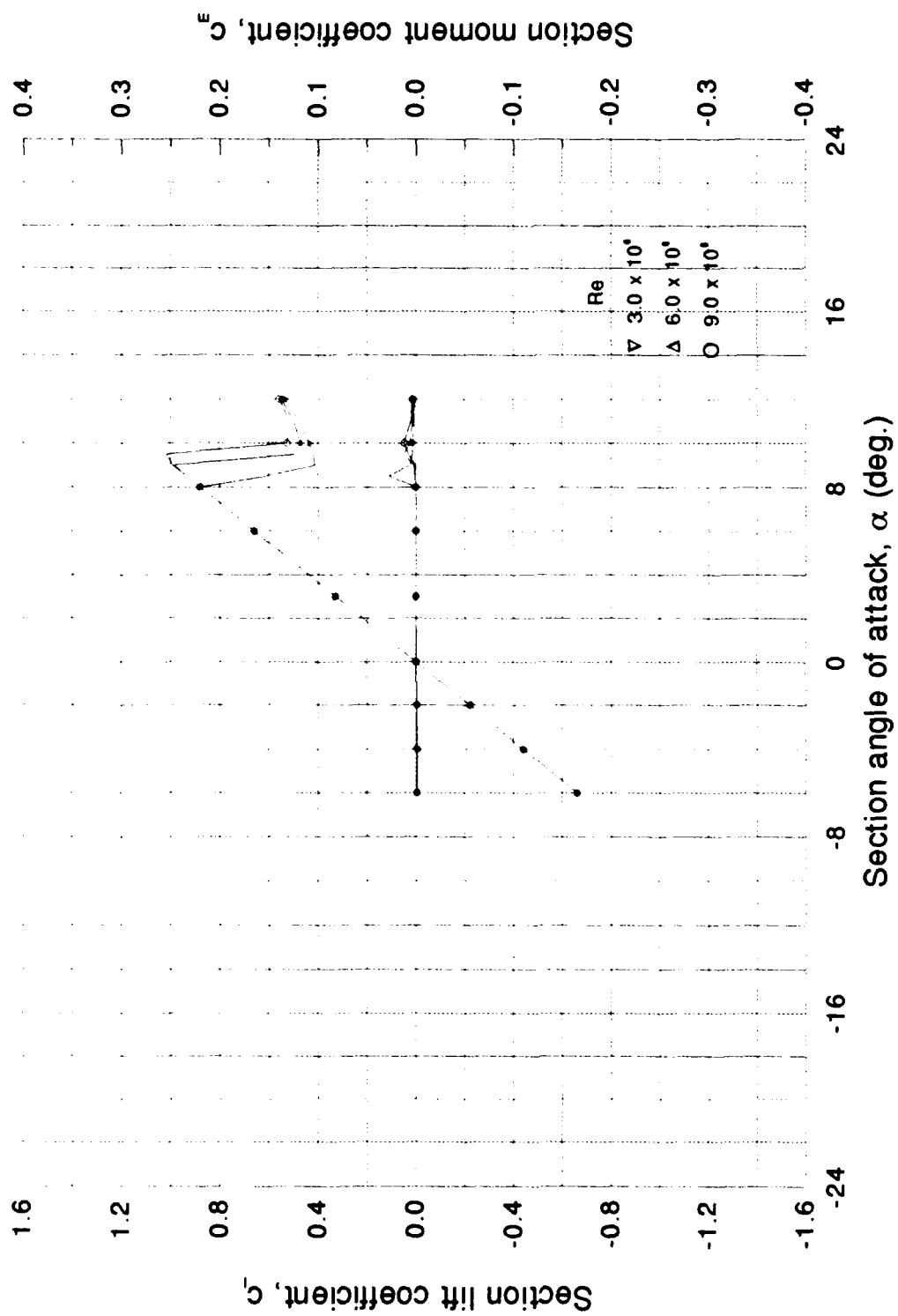


Figure 60. Airfoil T22 -  $C_l$ ,  $C_m$  vs  $\alpha$  Curves

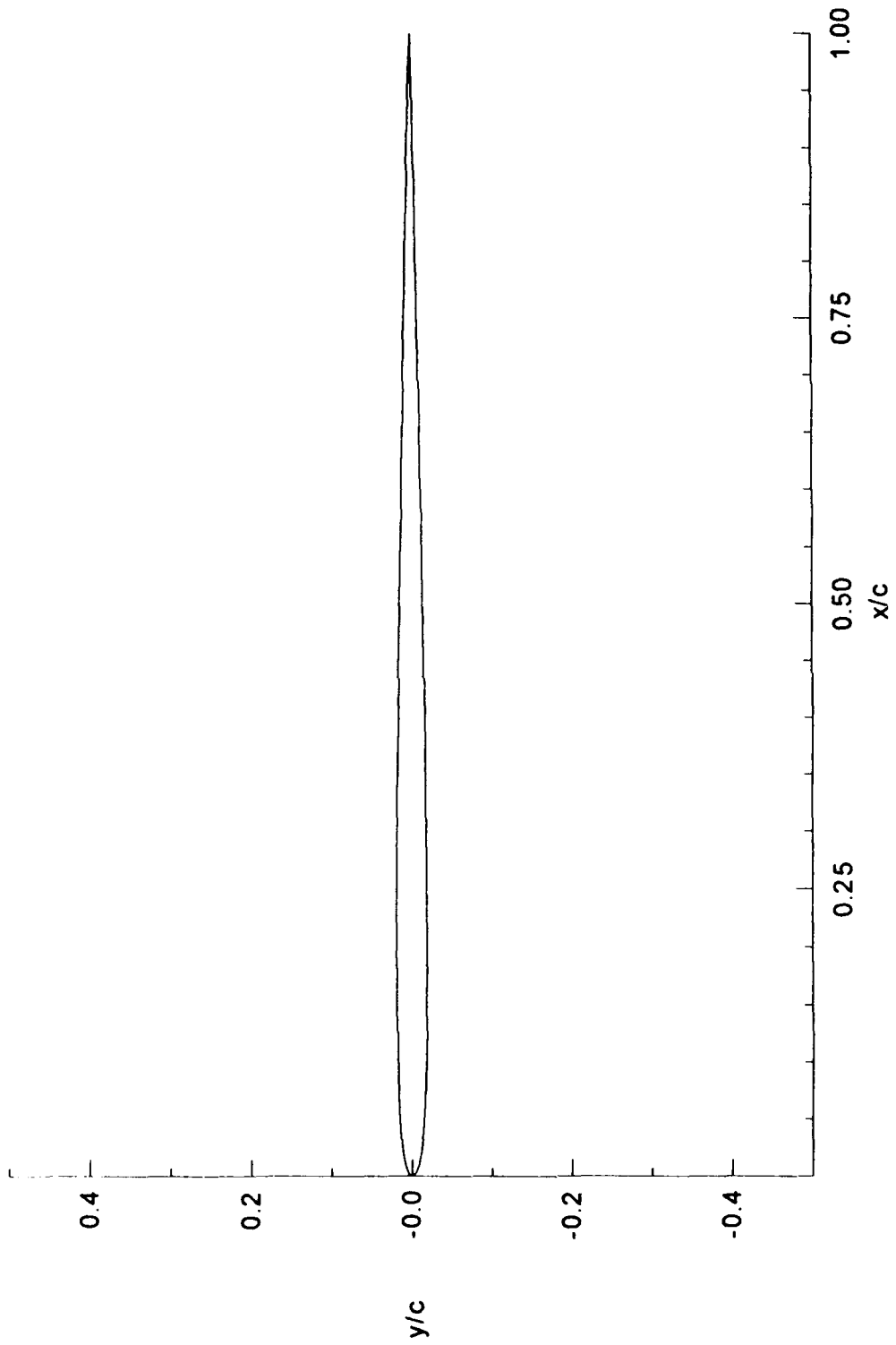


Figure 61. Airfoil T503 -  $t/c = 3.79\%$

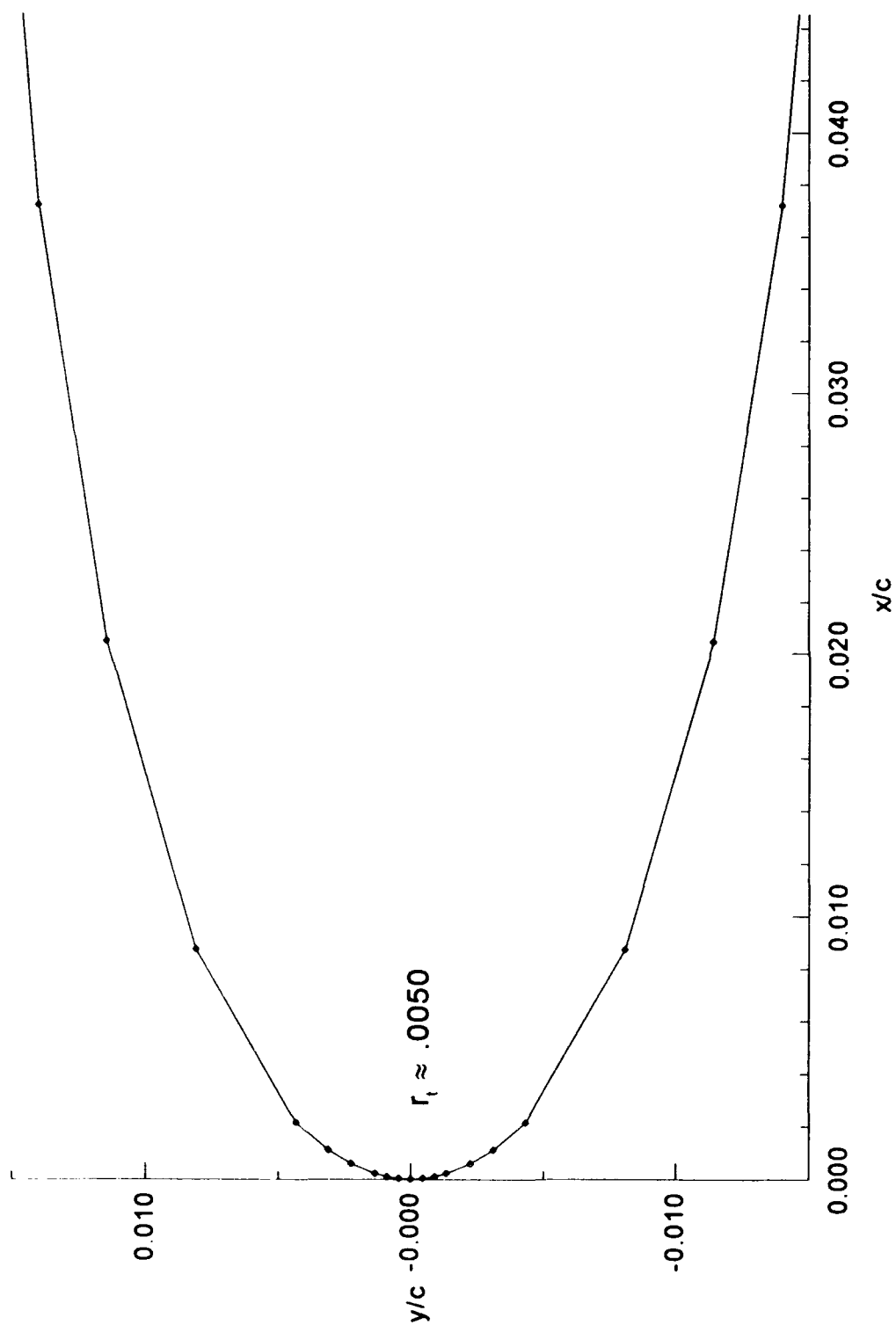


Figure 62. Airfoil T503 Leading-Edge -  $t/c = 3.79\%$

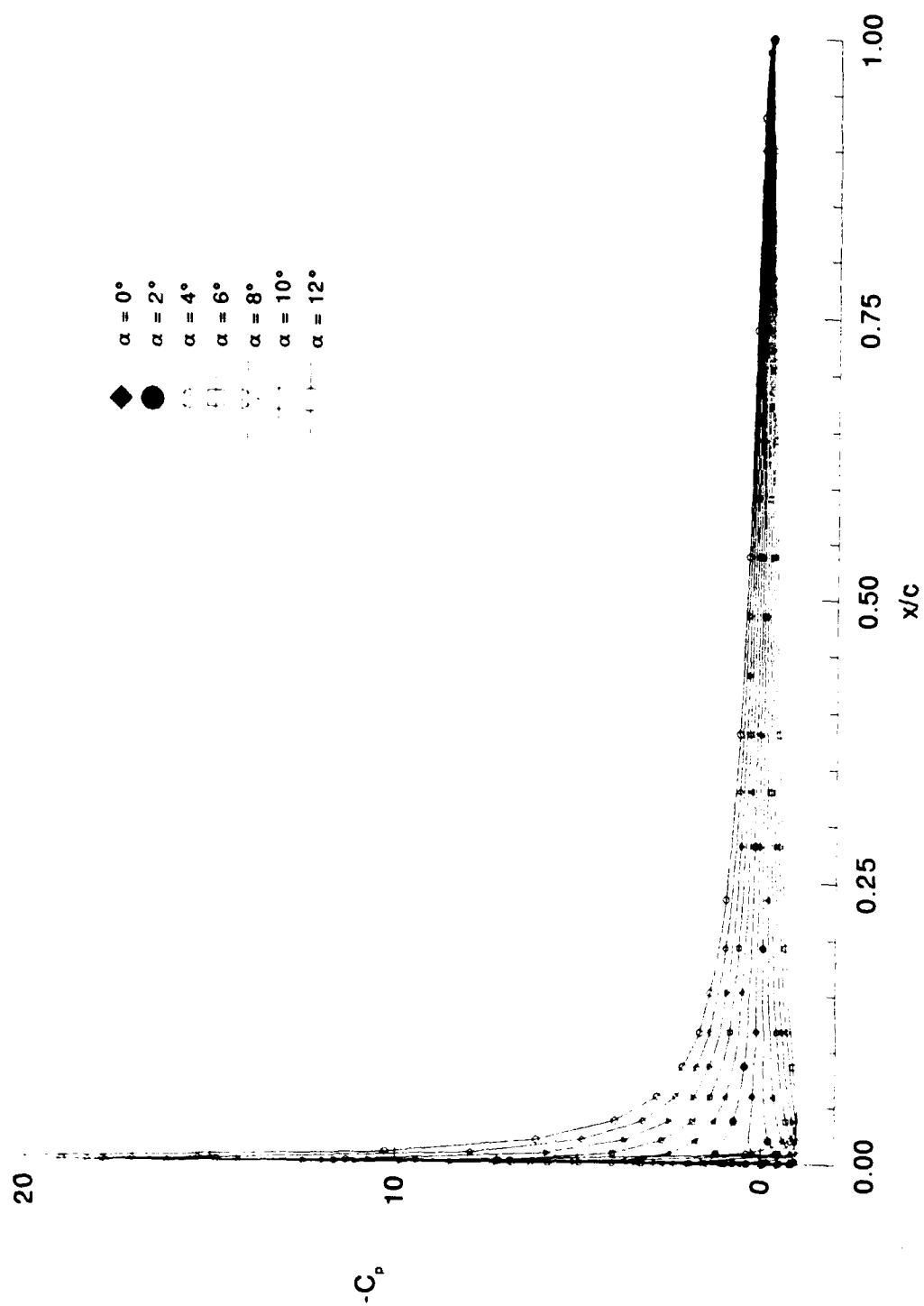


Figure 63. Pressure Distributions - T503 - Incompressible

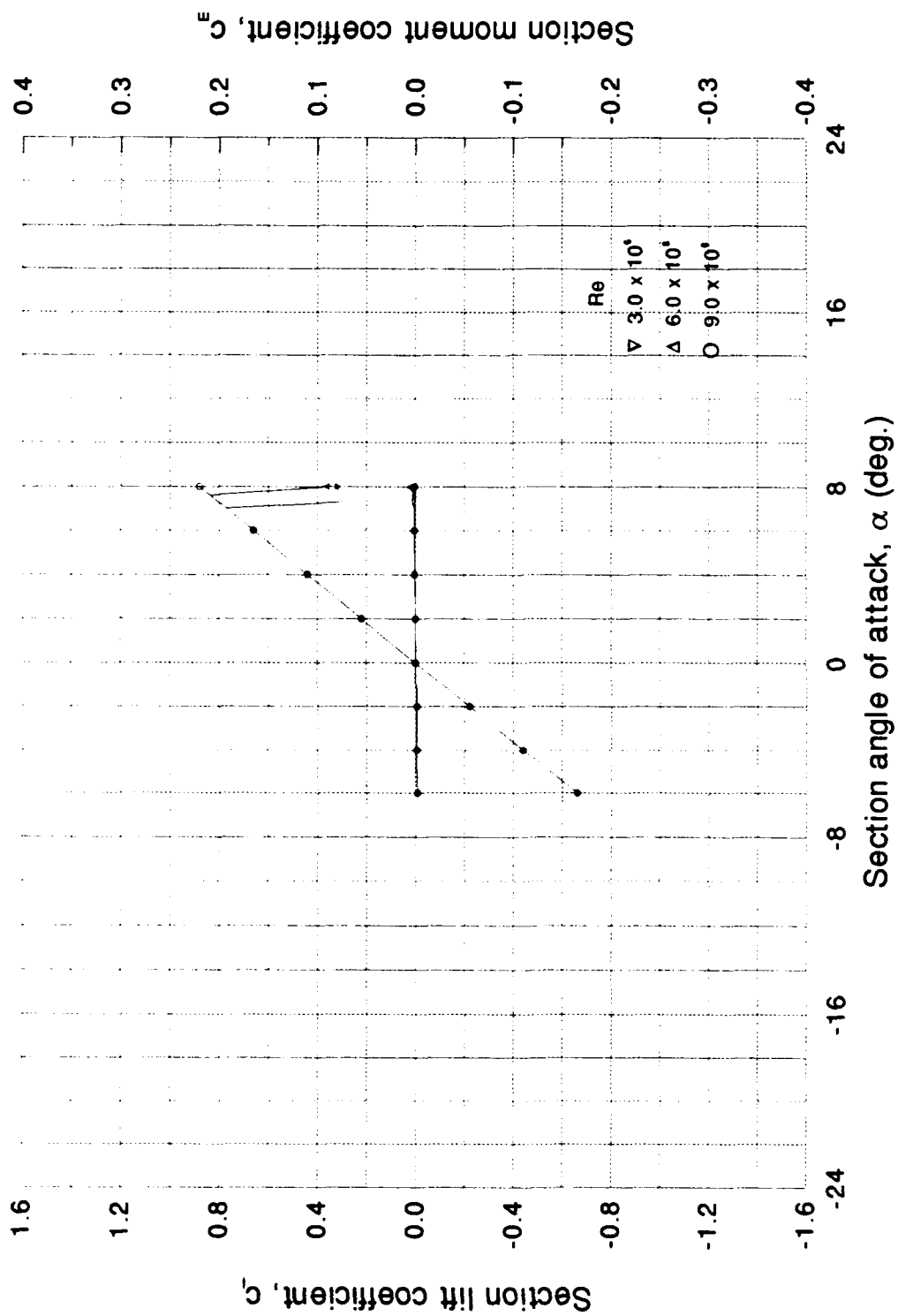


Figure 64. Airfoil T503 -  $C_l$ ,  $C_m$  vs  $\alpha$  Curves

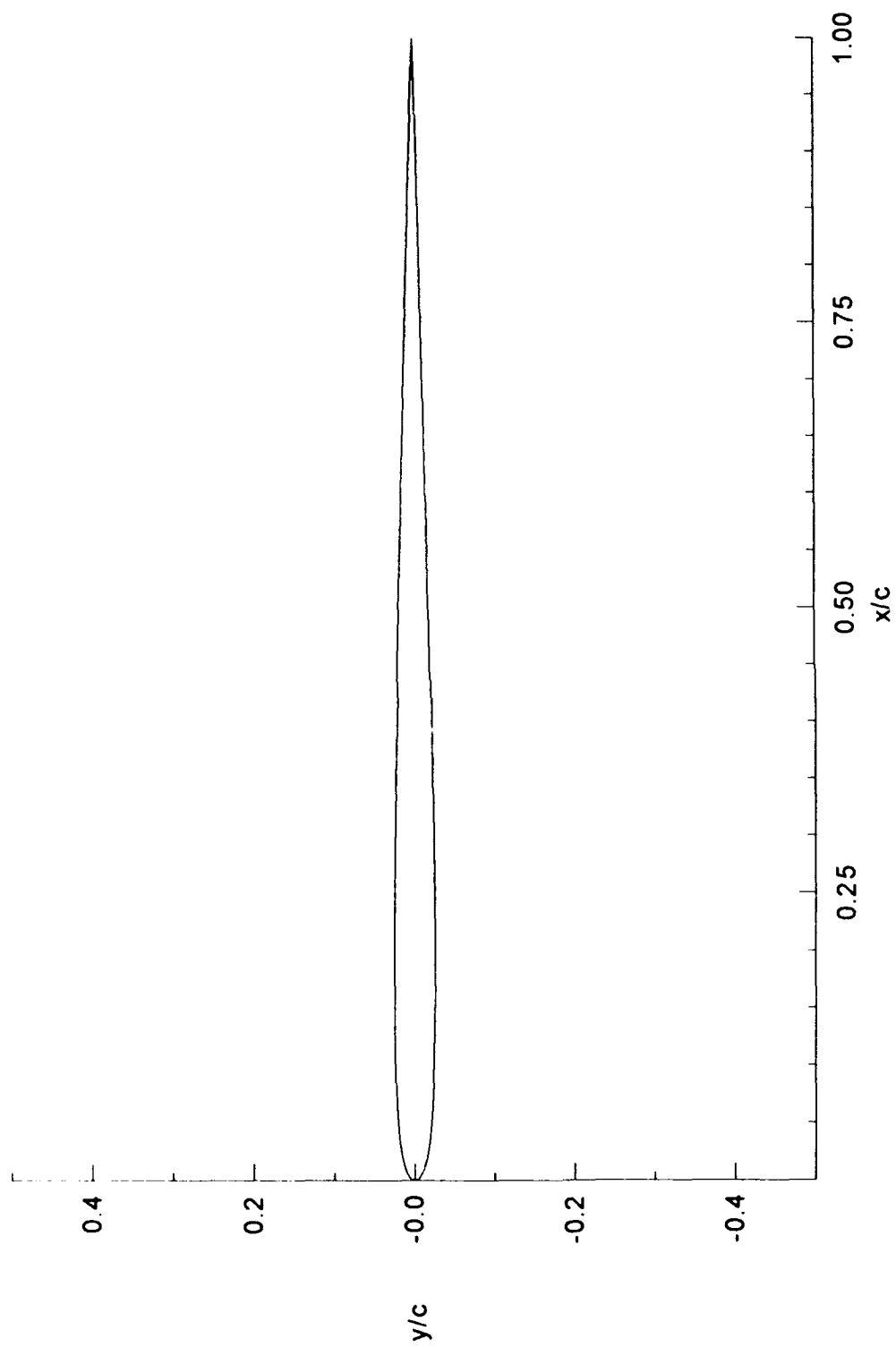


Figure 65. Airfoil T603 -  $t/c = 5.08\%$

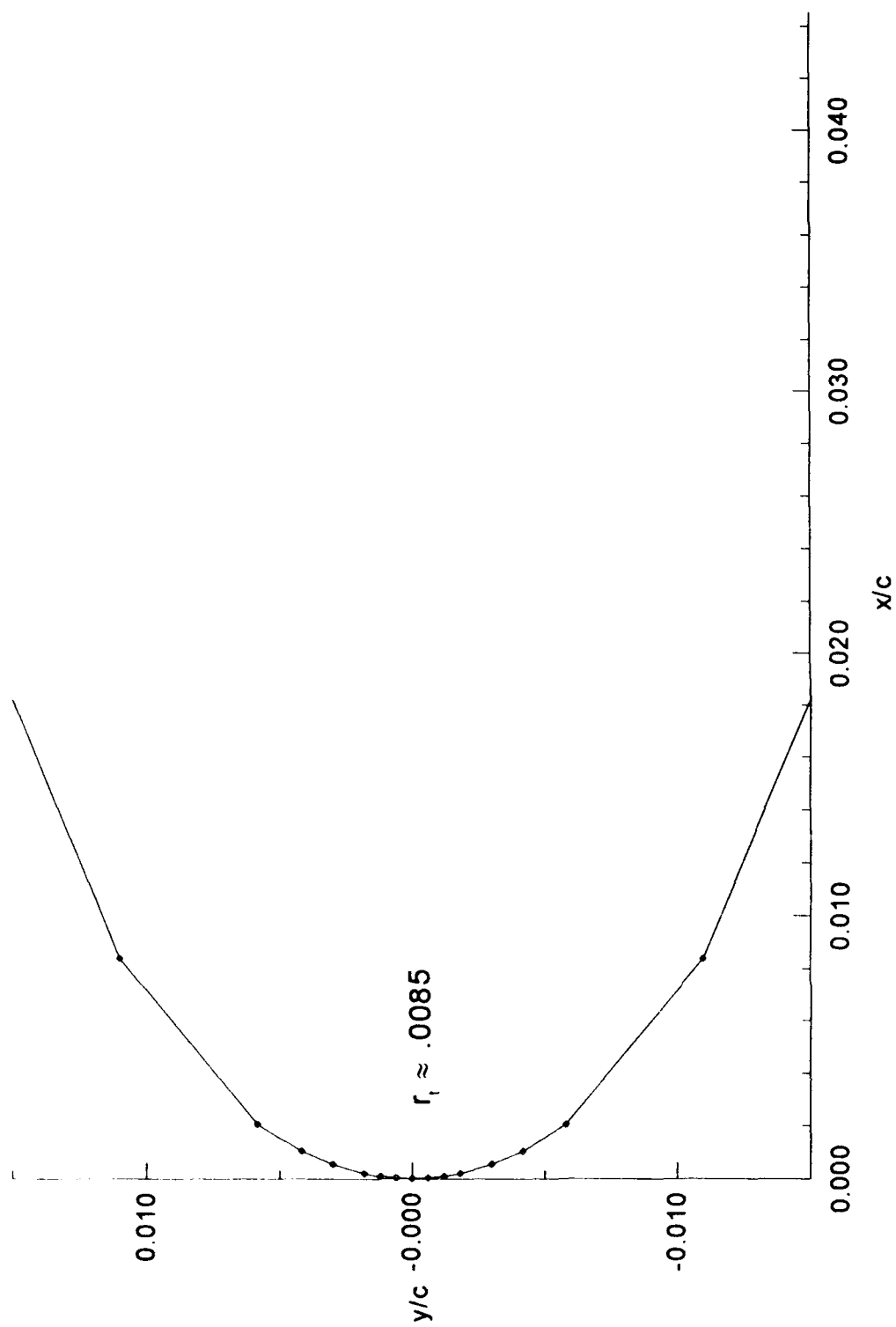


Figure 66. Airfoil T603 Leading-Edge -  $t/c = 5.08\%$

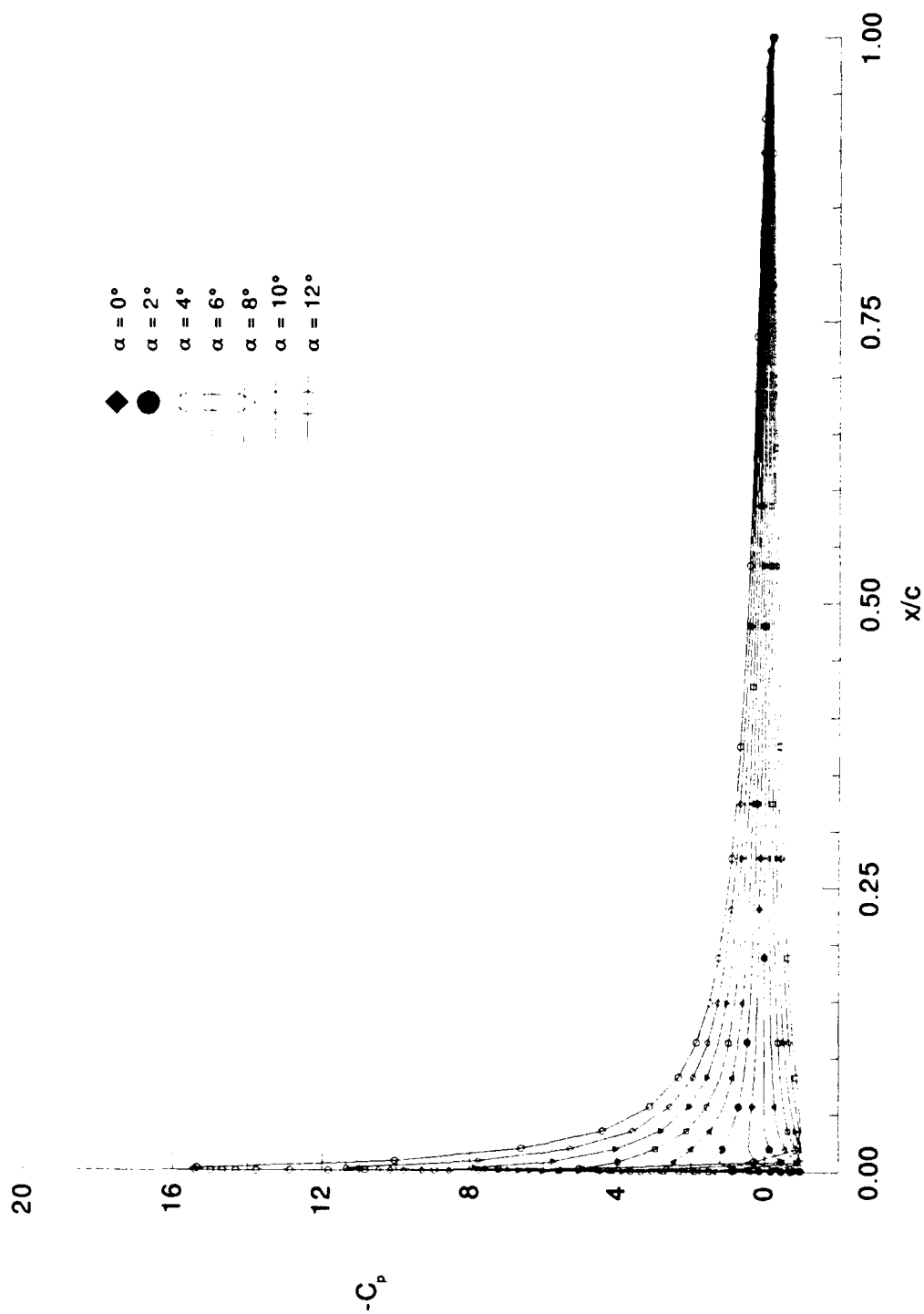


Figure 67. Pressure Distributions - T603 - Incompressible



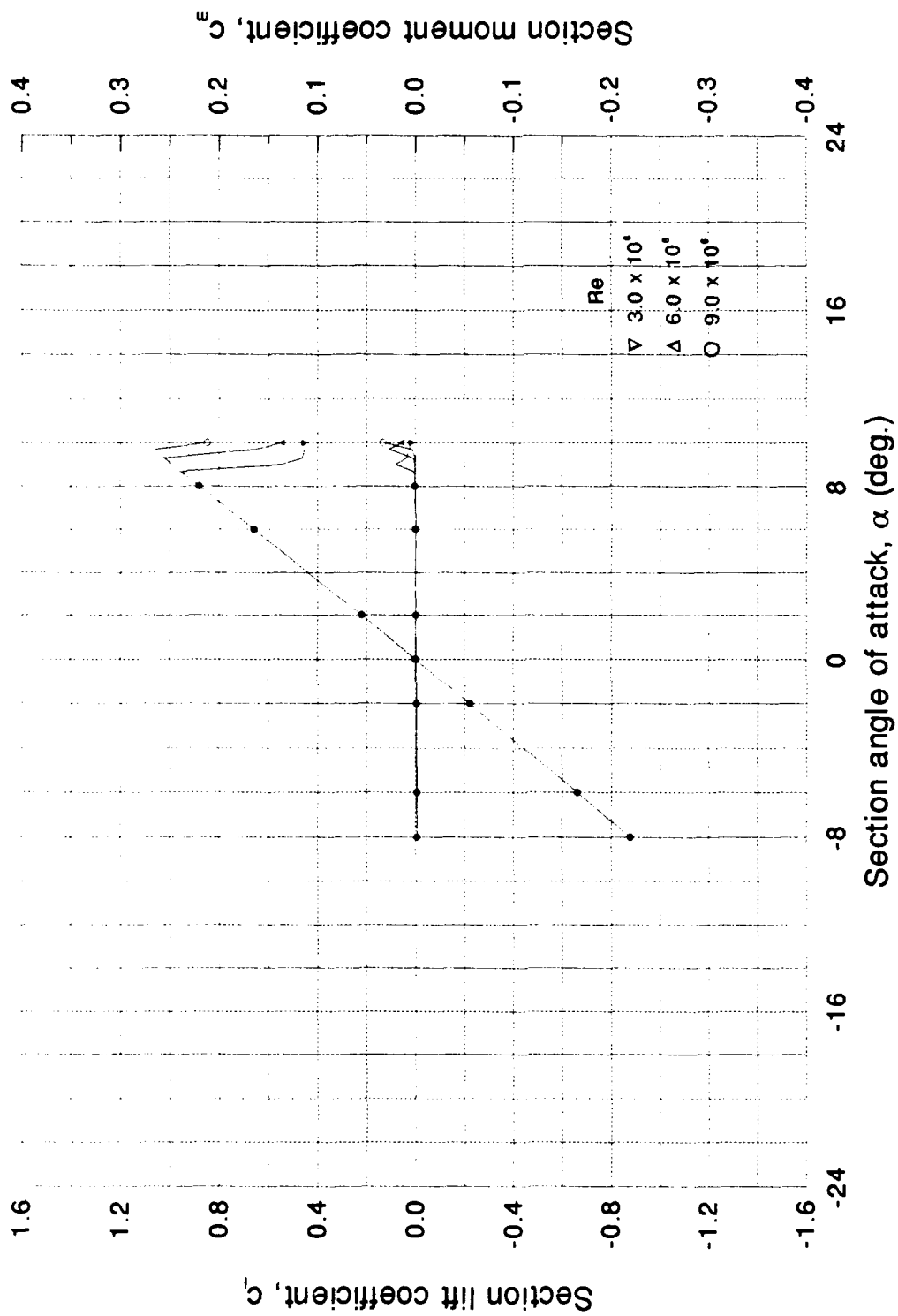


Figure 68. Airfoil T603 -  $C_l$ ,  $C_m$  vs  $\alpha$  Curves

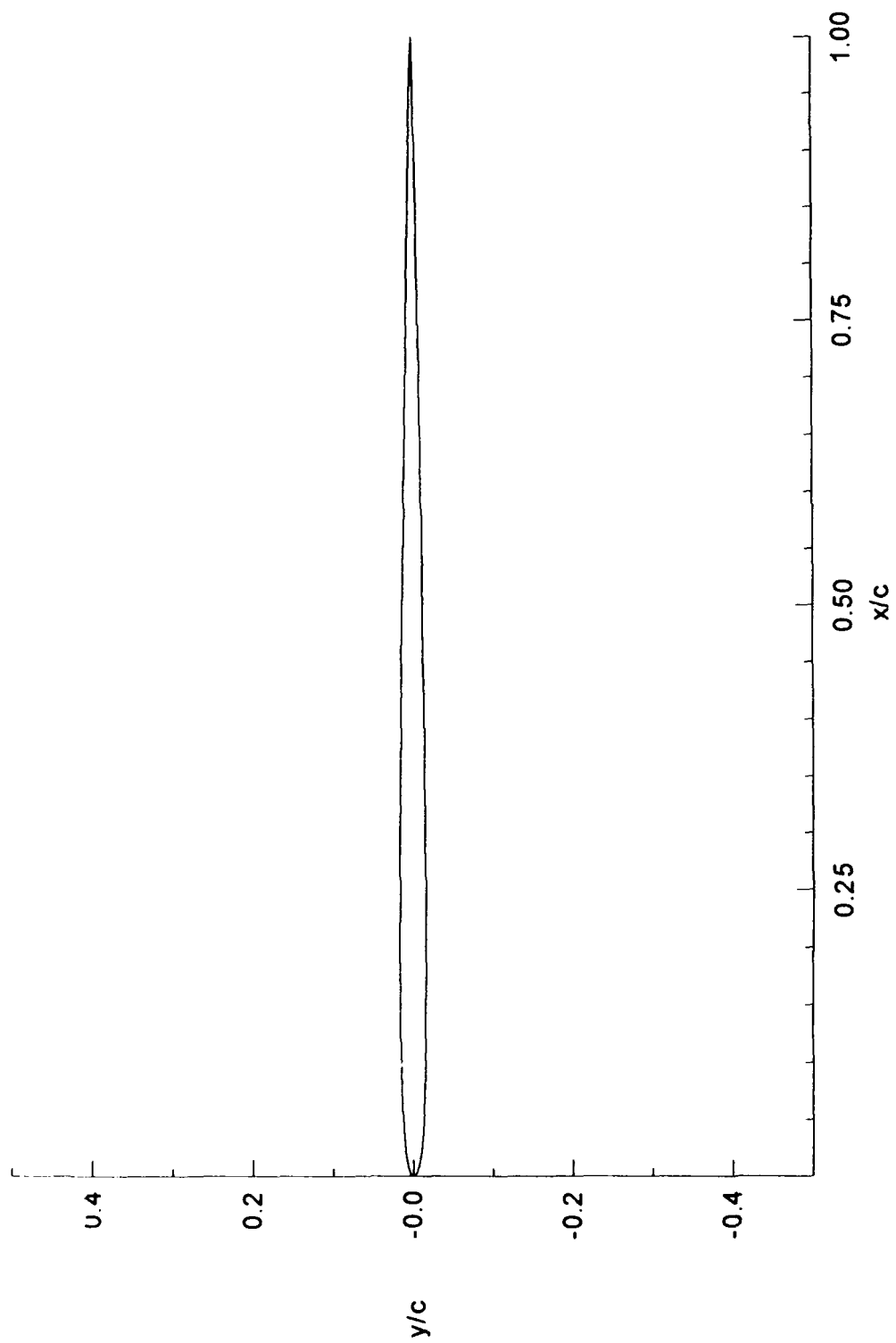


Figure 69. Airfoil T504 -  $t/c = 3.25\%$

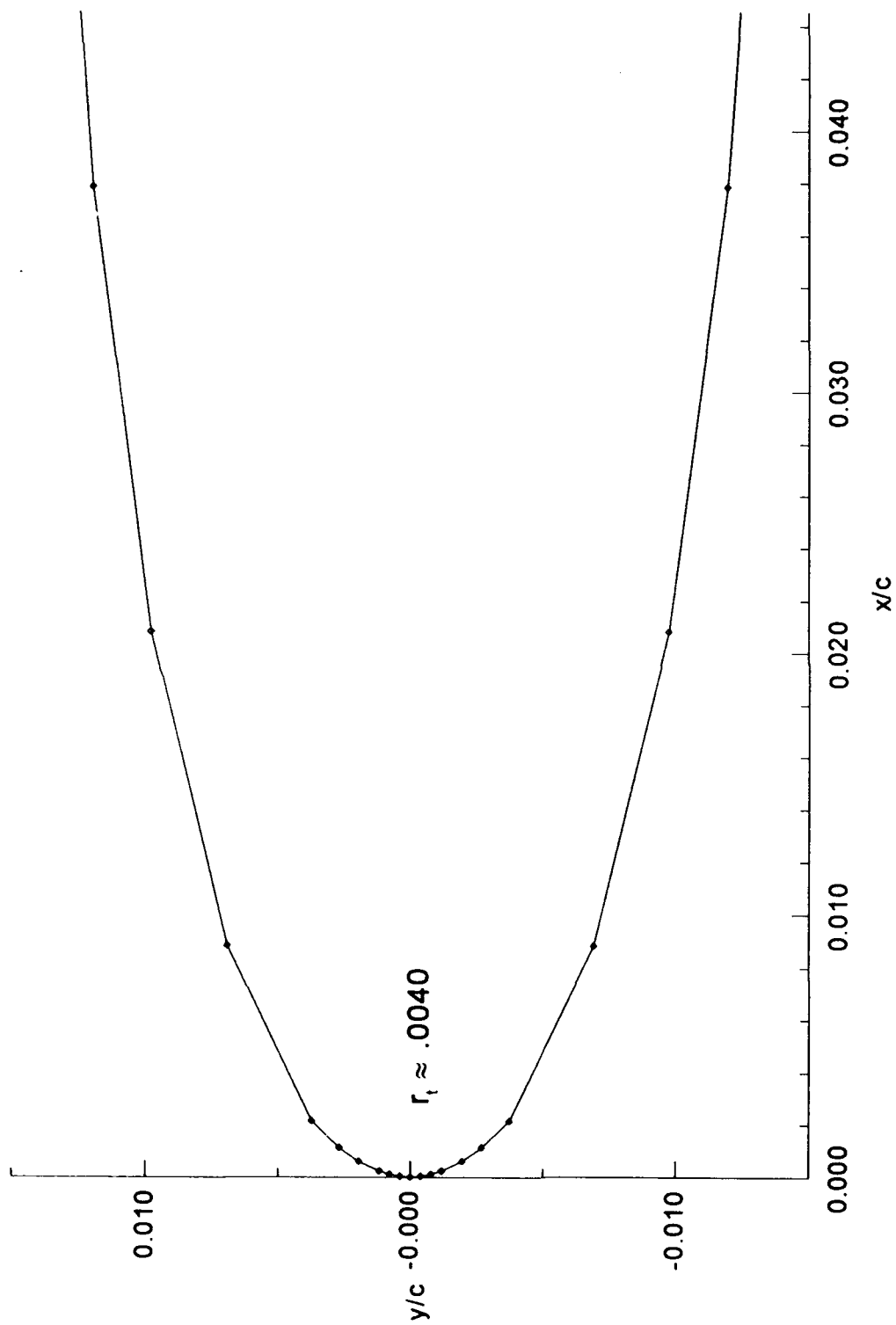


Figure 70. Airfoil T504 Leading-Edge -  $t/c = 3.25\%$

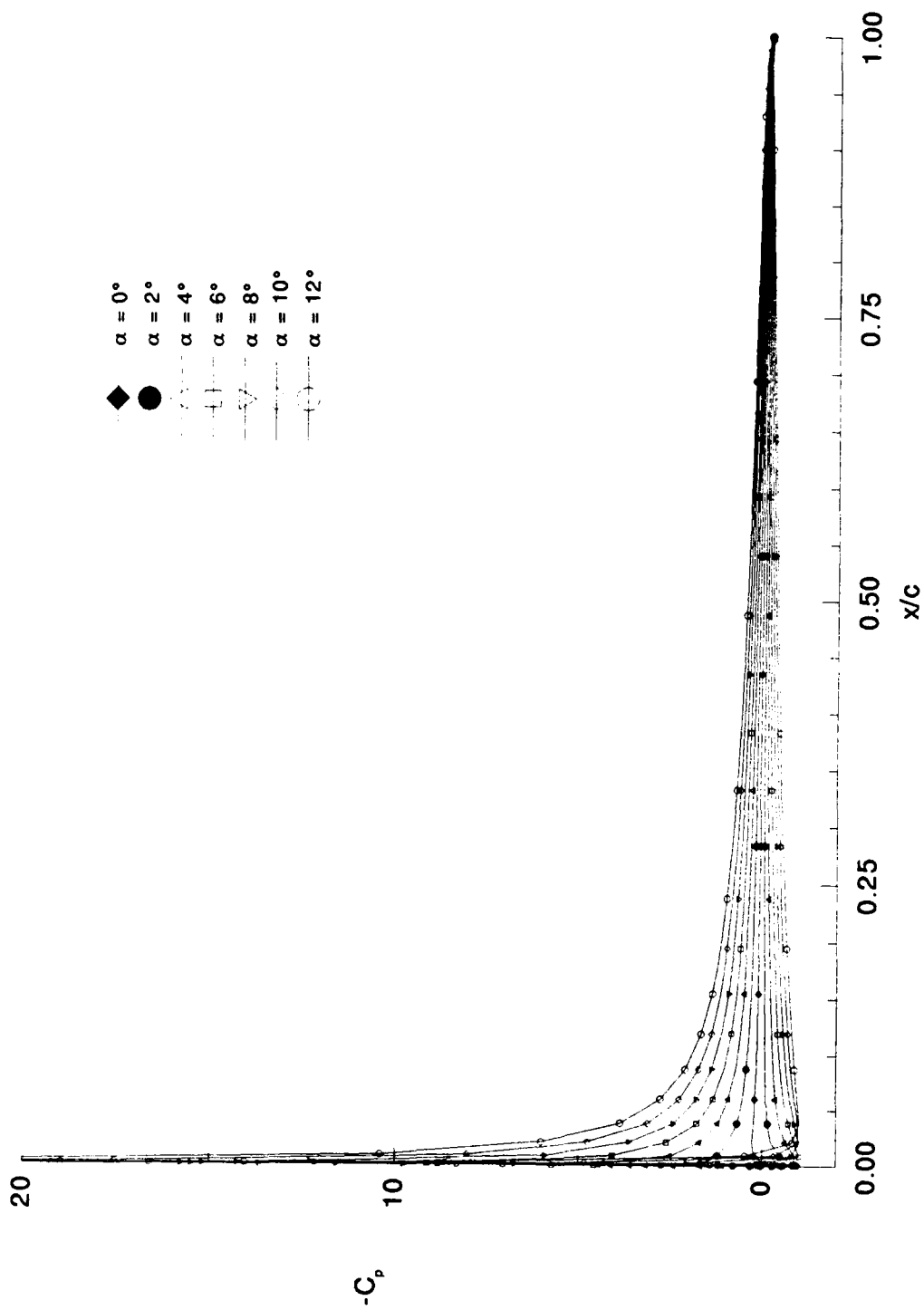


Figure 71. Pressure Distributions - T504 - Incompressible

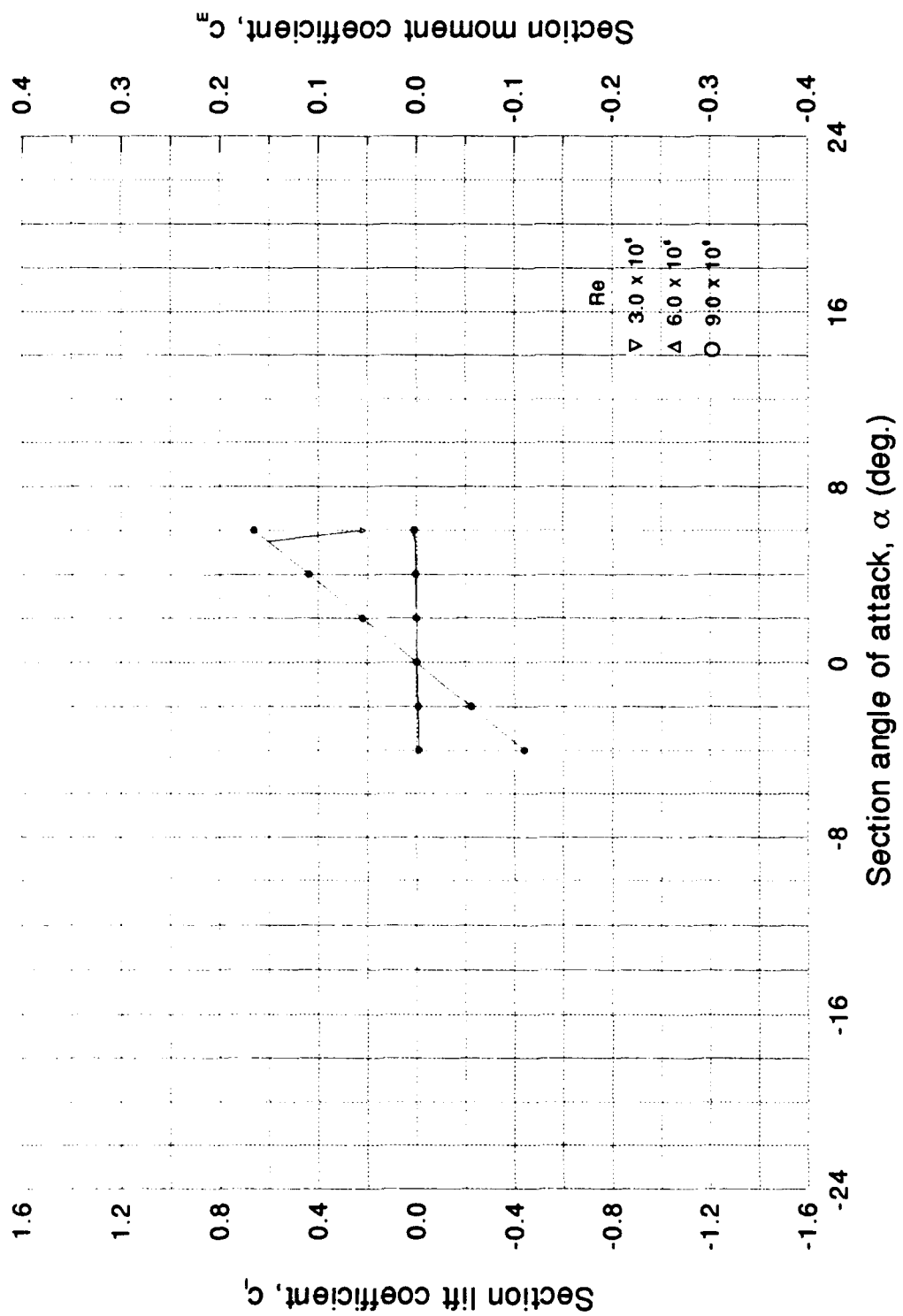


Figure 72. Airfoil T504 -  $C_l$ ,  $C_m$  vs  $\alpha$  Curves

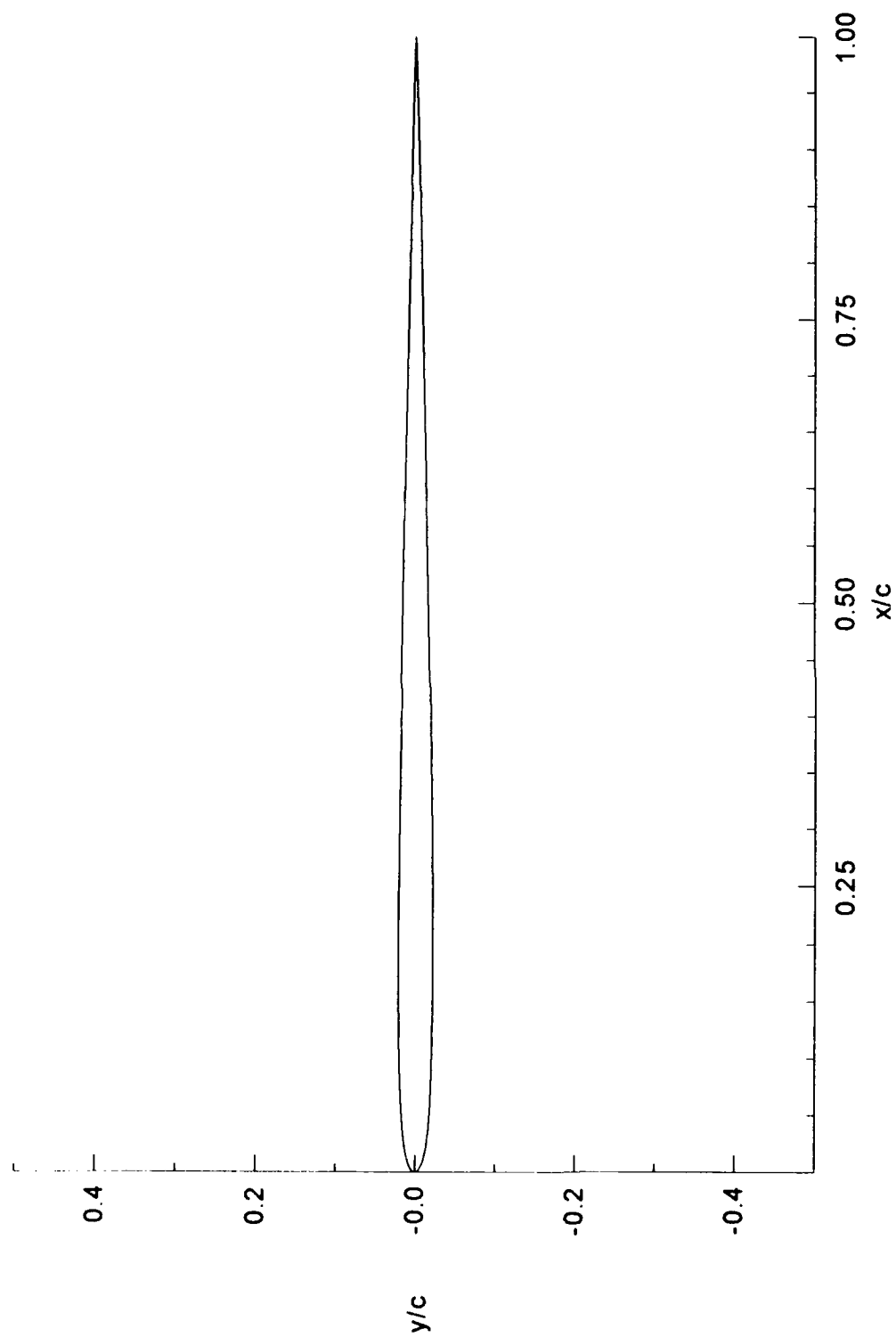


Figure 73. Airfoil T604 -  $t/c = 4.3\%$

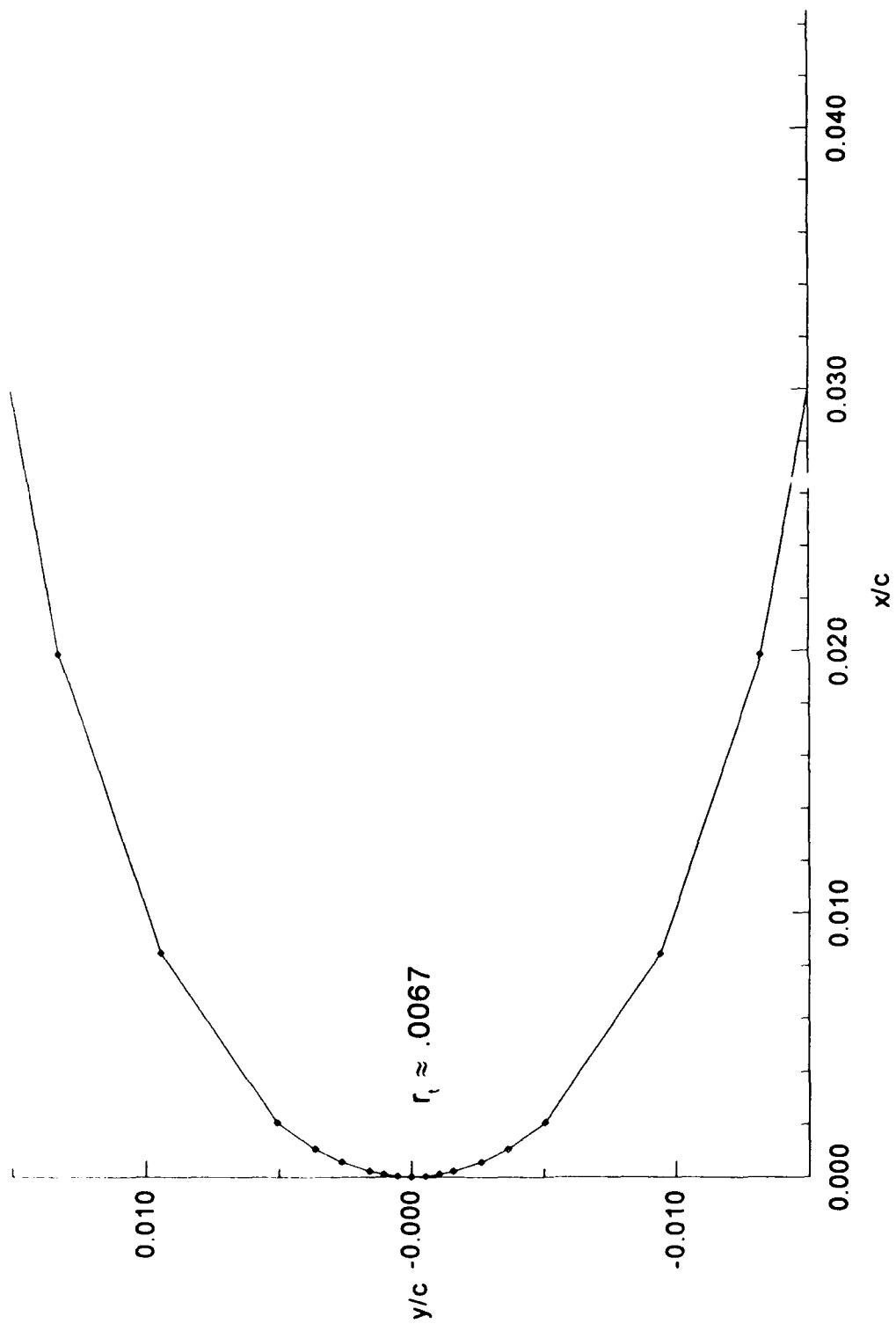


Figure 74. Airfoil T604 Leading-Edge -  $t/c = 4.3\%$

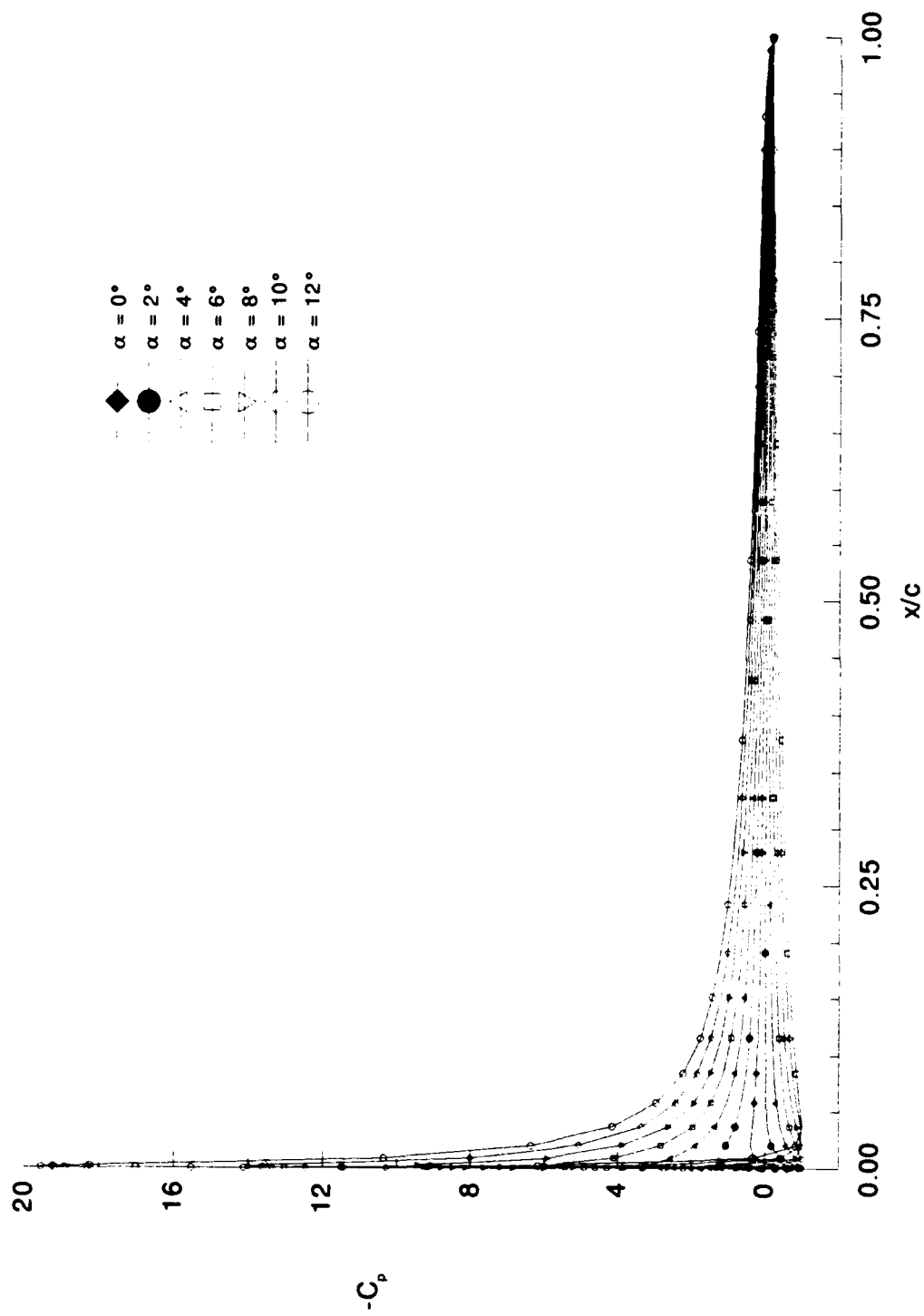


Figure 75. Pressure Distributions - T604 - Incompressible



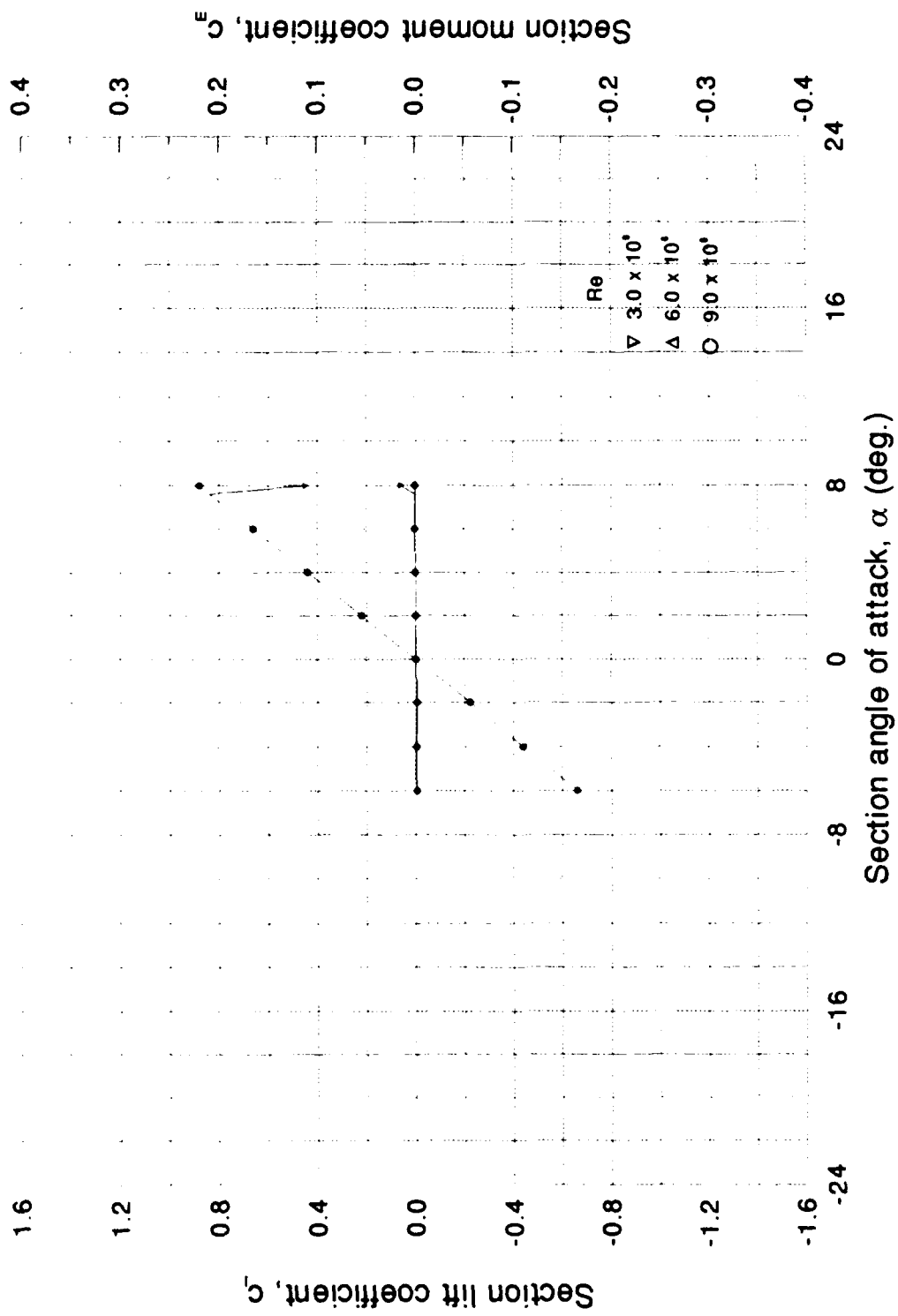


Figure 76. Airfoil T604 -  $C_l$ ,  $C_m$  vs  $\alpha$  Curves

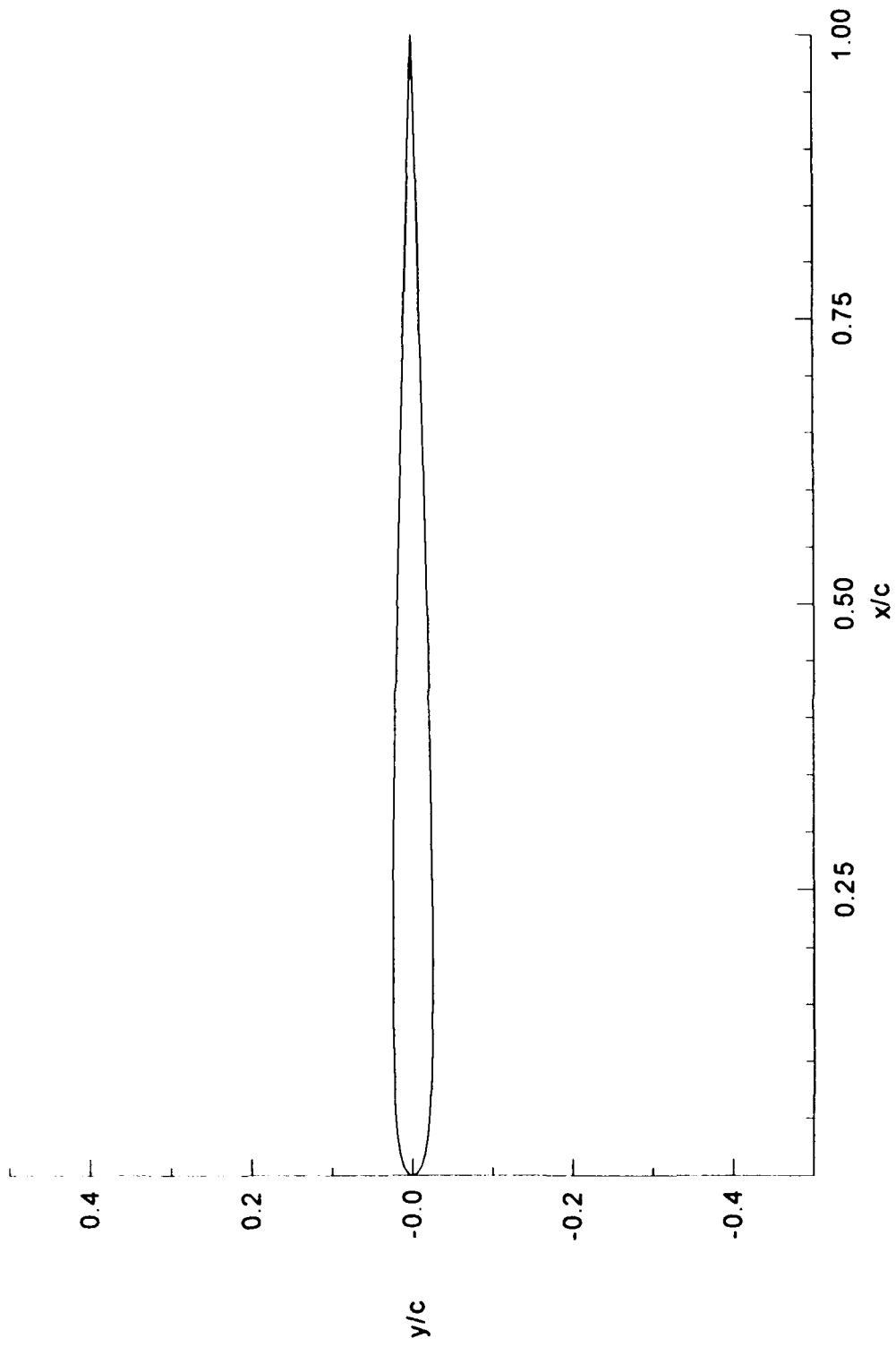


Figure 77. Airfoil T234 -  $t/c = 4.97\%$

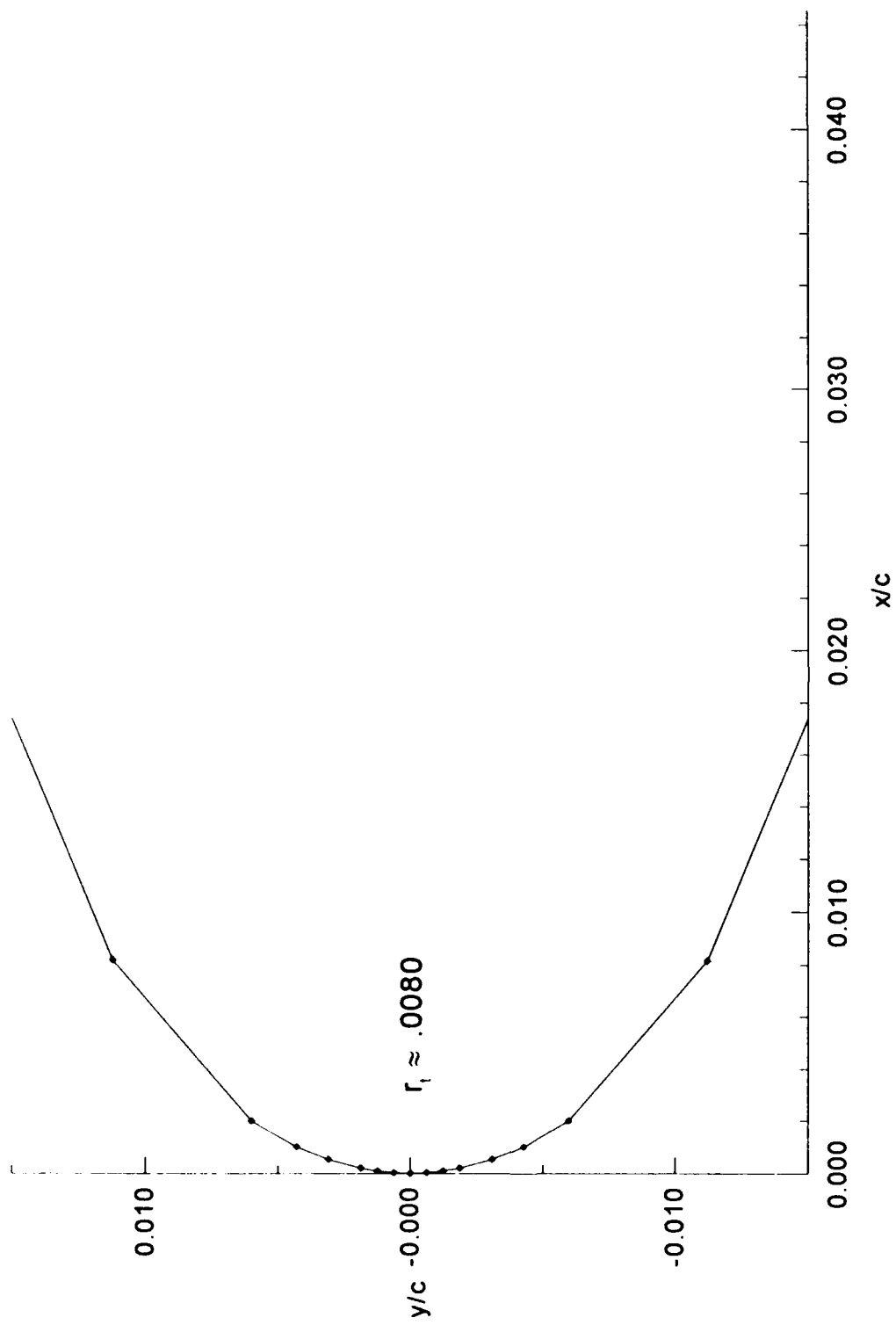


Figure 78. Airfoil T234 Leading-Edge -  $t/c = 4.97\%$

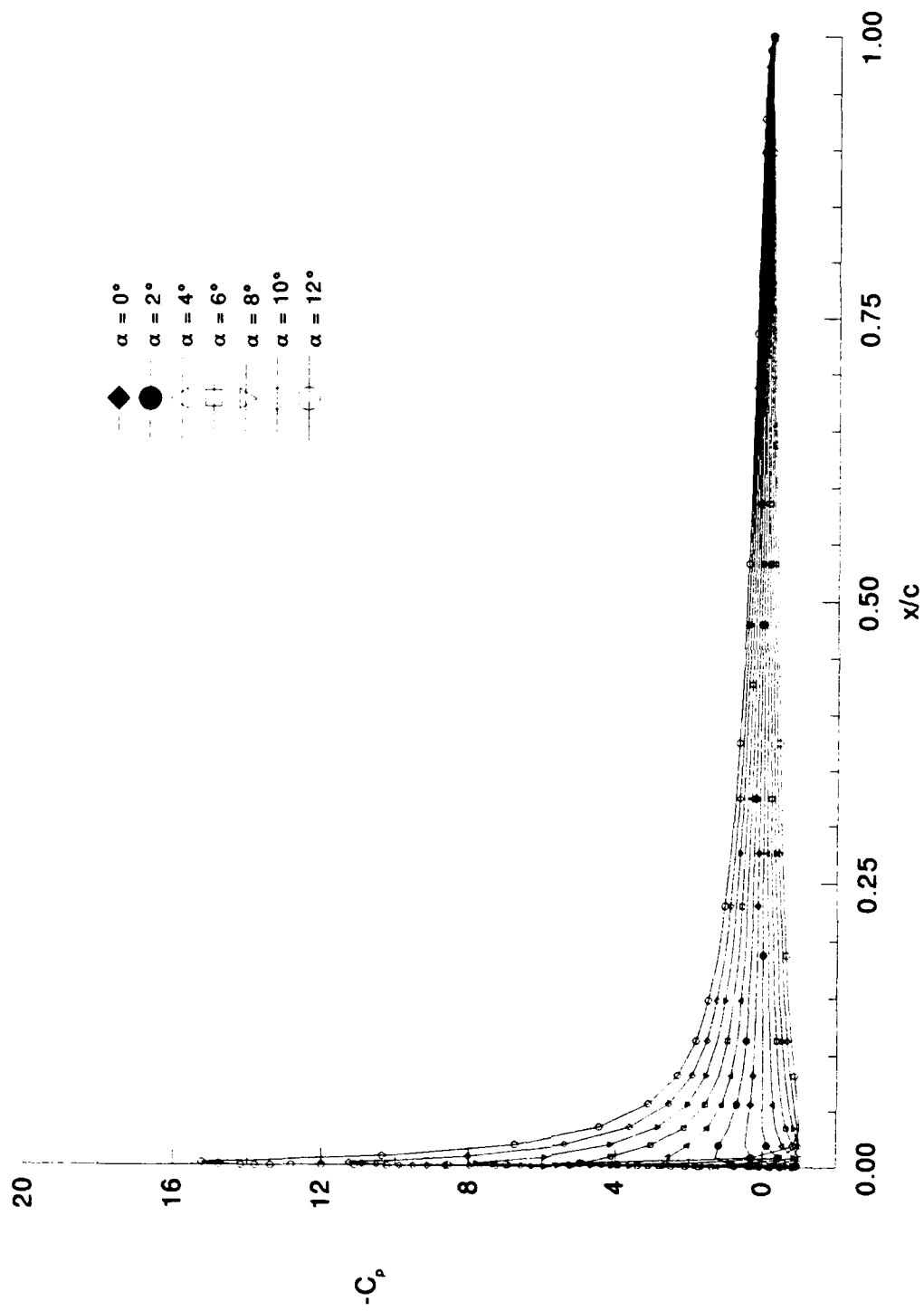


Figure 79. Pressure Distributions - T234 - Incompressible

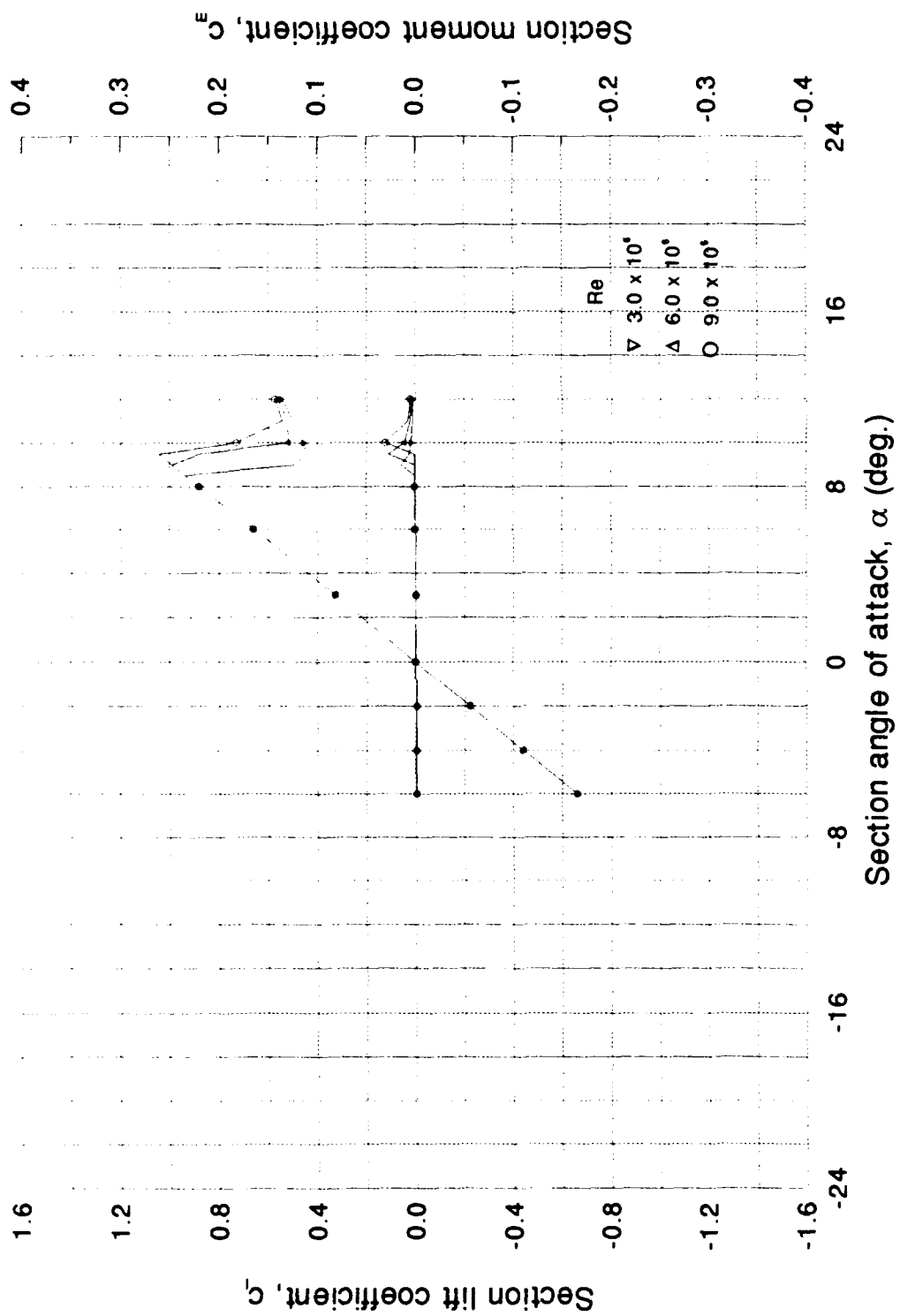


Figure 80. Airfoil T234 -  $C_l$ ,  $C_m$  vs  $\alpha$  Curves

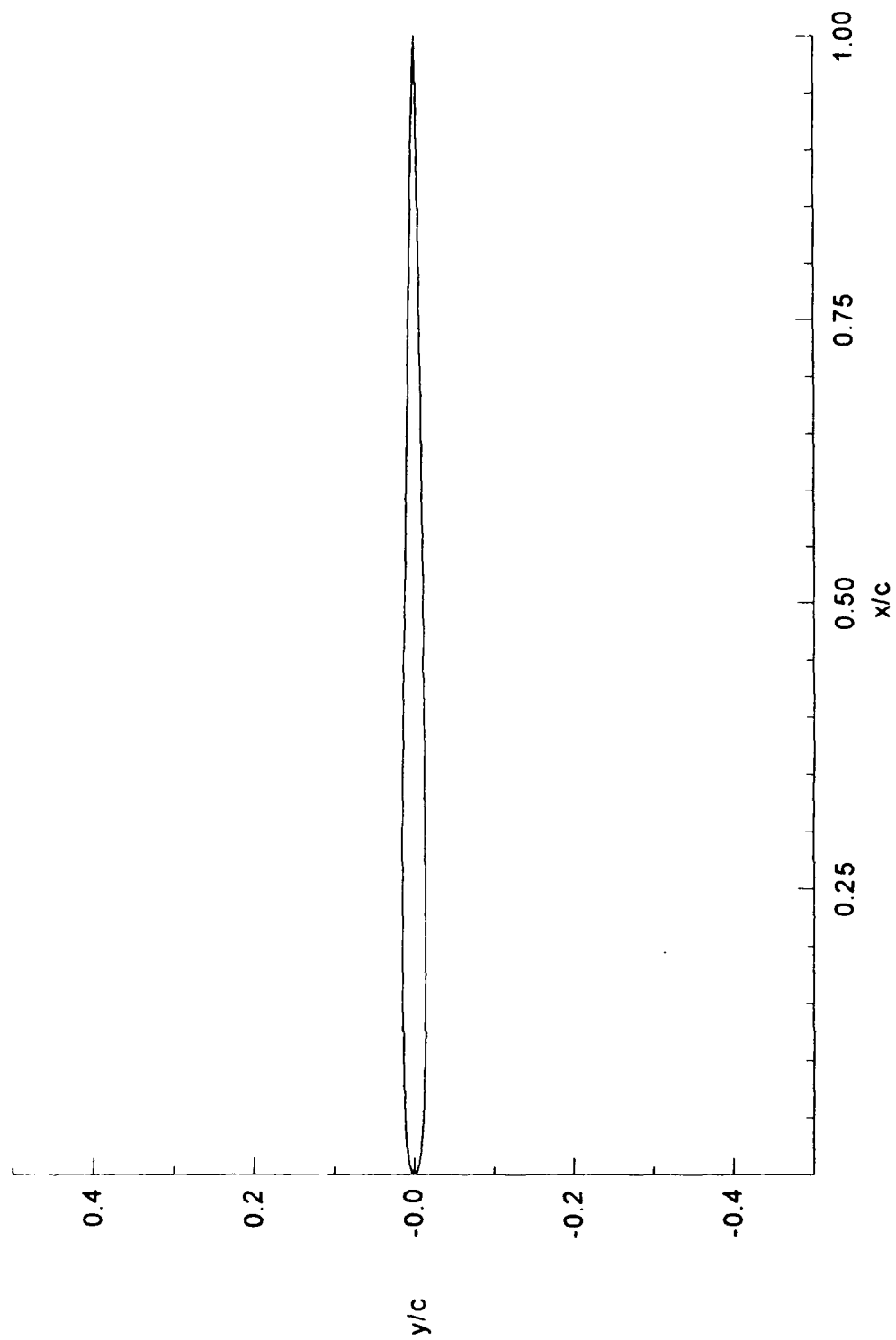


Figure 81. Airfoil T505 -  $t/c = 2.89\%$

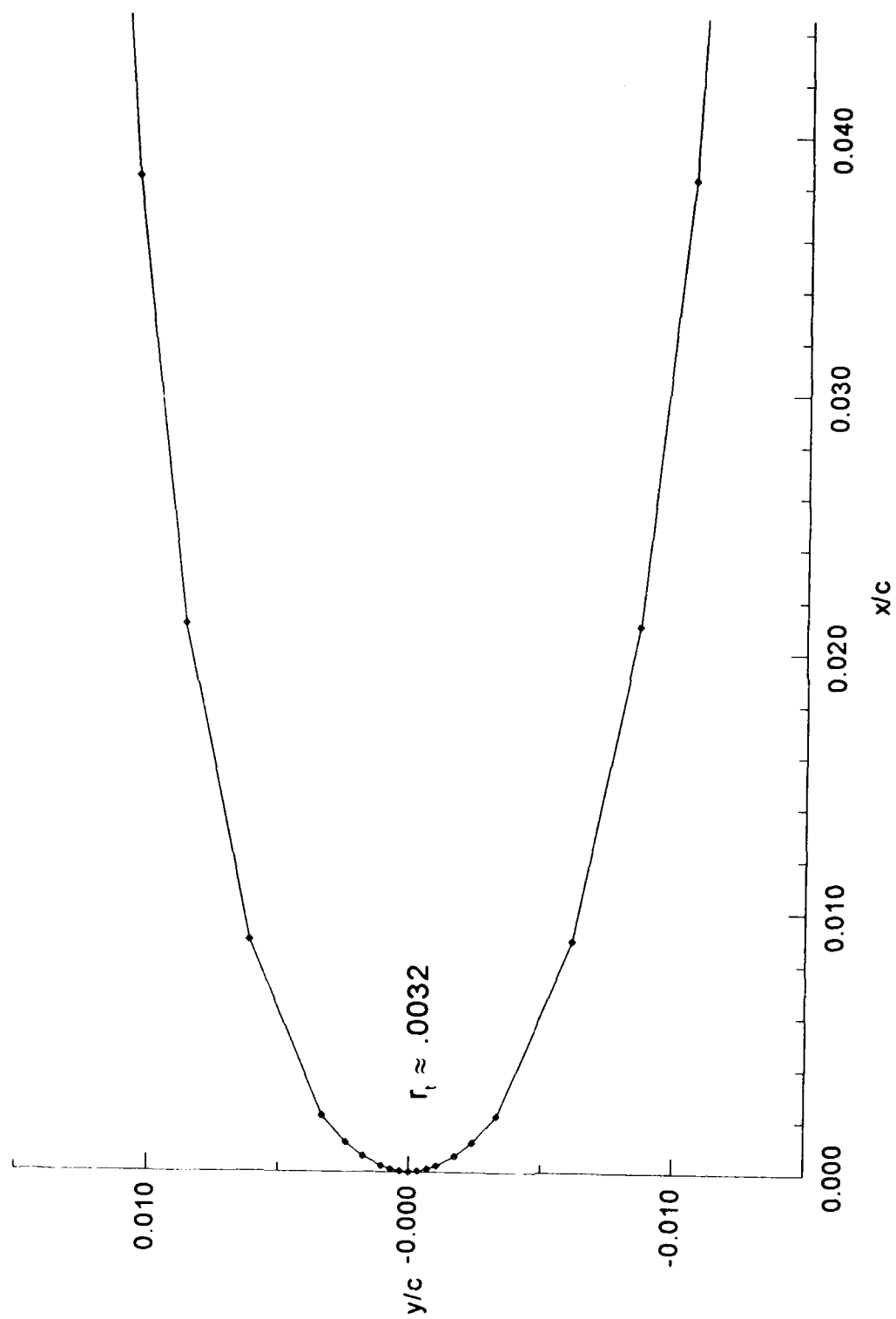


Figure 82. Airfoil T505 Leading-Edge -  $t/c = 2.89\%$

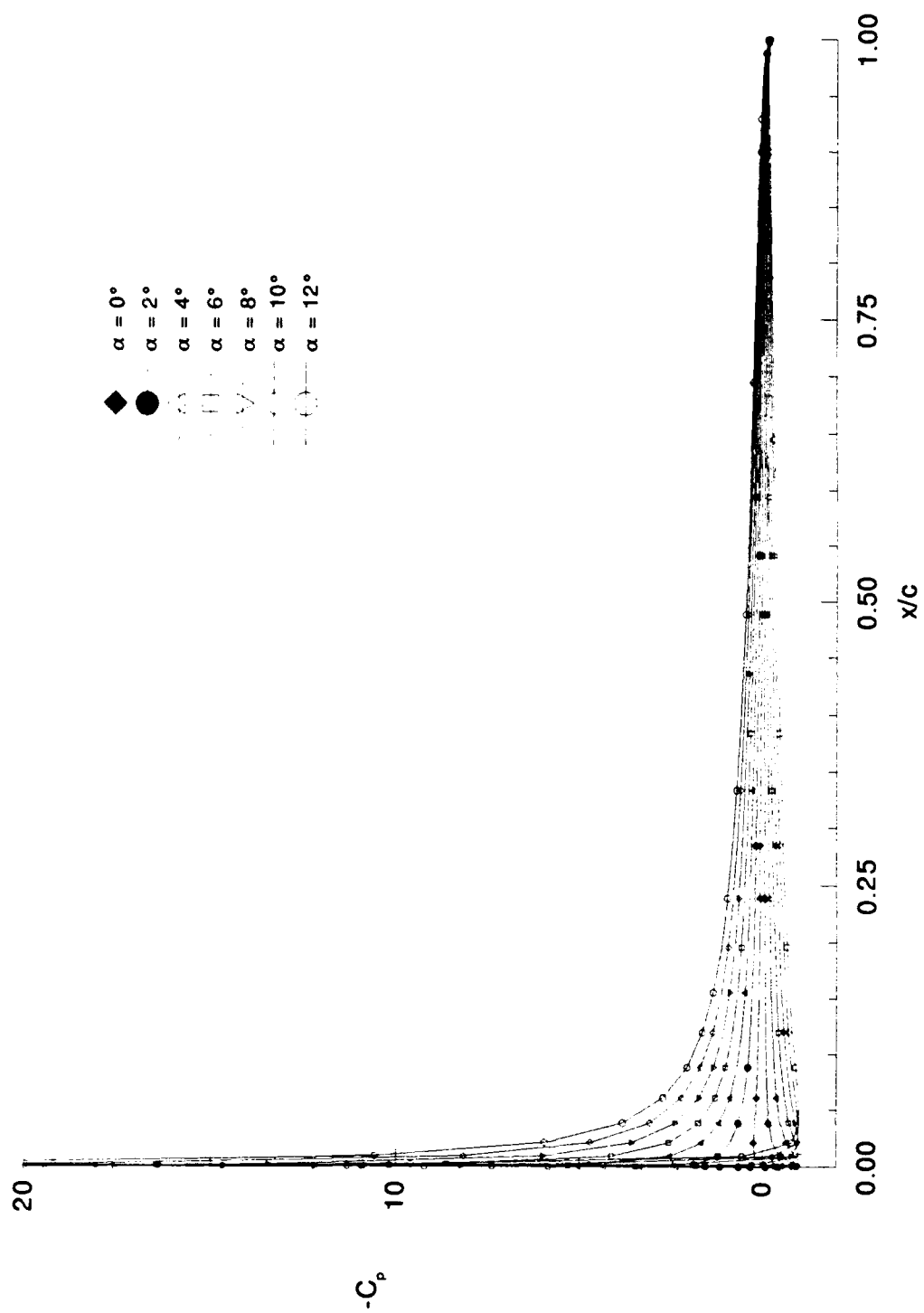


Figure 83. Pressure Distributions - T505 - Incompressible



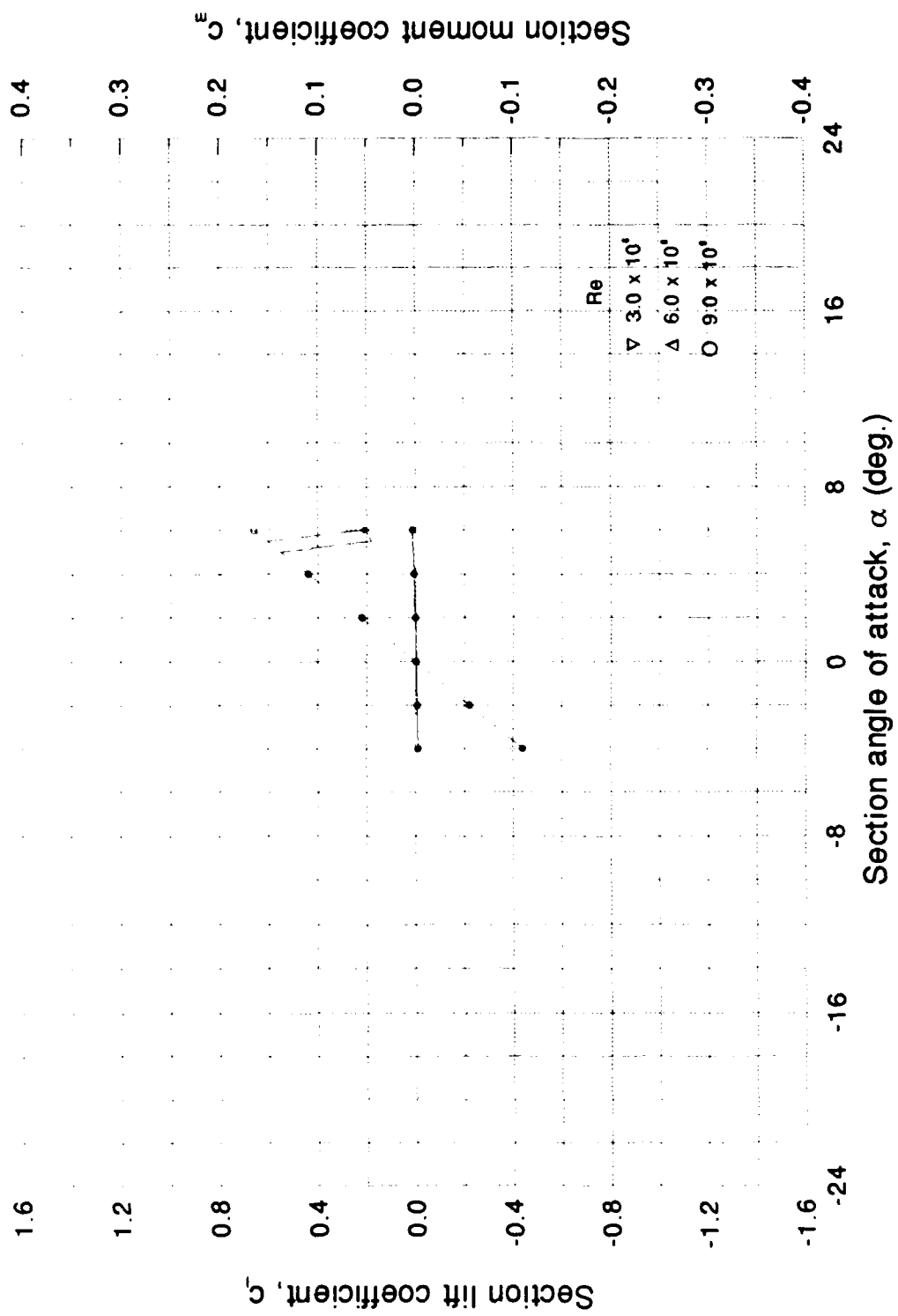


Figure 84. Airfoil T505 -  $C_l$ ,  $C_m$  vs  $\alpha$  Curves

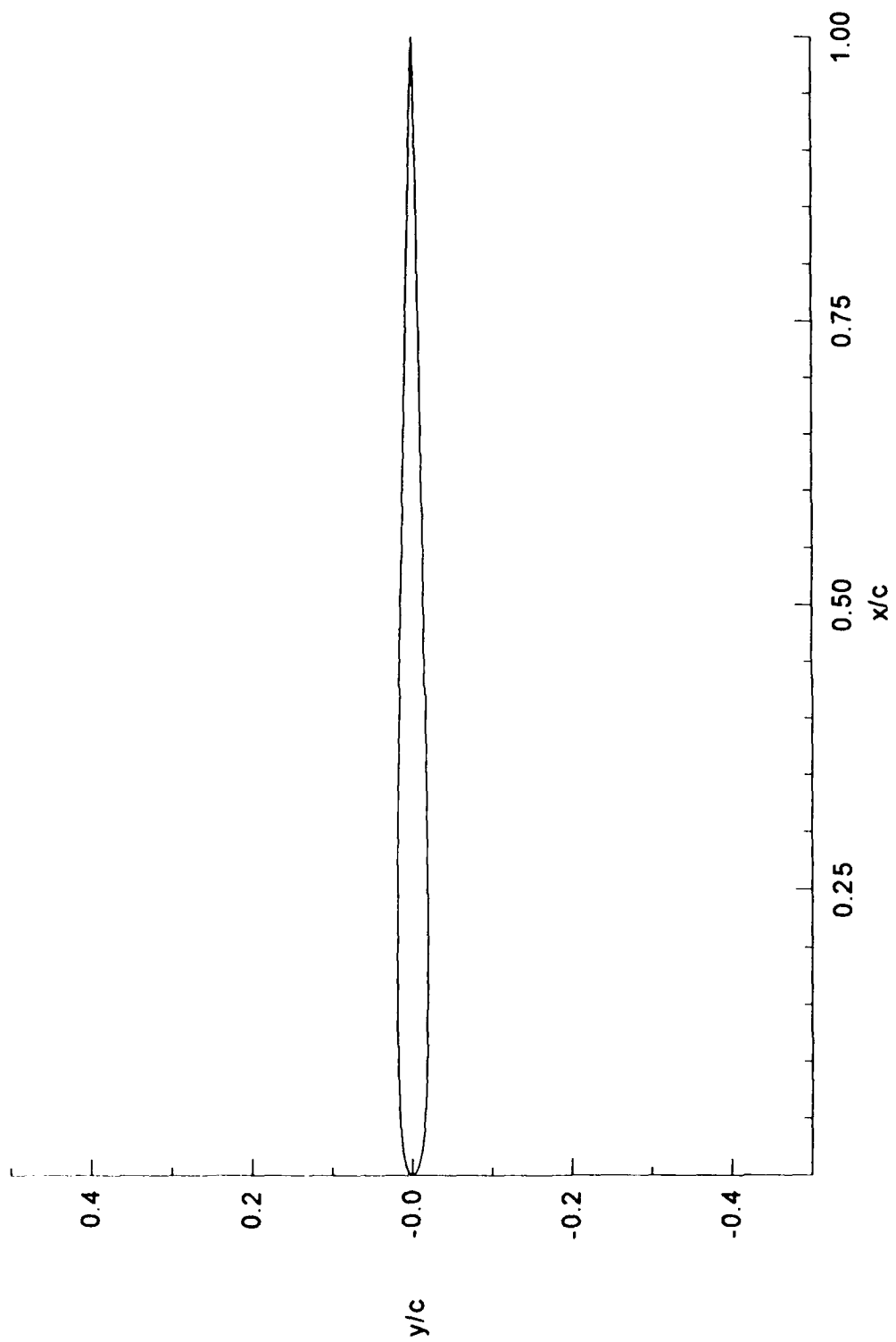


Figure 85. Airfoil T605 -  $t/c = 3.82\%$

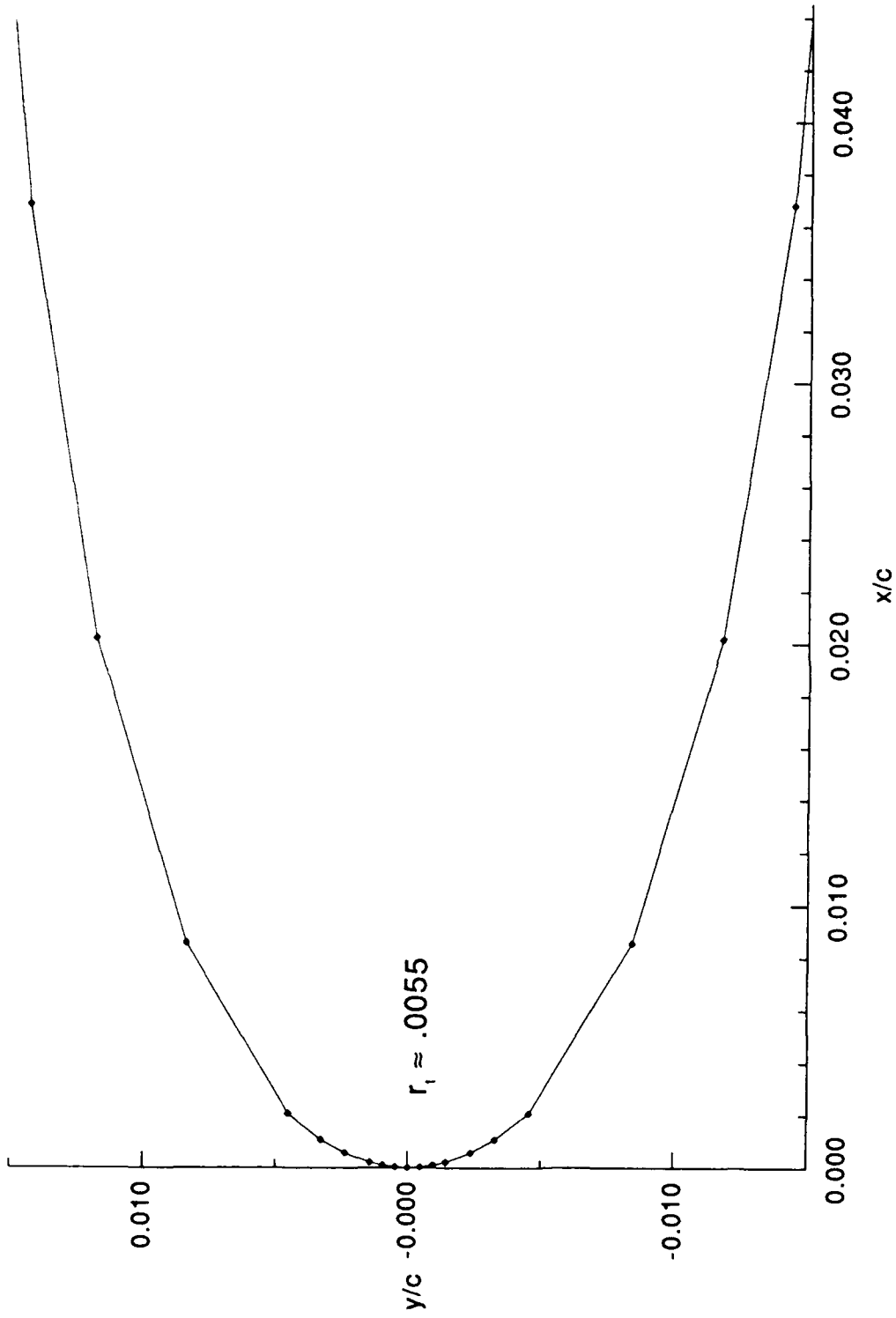


Figure 86. Airfoil T605 Leading-Edge -  $t/c = 3.82\%$

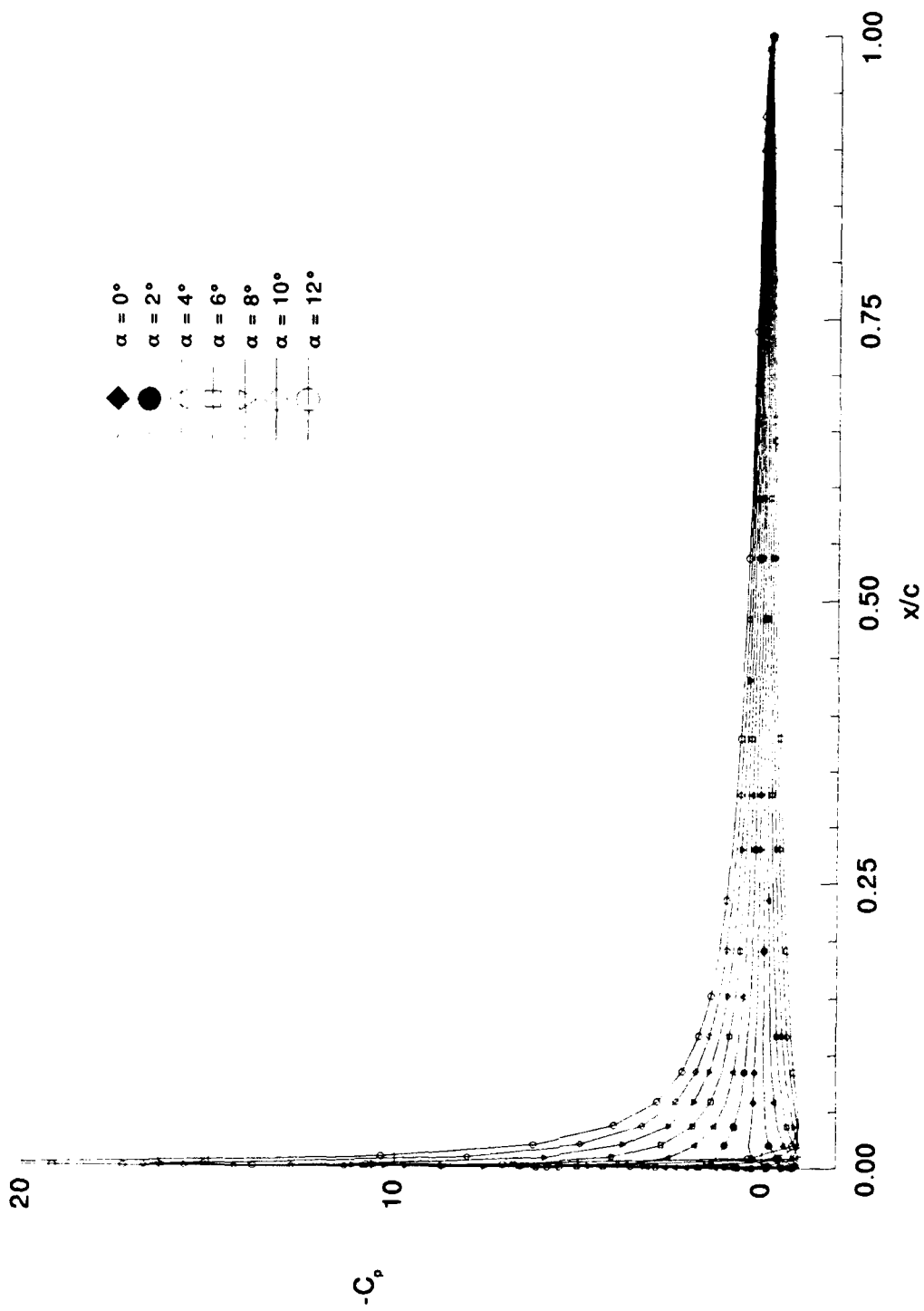


Figure 87. Pressure Distributions - T605 - Incompressible

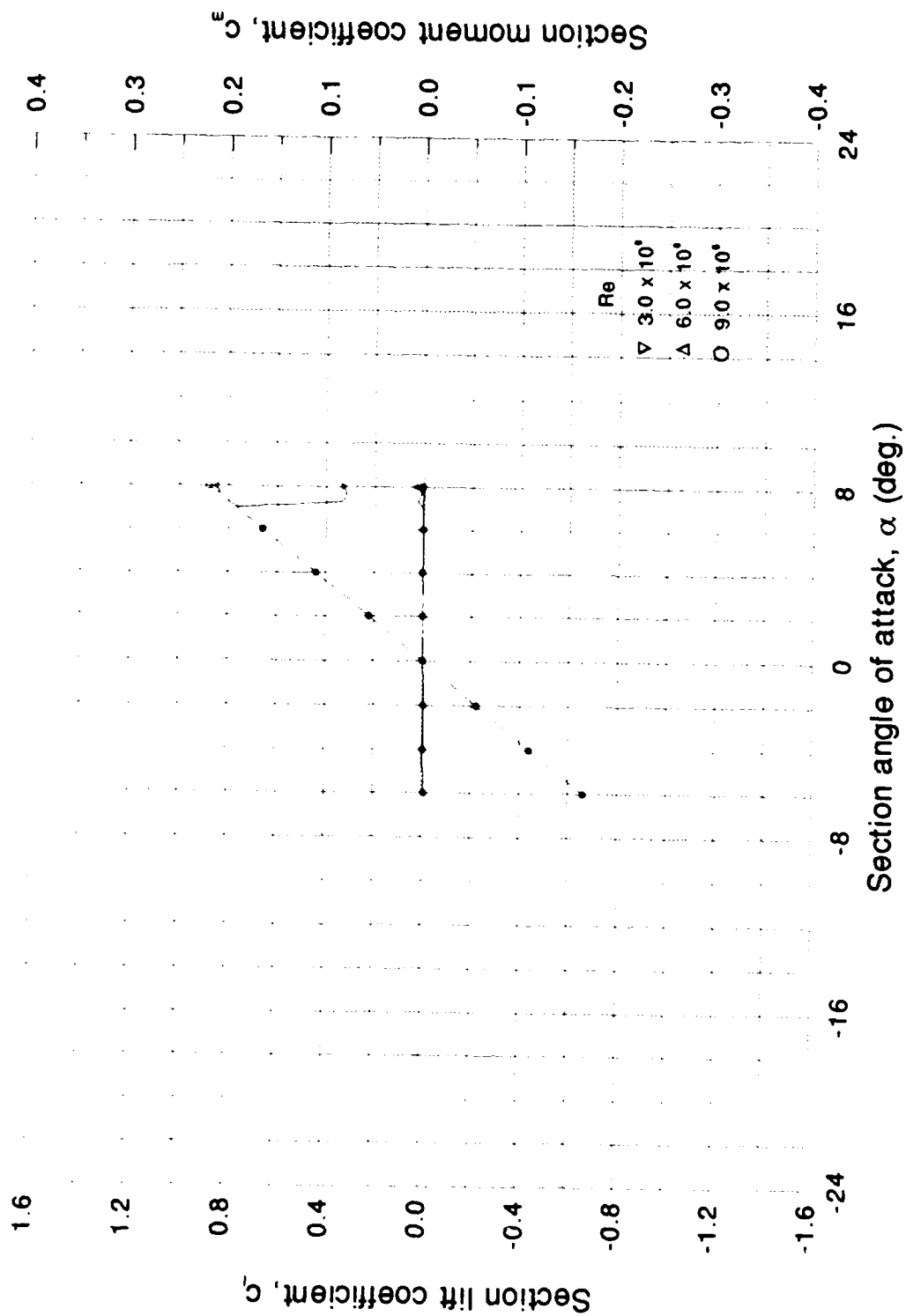


Figure 88. Airfoil T605 -  $C_l$ ,  $C_m$  vs  $\alpha$  Curves

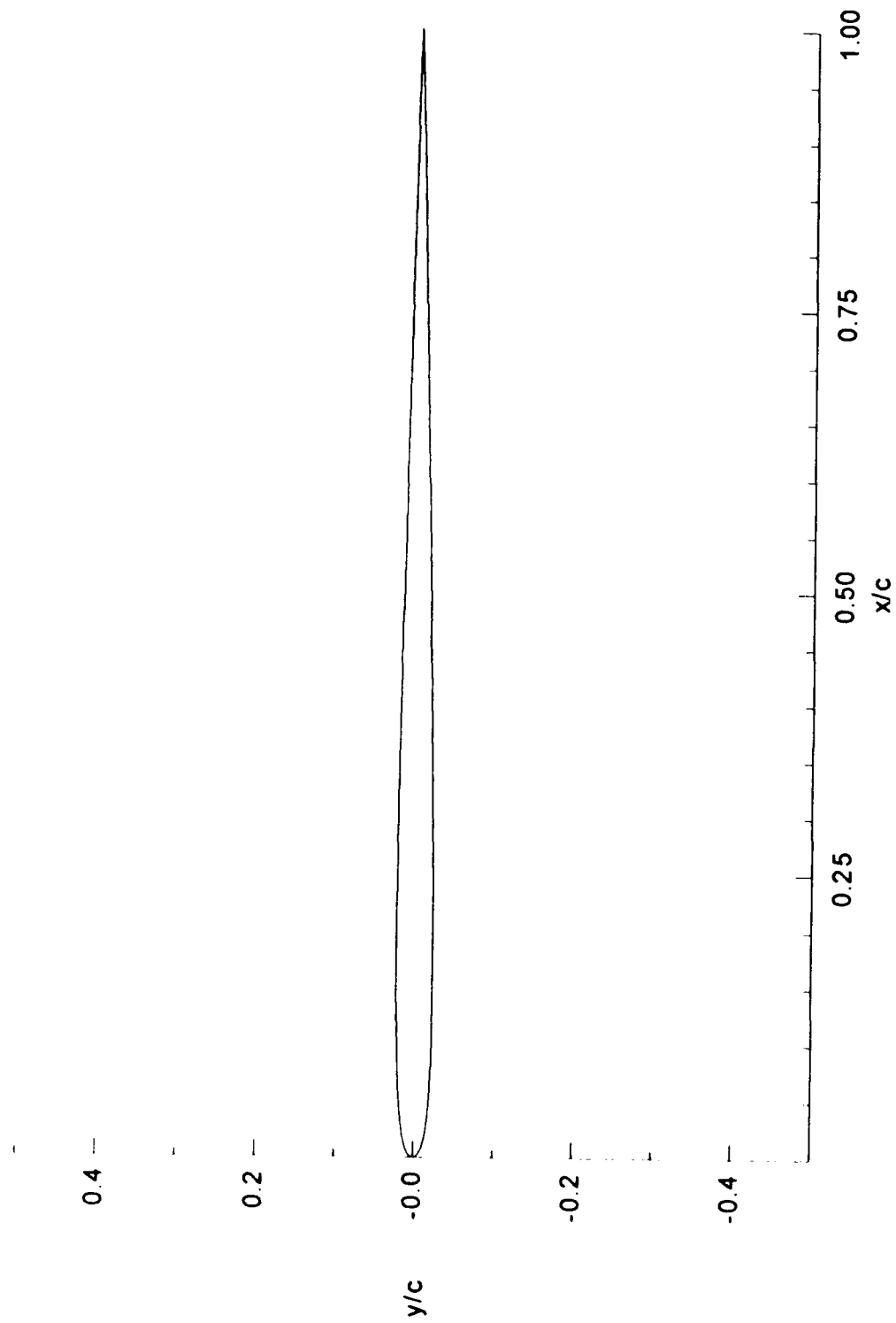


Figure 89. Airfoil T6605 -  $t/c = 4.58\%$

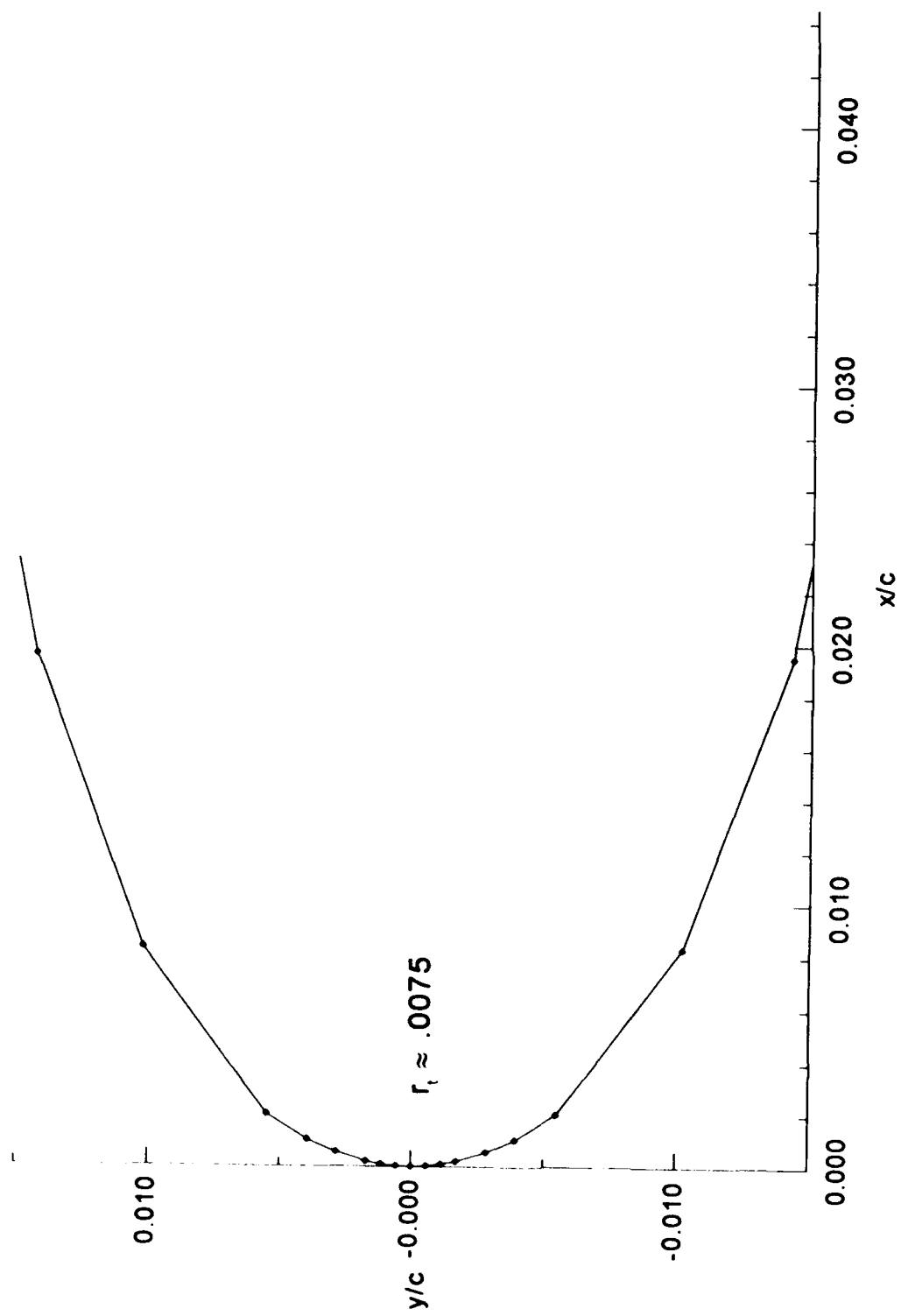


Figure 90. Airfoil T6605 Leading-Edge -  $t/c = 4.58\%$

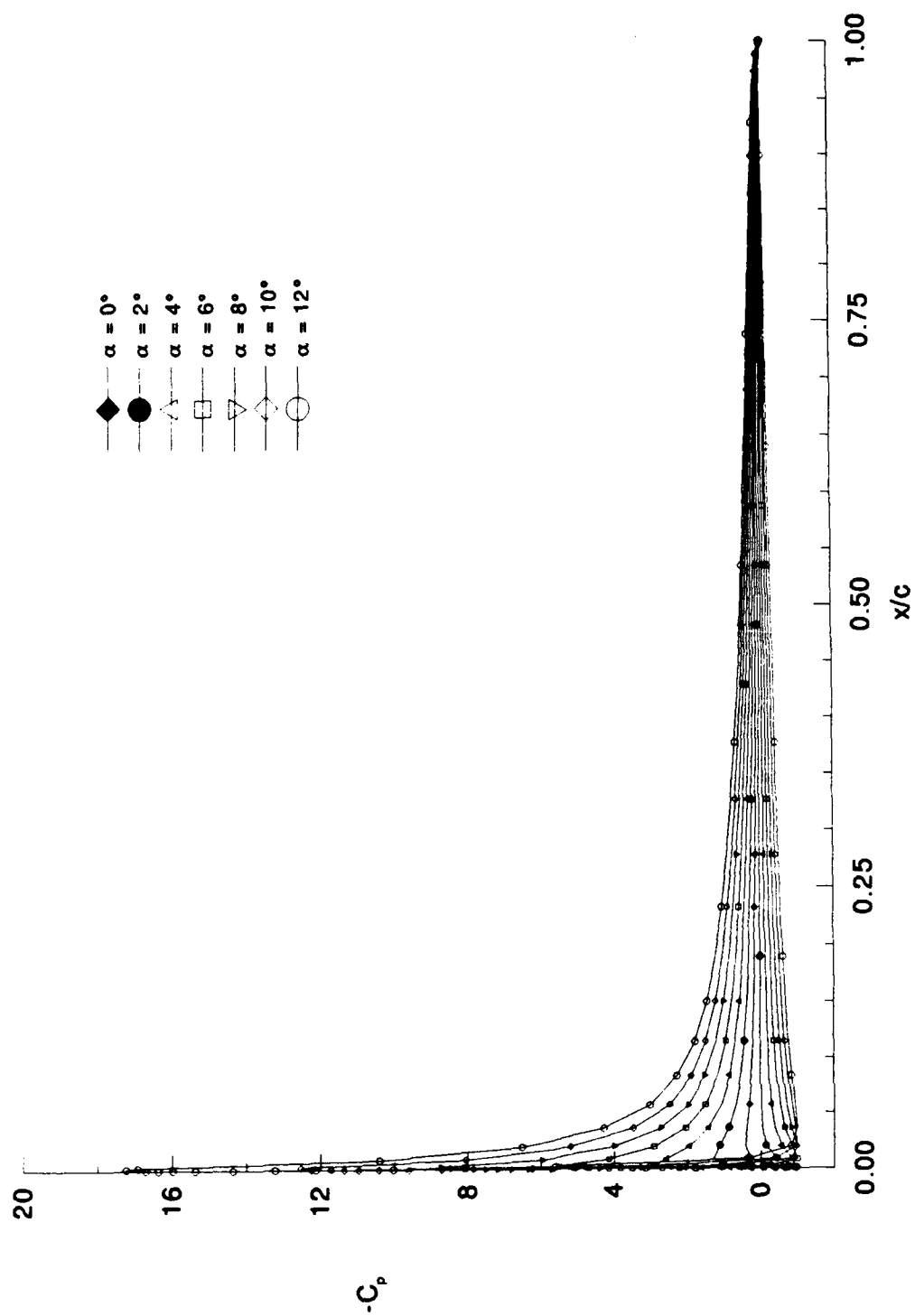


Figure 91. Pressure Distributions - T6605 - Incompressible



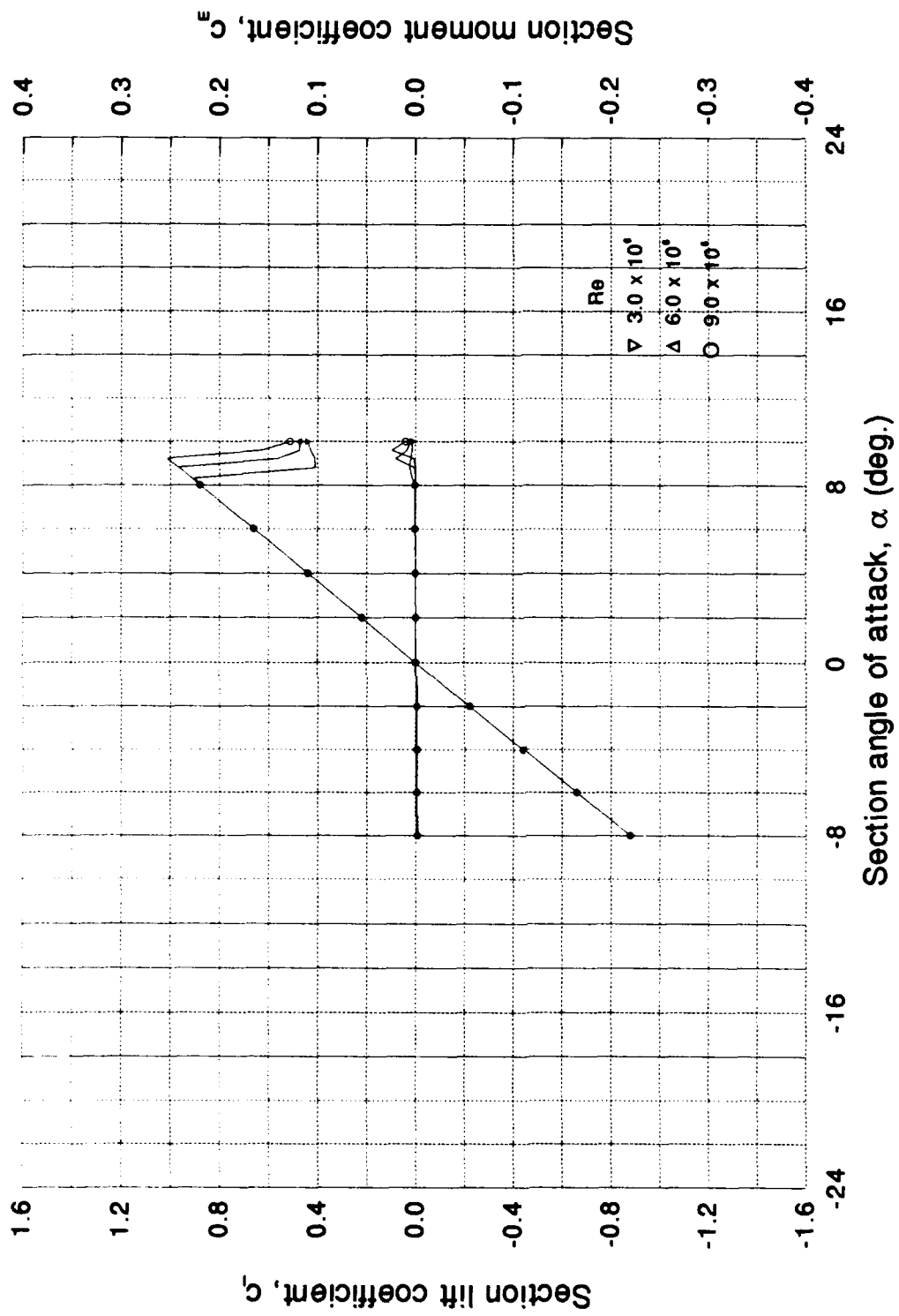


Figure 92. Airfoil T6605 -  $C_l$ ,  $C_m$  vs  $\alpha$  Curves

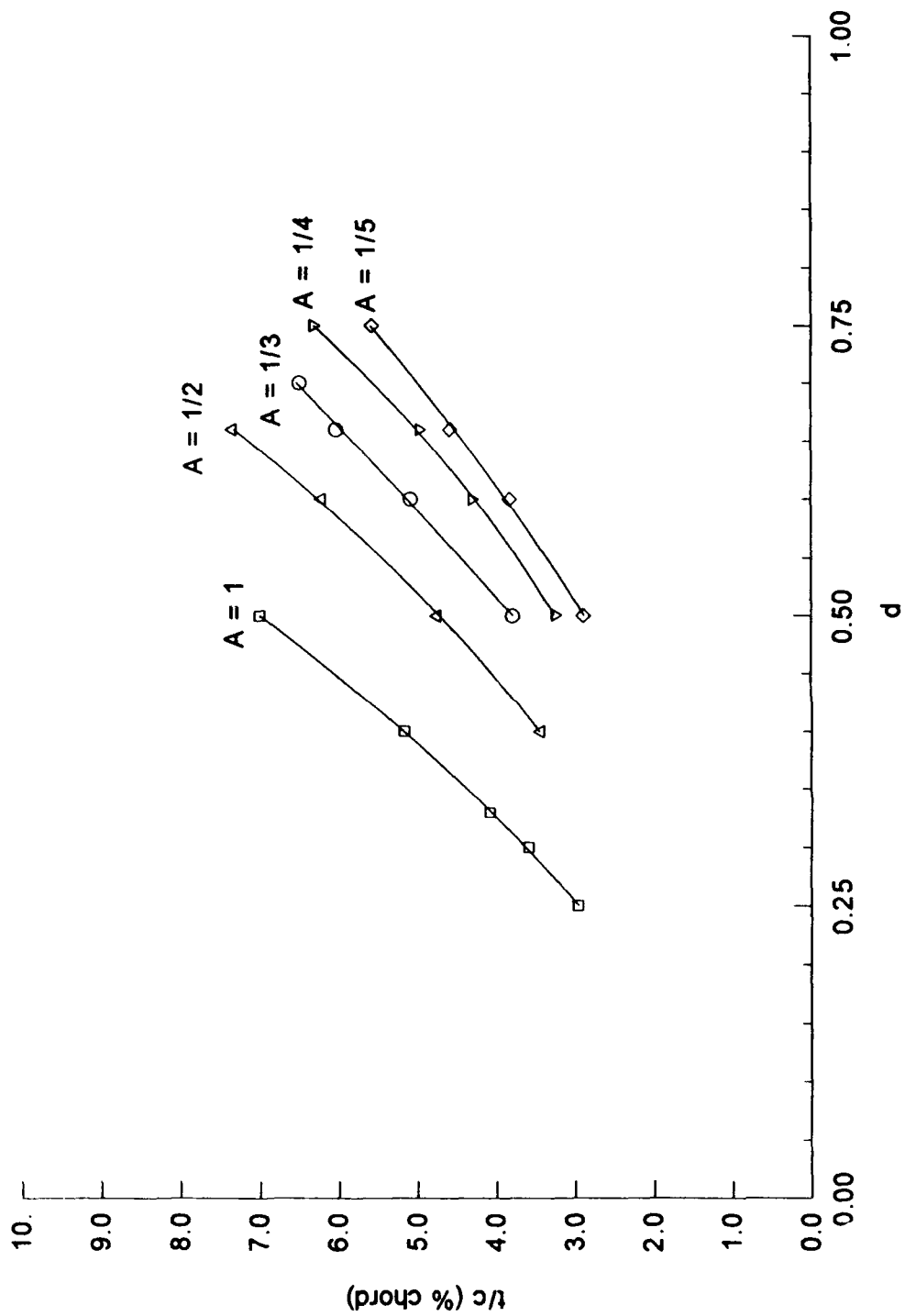


Figure 93. Thickness-to-Chord Ratio vs  $d$

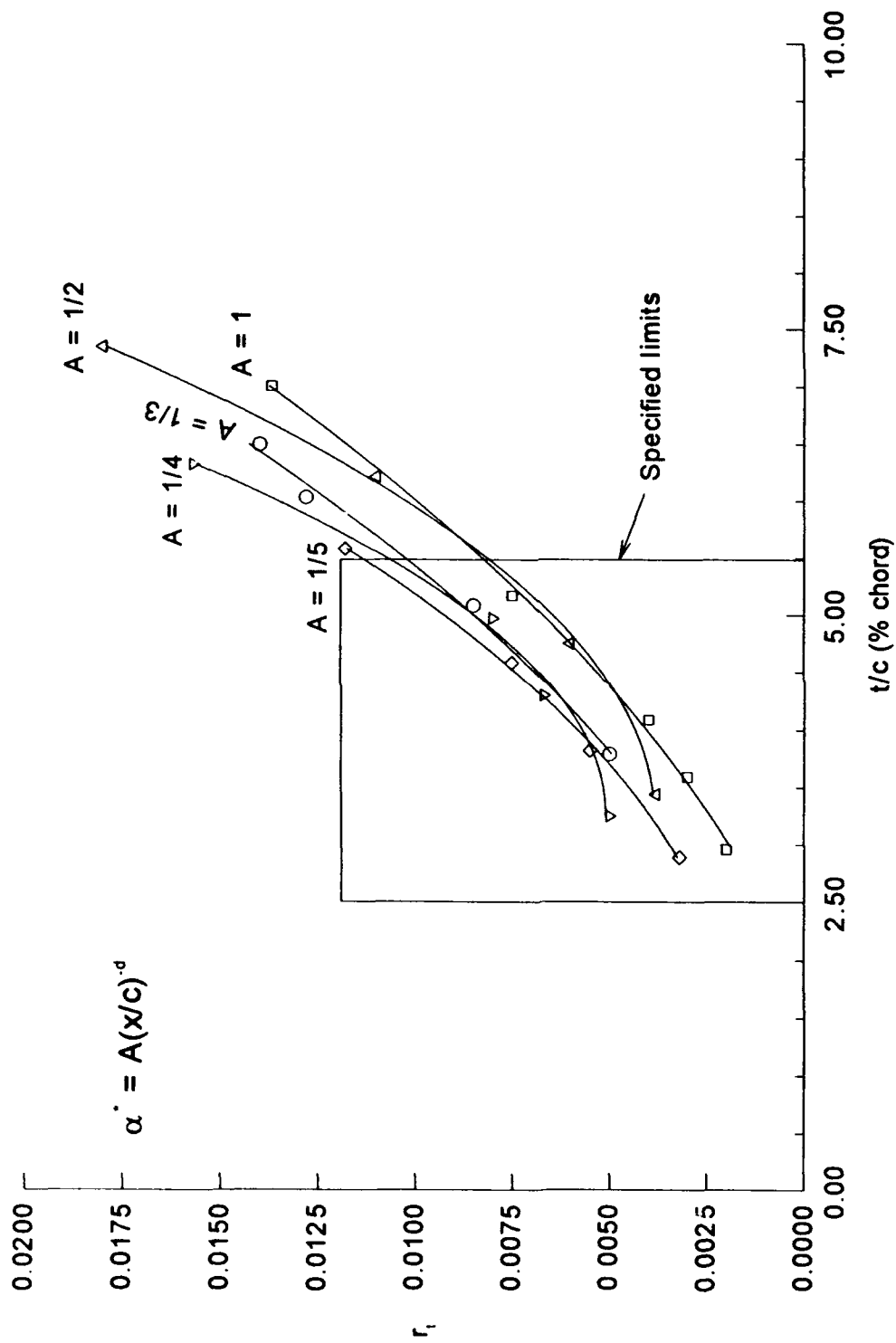


Figure 94. Leading-Edge Radius vs Thickness-to-Chord Ratio

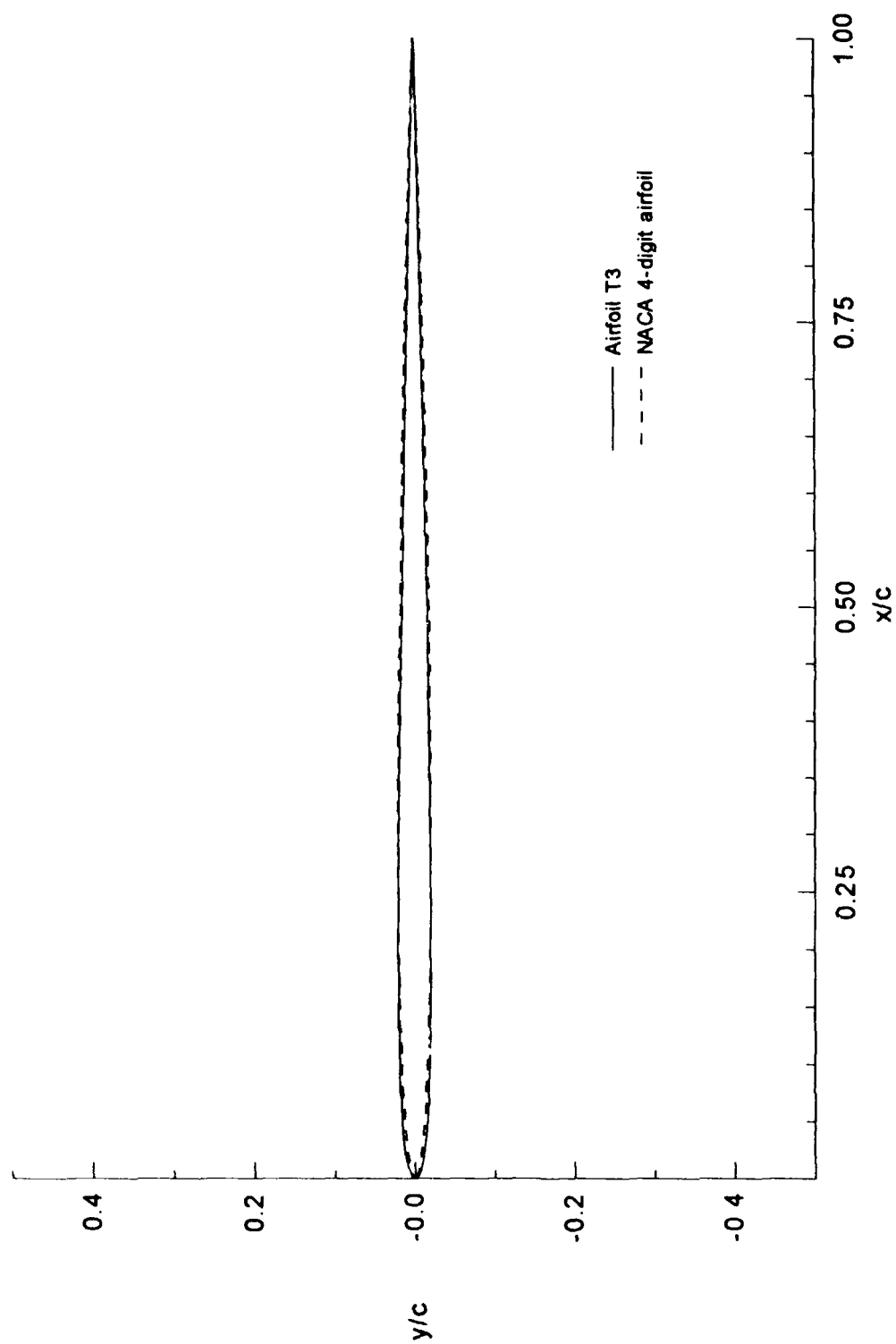


Figure 95. Airfoil T3 vs NACA 4-digit airfoil -  $t/c = 4.09\%$

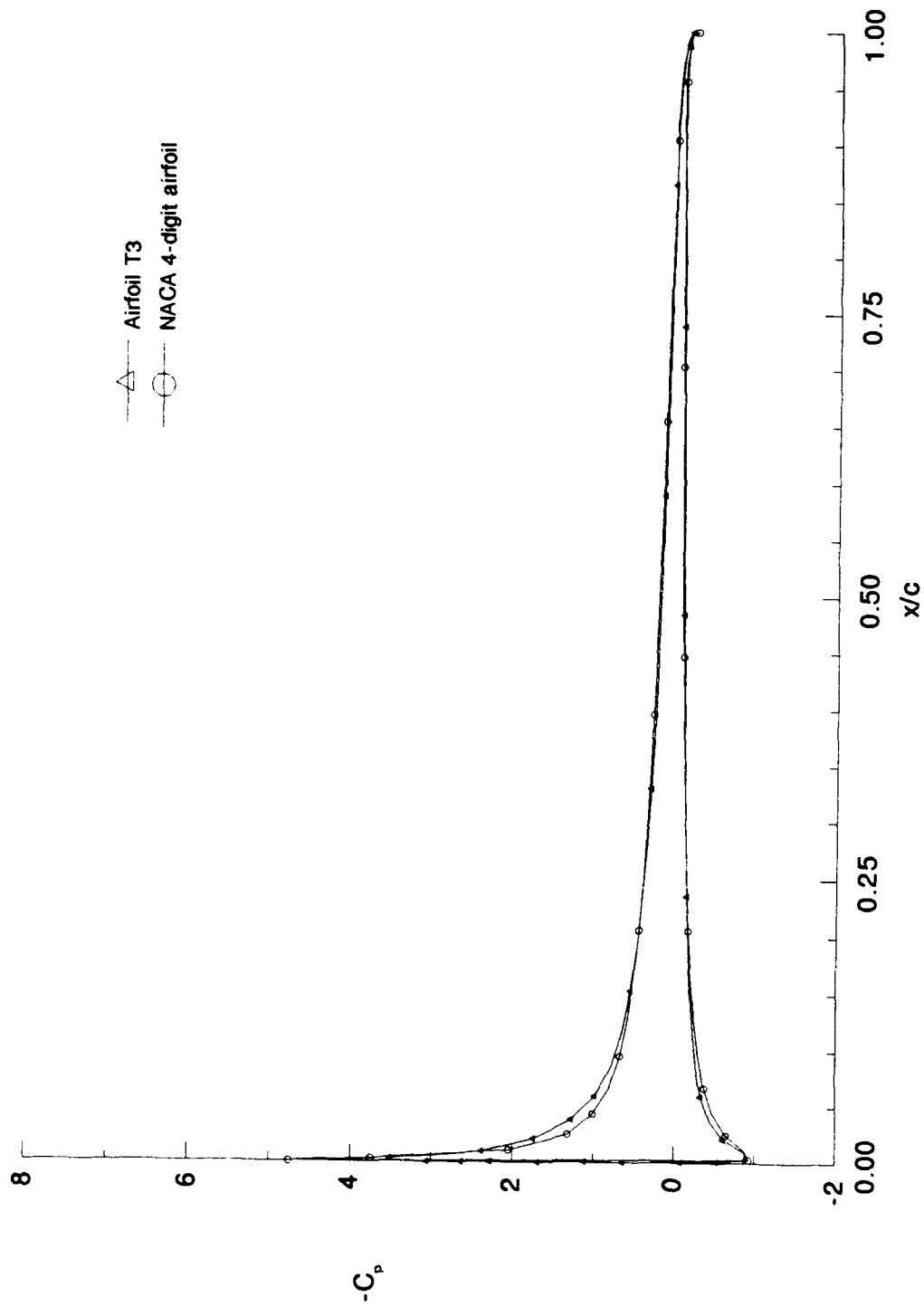


Figure 96. Airfoil T3 vs NACA 4-Digit Airfoil Pressure Distribution -  $\alpha = 4^\circ$  - Incompressible

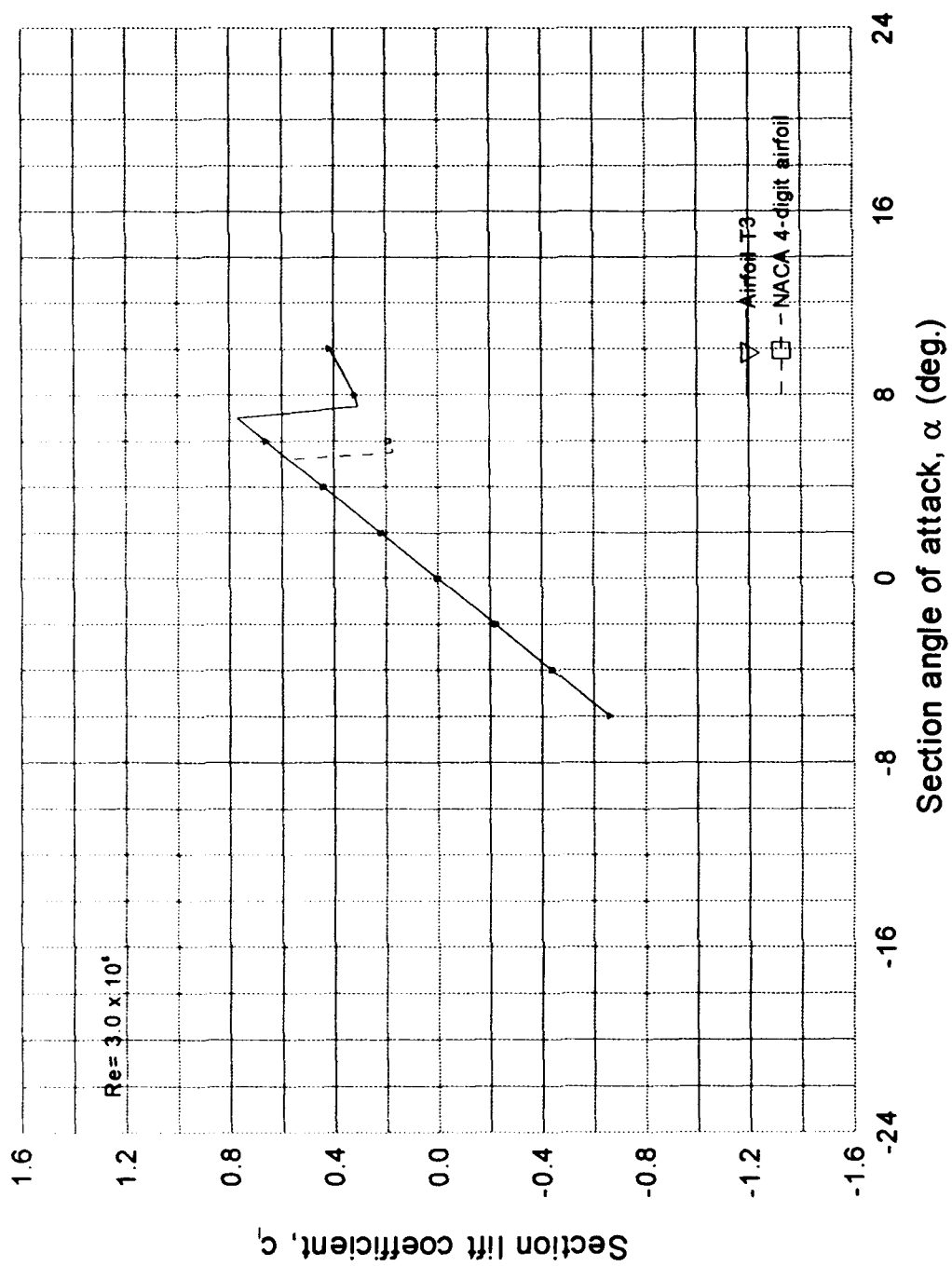


Figure 97.  $C_l(\alpha)$  Curve - Airfoil T3 vs NACA 4-Digit Airfoil

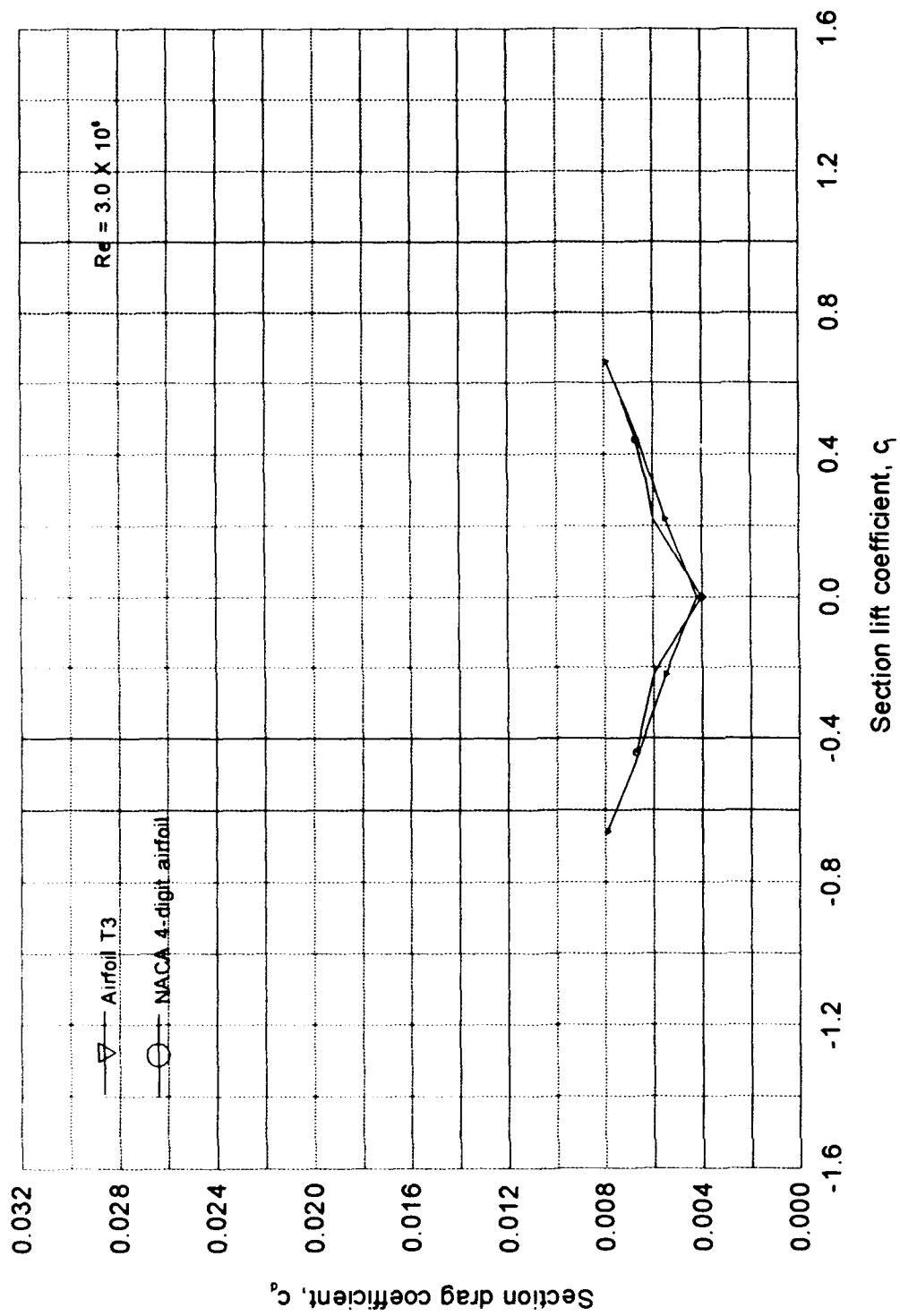


Figure 98.  $C_l - C_d$  plot - Airfoil T3 vs NACA 4-digit airfoil  
 $t/c = 4.09\%$

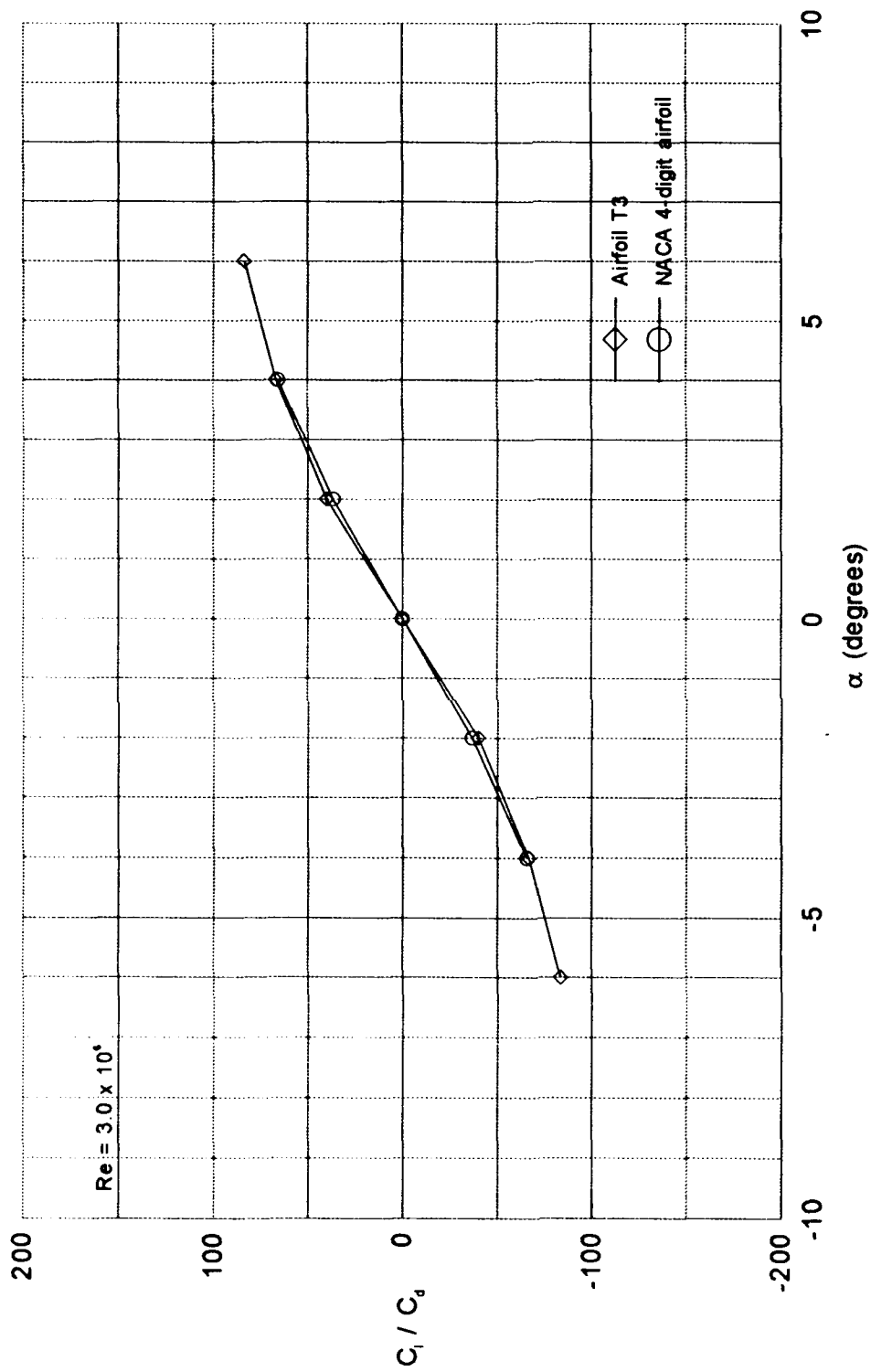


Figure 99. Lift-drag ratio - Airfoil T3 vs NACA 4-digit airfoil



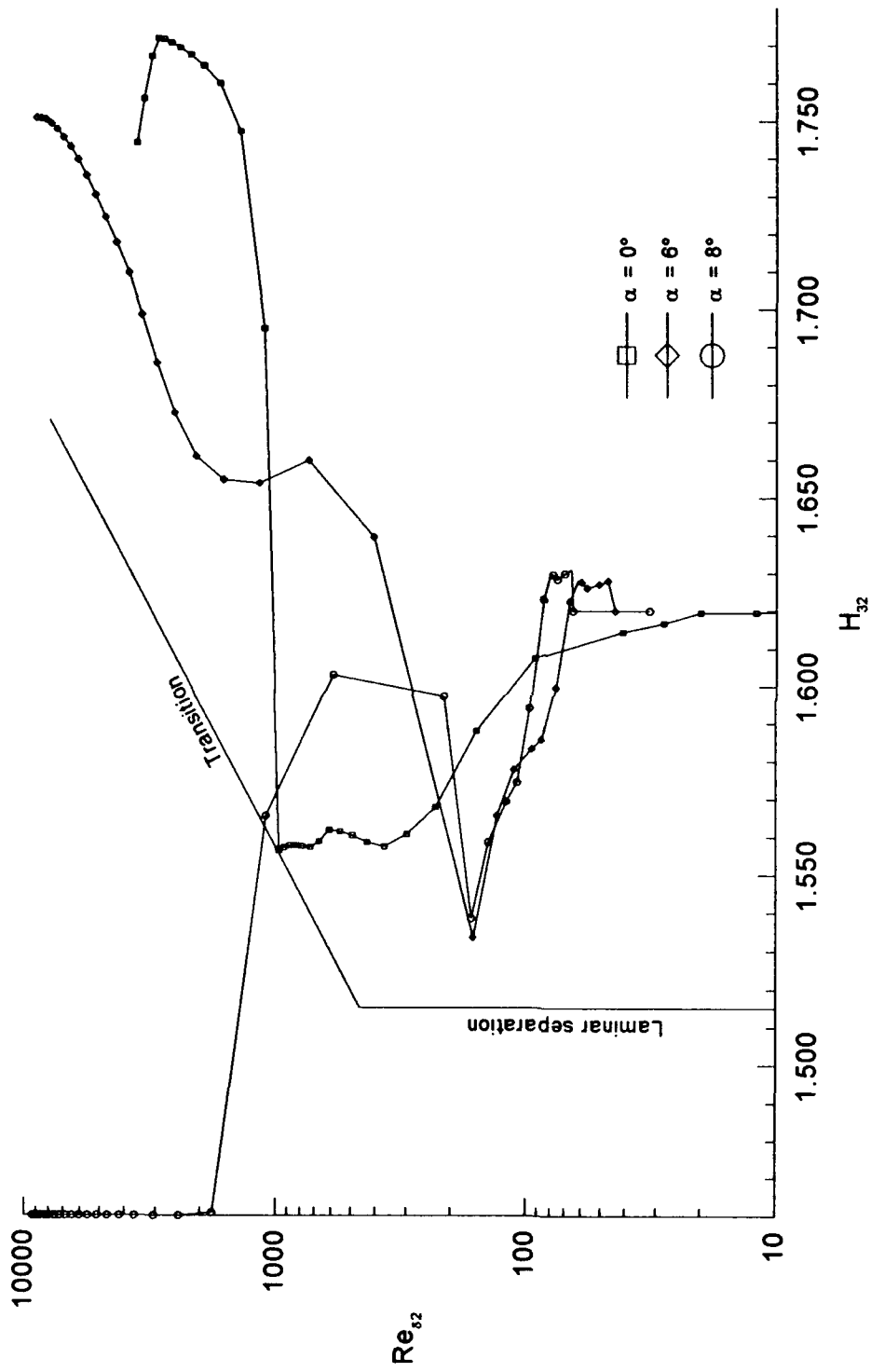


Figure 100. Boundary-Layer Development - Upper Surface - Airfoil T3  
 $Re = 3.0 \times 10^6$

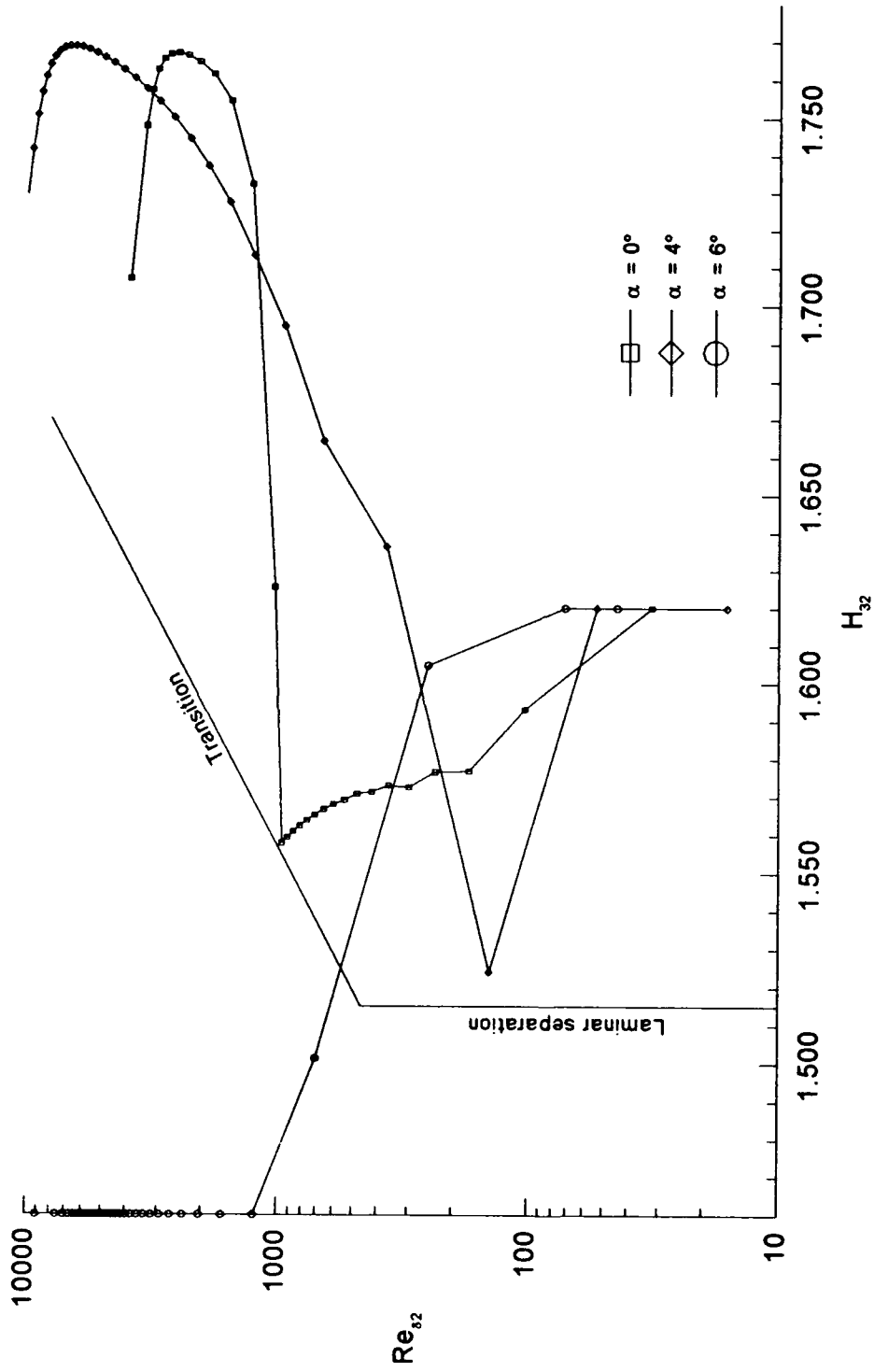


Figure 101 Boundary-Layer Development - Upper Surface - NACA 4-Digit Airfoil  
 $Re = 3.0 \times 10^6$

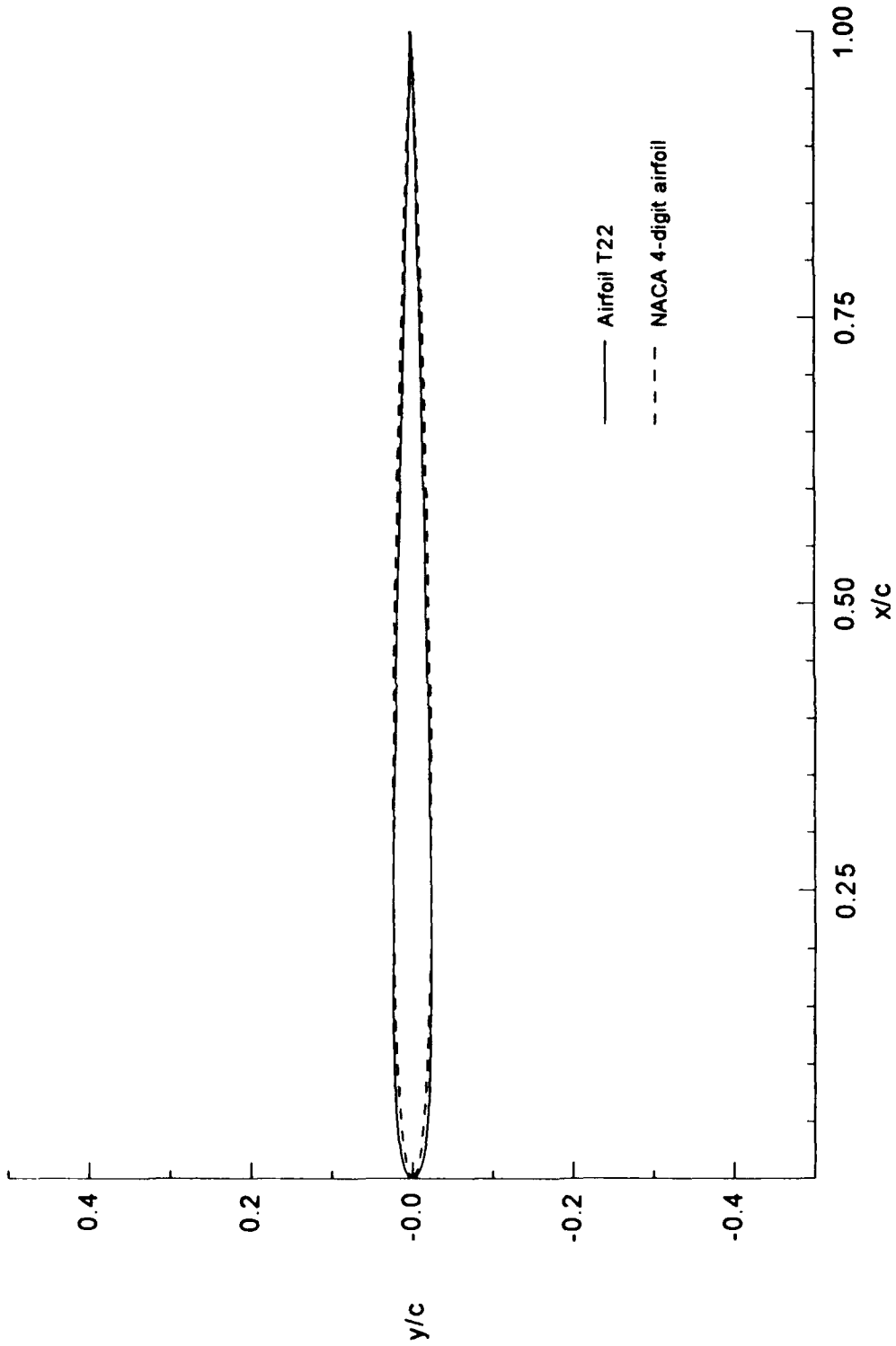


Figure 102. Comparison of NACA 4-Digit Airfoil vs Airfoil T22

$t/c = 4.75\%$

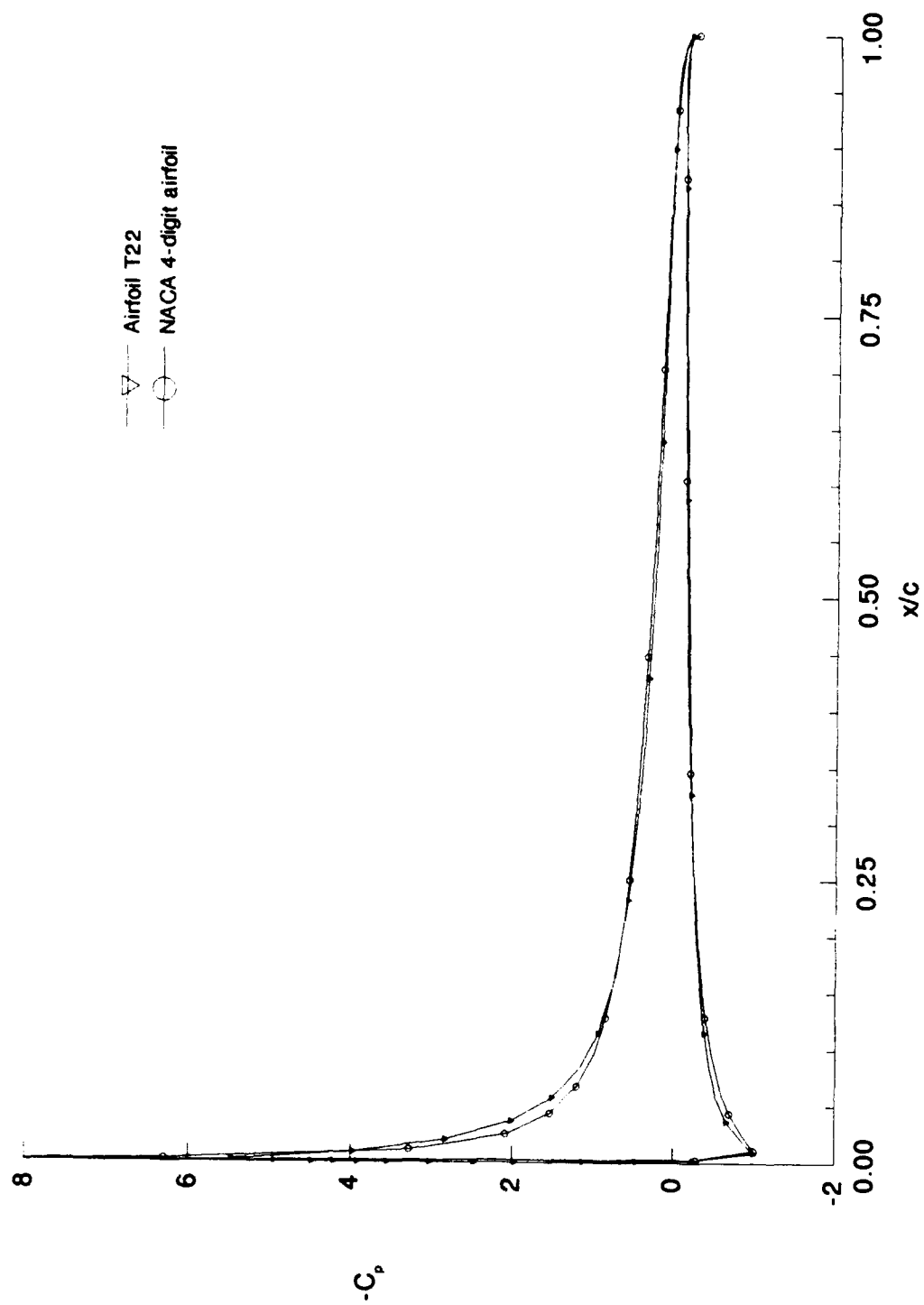


Figure 103. Airfoil T22 vs NACA 4-Digit Airfoil Pressure Distribution

$\alpha = 6^\circ$  - Incompressible

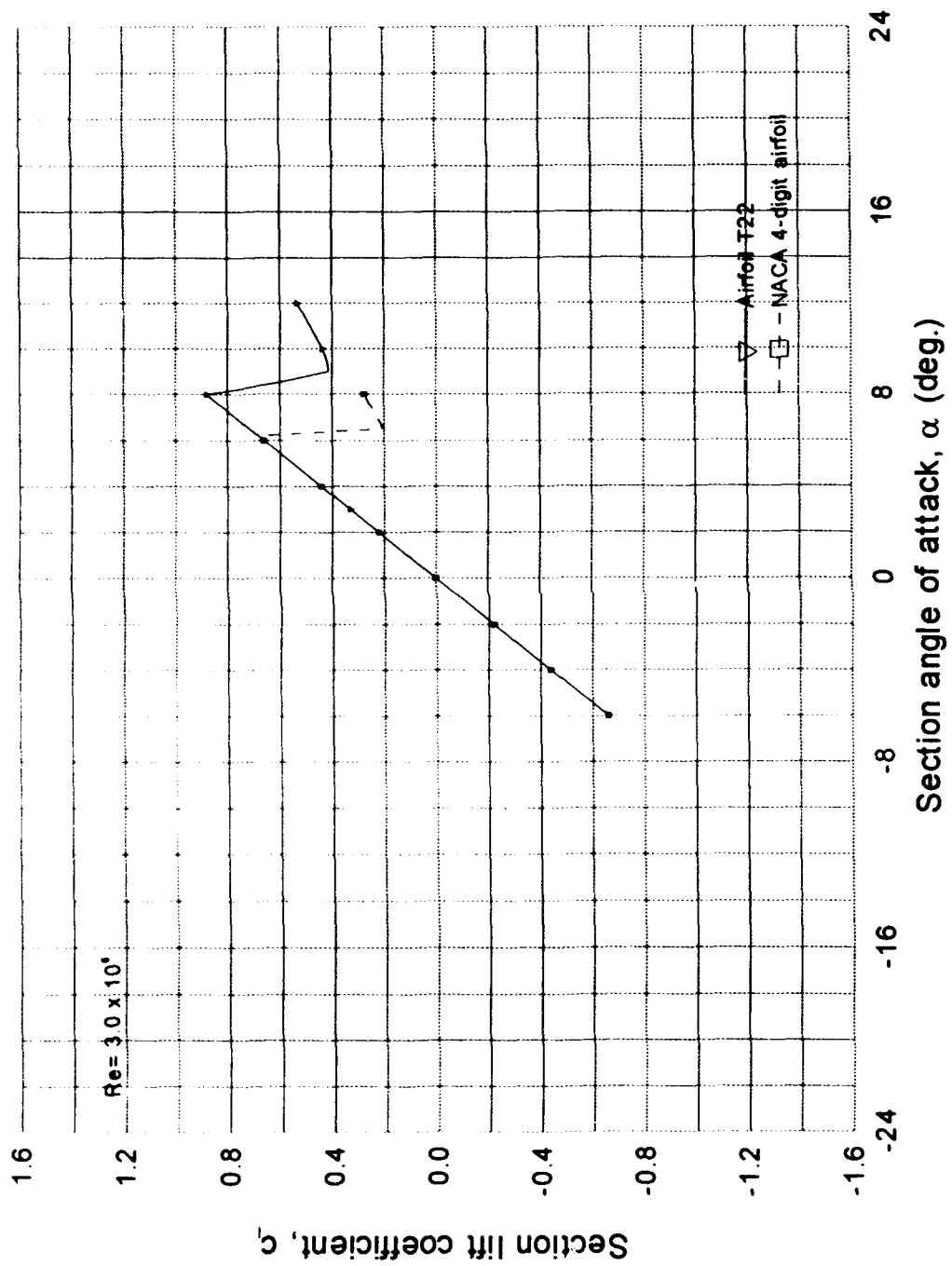


Figure 104.  $C_l(\alpha)$  Curve - Airfoil T22 vs NACA 4-Digit Airfoil

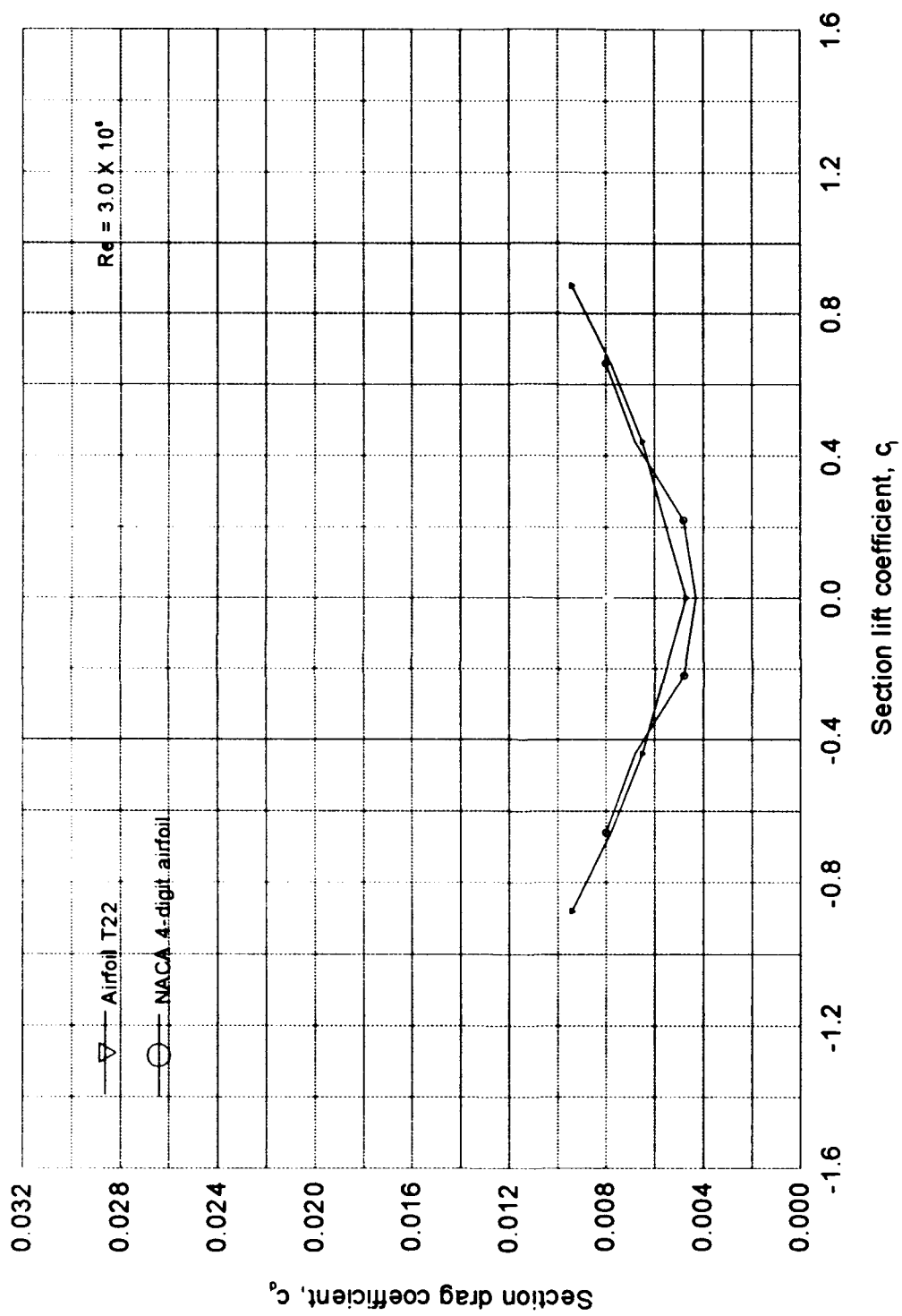


Figure 105.  $C_l - C_d$  plot - Airfoil T22 vs NACA 4-digit airfoil  
 $t/c = 4.75\%$

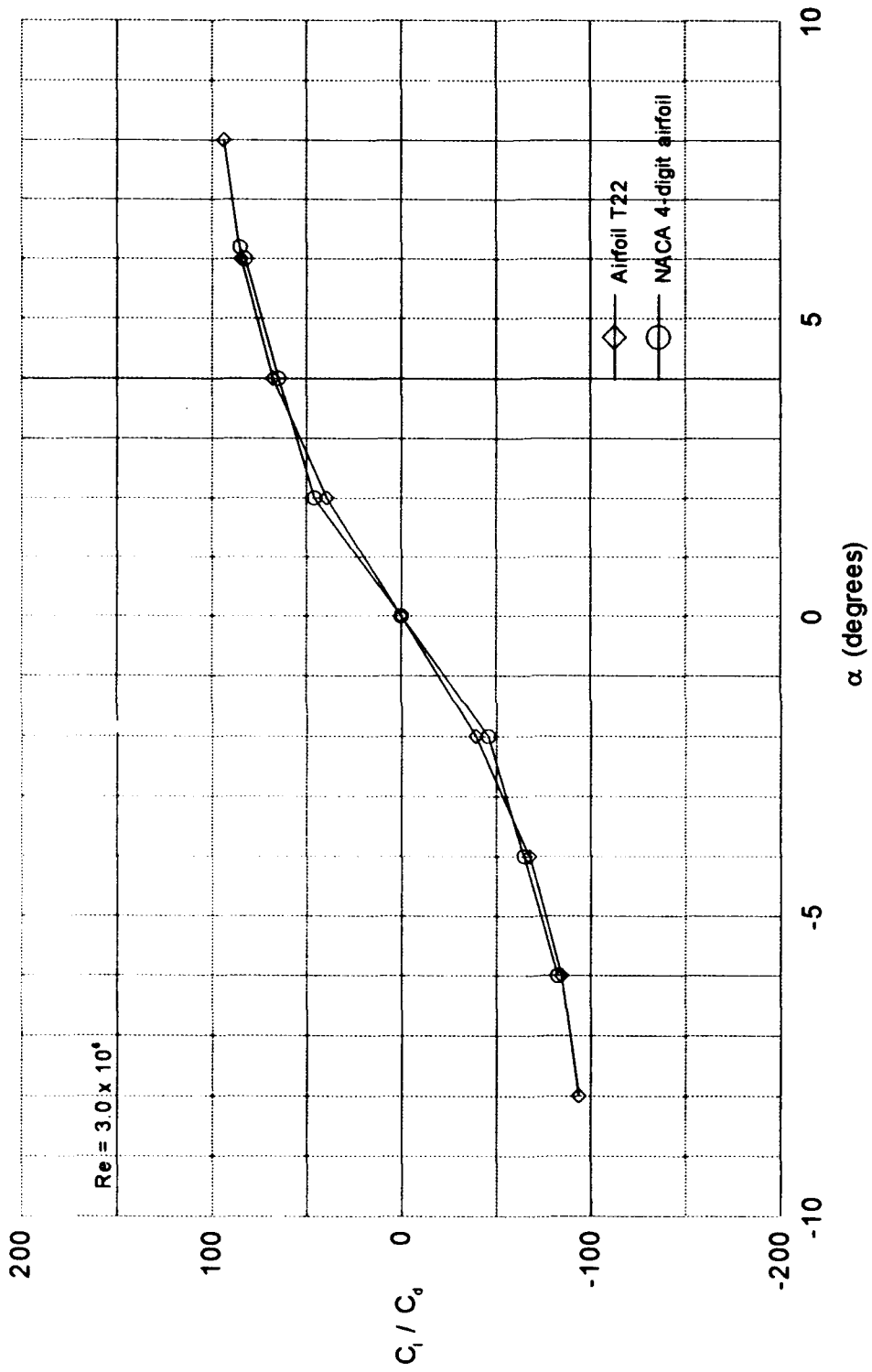


Figure 106. Lift-drag ratio - Airfoil T22 vs NACA 4-digit airfoil

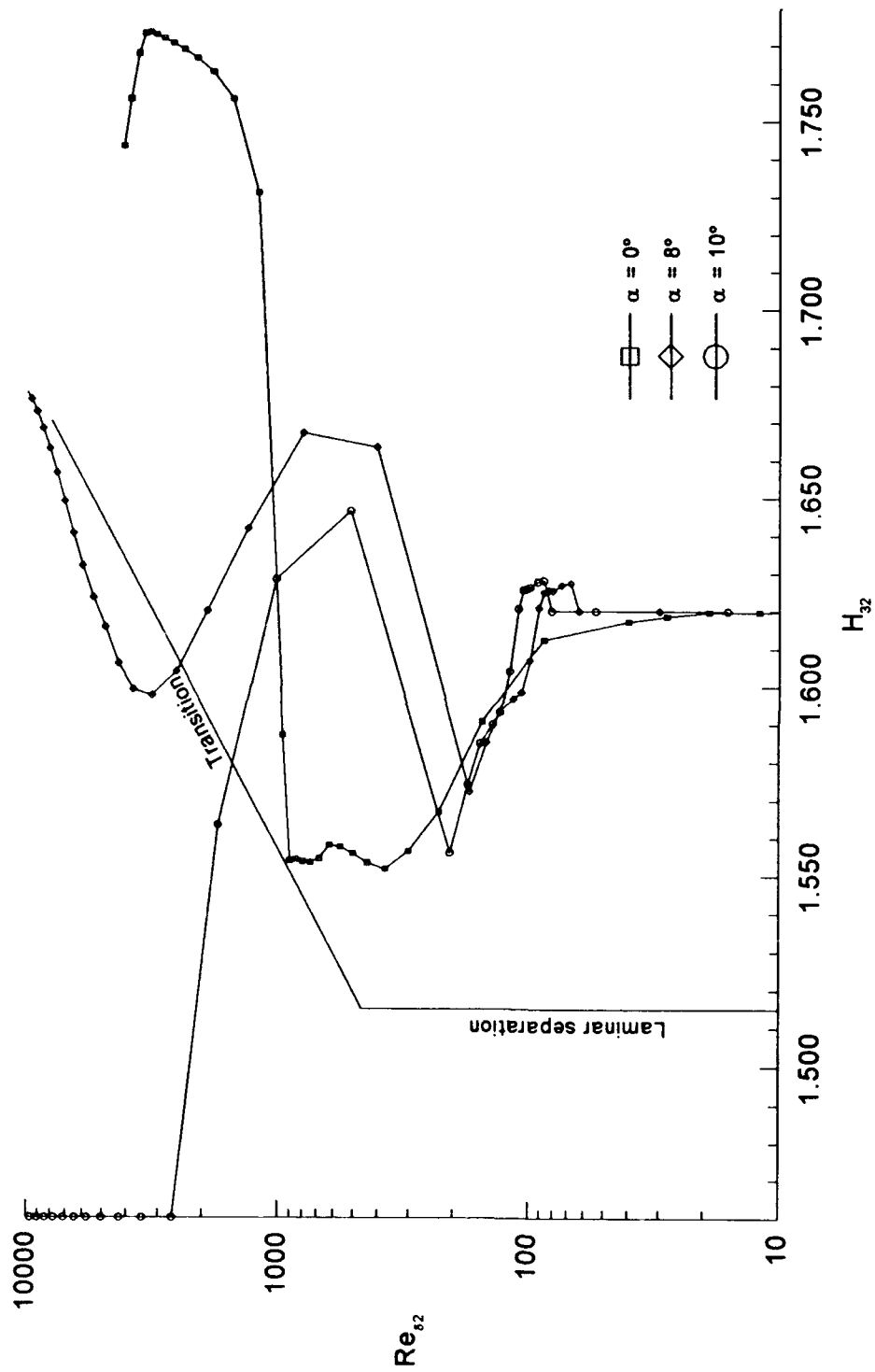


Figure 107. Boundary-Layer Development - Upper Surface - Airfoil T22  
 $Re = 3.0 \times 10^6$



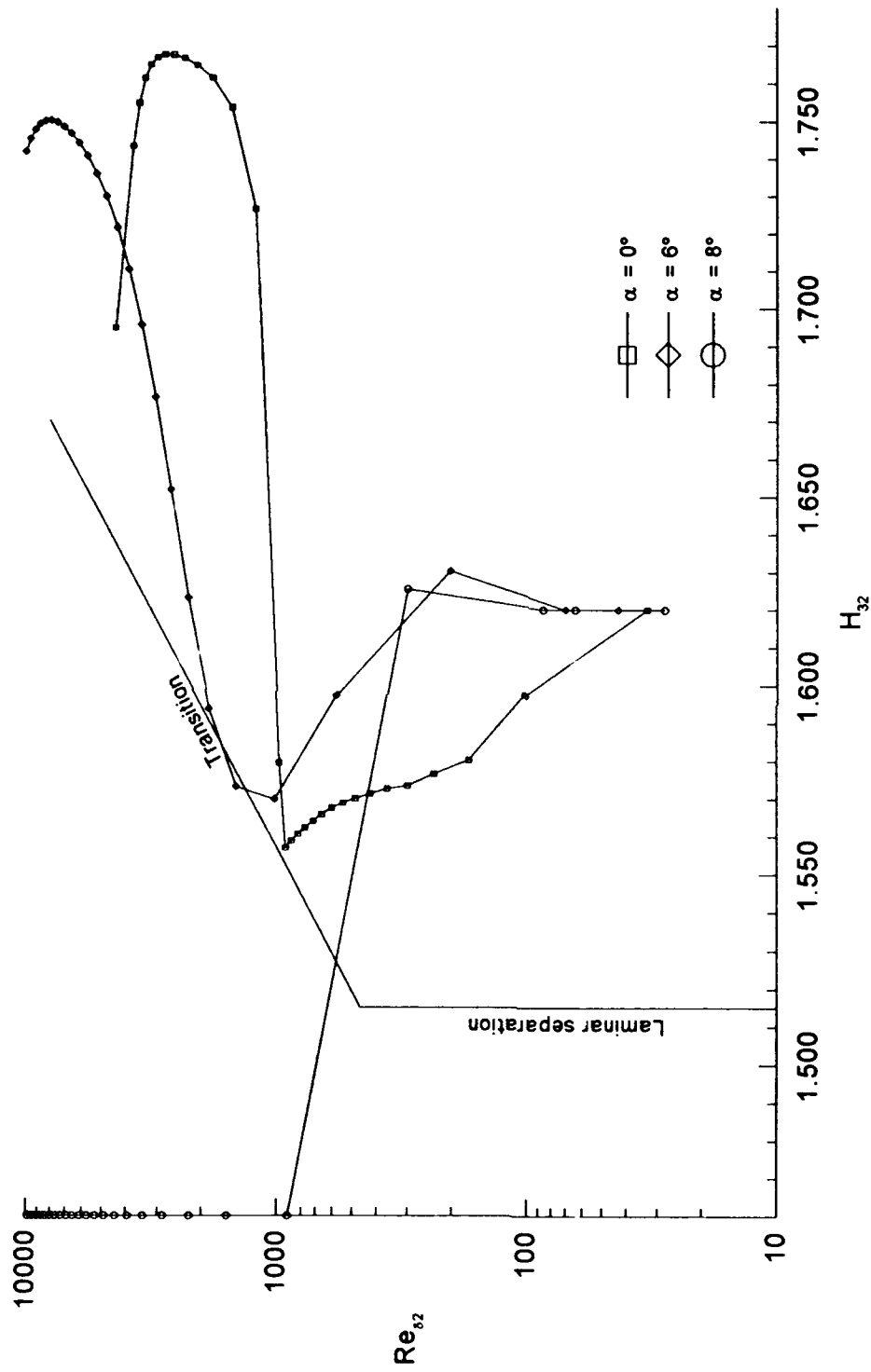


Figure 108. Boundary-Layer Development - Upper Surface - NACA 4-Digit Airfoil

$t/c = 4.75\%$  -  $Re = 3.0 \times 10^6$

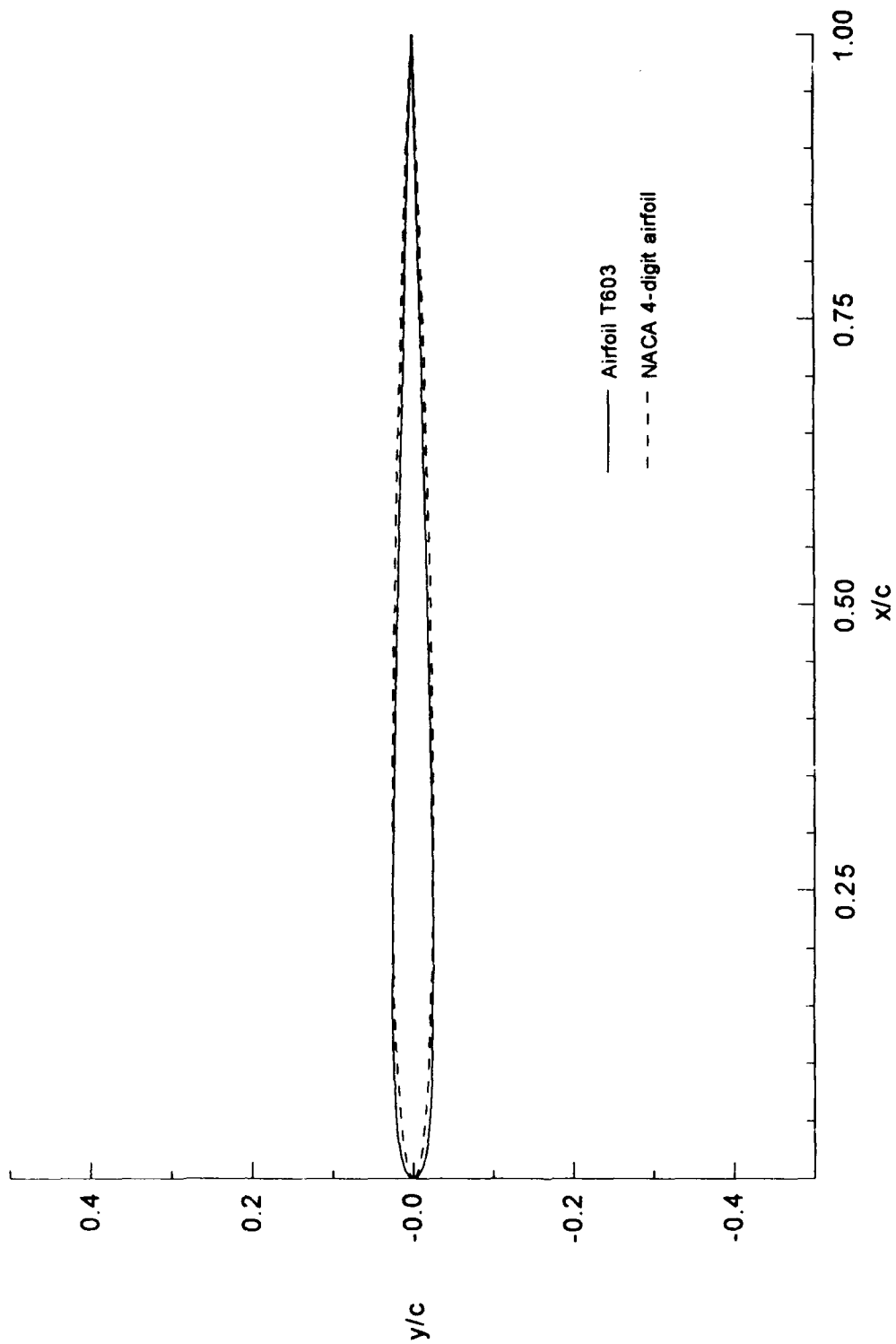


Figure 109. Comparison of NACA 4-digit airfoil vs Airfoil T603

$t/c = 5.08\%$

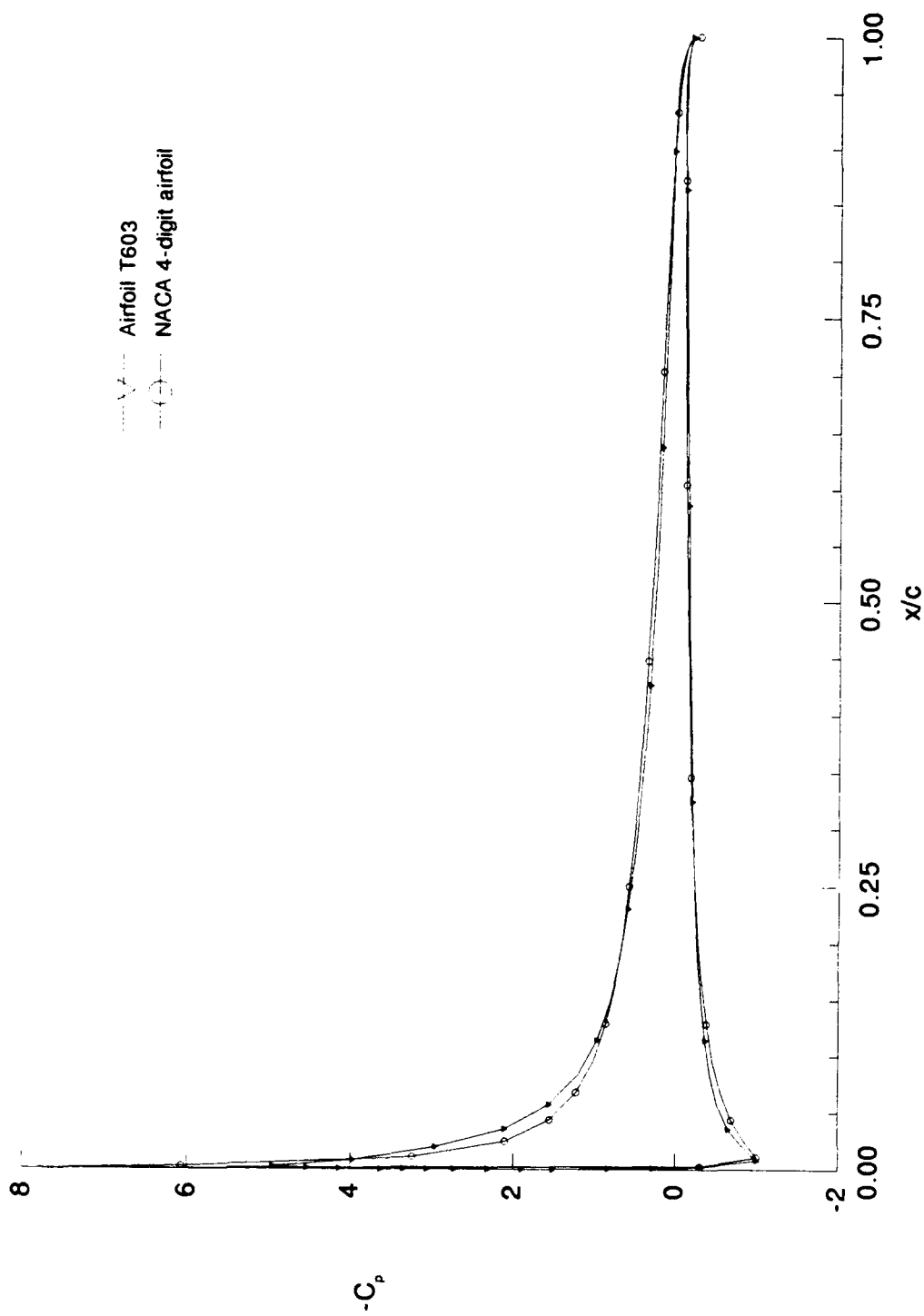


Figure 110. Airfoil T603 vs NACA 4-Digit Airfoil Pressure Distribution  
 $\alpha = 6^\circ$  - Incompressible

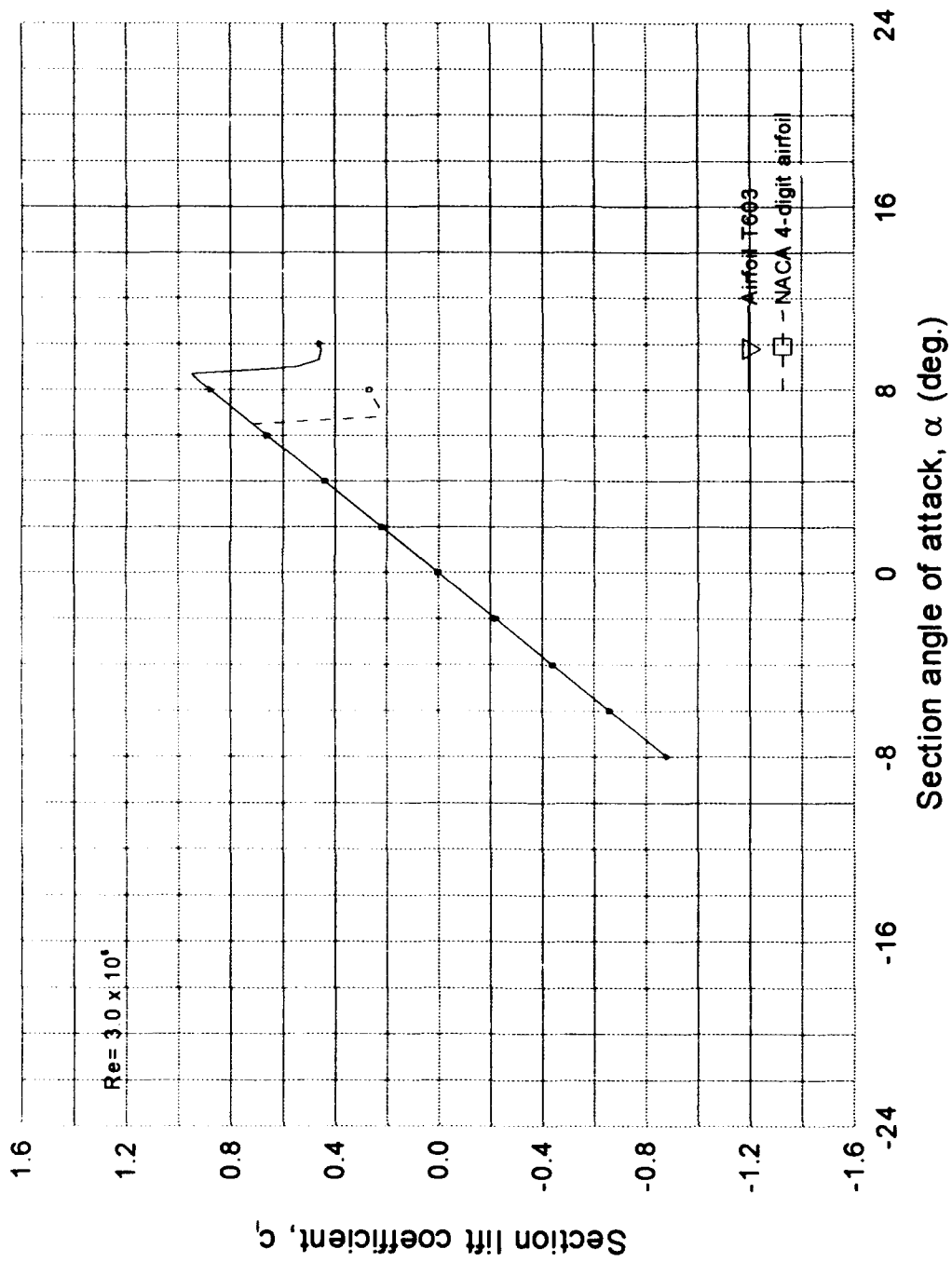


Figure 111.  $C_l(\alpha)$  Curve - Airfoil T603 vs NACA 4-Digit Airfoil

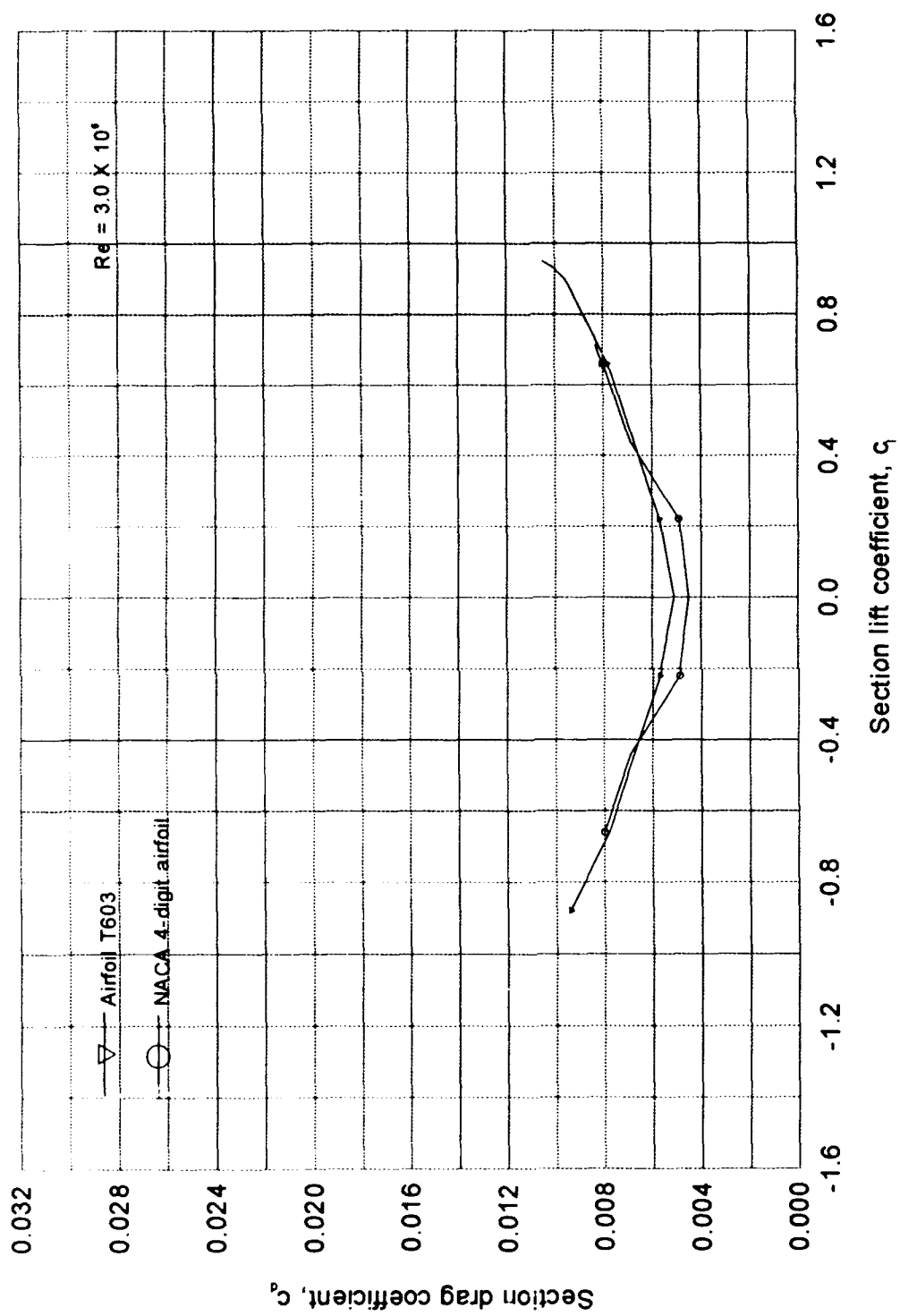


Figure 112.  $C_l - C_d$  plot - Airfoil T603 vs NACA 4-digit airfoil  
 $t/c = 5.08\%$

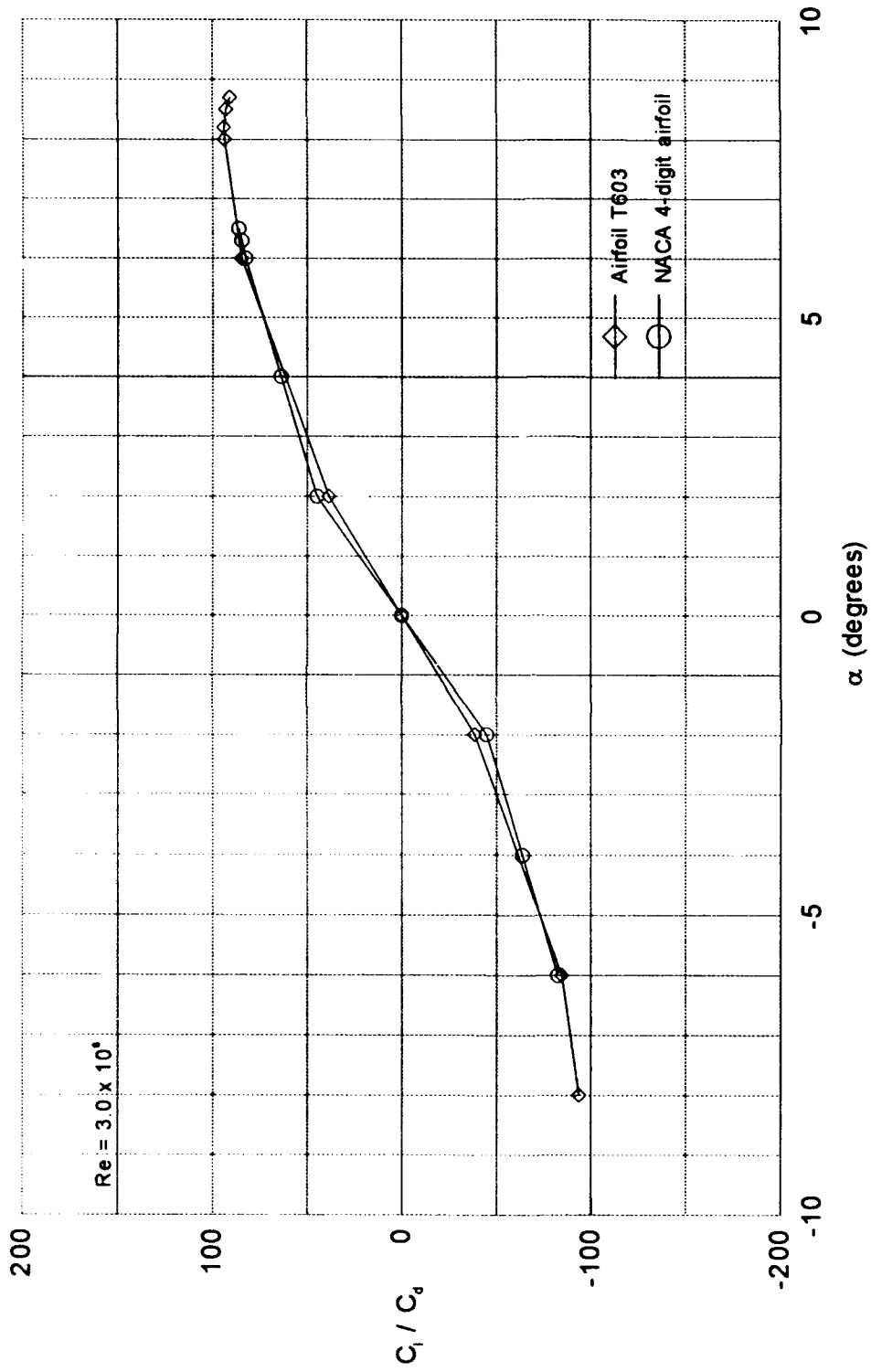


Figure 113. Lift-drag ratio - Airfoil T603 vs NACA 4-digit airfoil

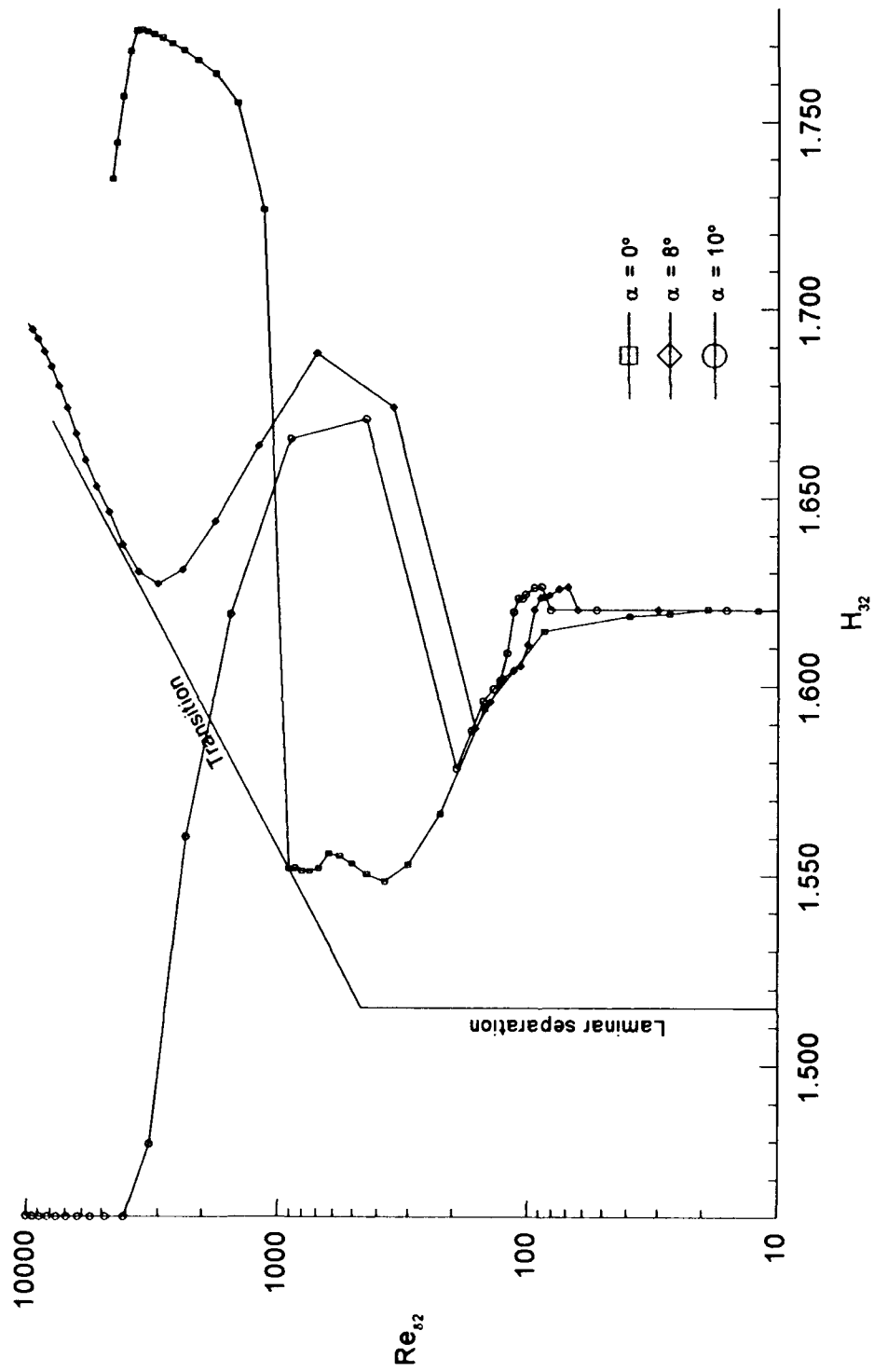


Figure 114. Boundary-Layer Development - Upper Surface - Airfoil T603  
 $Re = 3.0 \times 10^6$

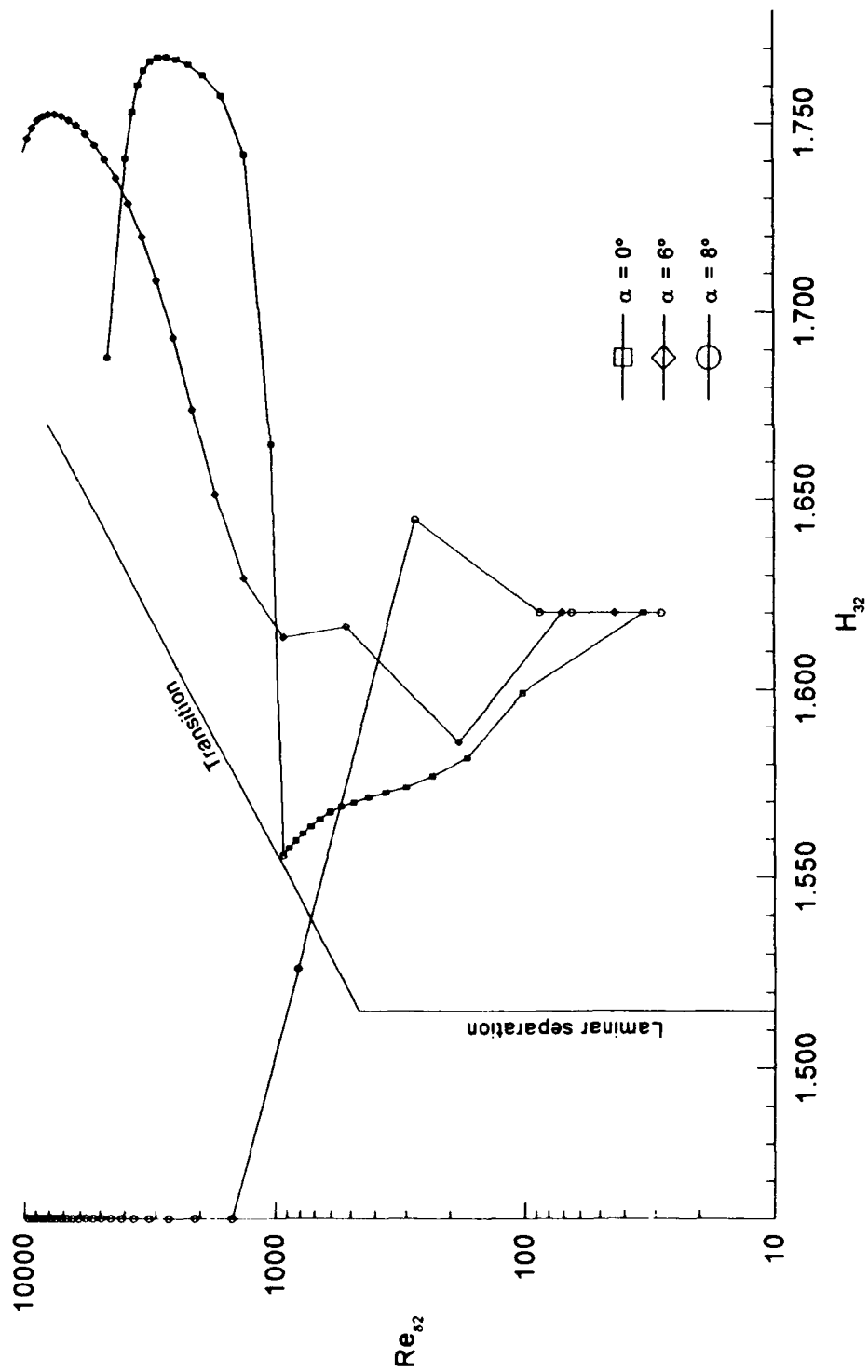


Figure 115. Boundary-Layer Development - Upper Surface - NACA 4-Digit  
 $t/c = 5.08\%$  -  $Re = 3.0 \times 10^6$



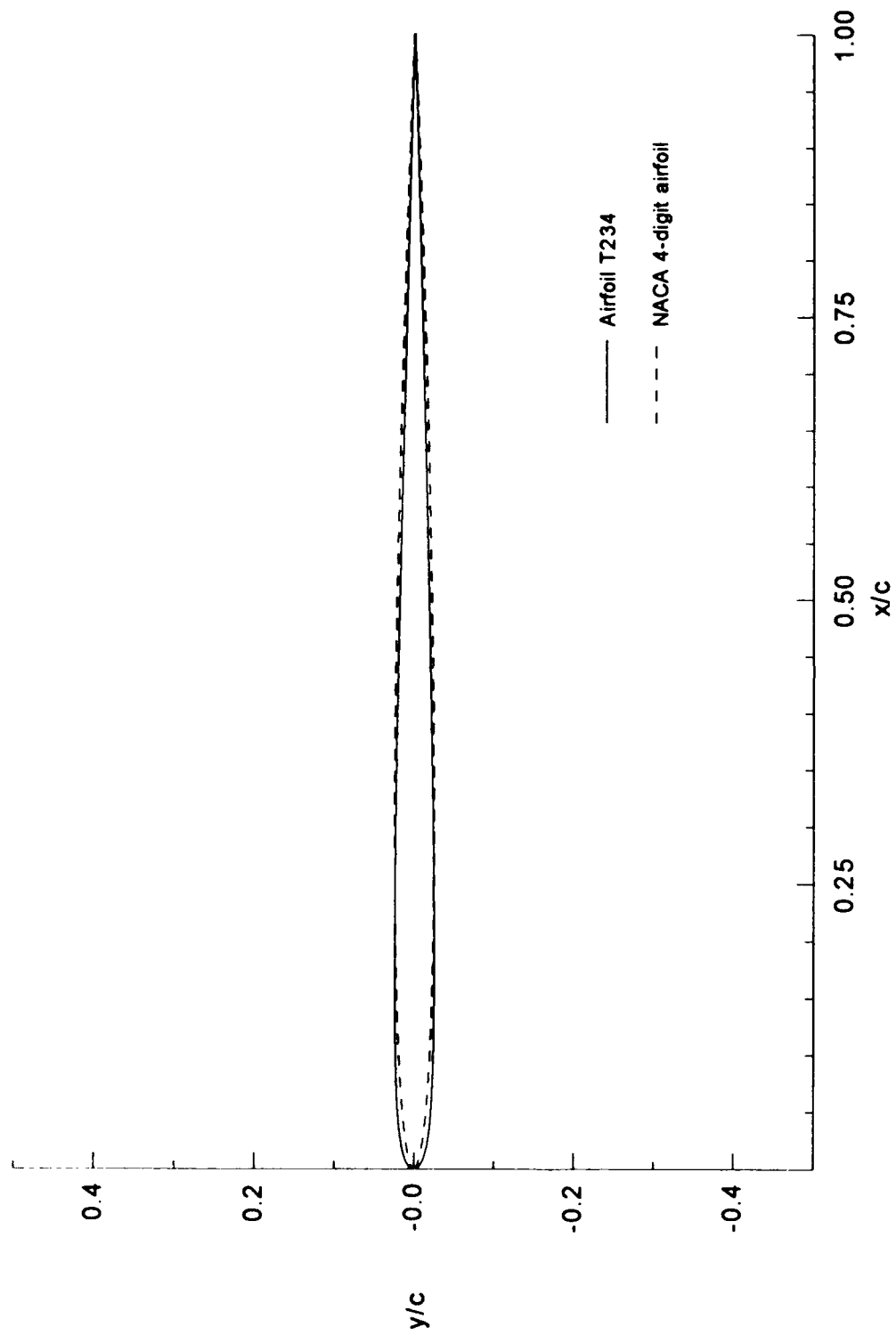


Figure 116. Comparison of NACA 4-Digit Airfoil vs Airfoil T234

$t/c = 4.97\%$

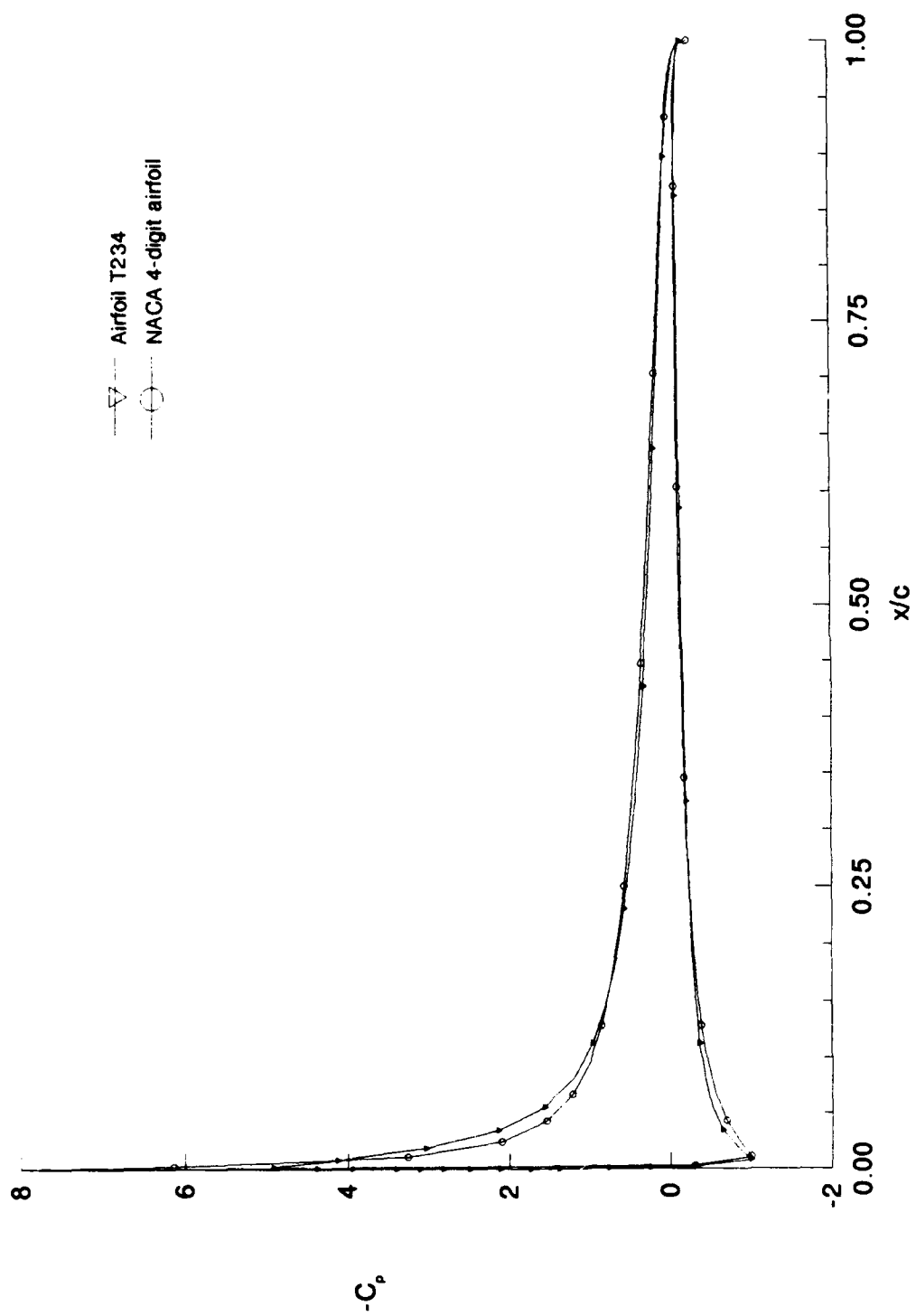


Figure 117. Airfoil T234 vs NACA 4-Digit Airfoil Pressure Distribution  
 $\alpha = 6^\circ$  - Incompressible

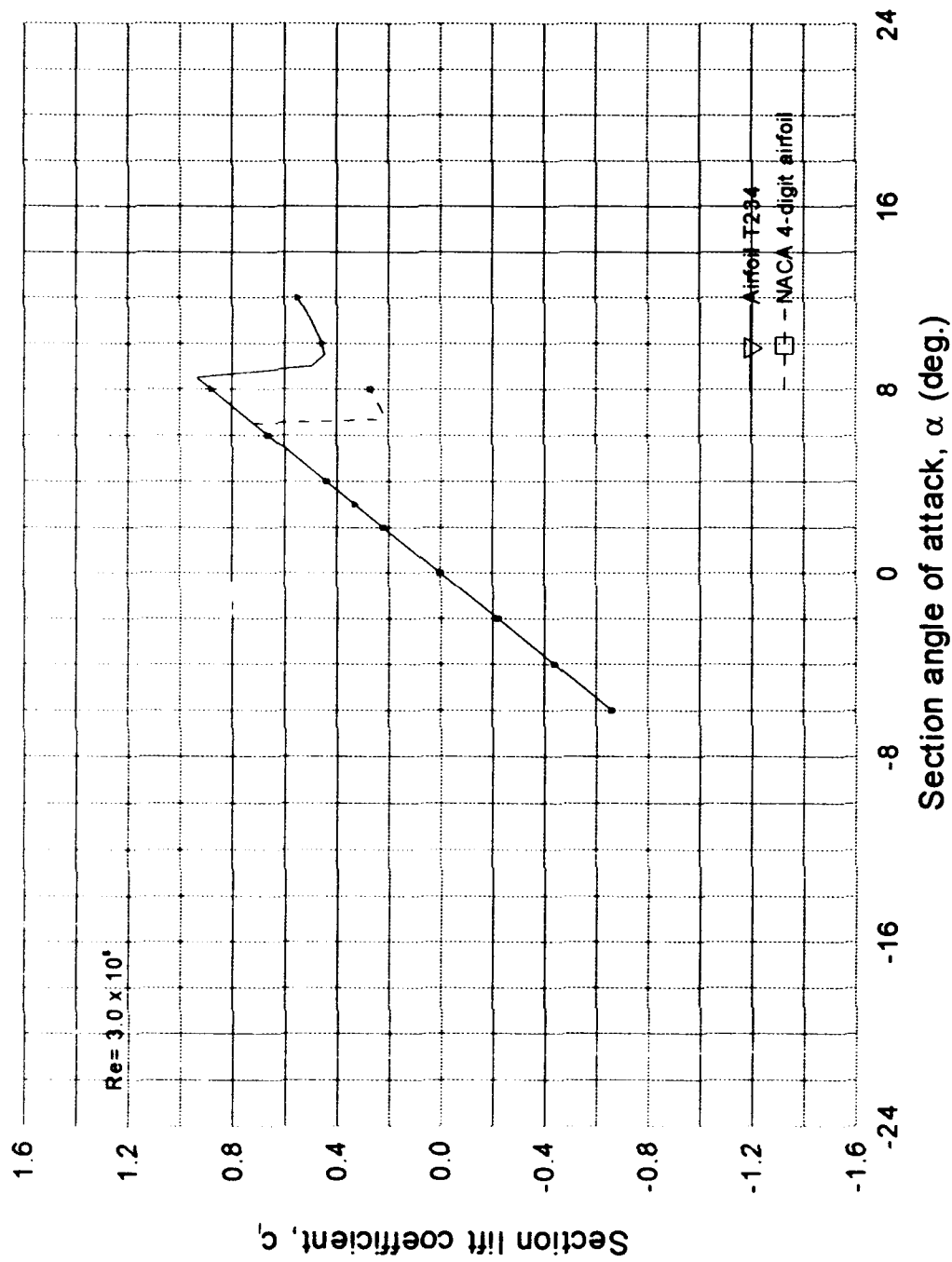


Figure 118.  $C_l(\alpha)$  Curve - Airfoil T234 vs NACA 4-Digit Airfoil

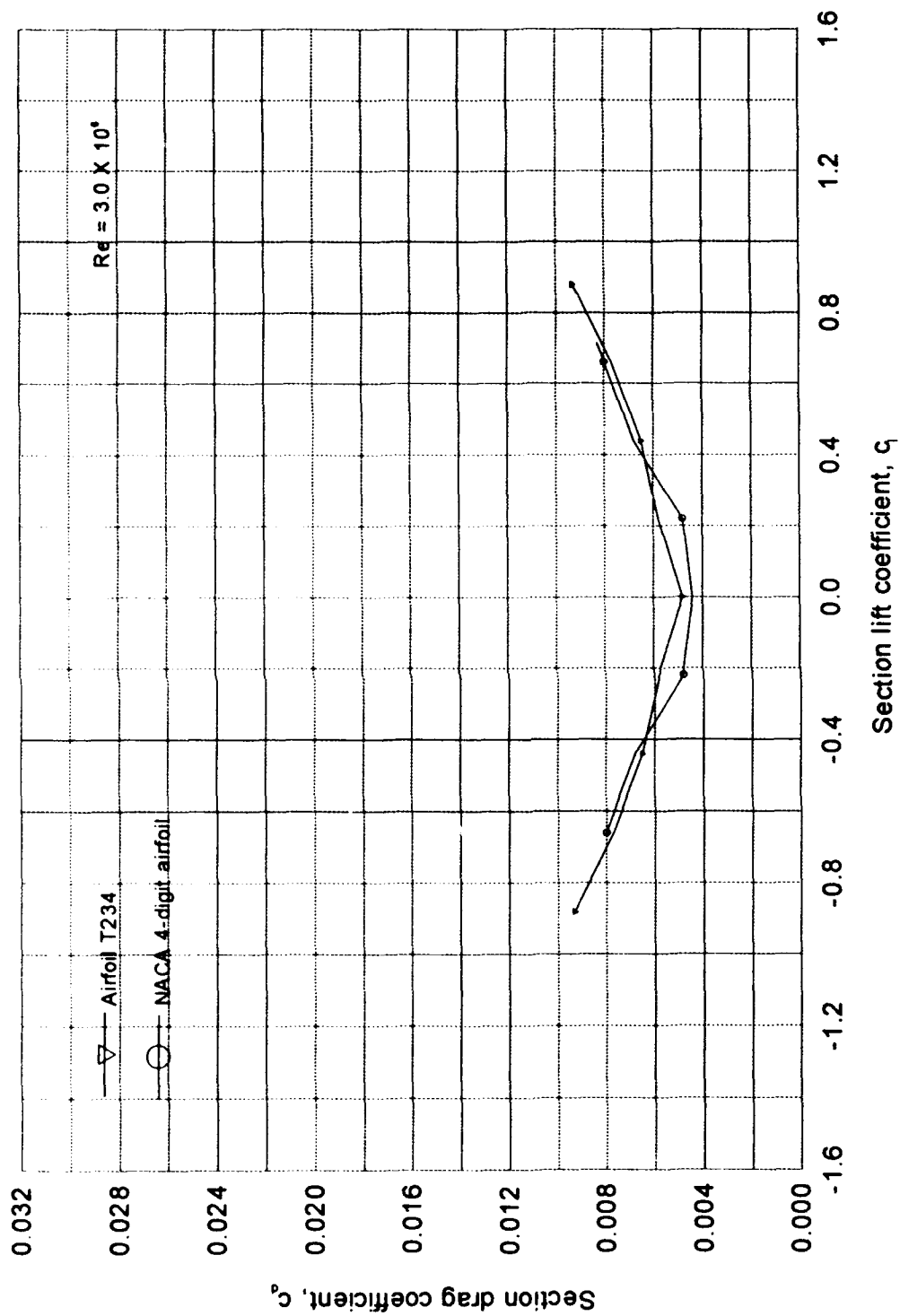


Figure 119.  $C_l - C_d$  plot - Airfoil T234 vs NACA 4-digit airfoil  
 $t/c = 4.97\%$

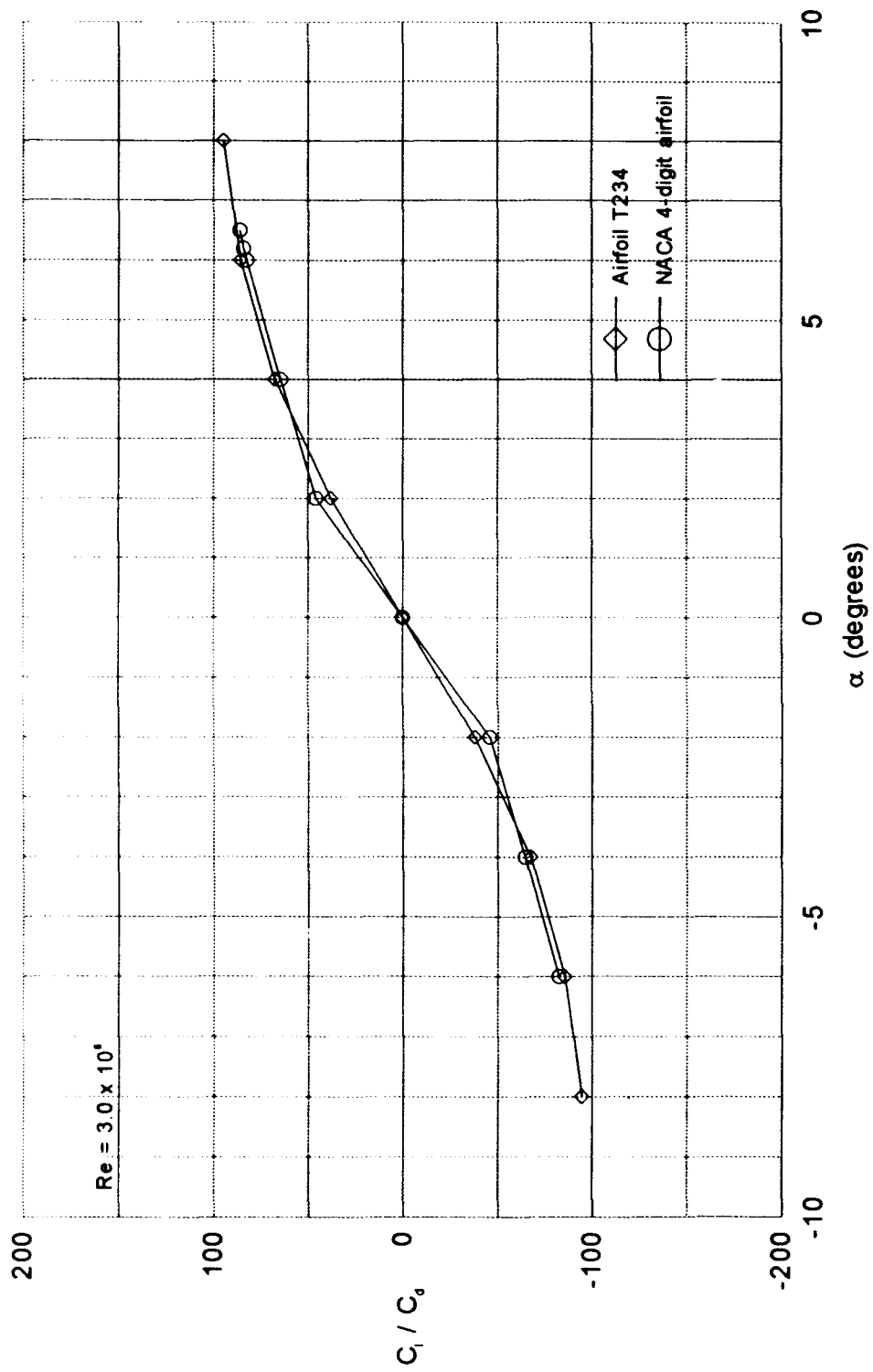


Figure 120. Lift-drag ratio - Airfoil T234 vs NACA 4-digit airfoil

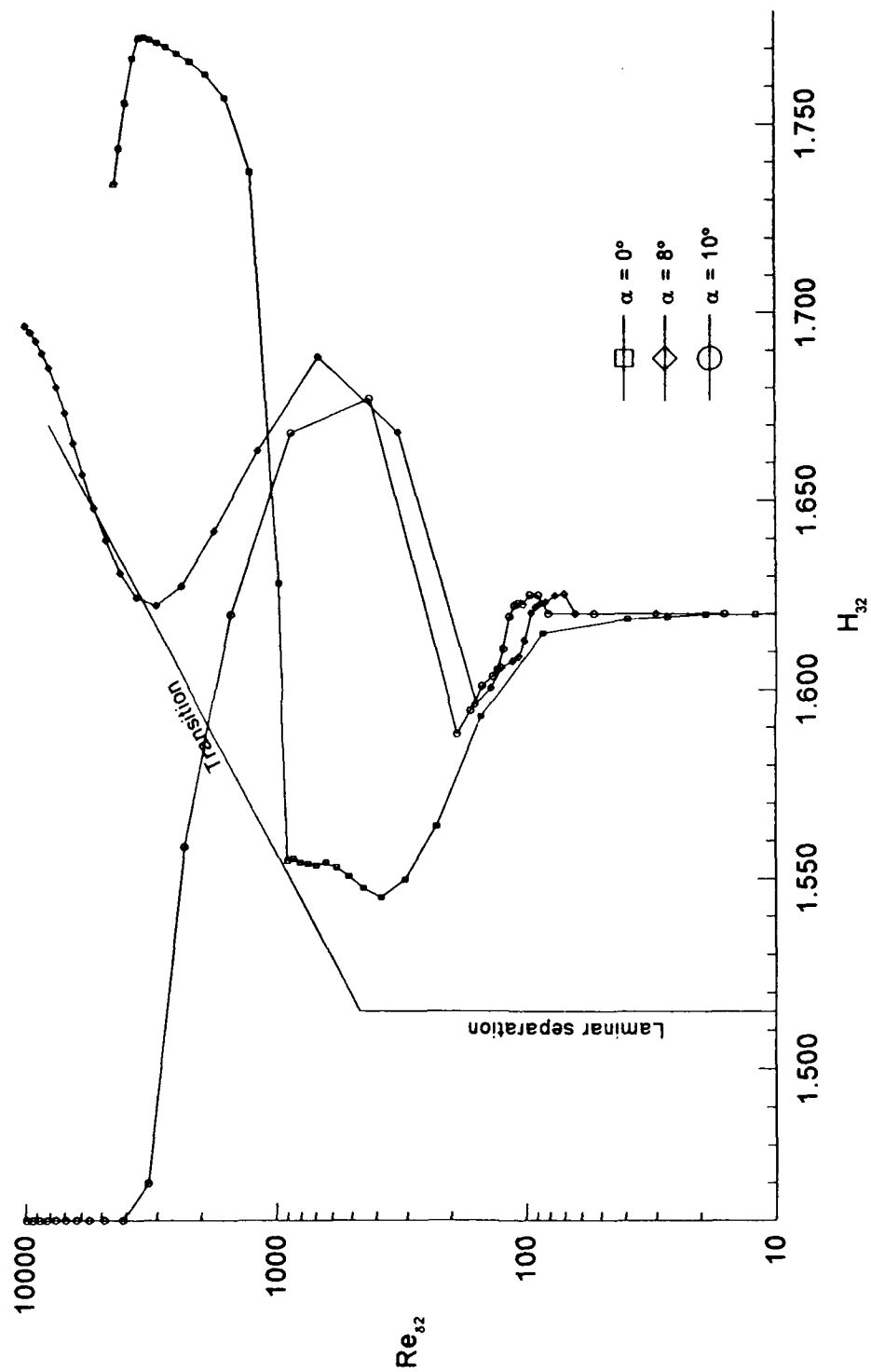


Figure 121. Boundary-Layer Development - Upper Surface - Airfoil T234  
 $Re = 3.0 \times 10^6$

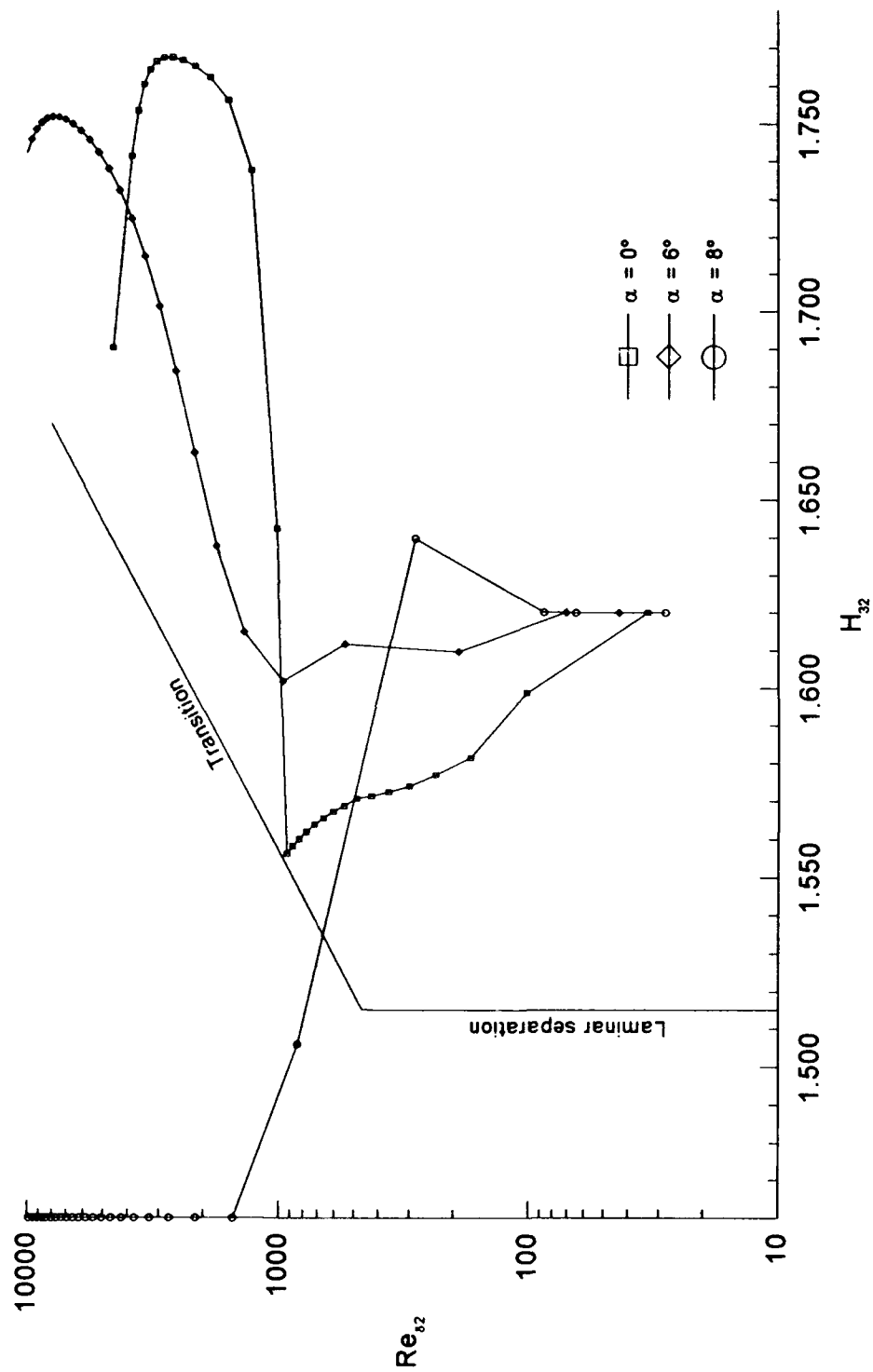


Figure 122. Boundary-Layer Development - Upper Surface - NACA 4-Digit Airfoil  
 $t/c = 4.97\%$  -  $Re = 3.0 \times 10^6$

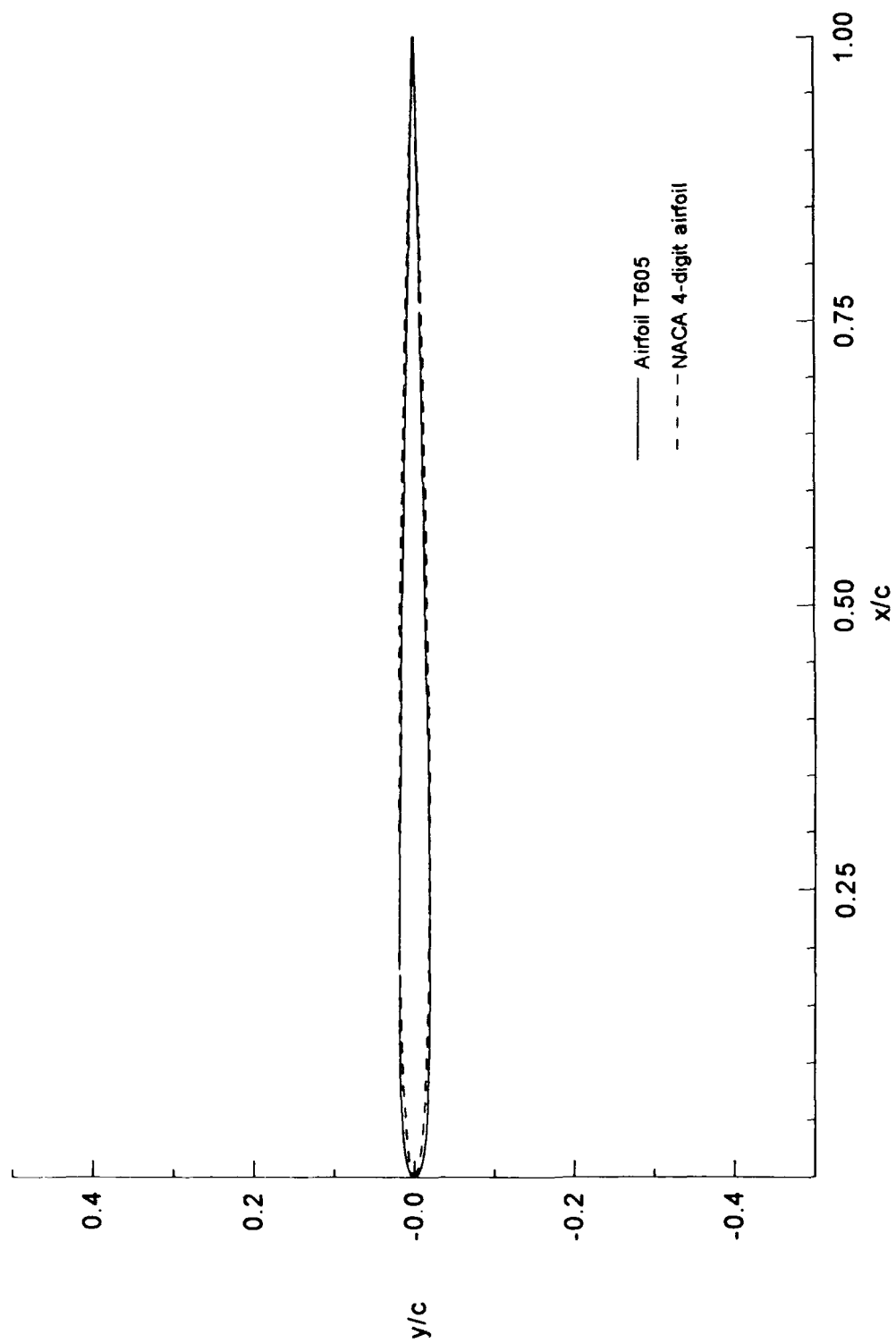


Figure 123. Comparison of NACA 4-digit airfoil vs Airfoil T605

$t/c = 3.82\%$



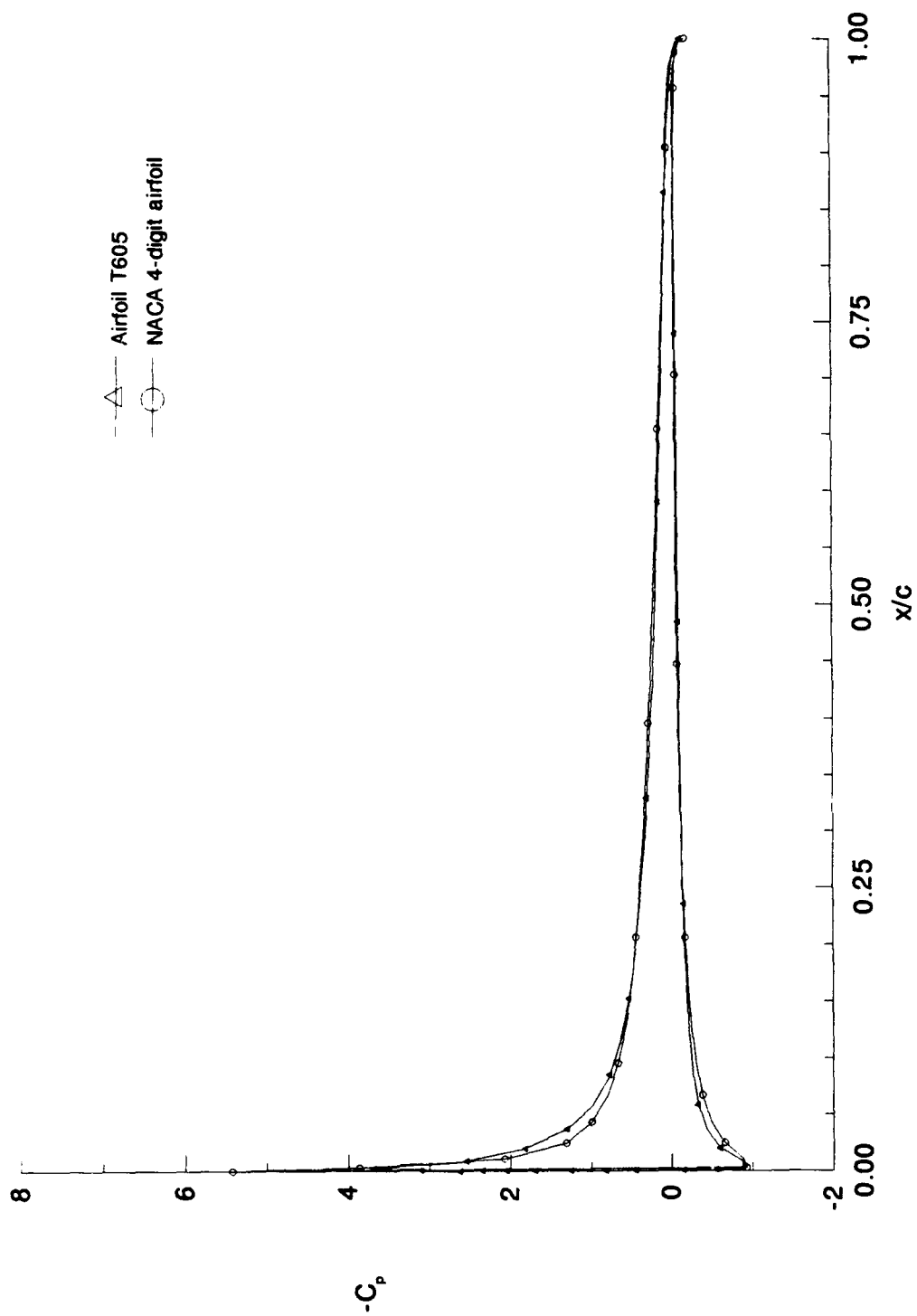


Figure 124. Airfoil T605 vs NACA 4-Digit Airfoil Pressure Distribution  
 $\alpha = 4^\circ$  - Incompressible

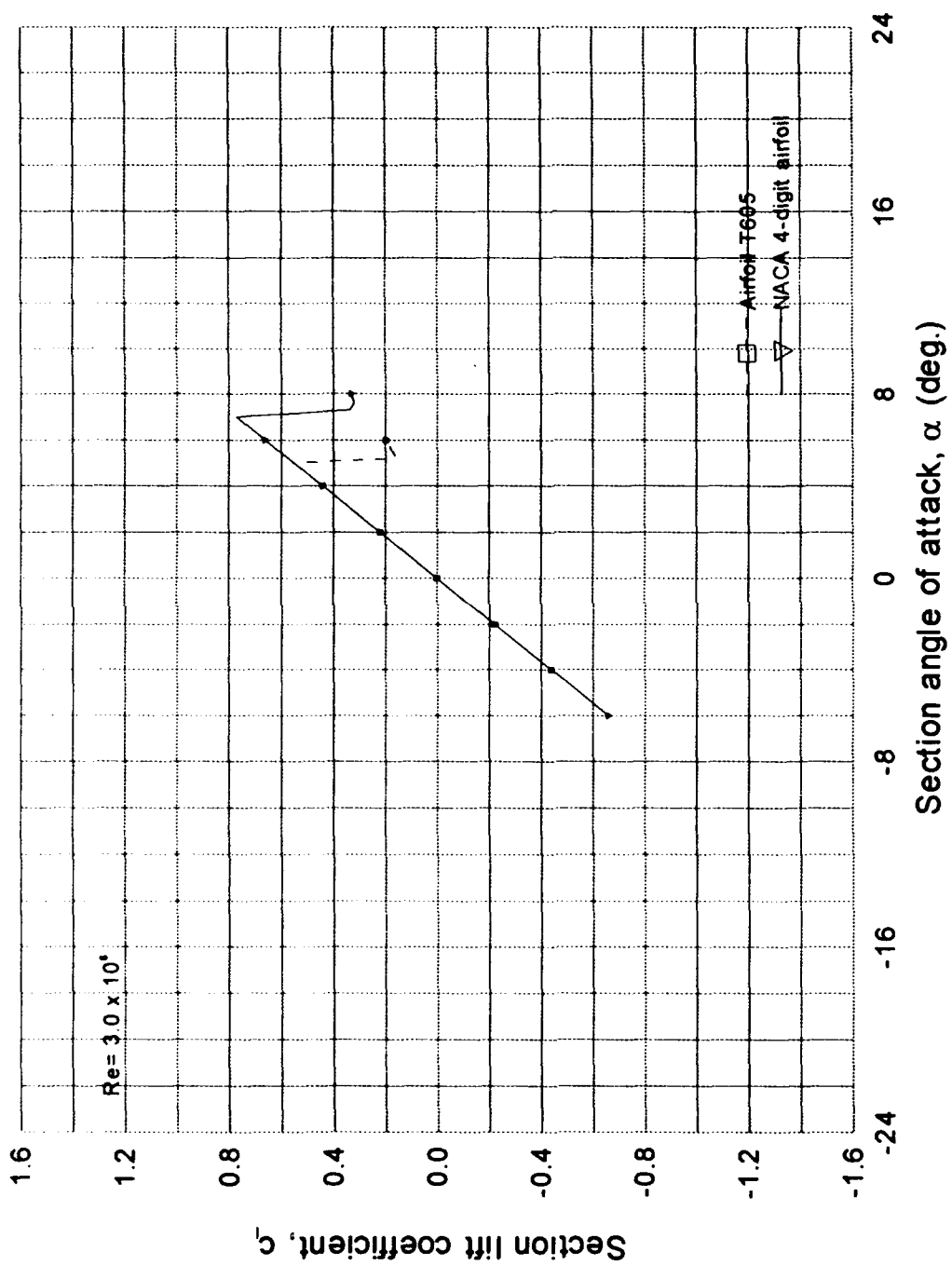


Figure 125.  $C_l(\alpha)$  Curve - Airfoil T605 vs NACA 4-Digit Airfoil

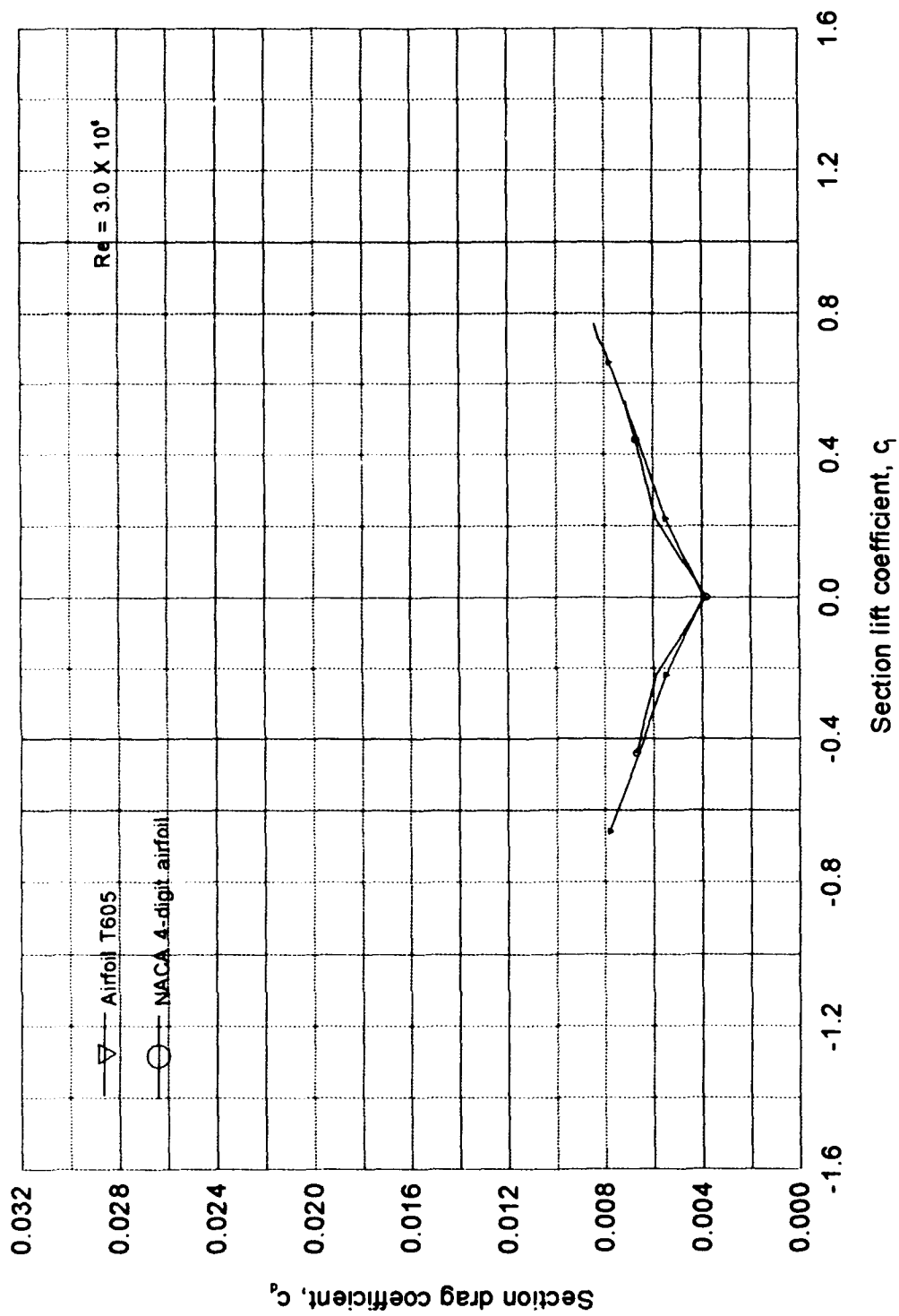


Figure 126.  $C_l$  -  $C_d$  plot - Airfoil T605 vs NACA 4-digit airfoil  
 $t/c = 3.82\%$

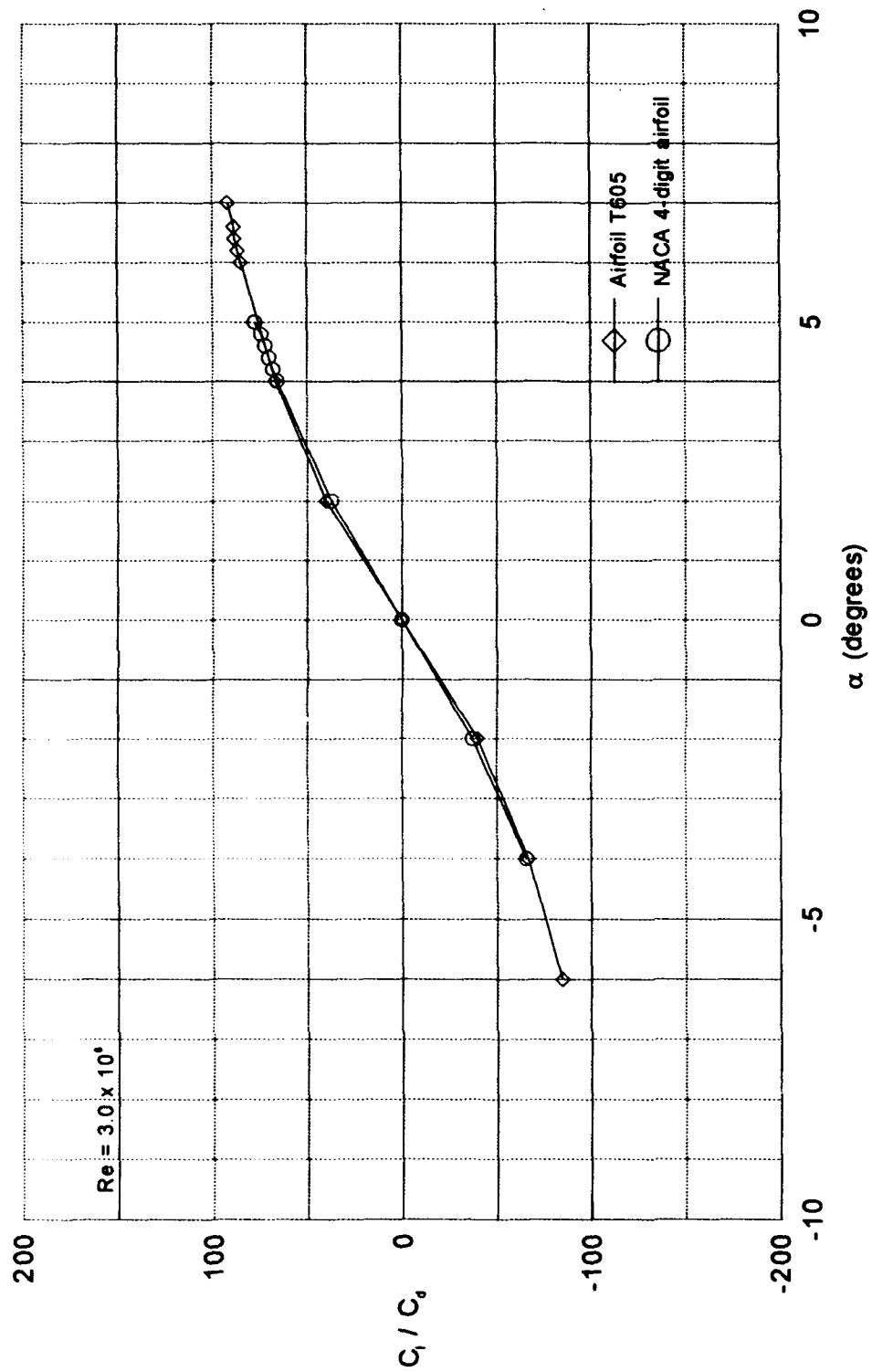


Figure 127. Lift-drag ratio - Airfoil T605 vs NACA 4-digit airfoil

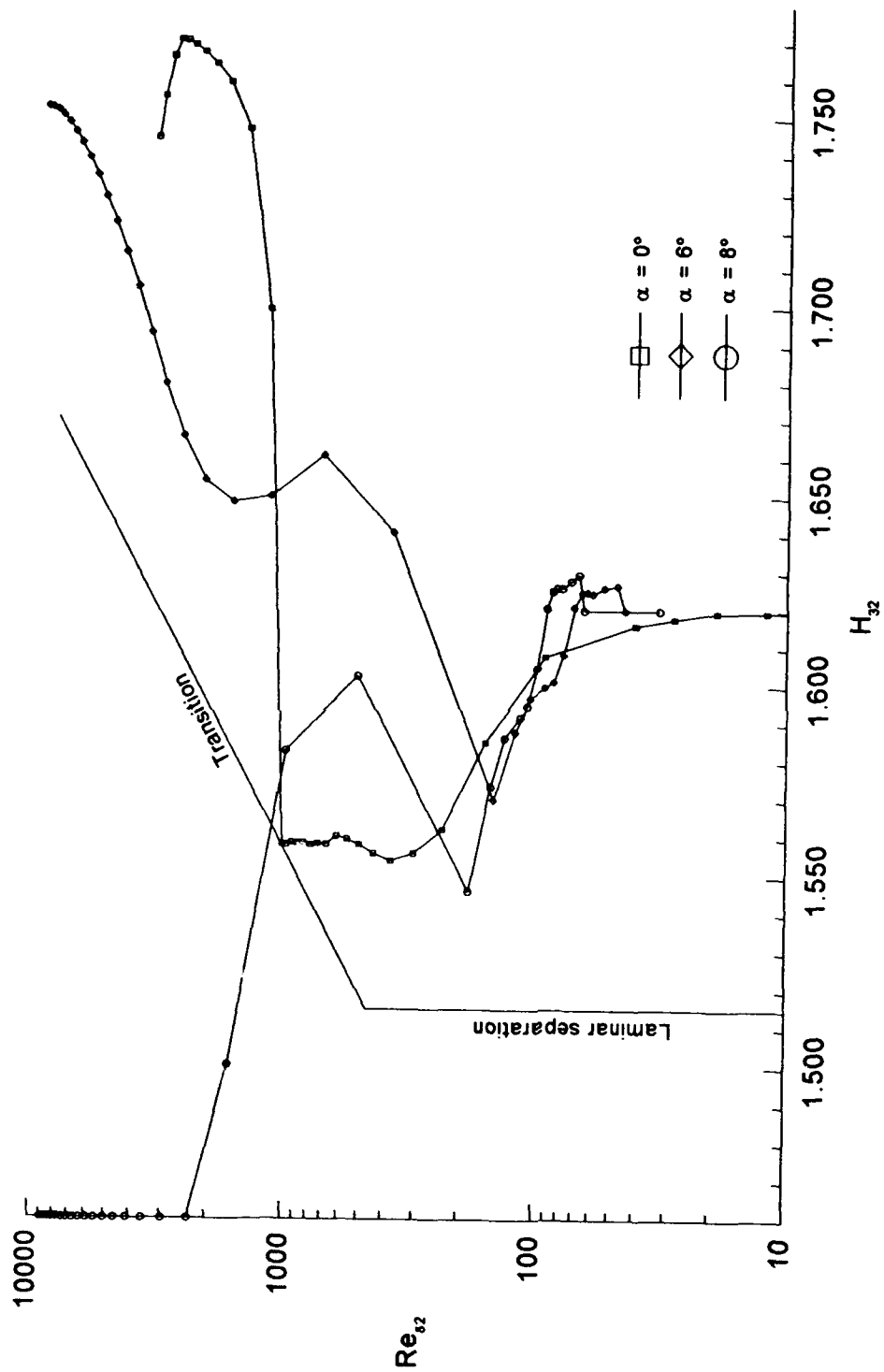


Figure 128. Boundary-Layer Development - Upper Surface - Airfoil T605  
 $Re = 3.0 \times 10^6$

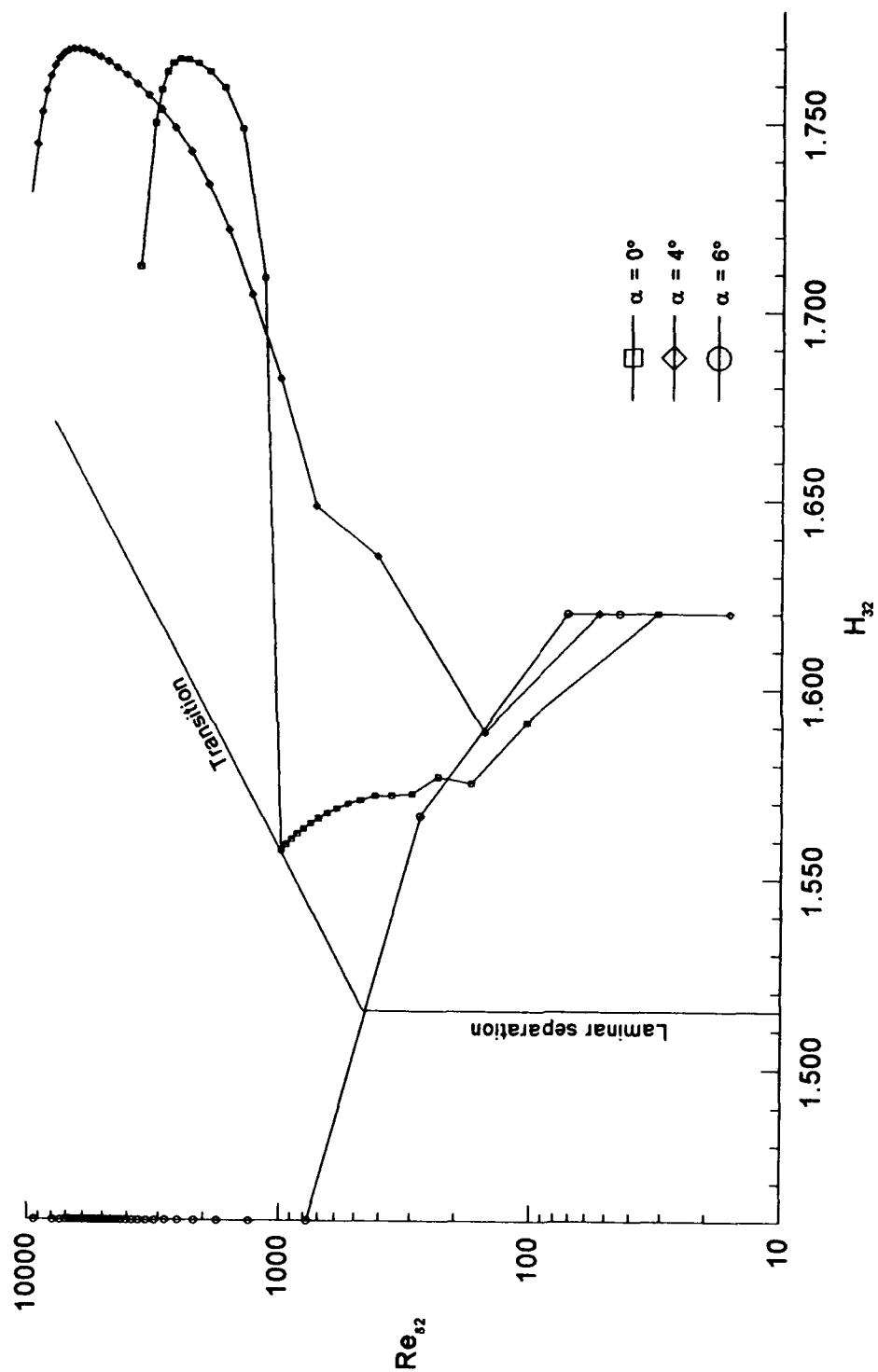


Figure 129. Boundary-Layer Development - Upper Surface - NACA 4-Digit Airfoil

$t/c = 3.82\%$  -  $Re = 3.0 \times 10^6$

#### Appendix A: Summary of the $(v_i, \alpha_i^*)$ Pairs

This appendix contains the  $(v_i, \alpha_i^*)$  pairs determined for the TA-series and the T-series airfoils. The TA-series airfoils were obtained by the hand-drawn curves of decreasing  $\alpha^*$ . The T-series airfoils were obtained for the power law relationship defined by Equation (67).

TABLE A.1

SUMMARY OF  $(v_i, \alpha_i^*)$  PAIRS FOR TA-SERIES AIRFOILS

i	$v_i$	TA2 $\alpha_i^*$	TA3 $\alpha_i^*$	TA4 $\alpha_i^*$	TA5 $\alpha_i^*$
1	5	0	0	0	0
2	10	2.2	.9	.2	0
3	15	5.5	1.7	.7	0
4	20	9	3	.9	0
5	25	13	5	1	0
6	26	19	9.5	2.5	0
7	27	19.6	11	3.8	.01
8	28	21.1	13	5.5	.2
9	28.3	23	16	9.7	1.2
10	28.7	24	16.8	10.8	1.9
11	29	25.1	18.2	13.2	3
12	29.3	26	19.7	16	4.5
13	29.6	27.3	21.9	20	7.8
14	0	30	30	30	30
15	30.4	-30	-30	-30	-30
16	30.7	-27.3	-21.9	-20	-7.8
17	31	-26	-19.7	-16	-4.5
18	31.3	-25.1	-18.2	-13.2	-3
19	31.7	-24	-16.8	-10.8	-1.9
20	32	-23	-16	-9.7	-1.2
21	33	-21.1	-13	-5.5	-.2
22	34	-19.6	-11	-3.8	-.01
23	35	-19	-9.5	-2.5	0
24	40	-13	-5	-1	0
25	45	-9	-3	-.9	0
26	50	-5.5	-1.7	-.7	0
27	55	-2.2	-.9	-.2	0
28	60	0	0	0	0



TABLE A.2

SUMMARY OF  $(v_i, \alpha_i^*)$  PAIRS FOR T-SERIES AIRFOILS ( $A = 1$ )

i	$v_i$	T25 $\alpha_i^*$	T30 $\alpha_i^*$	T3 $\alpha_i^*$	T4 $\alpha_i^*$
1	5	1.02	1.02	1.02	1.028
2	10	1.07	1.09	1.1	1.12
3	15	1.18	1.23	1.26	1.32
4	20	1.41	1.51	1.58	1.74
5	25	1.96	2.25	2.45	2.93
6	26	2.19	2.56	2.48	3.5
7	27	2.53	3.04	3.44	4.4
8	28	3.05	3.81	4.55	6.0
9	28.3	3.29	4.18	4.89	6.7
10	28.7	3.67	4.76	5.65	8.0
11	29	4.41	5.45	6.57	9.6
12	29.3	4.47	6.03	7.35	10.9
13	29.6	5.08	7.03	8.7	13.4
14	0	6.68	9.78	12.57	20.9
15	30.4	-6.68	-9.78	-12.57	-20.9
16	30.7	-5.08	-7.03	-8.7	-13.4
17	31	-4.47	-6.03	-7.35	-10.9
18	31.3	-4.41	-5.45	-6.57	-9.6
19	31.7	-3.67	-4.76	-5.65	-8.0
20	32	-3.29	-4.18	-4.89	-6.7
21	33	-3.05	-3.81	-4.55	-6.0
22	34	-2.53	-3.04	-3.44	-4.4
23	35	-2.19	-2.56	-2.84	-3.5
24	40	-1.96	-2.25	-2.45	-2.93
25	45	-1.41	-1.51	-1.58	-1.74
26	50	-1.18	-1.23	-1.26	-1.32
27	55	-1.07	-1.09	-1.1	-1.12
28	60	-1.02	-1.02	-1.02	-1.028

TABLE A.3

SUMMARY OF  $(v_i, \alpha_i^*)$  PAIRS FOR T-SERIES AIRFOILS ( $A = 1/2$ )

i	$v_i$	T402 $\alpha_i^*$	T22 $\alpha_i^*$
1	5	.51	.51
2	10	.56	.58
3	15	.66	.7
4	20	.86	1.0
5	25	1.5	1.9
6	26	1.7	2.4
7	27	2.2	3.2
8	28	3.0	4.65
9	28.3	3.4	5.4
10	28.7	4.0	6.75
11	29	4.8	8.45
12	29.3	5.4	10.0
13	29.6	6.7	12.9
14	0	10.4	22.35
15	30.4	-10.4	-22.35
16	30.7	-6.7	-12.9
17	31	-5.4	-10.0
18	31.3	-4.8	-8.45
19	31.7	-4.0	-6.75
20	32	-3.4	-5.4
21	33	-3.0	-4.65
22	34	-2.2	-3.2
23	35	-1.7	-2.4
24	40	-1.5	-1.9
25	45	-.86	-1.0
26	50	-.66	-.7
27	55	-.56	-.58
28	60	-.51	-.51

TABLE A.4

SUMMARY OF  $(v_i, \alpha_i^*)$  PAIRS FOR T-SERIES AIRFOILS ( $A = 1/3$ )

i	$v_i$	T503 $\alpha_i^*$	T603 $\alpha_i^*$
1	5	.34	.34
2	10	.38	.39
3	15	.47	.5
4	20	.66	.76
5	25	1.3	1.69
6	26	1.6	2.2
7	27	2.1	3.1
8	28	3.2	5.1
9	28.3	3.7	5.8
10	28.7	4.5	7.5
11	29	5.6	9.9
12	29.3	6.67	12.1
13	29.6	8.6	16.5
14	0	14.9	31.9
15	30.4	-14.9	-31.9
16	30.7	-8.6	-16.5
17	31	-6.67	-12.1
18	31.3	-5.6	-9.9
19	31.7	-4.5	-7.5
20	32	-3.7	-5.8
21	33	-3.2	-5.1
22	34	-2.1	-3.1
23	35	-1.6	-2.2
24	40	-1.3	-1.69
25	45	-.66	-.76
26	50	-.47	-.5
27	55	-.38	-.39
28	60	-.34	-.34

TABLE A.5

SUMMARY OF  $(v_i, \alpha_i^*)$  PAIRS FOR T-SERIES AIRFOILS ( $A = 1/4$ )

i	$v_i$	T604 $\alpha_i^*$	T234 $\alpha_i^*$	T504 $\alpha_i^*$
1	5	.26	.26	.26
2	10	.29	.3	.29
3	15	.38	.39	.35
4	20	.57	1.12	.5
5	25	1.27	1.5	.96
6	26	1.65	2.0	1.2
7	27	2.3	2.95	1.6
8	28	3.6	4.9	2.4
9	28.3	4.3	6.0	2.7
10	28.7	5.6	8.0	3.4
11	29	7.4	10.8	4.2
12	29.3	9.1	13.5	5.0
13	29.6	12.4	19.0	6.4
14	0	23.9	39.48	11.2
15	30.4	-23.9	-39.48	-11.2
16	30.7	-12.4	-19.0	-6.4
17	31	-9.1	-13.5	-5.0
18	31.3	-7.4	-10.8	-4.2
19	31.7	-5.6	-8.0	-3.4
20	32	-4.3	-6.0	-2.7
21	33	-3.6	-4.9	-2.4
22	34	-2.3	-2.95	-1.6
23	35	-1.65	-2.0	-1.2
24	40	-1.27	-1.5	-.96
25	45	-.57	-1.12	-.5
26	50	-.38	-.39	-.35
27	55	-.29	-.3	-.29
28	60	-.26	-.26	-.26

TABLE A.6

SUMMARY OF  $(v_i, \alpha_i^*)$  PAIRS FOR T-SERIES AIRFOILS ( $A = 1/5$ )

i	$v_i$	T505 $\alpha_i^*$	T605 $\alpha_i^*$	T6605 $\alpha_i^*$
1	5	.21	.20	.21
2	10	.23	.23	.24
3	15	.28	.30	.31
4	20	.40	.46	.5
5	25	.77	1.0	1.2
6	26	.97	1.3	1.62
7	27	1.29	1.87	2.4
8	28	1.9	3.0	3.9
9	28.3	2.2	3.5	4.8
10	28.7	2.8	4.5	6.4
11	29	3.38	5.6	8.6
12	29.3	4.0	7.2	10.8
13	29.6	5.16	9.9	15.2
14	0	8.94	19.1	31.6
15	30.4	-8.94	-19.1	-31.6
16	30.7	-5.16	-9.9	-15.2
17	31	-4.0	-7.2	-10.8
18	31.3	-3.38	-5.6	-8.6
19	31.7	-2.8	-4.5	-6.4
20	32	-2.2	-3.5	-4.8
21	33	-1.9	-3.0	-3.9
22	34	-1.29	-1.87	-2.4
23	35	-.97	-1.3	-1.62
24	40	-.77	-1.0	-1.2
25	45	-.4	-.46	-.5
26	50	-.28	-.30	-.31
27	55	-.23	-.23	-.24
28	60	-.21	-.20	-.21

## Appendix B: Code Input

The purpose of this appendix is to explain the function of the major input lines used in this investigation. Eppler (7) details all the input options for this program.

The sequence of the program's execution is managed by the named input lines. Once the program reads the name, it goes to the correct section of the code. After completing the assigned task, it returns back to the main program and reads the next input line. The following is a sample input file:

```
REMO1
TRA21      1000 -1 -.7 -.5 -.1 0 .1 .5 .7 1 1000
TRA1       22.5 0 0 2 37.5 -2 60 0
TRA21      4 29 1 .1 .95 4 29 1 .1 .95 3 .3 0 2
PAN 13
ALFA213    7 -6.,-4.,-2.,0.,2.,4.,6.
RE 130 0   03.0 3000 3.0 6000 3.0 9000
ENDE
```

The REMO1-line is used here to toggle between the free and formatted modes of input. The character "1" in the 5th position toggles to the free format mode.

The TRA1- and TRA2-line contain the information needed in the airfoil design. The first TRA21-line specifies the information for putting additional points at the leading edge. This information is triggered into use by specifying the character "2" as the 14th character in the second TRA21

line. The TRA1-line used here contains the  $(v_i, \alpha_i^*)$  pairs, where  $v_i$  is the specification of the  $i$ -th arc segment related to  $\phi_i$  by

$$v_i = \frac{N}{360^\circ} \phi_i. \quad (70)$$

The second TRA21-line specifies the following (rotating input line into vertical):

TRA21

4  $\lambda^*$  = beginning of closure contribution, upper side  
 29  $\lambda$  = beginning of main-pressure region, upper side  
 1 RMS<sub>us</sub> = recovery specification mode, upper side  
           (determines interpretation of next two inputs)

	RMS <sub>us</sub> =	0	1	2	3
.1	=	K	$\omega'$	$\mu$	$\mu$
.95	=	$\mu$	$\omega$	$\omega$	$\omega'$

4  $\bar{\lambda}^*$  = beginning of closure contribution, lower side  
 29  $\bar{\lambda}$  = beginning of main-pressure region, lower side  
 1 RMS<sub>ls</sub> = recovery specification mode, lower side  
           (determines interpretation of next two inputs)

	RMS <sub>ls</sub> =	0	1	2	3
.1	=	$\bar{K}$	$\bar{\omega}'$	$\bar{\mu}$	$\bar{\mu}$
.95	=	$\bar{\mu}$	$\bar{\omega}$	$\bar{\omega}$	$\bar{\omega}'$

3 ITMOD = trailing edge iteration mode  
 .3  $K_R$  = desired value of  $K_S$ ,  $K_S = K_H + \bar{K}_H$   
 0  $K_{tol}$  = tolerance on  $K_R$

- 2 Triggers use of first TRA21-line for additional points at the leading edge

The Pan-line switches the program from the design mode to the analysis mode (panel method). The ALFA-line specifies the  $\alpha$ 's, the angles of attack of the incoming flow in degrees, at which the airfoil should be evaluated. The RE-line specifies the Reynolds numbers for which the airfoil should be evaluated and which transition mode to use in the boundary-layer analysis. The ENDE-line terminates the program's execution.



### Appendix C: Summary of Input Files

This appendix contains the input files used to create the airfoils presented in this thesis.

# Airfoil TA2

```

REMO1
TRA21      1000 -1 -.7 -.5 -.3 -.2 -.1 0 .1 .2 .3 .5 .7 1 1000
TRA1       5 0 10 2.2 15 5.5 20 9 25 13 26 19 27 19.6 28 21.1
TRA1       28.3 23 28.7 24 29 25.1 29.3 26 29.6 27.3
TRA1       0 30 30.4 -30 30.7 -27.3 31 -26 31.3 -25.1
TRA1       31.7 -24 32 -23 33 -21.1 34 -19.6 35 -19 40 -13
TRA1       45 -9 50 -5.5 55 -2.2 60 0
TRA21      4 0 1 .1 .9 4 0 1 .1 .9 3 .3 0 2
PAN 13
ALFA213 13 -12.,-10.,-8.,-6.,-4.,-2.,0.,2.,4.,6.,8.,10.,12.
RE 130 0 03.0 3000 3.0 6000 3.0 9000
ENDE

```

# Airfoil TA3

```

REMO1
TRA21      1000 -1 -.7 -.5 -.3 -.2 -.1 0 .1 .2 .3 .5 .7 1 1000
TRA1       5 0 10 .9 15 1.7 20 3 25 5 26 9.5 27 11 28 13
TRA1       28.3 16 28.7 16.8 29 18.2 29.3 19.7 29.6 21.9
TRA1       0 30 30.4 -30 30.7 -21.9 31 -19.7 31.3 -18.2
TRA1       31.7 -16.8 32 -16 33 -13 34 -11 35 -9.5 40 -5
TRA1       45 -3 50 -1.7 55 -.9 60 0
TRA21      4 0 1 .1 .9 4 0 1 .1 .9 3 .3 0 2
PAN 13
ALFA213 13 -12.,-10.,-8.,-6.,-4.,-2.,0.,2.,4.,6.,8.,10.,12.
RE 130 0 03.0 3000 3.0 6000 3.0 9000
ENDE

```

# Airfoil TA4

```

REMO1
TRA21      1000 -1 -.7 -.5 -.3 -.2 -.1 0 .1 .2 .3 .5 .7 1 1000
TRA1       5 0 10 .2 15 .7 20 .9 25 1 26 2.5 27 3.8 28 5.5
TRA1       28.3 9.7 28.7 10.8 29 13.2 29.3 16 29.6 20
TRA1       0 25 30.4 -25 30.7 -20 31 -16 31.3 -13.2
TRA1       31.7 -10.8 32 -9.7 33 -5.5 34 -3.8 35 -2.5 40 -1
TRA1       45 -.9 50 -.7 55 -.2 60 0
TRA21      4 0 1 .1 .9 4 0 1 .1 .9 3 .3 0 2
PAN 13
ALFA213 13 -12.,-10.,-8.,-6.,-4.,-2.,0.,2.,4.,6.,8.,10.,12.
RE 130 0 03.0 3000 3.0 6000 3.0 9000
ENDE

```

# Airfoil TA5

```

REMO1
TRA21      1000 -1 -.7 -.5 -.3 -.2 -.1 0 .1 .2 .3 .5 .7 1 1000
TRA1       5 0 10 0 15 0 20 0 25 0 26 0 27 .01 28 .2
TRA1       28.3 1.2 28.7 1.9 29 3 29.3 4.5 29.6 7.8
TRA1       0 30 30.4 -30 30.7 -7.8 31 -4.5 31.3 -3
TRA1       31.7 -1.9 32 -1.2 33 -.2 34 -.01 35 0 40 0
TRA1       45 0 50 0 55 0 60 0
TRA21      4 0 1 .1 .95 4 0 1 .1 .95 3 .3 0 2
PAN 13
ALFA213 13 -12.,-10.,-8.,-6.,-4.,-2.,0.,2.,4.,6.,8.,10.,12.
RE 130 0 03.0 3000 3.0 6000 3.0 9000
ENDE

```

#### Airfoil T25

REMO1  
TRA21 1000 -1 -.7 -.5 -.3 -.2 -.1 0 .1 .2 .3 .5 .7 1 1000  
TRA1 5 1.02 10 1.07 15 1.18 20 1.41 25 1.96 26 2.19 27 2.53 28 3.05  
TRA1 28.3 3.29 28.7 3.67 29 4.41 29.3 4.47 29.6 5.08  
TRA1 0 6.68 30.4 -6.68 30.7 -5.08 31 -4.47 31.3 -4.41  
TRA1 31.7 -3.67 32 -3.29 33 -3.05 34 -2.53 35 -2.19 40 -1.96  
TRA1 45 -1.41 50 -1.18 55 -1.07 60 -1.02  
TRA21 4 0 1 .1 .9 4 0 1 .1 .9 3 .3 0 2  
PAN 13  
ALFA213 13 -12.,-10.,-8.,-6.,-4.,-2.,0.,2.,4.,6.,8.,10.,12.  
RE 130 0 03.0 3000 3.0 6000 3.0 9000  
ENDE

#### Airfoil T30

REMO1  
TRA21 1000 -1 -.7 -.5 -.3 -.2 -.1 0 .1 .2 .3 .5 .7 1 1000  
TRA1 5 1.02 10 1.09 15 1.23 20 1.51 25 2.25 26 2.56 27 3.04 28 3.81  
TRA1 28.3 4.18 28.7 4.76 29 5.45 29.3 6.03 29.6 7.03  
TRA1 0 9.78 30.4 -9.78 30.7 -7.03 31 -6.03 31.3 -5.45  
TRA1 31.7 -4.76 32 -4.18 33 -3.81 34 -3.04 35 -2.56 40 -2.25  
TRA1 45 -1.51 50 -1.23 55 -1.09 60 -1.02  
TRA21 4 0 1 .1 .9 4 0 1 .1 .9 3 .3 0 2  
PAN 13  
ALFA213 13 -12.,-10.,-8.,-6.,-4.,-2.,0.,2.,4.,6.,8.,10.,12.  
RE 130 0 03.0 3000 3.0 6000 3.0 9000  
ENDE

#### Airfoil T3

REMO1  
TRA21 1000 -1 -.7 -.5 -.3 -.2 -.1 0 .1 .2 .3 .5 .7 1 1000  
TRA1 5 1.02 10 1.1 15 1.26 20 1.58 25 2.45 26 2.84 27 3.44  
TRA1 28 4.55 28.3 4.89 28.7 5.65 29 6.57 29.3 7.35 29.6 8.7  
TRA1 0 12.57 30.4 -12.57 30.7 -8.7 31 -7.35 31.3 -6.57  
TRA1 31.7 -5.65 32 -4.89 33 -4.55 34 -3.44 35 -2.84 40 -2.45  
TRA1 45 -1.58 50 -1.26 55 -1.1 60 -1.02  
TRA21 4 0 1 .1 .9 4 0 1 .1 .9 3 0 0 2  
PAN 13  
ALFA213 13 -12.,-10.,-8.,-6.,-4.,-2.,0.,2.,4.,6.,8.,10.,12.  
RE 130 0 03.0 3000 3.0 6000 3.0 9000  
ENDE

#### Airfoil T4

REMO1  
TRA21 1000 -1 -.7 -.5 -.3 -.2 -.1 0 .1 .2 .3 .5 .7 1 1000  
TRA1 5 1.028 10 1.12 15 1.32 20 1.74 25 2.93 26 3.5 27 4.4  
TRA1 28 6 28.3 6.7 28.7 8 29 9.6 29.3 10.9 29.6 13.4  
TRA1 0 20.9 30.4 -20.9 30.7 -13.4 31 -10.9 31.3 -9.6  
TRA1 31.7 -8 32 -6.7 33 -6 34 -4.4 35 -3.5 40 -2.93  
TRA1 45 -1.74 50 -1.32 55 -1.12 60 -1.028  
TRA21 4 0 1 .1 .9 4 0 1 .1 .9 3 .3 0 2  
PAN 13  
ALFA213 13 -12.,-10.,-8.,-6.,-4.,-2.,0.,2.,4.,6.,8.,10.,12.  
RE 130 0 03.0 3000 3.0 6000 3.0 9000  
ENDE

# **Airfoil T402**

```

REM01
TRA21      1000 -1 -.7 -.5 -.3 -.2 -.1 0 .1 .2 .3 .5 .7 1 1000
TRA1       5 .51 10 .56 15 .66 20 .86 25 1.5 26 1.7 27 2.2 28 3
TRA1       28.3 3.4 28.7 4 29 4.8 29.3 5.4 29.6 6.7
TRA1       0 10.4 30.4 -10.4 30.7 -6.7 31 -5.4 31.3 -4.8
TRA1       31.7 -4 32 -3.4 33 -3 34 -2.2 35 -1.7 40 -1.5
TRA1       45 -.86 50 -.66 55 -.56 60 -.51
TRA21      4 0 1 .1 .9 4 0 1 .1 .9 3 .3 0 2
PAN 13
ALFA213 13 -12.,-10.,-8.,-6.,-4.,-2.,0.,2.,4.,6.,8.,10.,12.
RE 130 0 03.0 3000 3.0 6000 3.0 9000
ENDE

```

# **Airfoil T22**

```

REM01
TRA21      1000 -1 -.7 -.5 -.3 -.2 -.1 0 .1 .2 .3 .5 .7 1 1000
TRA1       5 .51 10 .58 15 .7 20 1 25 1.9 26 2.4 27 3.2 28 4.65
TRA1       28.3 5.4 28.7 6.75 29 8.45 29.3 10 29.6 12.9
TRA1       0 22.35 30.4 -22.35 30.7 -12.9 31 -10 31.3 -8.45
TRA1       31.7 -6.75 32 -5.4 33 -4.65 34 -3.2 35 -2.4 40 -1.9
TRA1       45 -1 50 -.7 55 -.58 60 -.51
TRA21      4 0 1 .1 .9 4 0 1 .1 .9 3 .3 0 2
PAN 13
ALFA213 13 -12.,-10.,-8.,-6.,-4.,-2.,0.,2.,4.,6.,8.,10.,12.
RE 130 0 03.0 3000 3.0 6000 3.0 9000
ENDE

```

# **Airfoil T503**

```

REM01
TRA21      1000 -1 -.7 -.5 -.3 -.2 -.1 0 .1 .2 .3 .5 .7 1 1000
TRA1       5 .34 10 .38 15 .47 20 .66 25 1.3 26 1.6 27 2.1 28 3.2
TRA1       28.3 3.7 28.7 4.5 29 5.6 29.3 6.67 29.6 8.6
TRA1       0 14.9 30.4 -14.9 30.7 -8.6 31 -6.67 31.3 -5.6
TRA1       31.7 -4.5 32 -3.7 33 -3.2 34 -2.1 35 -1.6 40 -1.3
TRA1       45 -.66 50 -.47 55 -.38 60 -.34
TRA21      4 0 1 .1 .9 4 0 1 .1 .9 3 .3 0 2
PAN 13
ALFA213 13 -12.,-10.,-8.,-6.,-4.,-2.,0.,2.,4.,6.,8.,10.,12.
RE 130 0 03.0 3000 3.0 6000 3.0 9000
ENDE

```

# **Airfoil T603**

```

REM01
TRA21      1000 -1 -.7 -.5 -.3 -.2 -.1 0 .1 .2 .3 .5 .7 1 1000
TRA1       5 .34 10 .39 15 .5 20 .76 25 1.69 26 2.2 27 3.1 28 5.1
TRA1       28.3 5.8 28.7 7.5 29 9.9 29.3 12.1 29.6 16.5
TRA1       0 31.9 30.4 -31.9 30.7 -16.5 31 -12.1 31.3 -9.9
TRA1       31.7 -7.5 32 -5.8 33 -5.1 34 -3.1 35 -2.2 40 -1.69
TRA1       45 -.76 50 -.5 55 -.39 60 -.34
TRA21      4 0 1 .1 .9 4 0 1 .1 .9 3 .3 0 2
PAN 13
ALFA213 13 -12.,-10.,-8.,-6.,-4.,-2.,0.,2.,4.,6.,8.,10.,12.
RE 130 0 03.0 3000 3.0 6000 3.0 9000
ENDE

```

#### Airfoil T504

REMO1  
TRA21 1000 -1 -.7 -.5 -.3 -.2 -.1 0 .1 .2 .3 .5 .7 1 1000  
TRA1 5 .26 10 .29 15 .35 20 .5 25 .96 26 1.2 27 1.6 28 2.4  
TRA1 28.3 2.7 28.7 3.4 29 4.2 29.3 5 29.6 6.4  
TRA1 0 11.2 30.4 -11.2 30.7 -6.4 31 -5 31.3 -4.2  
TRA1 31.7 -3.4 32 -2.7 33 -2.4 34 -1.6 35 -1.2 40 -.96  
TRA1 45 -.5 50 -.35 55 -.29 60 -.26  
TRA21 4 0 1 .1 .9 4 0 1 .1 .9 3 .3 0 2  
PAN 13  
ALFA213 13 -12.,-10.,-8.,-6.,-4.,-2.,0.,2.,4.,6.,8.,10.,12.  
RE 130 0 03.0 3000 3.0 6000 3.0 9000  
ENDE

#### Airfoil T604

REMO1  
TRA21 1000 -1 -.7 -.5 -.3 -.2 -.1 0 .1 .2 .3 .5 .7 1 1000  
TRA1 5 .26 10 .29 15 .38 20 .57 25 1.27 26 1.65 27 2.3 28 3.6  
TRA1 28.3 4.3 28.7 5.6 29 7.4 29.3 9.1 29.6 12.4  
TRA1 0 23.9 30.4 -23.9 30.7 -12.4 31 -9.1 31.3 -7.4  
TRA1 31.7 -5.6 32 -4.3 33 -3.6 34 -2.3 35 -1.65 40 -1.27  
TRA1 45 -.57 50 -.38 55 -.29 60 -.26  
TRA21 4 0 1 .1 .9 4 0 1 .1 .9 3 .3 0 2  
PAN 13  
ALFA213 13 -12.,-10.,-8.,-6.,-4.,-2.,0.,2.,4.,6.,8.,10.,12.  
RE 130 0 03.0 3000 3.0 6000 3.0 9000  
ENDE

#### Airfoil T234

REMO1  
TRA21 1000 -1 -.7 -.5 -.3 -.2 -.1 0 .1 .2 .3 .5 .7 1 1000  
TRA1 5 .26 10 .3 15 .39 20 1.12 25 1.5 26 2 27 2.95  
TRA1 28 4.9 28.3 6 28.7 8 29 10.8 29.3 13.5 29.6 19  
TRA1 0 39.48 30.4 -39.48 30.7 -19 31 -13.5 31.3 -10.8  
TRA1 31.7 -8 32 -6 33 -4.9 34 -2.95 35 -2 40 -1.5  
TRA1 45 -1.12 50 -.39 55 -.3 60 -.26  
TRA21 4 0 1 .1 .9 4 0 1 .1 .9 3 .3 0 2  
PAN 13  
ALFA213 13 -12.,-10.,-8.,-6.,-4.,-2.,0.,2.,4.,6.,8.,10.,12.  
RE 130 0 03.0 3000 3.0 6000 3.0 9000  
ENDE

#### Airfoil T505

REMO1  
TRA21 1000 -1 -.7 -.5 -.3 -.2 -.1 0 .1 .2 .3 .5 .7 1 1000  
TRA1 5 .21 10 .23 15 .28 20 .4 25 .77 26 .97 27 1.29 28 1.9  
TRA1 28.3 2.2 28.7 2.8 29 3.38 29.3 4 29.6 5.16  
TRA1 0 8.94 30.4 -8.94 30.7 -5.16 31 -4 31.3 -3.38  
TRA1 31.7 -2.8 32 -2.2 33 -1.9 34 -1.29 35 -.97 40 -.77  
TRA1 45 -.4 50 -.28 55 -.23 60 -.21  
TRA21 4 0 1 .1 .9 4 0 1 .1 .9 3 .3 0 2  
PAN 13  
ALFA213 13 -12.,-10.,-8.,-6.,-4.,-2.,0.,2.,4.,6.,8.,10.,12.  
RE 130 0 03.0 3000 3.0 6000 3.0 9000  
ENDE

# Airfoil T605

```

REM01
TRA21      1000 -1 -.7 -.5 -.3 -.2 -.1 0 .1 .2 .3 .5 .7 1 1000
TRA1       5 .20 10 .23 15 .3 20 .46 25 1. 26 1.3 27 1.87 28 3.
TRA1      28.3 3.5 28.7 4.5 29 5.6 29.3 7.2 29.6 9.9
TRA1       0 19.1 30.4 -19.1 30.7 -9.9 31 -7.2 31.3 -5.6
TRA1      31.7 -4.5 32 -3.5 33 -3. 34 -1.87 35 -1.3 40 -1.
TRA1      45 -.46 50 -.3 55 -.23 60 -.20
TRA21      4 0 1 .1 .9 4 0 1 .1 .9 3 .3 0 2
PAN 13
ALFA213 13 -12.,-10.,-8.,-6.,-4.,-2.,0.,2.,4.,6.,8.,10.,12.
RE 130 0 03.0 3000 3.0 6000 3.0 9000
ENDE

```

# Airfoil T6605

```

REM01
TRA21      1000 -1 -.7 -.5 -.3 -.2 -.1 0 .1 .2 .3 .5 .7 1 1000
TRA1       5 .21 10 .24 15 .31 20 .5 25 1.2 26 1.62 27 2.4 28 3.9
TRA1      28.3 4.8 28.7 6.4 29 8.6 29.3 10.8 29.6 15.2
TRA1       0 31.6 30.4 -31.6 30.7 -15.2 31 -10.8 31.3 -8.6
TRA1      31.7 -6.4 32 -4.8 33 -3.9 34 -2.4 35 -1.62 40 -1.2
TRA1      45 -.5 50 -.31 55 -.24 60 -.21
TRA21      4 0 1 .1 .9 4 0 1 .1 .9 3 .3 0 2
PAN 13
ALFA213 13 -12.,-10.,-8.,-6.,-4.,-2.,0.,2.,4.,6.,8.,10.,12.
RE 130 0 03.0 3000 3.0 6000 3.0 9000
ENDE

```

### Vita

Captain Gregory A. Sharp was born on 11 January 1964 in Cincinnati, Ohio. In 1982, he graduated from Milford High School located in Milford, Ohio. He entered the Reserve Officer Training Corps at the University of Cincinnati, where he received a Bachelor of Science degree in Aerospace Engineering in 1987. His first assignment at the Air Force Flight Test Center, Edwards AFB, California was as a Avionics/Weapons Flight Test Engineer for the F-15E Dual-Role Fighter. He was then selected to attend the Air Force Institute of Technology, beginning in June 1991. Upon graduation, Captain Sharp will be assigned to the Flight Dynamics Directorate of Wright Laboratory, Wright-Patterson AFB, Ohio.

Permanent Address: 3718 Benfield Dr.  
Kettering, Ohio 45429

REPORT DOCUMENTATION PAGE			Form Approved OMB No. 0704-0188	
<small>Please use this space to provide a brief summary of information requested in the report, including the time for reviewing instructions, searching existing data sources, gathering and maintaining the data needed, and completing and reviewing the collection of information. Send comments regarding this burden estimate or any other aspect of this collection of information, including suggestions for reducing this burden, to Washington Headquarters Services, Directorate for Information Operations and Reports, 1215 Jefferson Avenue, Suite 1204, Washington, DC 20540-4302, and to the Office of Management and Budget, Paperwork Reduction Project (0704-0188), Washington, DC 20503.</small>				
1. AGENCY USE ONLY (Leave blank)	2. REPORT DATE <b>Decemeber 1992</b>	3. REPORT TYPE AND DATES COVERED <b>Master's Thesis</b>		
4. TITLE AND SUBTITLE  <b>Application of the Program PROFILE for the Design of Low-Speed, Low-Observable Configuration Airfoils</b>		5. FUNDING NUMBERS		
6. AUTHOR(S)  <b>Gregory A. Sharp</b>				
7. PERFORMING ORGANIZATION NAME(S) AND ADDRESS(ES)  <b>Air Force Institute of Technology Wright-Patterson AFB, Ohio</b>		8. PERFORMING ORGANIZATION REPORT NUMBER  <b>AFIT/GAE/ENY/92D-09</b>		
9. SPONSORING MONITORING AGENCY NAME(S) AND ADDRESS(ES)  <b>WL/FIMM Wright-Patterson AFB, Ohio 45433</b>		10. SPONSORING MONITORING AGENCY REPORT NUMBER		
11. SUPPLEMENTARY NOTES				
12a. DISTRIBUTION AVAILABILITY STATEMENT  <b>Unlimited Distribution</b>		12b. DISTRIBUTION CODE		
13. ABSTRACT (Maximum 200 words)  <p>This study investigated the use of the program PROFILE for the design of low-speed, low-observable configuration airfoils. For our purposes, low-observable configuration is defined as being characterized by a small leading-edge radius of less than 1.18 percent chord and a thickness-to-chord ratio of 2.5 to 5.5 percent. A methodology was developed whereby the input parameters to prescribe the velocity distribution over the airfoil could be determined by a power law relationship. This relationship enables the designer to develop symmetric airfoils with the desired thickness-to-chord and leading-edge radius within the stated constraints. The resulting symmetric airfoils compared very well with NACA 4-digit airfoils of like thickness-to-chord ratio. The resulting airfoils have an increased stall angle compared to the NACA 4-digit airfoils.</p>				
14. SUBJECT TERMS <b>Low-Speed, Low-Observable, Symmetric Airfoils, Small Leading-Edge Radius, PROFILE, Small Thickness-to-Chord Ratio</b>		15. NUMBER OF PAGES <b>214</b>		16. PRICE CODE
17. SECURITY CLASSIFICATION OF REPORT  <b>UNCLASSIFIED</b>	18. SECURITY CLASSIFICATION OF THIS PAGE  <b>UNCLASSIFIED</b>	19. SECURITY CLASSIFICATION OF ABSTRACT  <b>UNCLASSIFIED</b>	20. LIMITATION OF ABSTRACT  <b>UL</b>	